Fraunhofer ISE

Fraunhofer Institute for Solar Energy Systems ISE

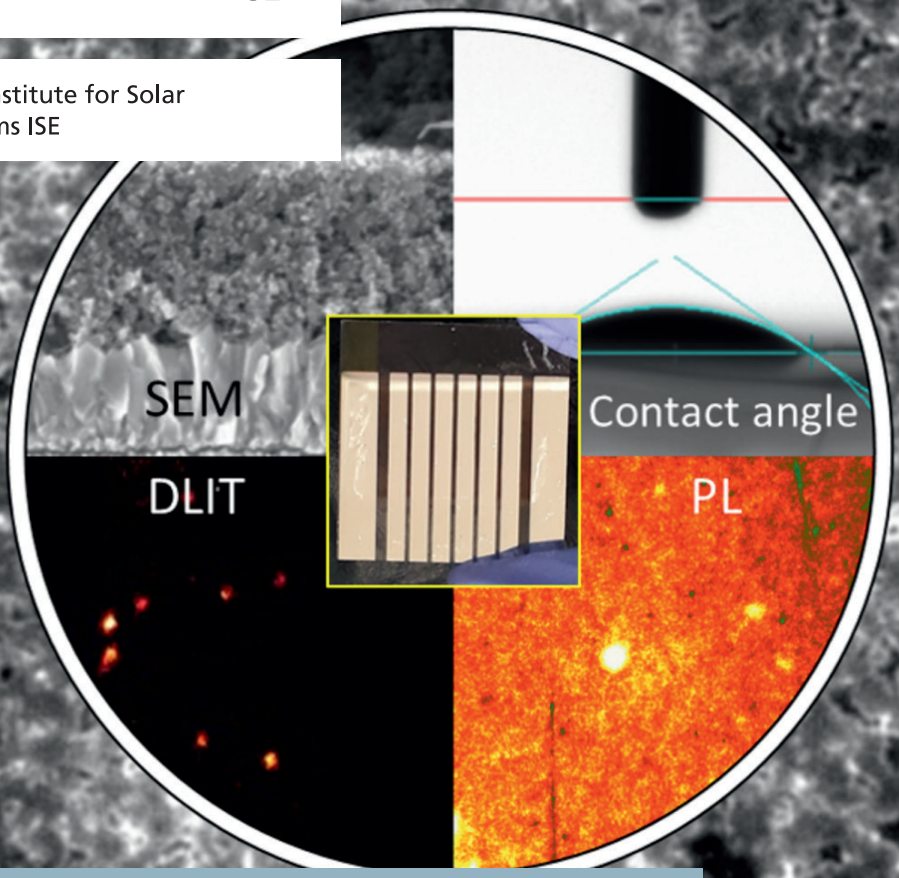

Solar Energy and Systems Research

Interfacial Analysis of Perovskite Solar Cells Using Sub-Cells

Gayathri Mathiazhagan

UNI FREIBURG

Fraunhofer Verlag

Fraunhofer Institute for Solar Energy Systems ISE

Solare Energie- und Systemforschung /
Solar Energy and Systems Research

Interfacial Analysis of Perovskite Solar Cells Using Sub-Cells

Gayathri Mathiazhagan

Fraunhofer Verlag

Contact:
Fraunhofer Institute for Solar Energy Systems ISE
Heidenhofstrasse 2
79110 Freiburg
Germany
Phone +49 761/4588-5150
info@ise.fraunhofer.de
www.ise.fraunhofer.de

Cover illustration: © Gayathri Mathiazhagan

Bibliographic information of the German National Library:
The German National Library has listed this publication in its Deutsche Nationalbibliografie; detailed bibliografic data is available in the internet at www.dnb.de.

ISSN: 2512-3629
ISBN: 978-3-8396-1839-4

Book Series: »Solare Energie- und Systemforschung / Solar Energy and Systems Research«

D 25

Zugl.: Freiburg, Univ., Diss., 2020

Print and finishing:
Fraunhofer Verlag, Mediendienstleistungen

This book was printed with chlorine- and acid-free paper.

Nobelstrasse 12
70569 Stuttgart
Germany
verlag@fraunhofer.de
www.verlag.fraunhofer.de

is a constituent entity of the Fraunhofer-Gesellschaft, and as such has no seperate legal status.

Fraunhofer-Gesellschaft zur Förderung
der angewandten Forschung e.V.
Hansastrasse 27 c
80686 München
Germany
www.fraunhofer.de

Interfacial Analysis of Perovskite Solar Cells Using Sub-Cells

Dissertation zur Erlangung des Doktorgrades der

Technischen Fakultät der

Albert-Ludwigs-Universität Freiburg im Breisgau

vorgelegt von

Gayathri Mathiazhagan

angefertigt am

Fraunhofer Institut für Solare Energiesysteme (ISE)

Commonwealth Scientific and Industrial Research Organisation (CSIRO)

gefördert durch die

Landesgraduiertenförderung – Baden-Württemberg

Dekan: Prof. Dr. Rolf Backofen

Erstgutachter: Prof. Dr. Stefan Glunz

Zweitgutachter: Prof. Dr. Aziz Dinia

Datum der mündlichen Prüfung: 23.10.2020

When learning is purposeful, creativity blossoms

When creativity blossoms, thinking emanates

When thinking emanates, knowledge is fully lit

When knowledge is lit, economy flourishes.

-Dr. A. P. J. Abdul Kalam

(1931 – 2015)

To my Amma

My Hero

My Angel

Table of Contents

List of Figures

List of Abbreviations

PSC	= Perovskite solar cells
HTL	= Hole transport layer
HTM	= Hole transport material
ETL	= Electron transport layer
ETM	= Electron transport material
c-ETL	= Compact electron transport layer
mp-ETL	= Mesoporous electron transport layer
CTL	= Charge transport layer
CG	= Carbon-graphite
CG-PSC	= Carbon-graphite based perovskite solar cell
PCE	= Power conversion efficiency
FTO	= Flurione tin oxide
CIGS	= Copper indium gallium selenide
CdTe	= Cadmium Telluride
DLIT	= Dark lock-in thermography
ALD	= Atomic layer deposition
SPD	= Spray pyrolysis deposition
PVD	= Physical vapor deposition
SEM	= Scanning electron microscope
TEM	= Tranmission electron microscope
HRTEM	= High resolution transmission electron microscope
EDX	= Energy dispersive X-ray
AFM	= Atomic force microscopy
XRD	= X-ray diffraction
XPS	= X-ray photoelectron spectroscopy
CA	= Contact angle
PL	= Photoluminescence
DLIT	= Dark lock-in thermography
MPPT	= Maximum power point tracking
V_{OC}	= Open-circuit voltage
J_{SC}	= Short-circuit current
OC	= Open circuit
SC	= Short circuit
VB	= Valence band
CB	= Conduction band
AZO	= Aluminium zinc oxide
E_g	= Bandgap energy
MAPI	= Methyl ammonium lead iodide
TCO	= Transparent conductive oxide
UV	= Ultraviolet
BL	= Blocking layer
DSSC	= Dye sentisized solar cell
CSIRO	= Commonwealth scientific and industrial research organisation
EM	= Electron microscope
SDD	= Silicon drift detector

BSE	= Back scattered electrons
SE	= Secondary electrons
PMT	= Photon-multiplier tube
ROI	= Region of interest
SAED	= Selected area electron diffraction
HOMO	= High energy occupied molecular orbital level
LUMO	= Low energy occupied molecular orbital level
UHV	= Ultra high vacuum
IR	= Infrared
OCVD	= Open-circuit voltage decay
PESA	= Photoelectron spectroscopy in air
RMS	= Root mean square
SL	= Spacer layer

Abstract

Perovskite solar cells (PSCs) are gaining increasing importance and attention in the last decade. Even though high conversion efficiencies have been reached, one of the major bottlenecks for the commercialization of PSCs is their stability. Issues at the interfaces in the multilayered PSC architecture are suspected to be the significant contributor in causing low stability.

This doctoral thesis focusses on the analysis of various interfaces present in PSCs and traces methods to improve them. The investigation of individual interfaces is performed by developing suitable sub-cells, i.e., comprising only the particular interface of interest. Various optical and structural characterisation methods are used to determine layer and interface properties. After this step, complete devices are manufactured from the sub-cells, and their final performance is investigated to conclude the role and optimization of the interfaces.

The thesis accounts for the analysis of the interfacial quality of different n-i-p perovskite solar cells configurations, being based on hole-transport-layer (HTL)/Au or HTL-free/carbon-graphite (CG) electrodes. In particular, the former has been developed in a 6-month study exchange in Commonwealth Scientific and Industrial Research Organisation (CSIRO), Melbourne, Australia, and the latter developed throughout three years at Fraunhofer ISE. This peculiarity of working with various perovskite solar cell architecture gives this work a broad and comprehensive overview of the role of interfaces, particularly when all the layers are processed in-room ambient.

Three different types of interfaces were studied using suitable sub-cell configurations, and complete devices investigated thereafter.

1. Firstly, a cell architecture involving slot-die coated **SnO_2** as an electron transport layer (ETL) was used to investigate the quality of the **ETL/perovskite** interface in a PSC. For this purpose, an ITO/SnO_2/perovskite sub-cell was used. UV treatment of the SnO_2/perovskite interface led to an improved device stability attributed to the passivation effect by excess PbI_2. This improvement resulted in retaining 80 % of the initial PCE value after 14 h of continuous AM 1.5 G illumination.

2. Various hole blocking layer (HBL) processing techniques were used to identify the quality and the role of the HBL in preventing recombination at the **FTO/perovskite interface** in a PSC. The layers were investigated through dark lock-in thermography (DLIT). An FTO/c-TiO_2/ μ-graphite sub-cell was used for this purpose. The results showed that **atomic layer deposition (ALD) of TiO_2** allows to fabricate pin-hole free, shunt-free HBLs, thereby reducing the recombination at the FTO/perovskite interface and achieving photo-voltages greater than 900 mV.
3. Thirdly, the role of the spacer layer in preventing recombination at the **mp-ETL/cathode** interface for an HTL-free PSC architecture was investigated. For the first time, **sputtered Al_2O_3** with thickness in the range of 10 – 100 nm was analyzed. FTO/c-TiO_2/ mp-TiO_2/Al_2O_3 sub-cell was used for quality analysis. The results showed that an ultra-thin 40 nm sputtered Al_2O_3 is sufficient to prevent the recombination at the mp-TiO_2/carbon-graphite (CG) interface. A stable photo-voltage of 1 V and power conversion efficiency (PCE) of 12.1 % was achieved. Thereby, a double-mesoscopic architecture for PSC has been introduced.

The thesis shows that developing suitable sub-cells allows to investigate the quality of the various interfaces of PSCs individually and thus to understand their role in device stability. Finally, the findings from the sub-cell analysis are compared with the performance of complete devices to verify their significance. Thereby, methods to improve the interfaces can be found to achieve higher device efficiencies without compromising its stability.

Chapter - 1

Introduction

1 Introduction

After describing the motivation for the thesis, this chapter explains the structure of the thesis, along with the expected details in each section. An illustration is provided at the end of this section to give a bird's eye view into this doctoral thesis.

1.1 Motivation

The ability of perovskite as a light harvester, the flexibility in engineering its bandgap, and low-cost production has attracted many groups across the world to be involved in its research and development. In a short span of 10 years, PSCs has attained efficiency up to 25.2%[1], and a market growth forecast by 2028 to over $500 million[2]. Even though high efficiencies competing with other thin-film technologies such as Copper Indium Gallium Selenide (CIGS) and Cadmiun Telluride (CdTe) have been achieved, one central challenging aspect of commercializing the perovskite solar cells is their stability. Also, the use of hazardous lead creates a constraint for lead-based PSCs to be implemented on a large scale. Various mechanical, chemical, temperature, and environmental conditions (i.e., oxygen and moisture) are known to affect the lead halide-based PSCs. Chemical engineering of the perovskite (e.g., multi-cation, multi-halide, 2D/3D) itself has shown to remarkably extend the cell lifetime; however, its **interfaces** with charge transport layers (CTLs) are critical to bring this technology to a truly exploitable level.

Thus, when the perovskite absorber is sandwiched between the CTLs, the interface of the perovskite with the inorganic CTLs and the interface of the CTLs with the surface of the electrodes are crucial. Excellent interface properties are essential to attain efficient charge collection and transport. Additionally, imperfections/defects at the interfaces become centers for non-radiative recombination where photo-generated charge carriers are lost. Most publications investigate device stability using a complete device. The performance, when attributed to an individual interface, is always interfered by the performance of the other interfaces.Therefore, for a multilayered PSC, it is imperative to understand the changes happening at every interface. The performance of the cell-based on the changes in electrical properties at various stages of cell production has to be investigated, which provides an understanding of the role of the interfaces in device performance and stability.

The central idea of the thesis is shown in Figure 1. The approach of this work is to use a suitable sub-cell to investigate the interface of interest individually. Optical and structural investigations provided information on the nature of the materials involved. These investigations provide information not only on individual material properties but also, importantly, improve the understanding of changes of the interface, when it gets in contact with photo-absorber and other charge transportation layers. The results help in choosing materials, their fabrication technique, and treatments that need to be used in the individual steps involved in the manufacturing of the perovskite solar cells. Thus, it is essential to study the cause of stability issues through specific interface analysis. Henceforth this doctoral thesis aims to establish quality analysis on suitable sub-cells, which later guides in identifying solutions and strategies to improve PSC's performance and stability.

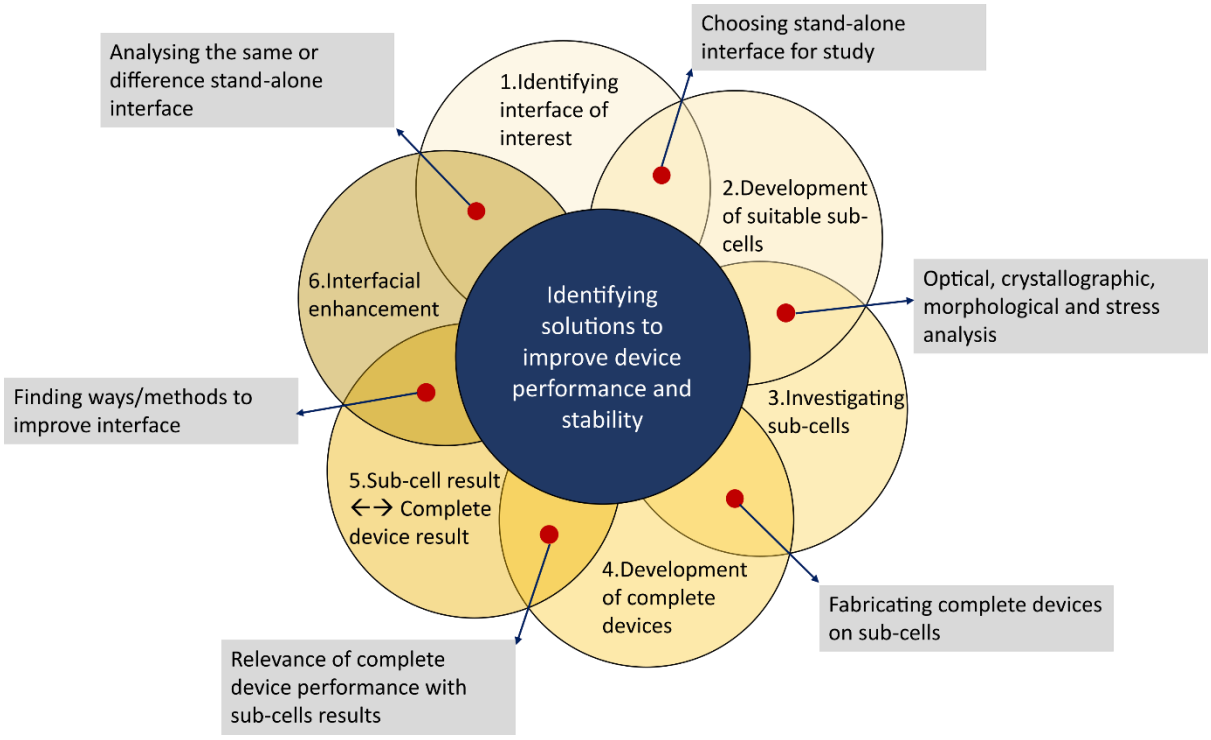

Figure 1: Central idea of this thesis

1.2 Thesis structure

The fundamental structure of this thesis is displayed in Figure 2. In the following, the content of the individual chapters is described.

Chapter 2 describes **the working principle and the structure of the perovskite solar cells (PSC)**. The cell architecture of PSCs is classified into three main categories, namely, planar,

mesoporous, and hybrid architecture. The differences, advantages, and disadvantages of each architecture are explained as sub-sections. Special attention is paid to the transport layer structure. Even though cheap and abundant materials are used as photo-absorbers in the main architecture of PSCs, using Spiro-OMeTAD and gold as hole transport layer and electrode, respectively, increases the production cost of PSCs drastically. The expensive materials were replaced by graphite to overcome this problem. This type of PSCs is called carbon-graphite based PSC (CG-PSC). The last part of Chapter 2 gives a detailed explanation of the role of each layer (i.e., blocking layer, ETL, insulation layer) present in CG-PSCs.

To improve the device performance, in this thesis, various **fabrication techniques** are involved in optimizing different layers of the device structure. Multiple fabrication techniques used are sputtering, slot-die coating, atomic layer deposition (ALD), spray-pyrolysis deposition (SPD), and screen printing. Chapter 3 explains the basic working principle of all the fabrication technique used. The explanation starts with the working principle, types involved in that technique, process parameters that influence the production of a reproducible layer, and finally, the manufacturing conditions/parameters that are optimized for the devices used in this thesis.

The working principle and setup of various **characterization techniques** are described in Chapter 4. It is mainly divided into two sub-sections, namely – structural and electrical characterizations. In each sub-section, a detailed explanation of characterization tools that are used to investigate the PSCs is given. Structural characterization mainly comprises of the crystallography and morphology analyzing tools such as scanning electron microscopy (SEM), electron diffraction (EDX), Transmission electron microscopy (TEM), atomic force microscopy (AFM), X-ray diffraction (XRD), and UV-vis spectroscopy. The electrical characterization sub-section comprises techniques used to investigate device performance and stability through Dark lock-in thermography (DLIT), J-V curve, maximum power point (MPP) tracking, and stable open-circuit voltage (V_{OC}) analysis. Time-dependent photoluminescence measurements and low light intensity measurements are also explained. This sub-section introduces unique data analysis and interpretation methods, especially for devices involved in this thesis.

Chapter 5 describes **the sub-cell characterization of the SnO_2/perovskite interface** involved in an n-i-p planar perovskite architecture. The sub-section begins with the purpose of investigating the ETL/perovskite interface. The experimental details are given, followed by

the result analysis. ITO/SnO_2/perovskite sub-cell is subjected to continuous UV stress for 500 h. The study shows that there is an excess concentration of PbI_2 at the perovskite surface of the sub-cell. However, completing device fabrication on the UV-treated sub-cell improves the stability through passivation introduced by excess PbI_2 in the perovskite. It is replicated in the continuous 1 sun illumination for 14 h, where only 20 % loss in the PCE was observed.

In Chapter 6, the role of **HBL at the FTO/perovskite interface in HTM-free carbon-graphite based PSCs** is investigated. A non-intrusive optical thermography technique, i.e., DLIT, is used and introduced as an essential tool to analyze the layer quality of the sub-cells. By using DLIT, HBL processed through spray-pyrolysis, sputtering, and ALD is compared using FTO/c-TiO_2/µ-graphite as the sub-cell. Results show an improved layer quality through the ALD technique. Complete devices were analyzed, and the results show that the recombination at the HBL interface has significantly been reduced, achieving more than 900 mV of photovoltage.

Chapter 7 focusses on the **ETL/graphite interface of HTM-free CG-PSCs**. The recombination at this interface is high, and the insulation layer (otherwise known as spacer layer) is mandatory in this kind of PSCs. Usually, a micrometer thick insulation layer is used. This section involves analyzing ultra-thin 40 nm of sputtered Al_2O_3 as a spacer layer. Morphological analysis of the mp-TiO_2/Al_2O_3 sub-cell shows that the sputtered layer does not hinder the perovskite infiltration into the charge transport layers. The results of complete devices show that the recombination at the ETL/graphite interface by the use of the ultra-thin layer is effectively reduced. This is reflected in a stable photovoltage of 1 V, along with a stable device performance achieving 12.1 %.

Finally in the conclusion (Chapter 8), the main results of this thesis are discussed. Future possibilities is given as outlook. A list of publications where I was the main author and co-author; and a list of conferences participated is provided at the end of the document.

Figure 2: Main device architectures (blue), the interfaces under investigation (orange), results (grey) and its conclusions (green).

Chapter - 2

Fundamentals

2 Fundamentals

Fundamentals chapter is dedicated to present the basics of a solar cell. The first half of this chapter explains the basic working principle of a solar cell. It is then followed by an introduction to the perovskite solar cells (PSCs) where different architectures of PSCs are explained. The last part of this chapter documents the role of each layer involved in the PSC. It also points out the issues that affect device performance as well as its stability.

2.1 Working principle of solar cell:

The solar cell works on the principle of the photoelectric effect. This principle involves the conversion of light energy into electrical energy. Following Plank's proposal in 1900 that light travels in discrete quanta or packets of energy, Albert Einstein proposed the law of photoelectric effect, which gave values for this packet of energy. These energy packets are named as photons, and their energy depends on the wavelength of light.

$$E\ (eV) = \frac{1.24}{\lambda\ (\mu m)} \qquad \textit{Eq 1}$$

where,

E = Energy of a photon (eV)

λ = Wavelength of light (µm)

2.1.1 Solid-state materials

Based on the distance between the valence band and conduction band, solid-state materials are classified into three categories, namely – metals, insulators, and semiconductors. The energy required for an electron to jump from the valence band to the conduction band is called the energy bandgap and is denoted as E_g. Figure 3 shows the graphical representation of all the solid-state materials.

- Metals – The valence band (VB) and conduction band (CB) overlap to ease the flow of electrons from the former to the later. No bandgap can be found.
- Insulators – The bandgap is very large such that electrons cannot be excited from the valence band to the conduction band. Hence, no flow of electrons.

- Semi-conductors – Bandgap is smaller than insulators. After absorbing energy equal or larger to the bandgap, the electrons can be excited from the valence band to the conduction band.

This characteristic feature of photogenerating electron-hole pairs in semi-conductors makes them ideal to be used in solar cell technology.

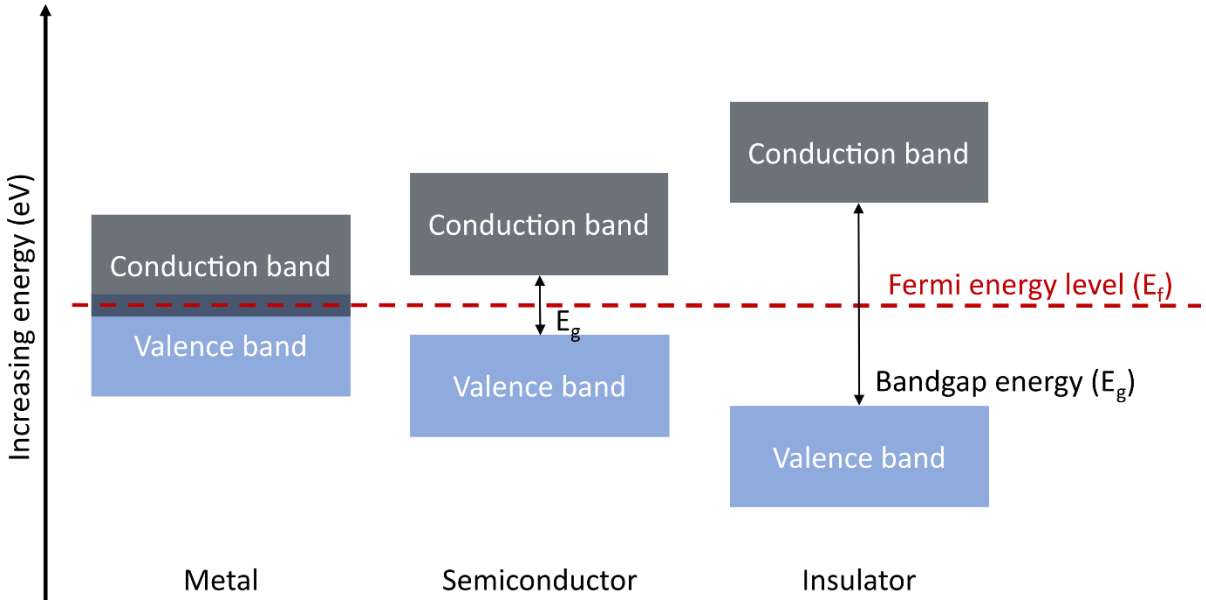

Figure 3: Graphical representation of solid-state materials

2.1.2 Photogeneration of charges

As shown in the previous section, in a semiconductor material, the valence band is found below the bandgap whereas, the conduction band is located above it. Figure 4 below represents the basic principle involved in a solar cell. The electrons are initially filled in the valence band. When a photon (sunlight) of energy equal or higher to their bandgap is incident on the material, the negatively charged electrons are excited to a higher energy level (i.e., the conduction band), leaving a space behind in the valence band. This space is the positively charged “hole”. Thus, an electron-hole pair is generated by an incident photon, and they are collectively called as photogenerated charges.

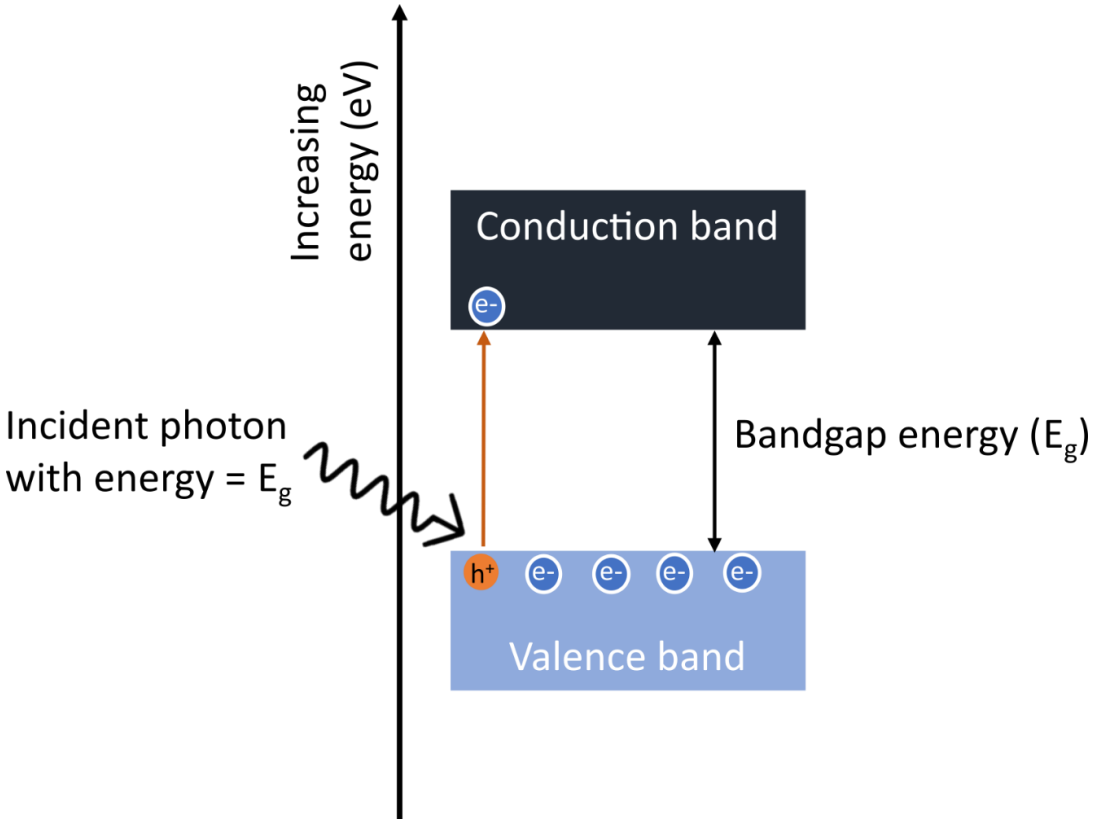

Figure 4: Schematic diagram of conduction in a semiconductor

It is to be noted that all incident solar energy cannot be harnessed into electrical energy. In 1960, Shockley and Queisser postulated that for a single semiconductor material only 30 % of the incident sunlight could be converted to useable power, which means that the maximum achievable solar cell efficiency for a single solar cell is around 30 % [3]. This limit resulting from a thermodynamic detailed balance theory is defined considering only the radiative recombination. Figure 5 shows the spectral losses and the wavelength window whose energy can be converted into electricity. 50 % of the sun's energy is lost due to the following reasons[4]:

- For photons with an energy higher than the bandgap, the excess energy after creating the photogenerated charge carriers is wasted as heat as the electron is rapidly thermalizing via phonon states to the lower edge of the conduction band.
- For photons with an energy lower than the bandgap, their energy is not sufficient to generate charges (*i.e.,* electron-hole pair).

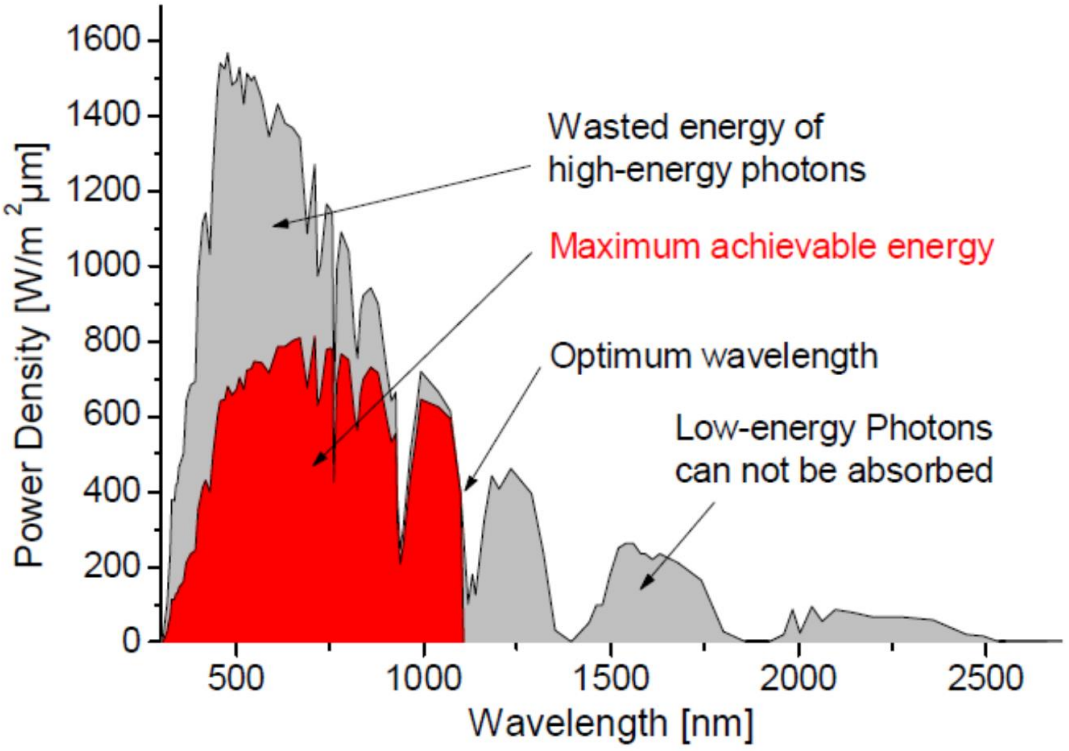

Figure 5: Maximum achievable energy based on the solar spectrum[4]

2.1.3 Extraction of photogenerated charges

Following the generation of photo-induced electron-hole pairs, their extraction is equally essential. Figure 6 shows the charge extraction in a solar cell. Two kinds of selective contacts are considered for this purpose. The primary role of these contacts is to pick-up one of the photogenerated charges (either electrons or holes). In an ideal solar cell, only charge selectivity is present, which means, as soon as the charges are created, they are attracted by their selective contacts.

However, in a practical solar cell construction, charge transport of the photogenerated charges to the selective contacts plays a crucial role. Imperfections in charge transport starts to introduce losses thereby the efficiency of a solar cell eventually reduces. Thus the charge transport should facilitate the occupation of specific charge well, such that the charges tend to move in the specified direction towards their selective contacts. Quasi-fermi level (E_f) represents the number of occupation states for a specific charge under illumination. The difference in the quasi-fermi levels in the photoabsorber give the maximum achievable photovoltage (V_{max}) of a solar cell. For electrons to be transported, more number of occupation states should be present near the conduction band of a material and more

number of occupation states should be present near valence band of a material for the hole transportation. When connected to an external circuit, depletion of the charges happenes near the selective contacts. At thermal equilibrium, a gradient of charge concentration is present that drives the transportation of charges towards their contacts provided the diffusion constant in the photoabsorber is large enough not to limit the current. Thereby, the charge current is given by Fick's law [5].

Considering only the chemical potential $\Phi_{chem,k}$, the charge current is:

$$j_k = -z_k q n_k D_k \frac{grad\ n_k}{n_k} = -\frac{\sigma_k}{z_k q} grad \Phi_{chem,k} \qquad \textit{Eq 2}$$

Considering the electrochemical potential, $n_k = \Phi_{chem,k} + z_k q \varphi$, which is identical to the quasi-fermi level $\mathrm{E_{f,k}}$, the charge current is:

$$j_k = \frac{\sigma_k}{q} grad\ E_{f,k} \qquad \textit{Eq 3}$$

where,

k = particles (electrons e or holes h)

$\mathrm{z_k q}$ = charge of the particle (C)

q = elementary charge (C)

φ = electrical potential (V)

$\mathrm{n_k}$ = electrochemical potential (J/mol)

$\mathrm{D_k} = \frac{\mu_k KT}{q}$ = diffusion co-efficient

σ_k = conductivity $(\Omega\ \mathrm{cm})^{-1}$

μ_k = mobility $(\mathrm{cm^2\ V^{-1}\ s^{-1}})$

T = Absolute temperature (K)

$grad\Phi_{chem,k}$ = chemical force

$\mathrm{E_{f.k}}$ = Quasi-Fermi level (eV)

Würfel et al. describes that at contact temperature and volume, the electrochemical potential of the particles makes the particles flow towards their transport layers and its differential conductivity transports the particles towards their respective contacts [5].

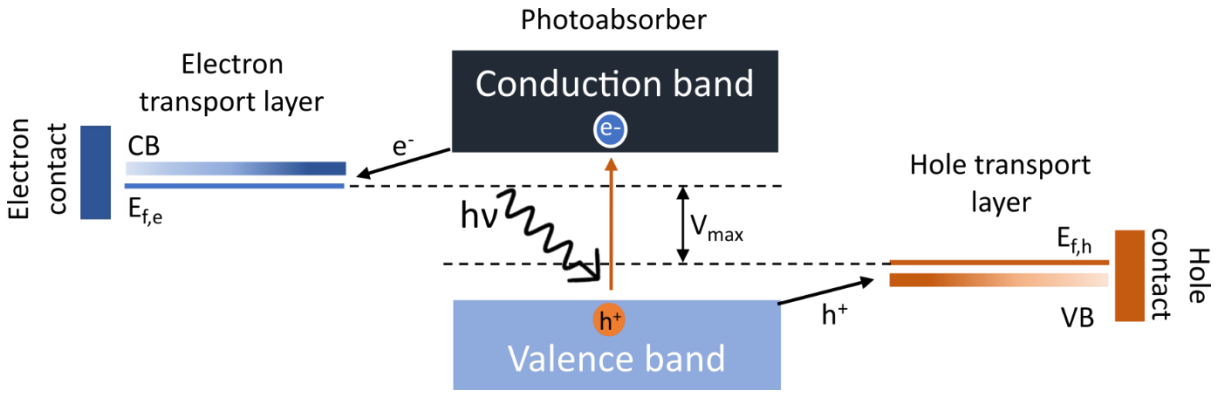

Figure 6: General working principle of a solar cell

2.2 Perovskite solar cells

Among innovative and potentially cheap novel solar cell technologies, Dye Solar Cells (DSC), and Organic solar cells emerge for their ease of fabrication and interest for future applications. These technologies have achieved about 11.9% and 11.5%, respectively [1]. Tunable bandgap, excellent absorption co-efficient, long carrier diffusion length, low exciton binding energies make them a promising material for the development of third-generation solar cell fabrication. The main advantage of these technologies also includes their low production cost and the potential of mass production in the future. Nevertheless, one of the main issues found in these technologies is their low stability. Perovskite solar cells are the newly evolving organic-inorganic solar cell technology coming from the DSCs as their base technology. They have gained attention since 2009 after their use in the liquid-based dye-sensitized solar cells by Miyasaka *et al.,* where dye molecules were replaced with perovskite crystals[6].

2.2.1 Perovskite crystal structure

Gustav Rose, in 1839 discovered the perovskite crystal structure [7,8] and named it after Lev Perovski, a Russian scientist [7]. Calcium titanium oxide was the first discovered perovskite. Hence, all the crystals that had a chemical structure AMX_3 were called perovskite. A single valence 'A' cation and two-valence 'M' cation are bound together by three 'X' anions resulting in a cubic structure. However, as the two-valent cation is forming an octahedral substructure with three anions, the ionic crystal structure is distorted, making perovskites tuneable. In particular, by changing the size and type of the charge balancing single-valence cation, perovskites with various electrical and optoelectronic properties can be obtained.

Goldschmidt tolerance factor 't' determines the stability of the perovskite crystal structure by calculating the difference between the average bond lengths of A-X and M-X [9]. It is given below as follows:

$$t = \frac{(R_M + R_X)}{\sqrt{2(R_A + R_X)}} \qquad \textit{Eq 4}$$

where,

t = tolerance factor

R_A = ionic radii of A cation (Å)

R_M = ionic radii of M cation (Å)

R_X = ionic radii of X anion (Å)

The value of the tolerance factor is ascribed to the various structure of perovskite crystals. They are:

1. t = 1 corresponds to the ideal cubic structure. Eg. $SrTiO_3$
2. 0.89 < t < 1 corresponds to cubic structure
3. t < 0.89 corresponds to the orthorhombic structure. Example: $GdFeO_3$
4. t > 1 corresponds to the hexagonal structure. Example: $BaNiO_3$

Even though perovskites have similar chemical structure, two major classifications based on the 'X' anion are:

(a) ***Inorganic oxide perovskite*** – Perovskites (AMO_3) where divalent 'A' cations such as Mg^{2+}, Ca^{2+}, Sr^{2+}, Ba^{2+}, $Pb^{2+,}$ and tetravalent 'M' cations such as Ti^{4+}, Si^{4+}, Fe^{4+} are bounded by 'O' anion. Example: $BaTiO_3$[7].

(b) ***Halide perovskites*** – Perovskite (AMX_3) where 'X' is halogen anions. The halide perovskites are further classified into two types based on the elements used for 'A' and 'M.'

i. *Alkali-halide perovskites* – Here, monovalent alkali metal such as Li^+, Na^+, K^+, Rb^+, Cs^+ for 'A' and divalent cations such as Be^{2+}, Mg^{2+}, Ca^{2+}, Sr^{2+}, Ba^{2+}, Zn^{2+}, Ge^{2+}, Sn^{2+}, Pb^{2+}, Fe^{2+}, Co^{2+}, Ni^{2+} for 'M' are joined by halogens such as F^-, Cl^-, Br^-, I^- as 'X' anions. Example: $KPbI_3$[10] .
ii. *Organo-metal halide perovskites* – Here, aliphatic or aromatic ammoniums such as methylammonium, tetramethylammonium, formamidium, or guanidium for 'A' cation

and divalent group 14 elements as mentioned in (i) for 'M' cations are coupled by 'X' halogen anions. Example: $MAPbI_3$[9].

Excellent opto-electronic properties, along with the possibility of low-temperature processing of group 14 elements, makes them an important candidate for 'M' cations. Among the two halide categories, even though alkali-halide perovskites are reported in the literature, they are so far not used in the fabrication of solar cells.

As explained in Bruschka's Ph.D. thesis, perovskite structure can be either 3D, 2D, or co-exist with each other. 2D perovskites are atomically thin 3D perovskites. While the 3D perovskites are denoted as AMX_3, 2D perovskites are represented as A_2MX_4 (Figure 7). In recent times, they are becoming popular in PSCs owing to their stability in the ambient environment. Also, their unique properties from the quantum confinement effect make them suitable for broader applications such as Light emitting diode (LED) and other photoelectronic applications[11]. The commonly found 2D perovskite is the Ruddleson-Popper perovskite, where a 2D structure is obtained without comprising the atomic thickness of the crystal structure [12]. These perovskites though not as efficient as 3D perovskites, are gaining popularity through its stability and ability to play diverse roles such as passivation layer or capping layer [13]. In this thesis, chapter 5 uses a multi-cation 3D perovskite, whereas chapters 6 and 7 consists of a mixed 3D/2D perovskite.

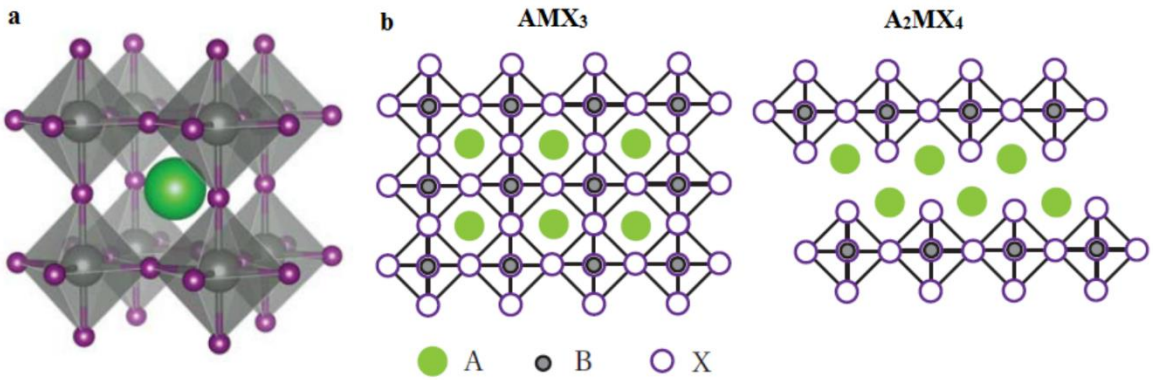

Figure 7: (a) AMX_3 perovskite crystal 3D view (b) Projected view of 3D and 2D structured perovskite solar cells [14]

2.2.2 Basic structure of PSCs and its working

To better understand the functioning of the PSCs, it is vital to be familiarised with its basic architecture. There are different architectures involved in it, which will be described in the next section.

Figure 8 shows the cross-sectional SEM of a planar PSC. It consists of the following layers:

Anode: In an n-i-p perovskite solar cell, layers are constructed on a conductive glass usually fluorine tin oxide (FTO), Indium doped tin oxide (ITO) or Aluminium Zinc oxide (AZO). ITO glasses are preferred in solar cells whose fabrication technique involves low-temperature processing. They are popular in solar cells, which are fabricated on flexible substrates such as polyethylene terephthalate. As ITO's conductivity is affected by higher temperatures, temperature stable low cost FTO glasses are used in cases where high processing/sintering temperatures are involved.

n-type electron transport layer (ETL): The primary function of this layer is to collect the photogenerated electrons and transport them to the anode. The most common ETL materials used are TiO_2, SnO_2, and ZnO, among which TiO_2 is popular in high-temperature PSCs and SnO_2 in low-temperature PSCs. According to the type of architecture involved, the ETL can be a single compact layer or a combination of a mesoporous layer on top of a compact layer.

Perovskite photo absorber layer: Above the ETL, a perovskite layer is processed. When the light is incident on this layer, electron-hole pairs are generated. The thickness of this layer is essential such that the photogenerated charges are extracted before recombination. The maximum absorber thickness 'L' is given by:

$$L < \sqrt{D * \tau_D} \qquad \textit{Eq 5}$$

where,

D = diffusion constant (nm)

τ_D = effective charge carrier lifetime (s)

The diffusion constant of the popularly used $CH_3NH_3PbI_3$ ($MAPbI_3$) is estimated to be 100 nm [15].

p-type hole transport layer (HTL): The photogenerated holes are extracted by this layer. Tress *et al.* report the three main functions of this layer [16].

1. To prevent the direct contact of the metallic cathode with the perovskite and ETL layer.
2. To decrease the recombination at the perovskite/Au interface. Therefore, to increase their photovoltage and internal quantum efficiency.
3. To increase absorption by providing a second path for the light that is reflected from the gold.

The commonly used HTL materials are 2,2',7,7'-tetrakis (N,N-di-p-methoxyphenylamine)-9,9'spirobifluorene(Spiro-OMeTAD), poly(3-hexylthiophene-2,5-diyl) called P3HT, 4-(dimethylamino)-benzaldehyde diphenylhydrazone (DEH) and poly (3,4 ethylenedioxythio penae) called PEDOT, among which Spiro-OMeTAD and PEDOT are the popular ones. They are usually spin-coated or slot-die coated.

Cathode: Usually, metals are used as the counter electrode. The popularly used metallic electrode is gold or silver, which is vacuum evaporated to form the electrode.

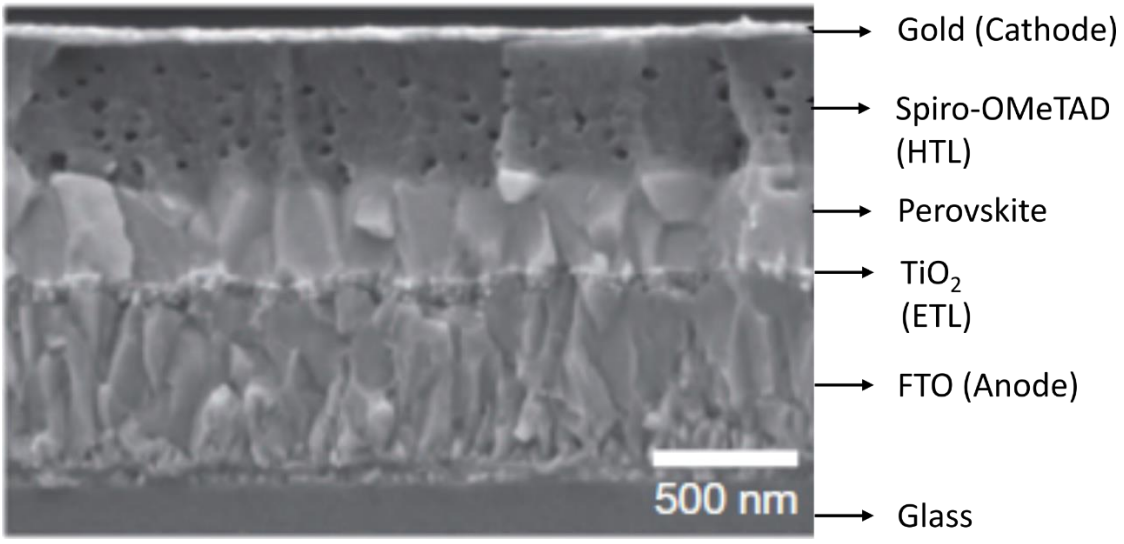

Figure 8: Cross-sectional SEM of a planar PSC [17]

The basic working principle of the PSC is explained using the energy band diagram of a Spiro-OMeTAD based PSC, as shown in Figure 9. The explanation is given considering an ideal solar cell whose layers are entirely fabricated without any defect. As seen in Figure 8, the perovskite light absorber is sandwiched between the ETL and the HTL. When an incident light with energy higher than the bandgap energy (E_g) reaches the perovskite, photogenerated charge carriers are created, as explained in section 2.1.2. The ETL and HTL are arranged such that the electrons from the CB of the perovskite only transfer to the lower-lying ETL's CB, and

the holes are transported from the VB of the perovskite only to the high-lying VB of the HTL. The energy band diagram of methylammonium lead iodide (MAPI) perovskite sandwiched between TiO_2 and Spiro-OMeTAD is shown. After photoexcitation, the electrons from the CB of perovskite at 3.93 eV can transfer only to the TiO_2's CB at 4.20 eV. Simultaneously, the holes from the VB of perovskite at 5.46 eV goes only to the higher VB (5.22 eV) of spiro-OMeTAD.

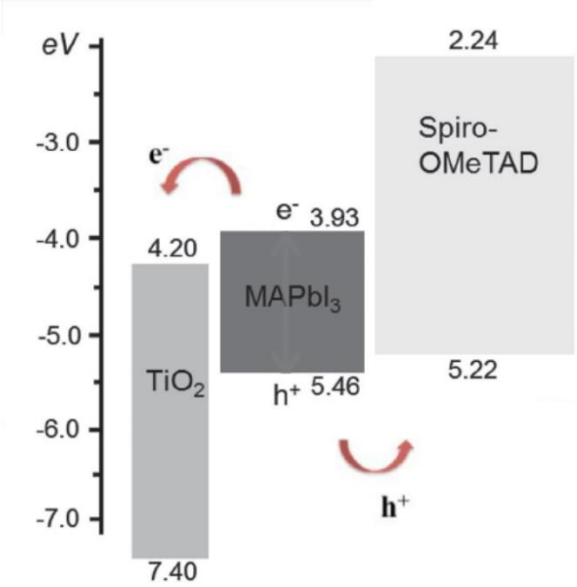

Figure 9: Energy band diagram of PSC [18]

2.2.3 Types of perovskite solar cell architecture

The three main classifications of perovskite solar cells shown in Figure 10 are:

- Mesoporous architecture
- Planar architecture
- Hybrid architecture

Additionally, the inverted architecture is also shown where the HTL is fabricated at the front electrode side.

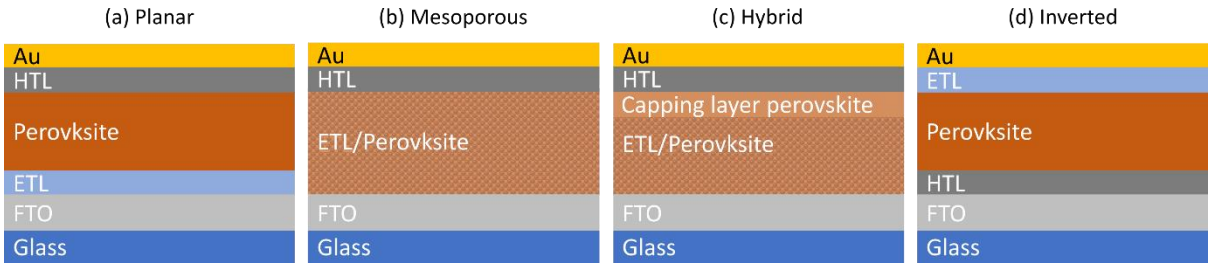

Figure 10: Perovskite solar cell architectures (a) Planar (b) Mesoporous (c) Hybrid and (d) Inverted architecture

Mesoporous architecture:

Miyasaka *et al.,* in 2009, introduced the use of perovskite as photo-sensitizer in the dye-sensitized solar cells starting with I and Br halides resulting in an initial efficiency of 3.8 % and 3.1%, respectively [6]. The major drawback was that the liquid electrolyte in a DSC degraded the perovskite faster under continuous illumination by dissolution. Thus in 2012, Kim *et al.* replaced the liquid electrolyte and the dye by filling the pores of a mesoporous TiO_2 (mp-TiO_2) electron collecting layer with the perovskite alone, thus, achieving 9.7 % of PCE with 880 mV of open-circuit voltage (V_{OC}) [19]. Here, the perovskite crystals, now acting as photoabsorber and hole transporting medium are formed inside the mesoporous layers over which the HTL and electrode are processed. To have excellent absorption co-efficient in PSCs, the mesoporous layer should be well filled with the perovskite crystals. Thus, the thickness of the mp-TiO_2, pore filling, and perovskite morphology plays a vital role in determining device performance.

Taking advantage of perovskite material as both light absorber and ambipolar charge transport, Snaith and his co-workers, in 2012, replaced the mp-TiO_2 with mp-Al_2O_3, which allowed the charges to flow in only one direction. These devices achieved 1.1 V as photovoltage with 10.9 % PCE [20]. Such a no-ETL architecture was called meso superstructure solar cells (MSSCs). Etgar *et al.,* in 2013, used the same property of the perovskite to design PSCs with HTL. He explained the build-in depletion zone near the contact interfaces that helped in charge extraction. Such a no-HTL PSC showed a performance of 8 % PCE [21].

Planar architecture:

In 2013, it was found that the diffusion length of the electron-hole pair in bulk perovskite was > 100 nm [15], which suggested that planar architecture was possible. This architecture omits the presence of a mesoporous layer. Thereby, the perovskite layer is produced between a compact ETL layer and an HTL layer. For this reason, the thickness, film quality, and perovskite morphology play a vital role in photogeneration and its extraction. Stranks *et al.* show that 400 nm of the perovskite layer with large crystals are required to have sufficient light absorption, photogenerated charge generation, collection, and transportation [15]. The first planar PSC produced by Snaith and his co-workers in 2012 showed only 1.8 % PCE due to poor perovskite film quality [20]. Later, the team improved the perovskite film quality by physical vapor deposition, reaching 15.4 % PCE [17]. Currently, a record efficiency of 23.3 % PCE has been reported for planar PSCs [22]. In this thesis, planar n-i-p PSCs are used for the discussion shown in chapter 5.

Another form of planar PSC is the inverted architecture (p-i-n) where the HTL is deposited onto the transparent conductive oxide (TCO). It means that the cathode now forms the front electrode. This architecture gained its popularity for its ease in low-temperature processing and thereby utilizing them in flexible photovoltaics. The first devices produced by Jeng *et al.* in 2013. They used poly(3,4-ethylene dioxythiophene): poly(styrene sulfonate) (PEDOT:PSS) as HTL and [6,6]-phenyl-C60-butyricscid methyl ester ($PC_{60}BM$) as ETL. ITO/ PEDOT: PSS/$MAPbI_3$/C_{60}/bathocuproine (BCP)/Al reached a PCE of 1.6 % [23]. By utilizing mixed-halide perovskites and double HTLs comprising of PEDOT: PSS and NiO, the efficiency of 15.47 % have been achieved by Tang and his co-workers [24]. Low efficiencies in the inverted PSCs are attributed to the undesirable electron-hole recombination pathway leading to losses through non-radiative recombination. Recently, Bakr and his colleagues showed the highest certified efficiency for inverted PSCs using alkyl chain length of alkylamine ligands (AAL). The 22.34 % PCE reported is attributed to the favored crystal orientation using Oleylamine ligands [25]. Additionally, it is reported to reduce defect densities in the grain boundaries and avoid ion migration.

Hybrid architecture:

The hybrid architecture utilizes the merits of both the planar and mesoporous architecture. Here, the perovskite crystals fill the mesoporous ETL and also forms a capping layer of pure perovskite. This compact capping layer prevents the recombination of photogenerated charges at ETL/HTL interface in a poorly-filled mesoporous architecture. In this architecture, the thickness optimization of both the ETL and perovskite layer is essential.

This architecture was utilized by Heo *et al.* in 2013, where 600 nm of mp-TiO_2 with a perovskite capping layer of 200 – 300 nm was used. Using Poly[bis(4-phenyl)(2,4,6-trimethylphenyl)amine (PTAA)as HTL, the device performance reported was 12 % with 997 mV of V_{OC} [26]. However, the current density was less with only 16.5 mA/cm^2 as a result of the poor surface morphology of the capping layer. Recent advancements in this architecture have reached a PCE of 19.3 % with 1.1 V and 23 mA/cm^2 using a doped TiO_2 ETL layer with a capping layer thickness of 300 nm [27].

2.2.4 Graphite-based PSCs

Cost, efficiency, and lifetime are considered to form the 'golden triangle' of perovskite solar cell commercialization [28]. While concentrating on increasing the efficiency and stability of the PSCs, it is also vital to reduce the cost of its production. In the above-mentioned PSC architectures, widely, Spiro-OMeTAD and gold (or other noble metals) are used as HTL and electrode material. Material cost, together with high power consumption for the vacuum deposition of noble metals, increase the production cost of PSCs. Moreover, prolonged exposure to temperatures such as 85 ^oC initiates ion exchange between perovskite and Spiro-OMeTAD, which results in the reduction reaction of Spiro-OMeTAD [29]. It reduced the hole conductivity of the device [30]. Thus, to reduce the cost and to increase stability simultaneously, it is necessary to replace Spiro-OMeTAD and gold with cheap and abundant material, *i.e.,* carbon.

First carbon-based dye sentisized solar cell (DSSC) with PCE of 6.7 % encouraged the use of them also in PSCs [31]. They are used to replace both HTL and electrode. Since carbon is not a charge selective material, this type of PSC is also called as HTL-free PSCs. The counter electrode usually consists of graphite flakes along with carbon particles. Hence the term carbon-graphite based PSC (CG-PSC) is also used. Figure 11 shows the architecture of CG-PSCs,

together with its energy band diagram. One of the main differences from Spiro-OMeTAD based PSCs is the introduction of an insulation layer or a spacer layer. mp-ZrO_2 or mp-Al_2O_3 is widely used as the spacer layer material. To prevent shunts through direct contact of mp-TiO_2 with a counter electrode, the presence of a spacer layer is vital in CG-PSCs.

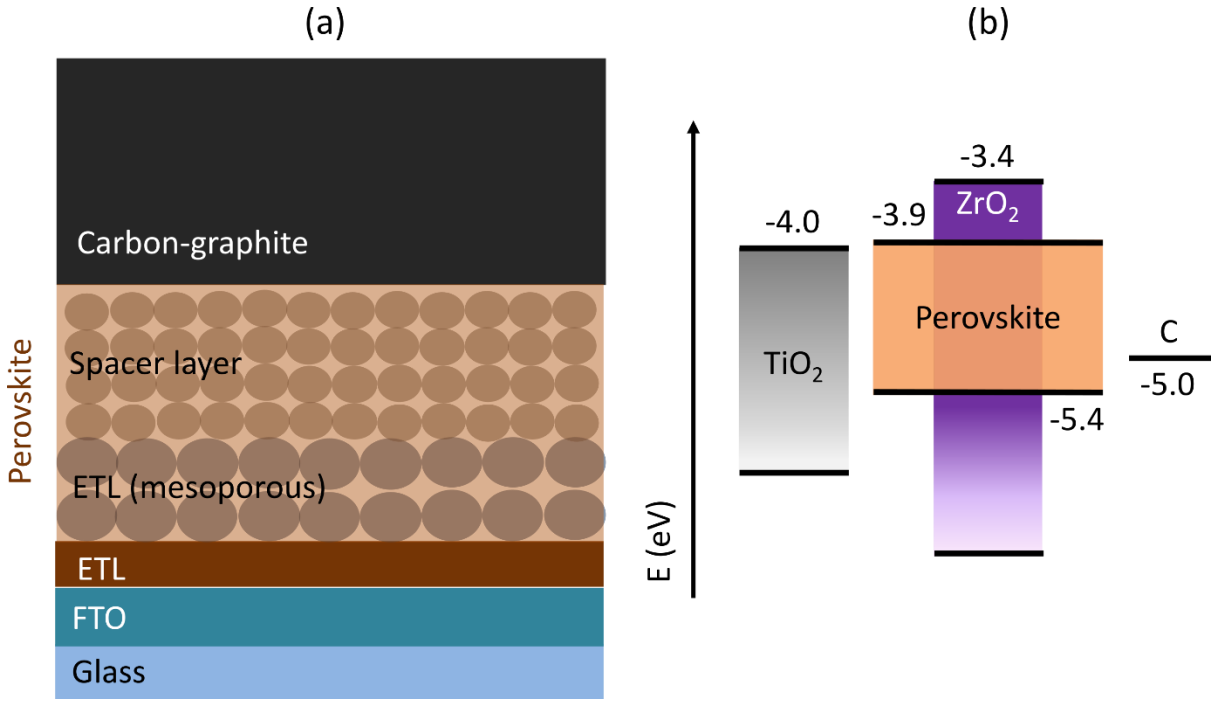

Figure 11: (a) Schematic representation of Carbon-graphite based perovskite solar cell (CG-PSCs) (b) Energy band diagram of a CG-PSC with ZrO_2 as the spacer layer [32]

In CG-PSCs, all the inorganic layers are fabricated first, and the perovskite solution is infiltrated as the last processing step. Thus, it is crucial to optimize all the layers to achieve better device performances. The critical factors that affect the efficiencies are:

1) **Thickness of the space layer:** It is essential not to have too thick space layer such that the photogenerated electrons should travel a long distance to reach the ETL. It is equally important not to have a thin spacer layer such that the charges recombine soon after photogeneration. More details are given in section 2.3.4.
2) **Pore filling of perovskite:** Since perovskite solution comes in as the last step in CG-PSCs, the challenge lies in complete pore filling of the underlying mesoporous ETL and spacer layer. Thereby, after annealing, the perovskite crystals are well incorporated into the mesoporous layers. Poor pore filling affects the light absorption significantly, thus reducing the current density (J_{SC}) and fill factor (FF).

3) **Temperature of substrate and solution:** It is found to be one way to ease the infiltration of perovskite solution into the inorganic layers to achieve better pore filling. The rise in temperature reduces the viscosity of the solution to facilitate improved infiltration [33].
4) **Graphite type and its layer thickness:** The materials and thickness of the counter electrode play a vital role in the conductivity of this layer. An optimized thickness resulting in high conductivity should be used. Also, this thickness should not affect the infiltration of the solution to fill the pores of the underlying mp-ETL and spacer layer. In general, a thick CG layer is preferred to increase conductivity and also to act as a water-retaining layer [32]. As the graphite layer consists mostly of thin flakes, no infiltration issue because of the graphite layer's porosity itself is reported so far.

2.3 Importance of interfaces in the performance enhancement of PSCs

A high amount of photogeneration, together with efficient photo-generated carrier extraction, is required for a promising perovskite solar cell in terms of its PCE and stability. As the PSCs are a construction of organic-inorganic layers, one on top of each other, their interfaces play a significant role in photogenerated charge extraction. To develop various ways to achieve efficient interfaces, the problem at the interfaces should be understood. Factors like charge recombination at the interface, ion migration, defects, poor energy band alignment, etc. significantly affect the device performance. Suppression of these losses has been reported by modifying the interfaces or by improving the properties of ETL or HTL.

This section firstly explains the basic recombination mechanisms and pathways found in the PSCs. It later documents already published reports which involved interfacial enhancement that is relevant to the interfaces investigated in this thesis.

2.3.1 Recombination mechanism and its pathways

Recombination is the mechanism when the photogenerated electrons and holes recombine to lose its energy in the form of heat or light (i.e., photon). There are two main types of recombination, namely:

1. Radiative recombination
2. Non-radiative recombination

Radiative recombination:

Radiative recombination is a direct band-to-band recombination process (Figure 12b). Here the electrons in the conduction band recombine with a hole in the valence band. The rate of recombination here depends on the concentration of electrons and holes present in a solar cell. During this process, the energy is released as a photon.

Non-radiative recombination:

This recombination process is unwanted as the energy stored in the electron-hole pair is released only as heat. They are further classified into four types:

- **Shockley Read Hall (SRH) recombination:** The most common type of non-radiative recombination is the recombination via the defect levels. Defects are introduced in the electron state in the forbidden energy gap (the energy gap between CB and VB) due to the presence of impurities. Sometimes, energy states are also introduced in the forbidden gap because of the "trap states" found in crystal lattices (Figure 12d). The probability of finding such defect states in the middle of the forbidden gap is higher.
- **Auger recombination:** This type of non-radiative recombination involves two charge carriers (Figure 12c). When the electron from the CB relaxes to a hole in the VB, a photon is released. The energy from this photon is absorbed by an electron in the CB, which is then excited to a higher energy state. It then relaxes with subsequent loss of energy through thermalization.
- **Surface recombination:** This non-radiative recombination mechanism is due to the presence of surface defects. To reduce this type, commonly, a passivation layer is deposited.
- **Excitonic recombination:** Photogenerated charges are bound together by Coulomb forces (Figure 12e). The difference in their energy is usually less than Eg, and thus at times, these excitons recombine contributing to the carrier loss mechanism in PSCs [34].

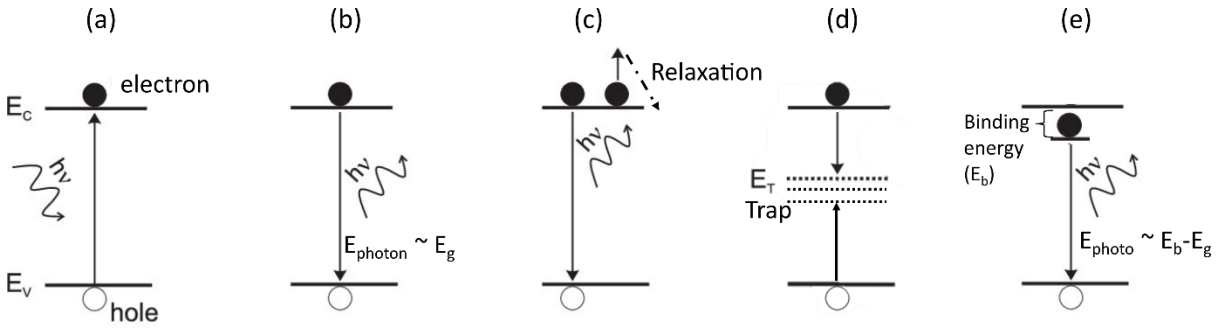

Figure 12: Absorption and recombination mechanisms (a) Absorption (b) Radiative band-to-band (c) Auger (d) SRH and (e) Excitonic recombination [34]

Recombination pathways in PSCs:

The majority of charge loss happens at the interface due to charge recombination. Marchioro *et al.* explain the charge separation steps and the various charge recombination pathways [35]. No detailed investigation has been done so far to determine which type of charge (electron or hole) is extracted first by their respective selective layer.

If electron injection is considered as the primary charge separation step, the following pathway is observed: ETM is the electron transport material, and HTM is the hole transport material

$$(e^-\ldots h^+)_{perovskite} \rightarrow e_{cb}^-(ETM) + h^+(perovskite) \qquad Eq\ 6$$

$$h^+(perovskite) \rightarrow h_{vb}^+(HTM) \qquad Eq\ 7$$

If hole injection is considered as the primary charge separation step, the following pathway is observed:

$$(e^-\ldots h^+)_{perovskite} \rightarrow h_{vb}^+(HTM) + e^-(perovskite) \qquad Eq\ 8$$

$$e^-(perovskite) \rightarrow e_{cb}^-(ETM) \qquad Eq\ 9$$

In the absence of charge separation, exciton annihilation occurs:

$$(e^-\ldots h^+)_{perovskite} \rightarrow h\gamma\ (photon) \qquad Eq\ 10$$

$$(e^-\ldots h^+)_{perovskite} \rightarrow \nabla\ (heat) \qquad Eq\ 11$$

Other recombination pathways are as follows:

The electron from the ETM recombines with holes in the perovskite

$$e_{cb}^-(ETM) + h^+(perovskite) \rightarrow \nabla \qquad Eq\ 12$$

Holes from the HTM recombines with electrons in the perovskite

$$h_{vb}^{+}(HTM) + e^{-}(perovskite) \rightarrow \nabla \qquad Eq\ 13$$

Electrons in the ETM recombines with the holes in the HTM

$$e_{cb}^{-}(ETM) + h_{vb}^{+}(HTM) \rightarrow \nabla \qquad Eq\ 14$$

Figure 13 shows a simplified diagram of the charge extraction and recombination pathways. The pathway and its corresponding equation number are marked in the picture for easier understanding.

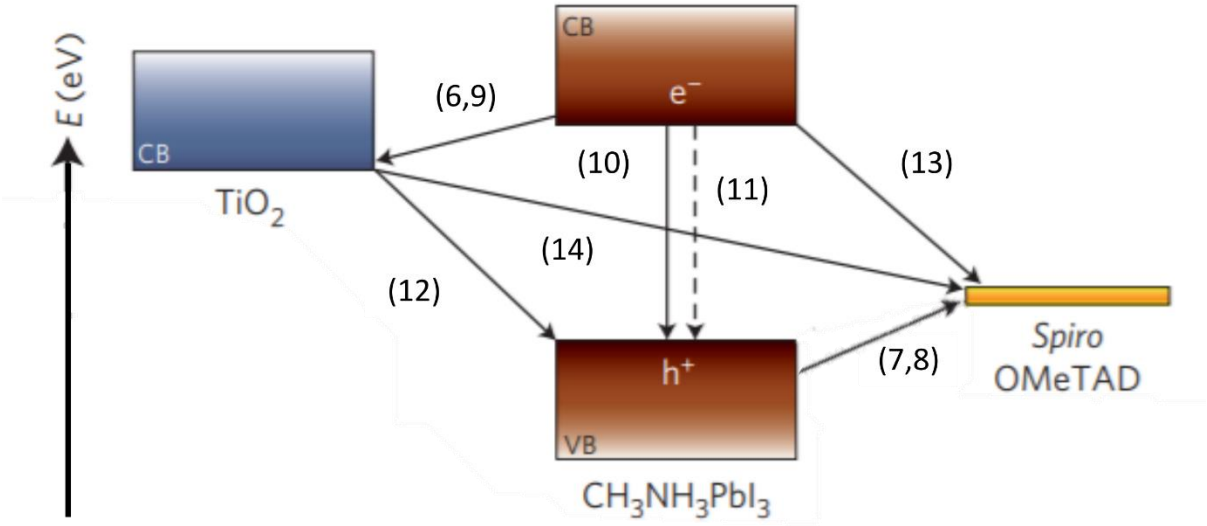

Figure 13: Recombination pathways in PSC [35]

2.3.2 Role of ETL and ETL/perovskite interface in planar architecture

As explained in section 2.2.3, the role of the electron transport layer (ETL) in a planar architecture is to collect and transport the photogenerated electrons to the anode, as shown in equations (Eq 6 and Eq 7). For a material to be preferred as ETL, it should have the following properties:

- Wider bandgap
- High electrical conductivity
- High electron mobility
- Good chemical stability

The most widely used ETL is TiO_2. As the planar architecture is commonly used in low-temperature processing of PSCs, TiO_2's ability to form a crystalline structure (anatase) at low temperatures is difficult. Moreover, its photocatalytic nature in the presence of UV light developing deep trap states in the presence of oxygen makes it an undesirable material in low temperature processed PSCs. Kelly *et al.* reported ZnO, a promising candidate due to its high bulk electron mobility (205 – 300 $cm^2V^{-1}s^{-1}$). However, the presence of hydroxyls groups and acetate ligands led to the faster degradation of perovskite.

With broader research, many other transparent electron transport materials have been reported. Some of them are $ZnSO_4$, WO_3, In_2O_3, $SrTiO_3$, and $BaSnO_3$. Among all the alternatives said, SnO_2 is considered the most promising candidate to replace TiO_2. Owing to its properties such as high mobility (240 $cm^2V^{-1}s^{-1}$), better CB alignment with perovskite, high transmittance, wider bandgap (-3.6 eV to -4.0 eV) with deep CB and VB, and low-temperature processability makes it a suitable ETM for planar PSCs[36]. The highest efficiency of 23.32 % PCE has been reached with SnO_2 as ETL in planar PSCs through surface passivation of perovskite/HTL interface using phenethylammonium iodide (PEAI) [22].

Even with many advantages, localized crystallization induced defects such as oxygen defects, tin interstitial, and surface defects have been observed in SnO_2, leading to imperfect energy band and charge accumulation at the interface [37]. To overcome these defects, SnO_2 is doped with suitable elements to alleviate energy mismatch and thus reduce defects. Ga doped SnO_2 was observed to reduce the trap state densities, thereby reducing the recombination rate resulting in 16.4 % PCE [38]. Doping SnO_2 with ethylene diamine tetraacetic acid (EDTA) resulted in a certified PCE of 21.52 % in 2018 [39]. The higher efficiency was owed to its better Fermi level alignment with perovskite, increase of electron mobility by three-fold, and also better wettability for the production of the defect-free perovskite layer. Recently in 2020, Graphite carbon nitride (g-C_3N_4) based SnO_2 has been reported to have a high PCE of 22.13 % PCE [37] with 1.17 V of V_{OC} owing to the elimination of surface/bulk defects in SnO_2 together with its reduced oxygen vacancies which prevented the interfacial recombination.

Thus, it can be noticed that energy mismatch, oxygen defects, surface defects are the most common problems faced at the ETL/perovskite interface that leads to charge accumulation at this interface leading to non-radiative recombination losses.

2.3.3 Role of blocking layer and FTO/perovskite interface enhancement in mesoporous architecture

The blocking layer (BL) in a PSC is processed mostly as a compact layer. It is an additional layer prepared between the FTO and the perovskite-filled mesoporous ETL. The role of BL is not only to transfer the electrons from mesoporous ETL to FTO but mainly to block the electron-hole pair recombination at the front electrode. Hence this layer can also be called a hole blocking layer (HBL). Thus, the BL should be thin enough to allow the movement of electrons from ETL to FTO but also should be efficient enough not to permit the back transfer of electrons to perovskite. It is thereby preventing the recombination of electrons with holes (in perovskite) at the front electrode.

For the HBL to be efficient, the chosen material should have the following properties:

- Highly transparent in the visible region
- Expanded UV transparency
- Excellent electron extractor
- Fast electron mobility
- Low transport resistance
- Have suitable conduction band level and Fermi level

For an HBL to perform well, it should be a defect-free, pin-hole free, homogeneous layer with the flexibility to control its thickness. Usually, a thin layer is used as a compact HBL in mesoporous PSC architecture. As mentioned earlier, TiO_2 is the widely used material as a compact layer (referred to as c-TiO_2). Several other n-type materials like SnO_2 [40–43], ZnO [44–46], fullerenes [47], graphene [48], and CdS [49] have been researched and proven suitable as HBLs along with anatase-TiO_2 [50,51]. Improvements in this layer are made by using new materials, doping TiO_2, or by using different deposition techniques [40,52–62].

The widely used replacement material for TiO_2 is SnO_2. Dong et al., in 2017, shows a blended-interfacial-layer (BIL) [63] with SnO_2 as the major component. A PCE of 18.16 % was achieved where the improvement was attributed to lower series resistance and enhanced shunt resistance with reduced interfacial degradation. $ZnO/ZnSO_4$ [64], Nb_2O_5 [65], and TiO_2 quantum dots [66] (QD) are other materials that were used to improve the interface through bandgap enhancement and low series resistance, respectively. High efficiency of 20.05 % PCE with

1.12 V of V_{OC} was achieved by a passivating ZnO layer with MgO and protonated ethanolamine (EA) [67].

Doping is another technique used to improve the HBL/perovskite interface. Elements such as Niobium (Nb), Tantalum (Ta) [68], Lanthanide (La) [69], and Magnesium (Mg) [70] doping are some of the reports on using the doped layer as HBL. PCE > 14 % is reported for Nb-doped and Ta-doped TiO_2, attributing to fast electron transfer and reduced recombination. Mg-doped TiO_2 shows deeper VB, which enhances the hole blocking effect. 15.31 % of PCE was achieved by doping La with TiO_2. Spray pyrolysis of La-doped-TiO_2 was claimed to produce smooth layers, improved charge transfer, and reduced recombination. Recently, a double compact layer comprising of the Mg-doped-SnO_2 layer processed on c-TiO_2 was used in a CG-PSC whose PCE was 13.01 %. The efficiency improvement compared to c-SnO_2 was attributed to improved interfacial contact with perovskite and higher electronic extraction capacity.

Various deposition techniques are also used to improve efficiency through better morphology. Atomic layer deposition (ALD) [71], sputtering [72], chemical bath deposition (CBD) [73], spray pyrolysis, spin coating [74,75], electrodeposition [76], dip coating [77], and sol-gel techniques [78] are some of the reports published to report on the interfacial improvement by varying the deposition method. Among this, 200 nm ALD TiO_2 showed 15 % PCE due to high conductivity, homogenous defect-free layer, and fast electron transfer. The articles mentioned above in this sub-section shows the PCE attained for a MAPI perovskite with Spiro-OMeTAD as HTL and Au as the counter electrode.

Thus, it is seen that the HBL at FTO/perovskite interface needs small series resistance, large shunt resistance, deeper VB, faster electron transfer, smooth layer to prevent charge accumulation later leading to non-radiative recombination.

2.3.4 Role of the spacer layer and ETL/graphite interface in CG-PSCs

Sub-sections 2.3.2 and 2.3.3 dealt with HTL-based PSCs where Spiro-OMeTAD is popularly used as HTL. As introduced in section 2.2.4, Spiro-OMeTAD and gold counter electrode is replaced with a carbon-graphite (CG) layer. In this CG-PSCs, the primary role of the spacer layer or the isolation layer is to prevent the direct ohmic shunt pathway between mp-ETL and CG. Factors that influence to achieve an optimal space layer is as follows:

- Thickness
- Perovskite pore filling
- Morphology of perovskite within the pores
- Uniformity of coating

Thick 1µm screen printed mesoporous ZrO_2 is widely used as an insulating layer. Liu *et al.* describe all the critical parameters involved in this architecture to achieve the best performance [33]. Among all the parameters, the thickness of the space layer plays a crucial role. Even though the spacer layer is essential, a high thickness of over 1µm affects the photovoltage and fill factor (FF) due to charge recombination. Limited electron diffusion length (100 nm) of the perovskite and the light-harvesting is reduced if its thickness is < 1 µm. In 2016, the efficiency of this architecture was improved by using a space layer where the TiO_2 particles were surrounded by 5nm ZrO_2 particles. This TiO_2@ZrO_2 was used as a spacer layer in addition to mp-TiO_2. It resulted in certified efficiency if 13.8 % from 10% with 935 mV [79]. The highest 15 % of PCE has been achieved due to improved hole extraction with ZrO_2 as a spacer layer and by incorporating CuSCN in the perovskite precursor solution [80]. Team at Fraunhofer ISE have published a stable photovoltage of 1V through a molten-salt approach, attaining stabilized PCE of 12.6 % [81]. It is the highest certified stable photovoltage reported so far in CG-PSCs with ZrO_2 as the insulating layer.

Another popularly used spacer layer is Al_2O_3. Widely 500 nm – 1 µm thick Al_2O_3 is used. 15 % PCE has been achieved in such devices with NMP as the solvent for precursor solution [82]. Further 1% improvement in PCE has been achieved by incorporating $SrCl_2$ in precursor solution resulting in $CH_3NH_3PbI_3(SrCl_2)_{0.1}$. The high 16% PCE is attributed to the improved morphology and low crystal defects when Sr^{2+} occupies Pb sites [83]. The highest PCE was achieved when NiO is used as an HTL layer along with triple cation perovskite resulting in 17% PCE with over photovoltage of 1 V [84]. There is also architecture that uses both Al_2O_3 and ZrO_2. Xiong *et al.* show the improvement in voltage through surface modification and space tuning by introducing a vacuum evaporated 50 nm Al_2O_3 as an interlayer between 1µm ETL and 1µm ZrO_2 as space layer achieving 14.26 % PCE unstabilized [85].

This architecture further proves to be the promising architecture regarding long term stability. A large area encapsulated module with PCE of 10% (active area of 100 cm^2) along with the stability of 2136 h at ambient temperature has been reported [86]. The highest efficiency in

large scale modules has been reported by Bashir *et al.,* where a 12.1 % PCE has been reported for an active area of 70 cm^2. Such high efficiencies have been achieved by adding a nano-thick Cu doped NiO as HTL. These cells also show an incredible shelf life in ambient atmospheric conditions for 4500 h without encapsulation, with only a 5 % decrease from the initial PCE value [87]. The longest stability of CG-PSCs has been reported by Gracini *et al.,* where 10 x 10 cm^2 module providing 11.2 % PCE showed stability > 10,000 h [88]. These cells show the potential of this type of architecture for future commercialization of PSCs.

Thus, it can be noticed that the spacer layer is widely a 1 µm thick layer, which uses an insulating material for this purpose. Reports suggest that a decrease in spacer layer reduces V_{OC} due to reduced light harvesting, whereas increasing its thickness leads to increased path length for the charge carriers to reach the ETL [33]. The major challenge is to get a perfect pore filling in the spacer layer and also in the underlying mp-ETL, as it plays a crucial role in light-harvesting.

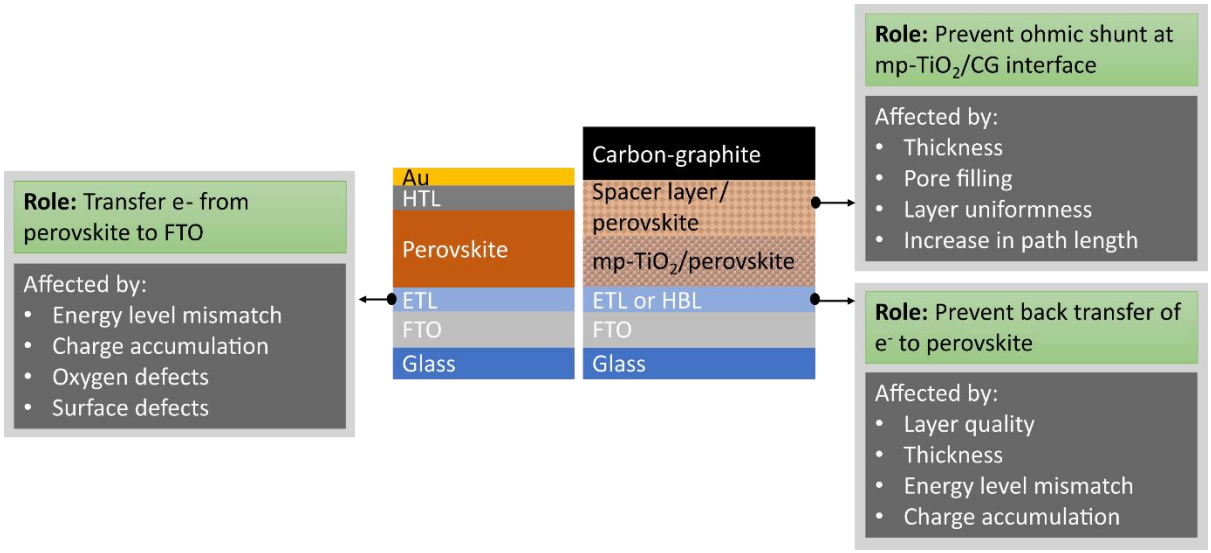

Figure 14: Role of various interfaces and factors influencing them for the two different device architectures studied in the thesis.

Thereby, in this chapter, the fundamentals involving the working principle of the solar cell were described, followed by a detailed introduction to perovskite solar cells and its different architectures. In the last sub-section, the importance and role of interfaces in PSCs (relevant to the thesis) was given, together with the factors that are affecting their performance and stability. The status-quo of the research in this aspect was also provided. In the next section, the methods that have been used to fabricate the PSCs used in the thesis will be detailed.

Chapter - 3

Fabrication Methods

3 Fabrication Methods

This chapter is dedicated to explain the basic principles involved in various deposition techniques that are used in the device fabrication reported in this thesis. The techniques involved here are - sputtering, spray pyrolysis deposition, atomic layer deposition, screen printing, and slot-die coating. As this thesis concentrates on using methods that can be transferred to modules for future production, already established industry level processes are employed.

3.1 Sputtering

The physical vapor deposition (PVD) technique is widely used to process thin metallic or dielectric layers in the range of 1 nm to a few micrometers. Sputtering is one of the PVD techniques used to deposit materials that have a high melting point, particularly metal alloys. The basic principle involved in sputtering is that a target material is bombarded with high-speed ions. It removes the atoms from the target's surface, which travels towards the substrate where the thin film deposition is required. Possibilities such as sputtering of alloys, organic compounds, materials with a high melting point at low temperature, uniform coating on a larger area, and reduced maintenance make it one of the easiest fabrication techniques for coating thin films.

A schematic representation of a standard sputtering technique is shown in Figure 15. At first, a vacuum is achieved to reach low pressure. Further, in order to obtain a working pressure of 10^{-3} torr in the chamber, argon gas is introduced. A voltage is applied between the substrate (cathode) and the target (anode). A stray electron from the cathode initiates the process. It hits the applied neutral gas atom (usually inert gas like Argon), resulting in a positively charged ion. During this process, secondary electrons are also created, which reacts with more neutral gas atoms to produce ions. The process repeats in a cascading manner forming more secondary ions. These ions in a gaseous form exhibiting a collective behavior are called plasma. When ions in the plasma collide with the target, the momentum and the kinetic energy is transferred to the target knocking out the surface atom. Sputtered atoms then diffuse to the substrate. Increasing ionic energy leads to a larger plasma area resulting in a homogenous thin film deposition on the substrate.

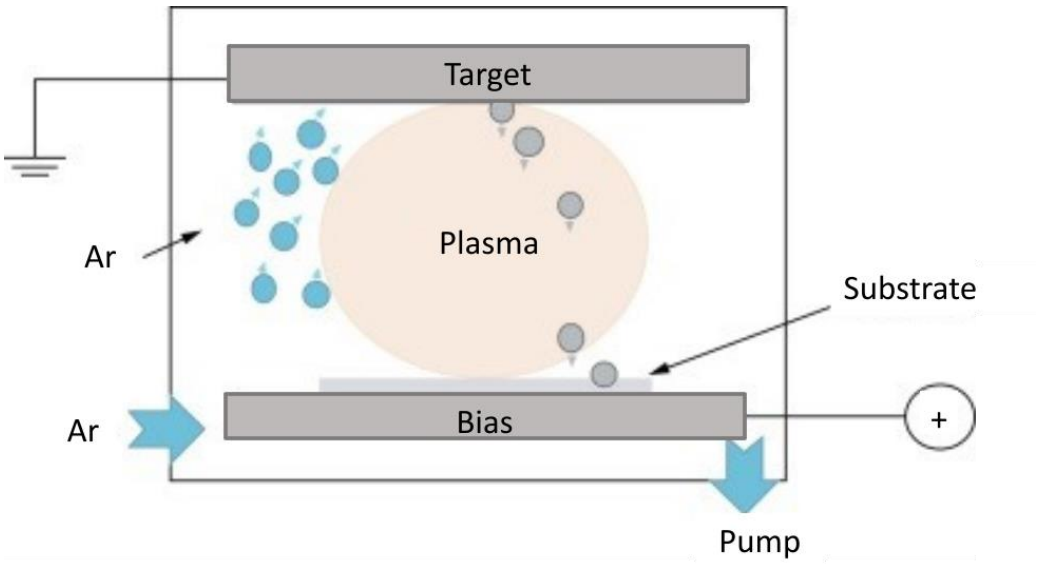

Figure 15: A schematic representation of the standard sputtering process [89]

Initially, the current is low. It leads to an increase in voltage at the dark discharge regime. After the breakdown voltage, more secondary ions are produced high enough to maintain the plasma. In some cases, instead of producing secondary electrons, the collision results in a glow. This phenomenon is called a glow discharge regime, which is accompanied by a voltage drop. A uniform current density across the cathode is maintained by increasing the power. Thus, the sputtering starts to occur in an abnormal glow discharge regime (F-G point in Figure 16). Further increase in the current with continuous bombardment of the ions leads to heating up of the target, moving to the arc discharge regime where the destruction of the target will occur.

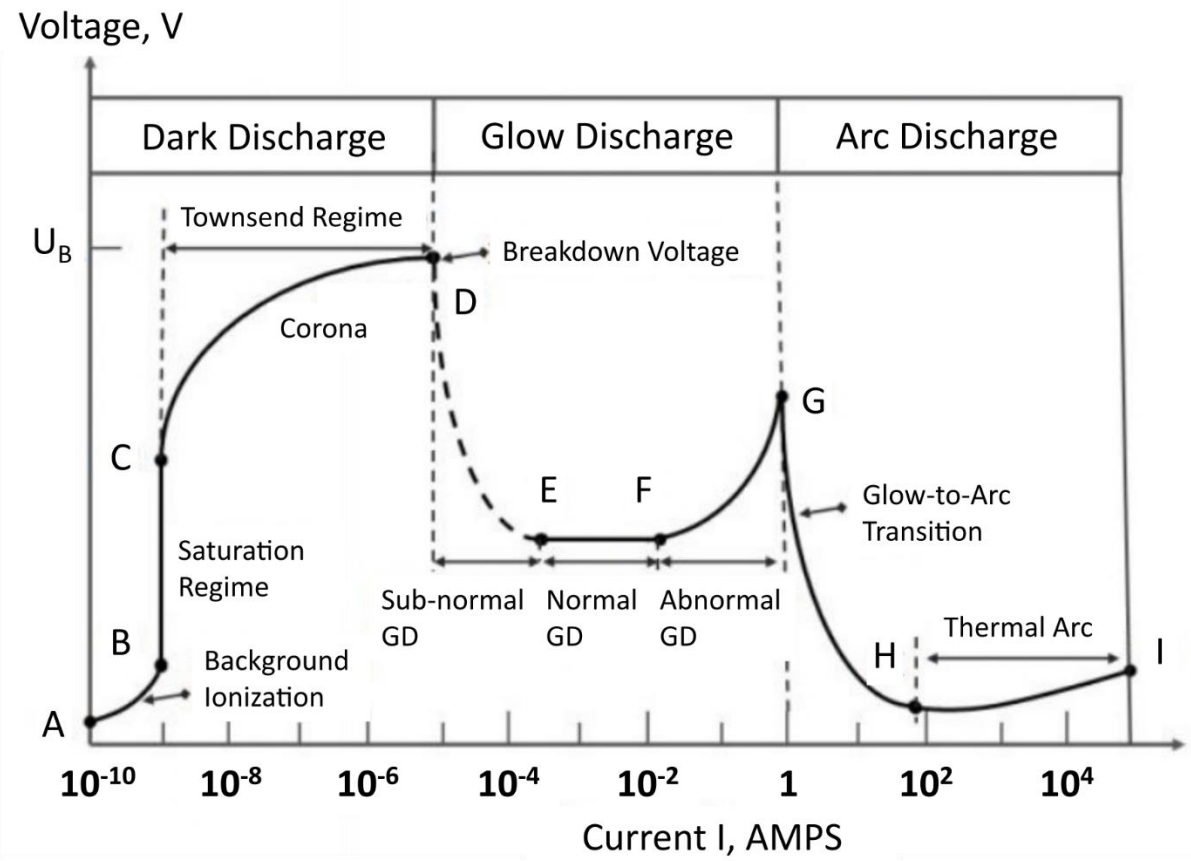

Figure 16: Current-voltage characteristics of direct current electrical discharges [90]

Various parameters are involved in achieving successful sputtering. They are:

1. Argon pressure
2. Sputter voltage
3. Substrate temperature

Optimum pressure is required to maintain the plasma. Low-pressure results in a reduced number of collisions between the ions and the atoms, and at high pressure, more collisions happen, which doesn't provide enough time for the production of ions and electrons through energy transfer. Higher voltages result in higher particle energy. It is also noticed that the particle energy and the substrate temperature is directly proportional to the sputtering voltage. All the parameters are to be optimized to have an excellent sputtering process. The efficiency of the sputtering process is defined by the term sputter yield (S) which is:

$$Sputter\ yield\ (S) = \frac{Number\ of\ sputtered\ atoms}{Number\ of\ incident\ ions} \qquad Eq\ 15$$

Its value depends on the type of target atom, binding energy of the target atom, relative mass of ions and atoms, incident ion energy, and angle of incidence of ions. Typically, its value is the range between 0.1 to 10.

Thus, in the sputtering technique, the characteristics and thickness of the thin film deposition are controlled by varying the chamber pressure, the partial pressure of the reactive gas, power density, target to substrate spacing, deposition rate, etc.

3.1.1 Types of sputtering

Even though various parameters are involved, the optimization of them varies according to the target material. Thus, for multiple applications, different types of sputtering are preferred. The four main types of sputtering are [91]:

- **DC sputtering:** DC sputtering involves applying a DC voltage between the target and the substrate. To maintain the glow discharge, 1-5 Pa is used. Usually, this type of sputtering is used for metal targets.
- **RF sputtering:** In the case of an insulator target, to avoid the build-up of ions on the surface of the target, RF sputtering is used. Here RF voltage is supplied.
- **Magnetron sputtering:** It is used to have higher deposition rates in the presence of low sputtering pressure. In this system, a magnetic field is superimposed on the cathode, which helps to circulate the secondary electrons in a closed loop to increase the collision rate, thereby increasing the deposition rate even at low pressure in the range of 0.5 – 1 Pa.
- **Ion beam sputtering:** To avoid the inclusion of gas molecules in the substrate, the target sputtering and the ion source are separated. The ion energy is maintained between 0.5 – 2.5 kV. As the target chamber is separate, further reduction in the chamber as low as 1×10^{-3} Pa can be achieved.

3.1.2 Sputtering parameters optimized for this thesis

3.1.2.1 Sputtering machine details

The sputtering machine used is the horizontal in-line medium-frequency (MF) magnetron sputtering unit from Interpane located at Fraunhofer ISE. A stable plasma is maintained by controlling the argon and oxygen gas flow. No additional substrate heating is used.

3.1.2.2 Sputtering of c-TiO_2

For sputtering c-TiO_2, a dual ceramic tube TiOx target was used. An Ar/O_2 working gas mixture was let into the chamber with an Ar/O_2 ratio of 6:1. The resulting chamber pressure was $1.7*10^{-3}$ hPa.

3.1.2.3 Sputtering of Al_2O_3

The deposition of Al_2O_3 is carried out with a dual metallic tube Al target. Once the stable plasma is maintained with argon gas, oxygen is fed to the chamber till fully stoichiometric aluminum oxide is achieved. The sputtering power density used is 2.59 $W/cm^{2,}$ and the chamber pressure was set as 4.5×10^{-3} hPa to obtain films with a nano-porous structure.

To have stable working conditions, a voltage-controlled process or current-controlled process is preferred. The commonly used technique is a current-controlled process where the pressure and current are kept constant by varying the O_2 flow. Figure 17 below shows a sharp transition from metallic to an oxidic state of Al at 170 sccm of $O_{2,}$ which makes it a complicated process. However, keeping the voltage constant at 250 V in a voltage-controlled process for Al, a smooth transition to the oxidic state is noticed through the sharp increase in sensor current after 60 sccm O_2. Thus, the Al_2O_3 layer is sputtered with an O_2 flow of 90 sccm for the devices reported in this thesis.

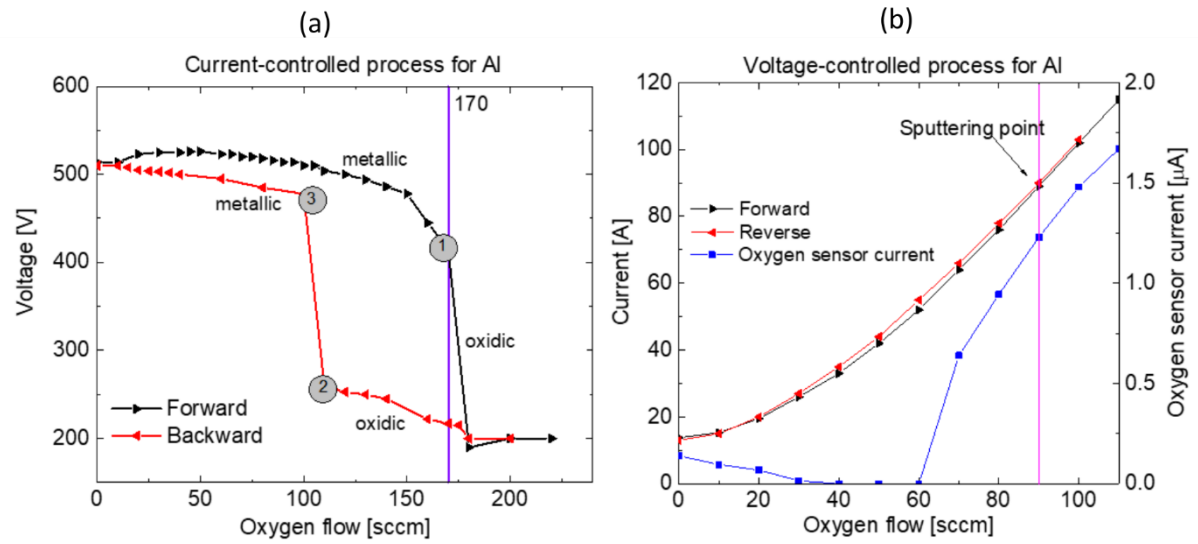

Figure 17: (a) Current-controlled process of sputtering Al at a constant current of 70 A and (b) Voltage-controlled process for sputtering Al at 250 V.

3.2 Atomic Layer Deposition

Atomic layer deposition (ALD) is a thin film processing technique based on chemisorption and self-limiting growth mechanism that is mainly used in microelectronics. It was invented in the 1970s; however, its commercial success came after its application in microelectronics. ZnS and Al_2O_3 were initially coated with ALD technique as insulator layers in flat-panel displays, later deposition methods for various other inorganic materials such as oxides, nitrides, and some metal layers were developed.

Achieving conformal coating on high aspect ratio structures, pin-holes, trenches around nanostructures made it a popular deposition technique in the microelectronics industry. Other advantages also involve thickness control in the angstrom scale resulting in ultra-thin layers, industry level scalability, large-area deposition, and simultaneous deposition of many substrates in batch reactors.

All the reactions happen inside a reaction chamber. The setup of ALD is shown in Figure 18a. The basic principle of the ALD technique involves four stages per cycle (Figure 18b) involving two precursors, each accompanied by an evacuation process or a gas surge process.

- **Step 1:** The substrate already has OH groups on its surface because of the reaction from the atmosphere. Precursor 1 is sent into the reaction chamber. Chemisorption of the reactor with the surface OH takes place until the OH groups are depleted.

However, due to the self-limiting mechanism, precursor 1 doesn't react with itself. Thus, chemisorption plus self-limiting mechanism results in one layer.

- **Step 2:** The next step involves either purging gas (such as N_2) or evacuating the chamber. During this process, by-products from step 1 and excess precursor 1 are removed from the chamber.
- **Step 3:** Precursor 2 is now sent into the reaction chamber. Usually, H_2O is used for creating oxide layers. H_2O reacts with the first layer and forms the OH surface making it ready for the next cycle.
- **Step 4:** By-products and excess precursor 2 is evacuated from the reaction chamber.

Thus step 1 to step 4 forms one reaction cycle in the ALD process. The thickness of the layer is then controlled by the number of reaction cycles.

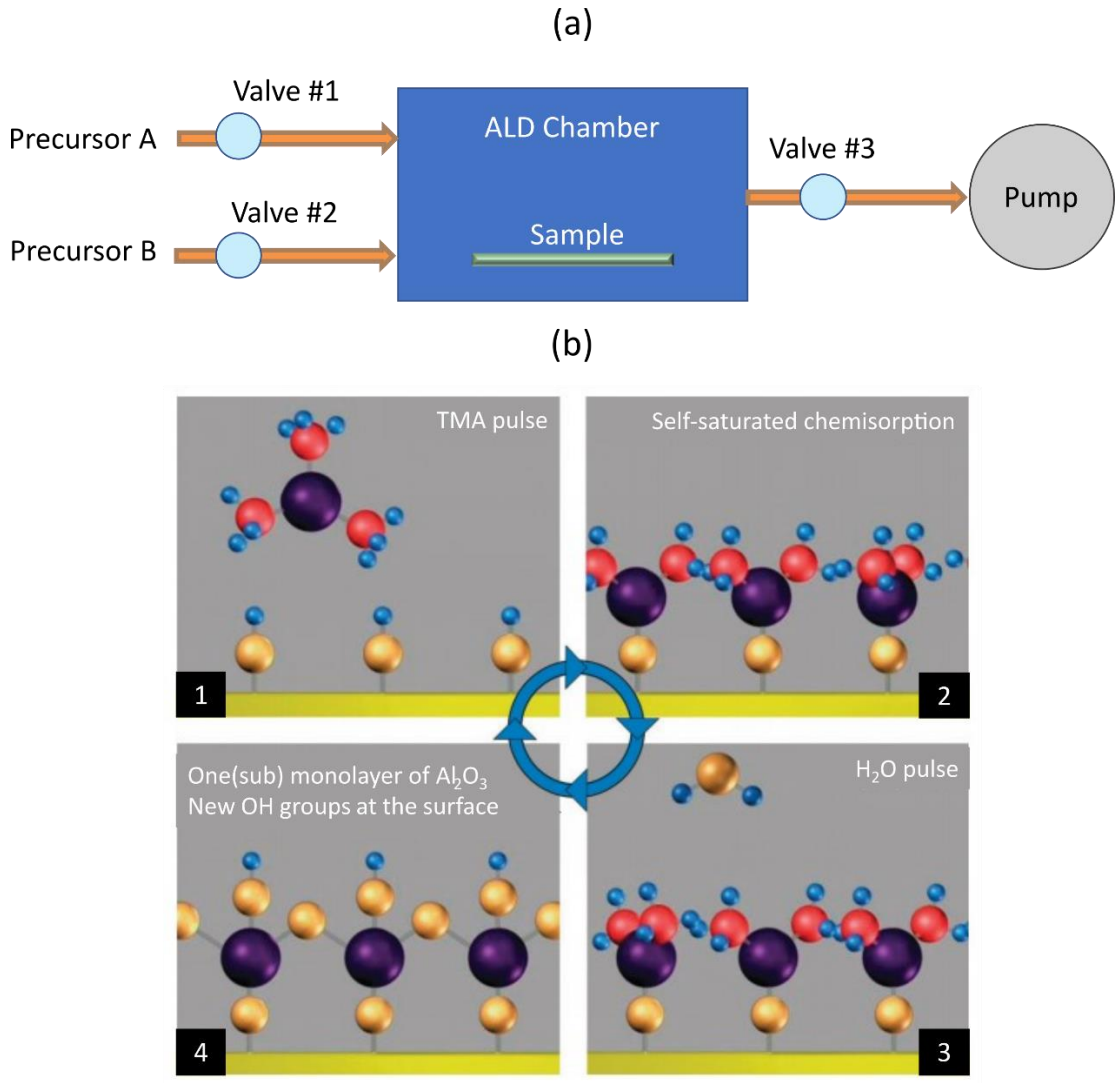

Figure 18: (a) Basic ALD reactor [92] *(b) ALD growth cycle* [93]

The growth of the desired material is not a linear mechanism concerning the reaction cycle (non-ideal case). According to the texture of the substrate, a precursor used, and temperature, it takes some time to achieve saturation in growth. Growth per cycle (GPC) defines the thickness of the material deposited in one cycle. Surface reaction sites and morphology plays a vital role in determining the GPC. For a perfect layer to be deposited, the ALD window has to be set. For thermal ALD, the ALD window is a temperature range where saturated GPC is observed. Figure 19 below explains the change in the GPC according to the temperature.

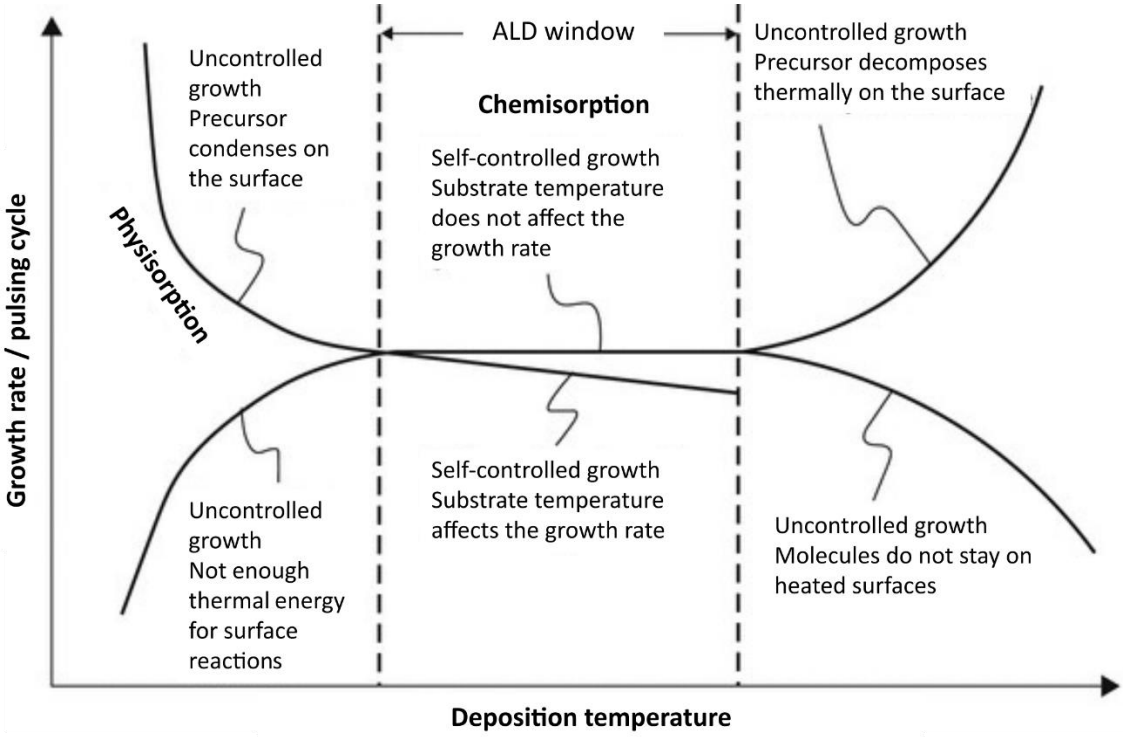

Figure 19: ALD growth rate cycle [94]

At low temperatures, some cases have high kinetics because of the physisorption of the reactant. Still, in most cases, it results in low kinetics as the temperature is not sufficient to initiate the surface reaction. High temperature also results in two possibilities where the low kinetics occurs due to evaporation, and high kinetics is observed as a result of the decomposition of the reactant. Thus, to obtain a monolayer, an ideal ALD window has to be selected.

3.2.1 ALD parameters optimized for this thesis

For the ALD deposition of c-TiO_2, a plasma ALD technique is used in a FlexAL ALD system from Oxford instruments located at Fraunhofer ISE. Titanium tetraisopropoxide (TTIP) is used as a precursor. Plasma O_2 (as oxidizer) is generated by a radio frequency coil powered at 300 W with a frequency of 15.6 MHz. One cycle consists of a TTIP dose for 1 s followed by purging Ar for 3 s, then plasma gas is stabilized for 1.5 s, and it is maintained for 6 s at a pressure of 80 mTorr. The base temperature used is 200 ^{o}C degrees, where the GPC of 0.045 nm/cycle is used.

3.3 Spray pyrolysis

Spray pyrolysis comes under the category of liquid-phase chemical vapor deposition (CVD) technique used for the fabrication of thin and thick films. The smooth process has made its entry into various applications such as solar cells, sensors, fuel cells, etc. The main advantage found in this process is its easy method at a low cost. Multi-layer processing and no restrictions in substrate quality are few other advantages of this kind of fabrication technique.

The setup of spray pyrolysis is shown in Figure 20. The main components involved in spray pyrolysis are

1. Atomizer
2. Precursor solution
3. Substrate heater and controller

Atomizer

An atomizer is where the bulk liquid is broken down into small droplets. There are three different types of atomizers based on the source used to create the process [95].

- Air blast atomizer – where it uses pressurized air to break down the particles
- Ultrasonic waves – where short wavelengths are used
- Electrostatic – where the liquid is exposed to the high electric field for its breakdown to occur

In lab setup small spray pyrolysis, it consists of a spray gun, precursor solution, and a hotplate for substrate heating and control. Here, the spray gun uses an air blast atomizer technique.

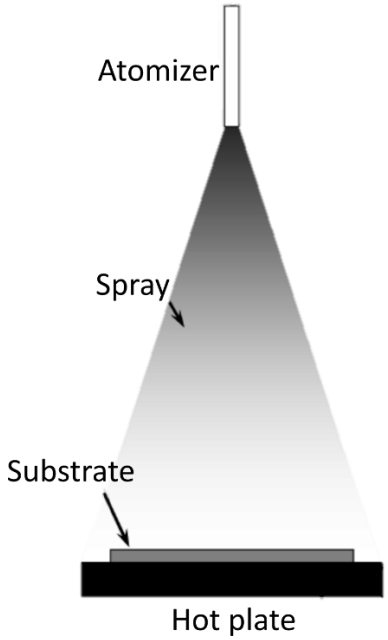

Figure 20: The set-up of spray pyrolysis deposition [95]

Many processes are simultaneously involved during spray pyrolysis that forms the basis for the film quality acquired at the end of the process. The steps observed in the film formation is shown in Figure 21 and is explained as follows:

1. The droplets are formed inside the atomizer, and they are sprayed at a particular velocity and pressure that determines the droplet size
2. Due to the high temperature being involved, the solvent evaporates from the surface of the droplet
3. Precipitation occurs as the further evaporation of the droplet occurs
4. Pyrolysis (i.e., decomposition of materials at high temperature) of the precipitate occurs as the next stage as they are near the substrate which is at high T
5. The broken-down particles are deposited on the substrates which trigger nucleation
6. Formation of a thin layer on a substrate

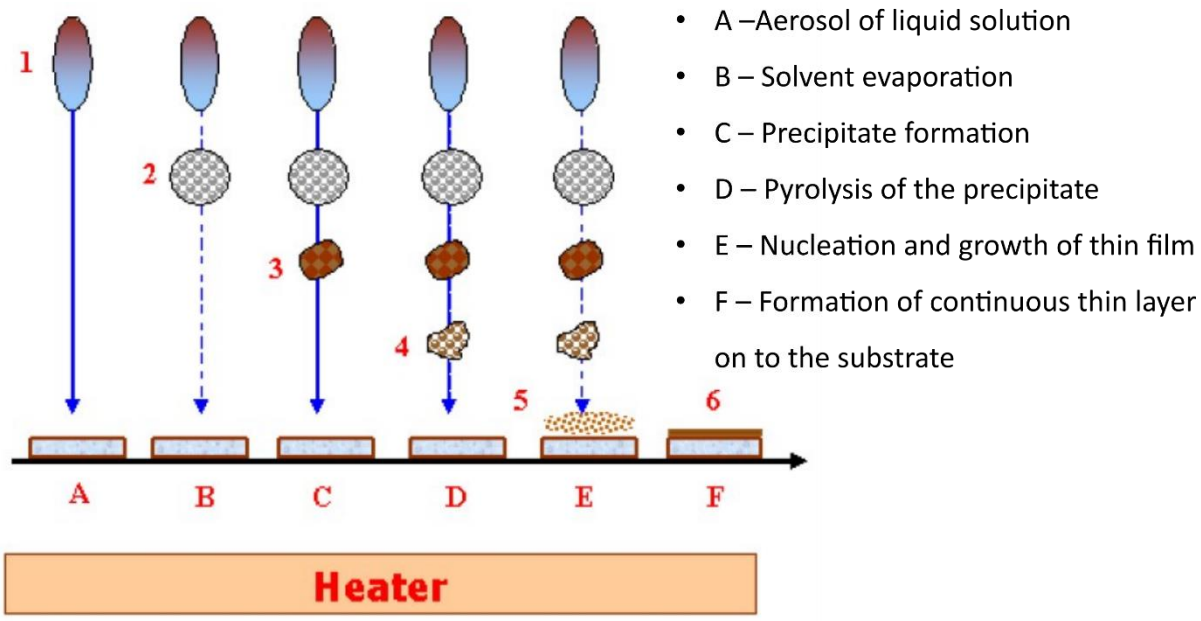

Figure 21: Steps observed in the film formation through SPD [96]

Following the process, the optimization of these layers is essential. Various factors are involved in achieving a good quality film through this technique. From a broad perspective, the factors involved in influencing the SPD film quality are:

- **Precursor solution**
- **Temperature of solution**
- **Type of salt**
- **Solvent**
- **Concentration of precursor solution:** Higher concentration of solution results in larger grain size, and the rate of growth is influenced by the pH of the precursor solution.
- **Viscosity and surface tension:** It influences the droplet size, its velocity, and the rate of atomization.
- **Substrate temperature:** Higher the temperature more porous is the resultant film.

However, adding additives to the precursor solution and also by using an optimum substrate temperature, highly crystalline films can be formed. Exposing the underlying layer to surface treatments such as plasma or UV-ozone tends to improve the homogeneity of the resulting layer. Other factors that influence the film quality is the pressure at which the droplets escape the nozzle of a spray gun (determines droplet size), the angle of spray and the distance between the spray gun's nozzle and the substrate.

3.3.1 SPD parameters optimized for this thesis

c-TiO_2 has been produced through spray pyrolysis. 0.05 M of Titanium di-isopropoxy (bis) acetylacetonate diluted in Ethanol (≥ 99.5 %) was used. The substrates are kept at the temperature of 470 ^oC to achieve crystalline TiO_2 in the anatase phase. As the setup involved a spray gun with pressured air as input, the larger substrates (10 x 10 cm) are sprayed following a left-right motion. Left-right-left motion forms 1 cycle. Thus, the thickness is determined by a number of cycles in our home setup. A distance of approx. 30 cm is maintained between the spray gun and the substrate. Wait time of 10 s is given after each cycle to maintain the temperature of the substrate, thereby preventing temperature shock in them.

3.4 Slot-die coating

Slot-die coating is a widely known coating technique for thin-films. The industry level large-scale fabrication technique such as roll-to-roll technique and sheet-to-sheet deposition technique works on a similar principle. Thus, researchers wisely use a slot-die coating technique to optimize the parameters that can be easily transitioned to pilot level manufacturing. Therefore, the slot-die coating is one of the preferred techniques over spin-coating. The thickness of the thin-film obtained can be in the range of tens of nm to 100 mm by changing their process parameters. They are the flow-rate of the solution from the slot-die head, meniscus height, and speed at which the substrate is moving. Care should be taken to obtain uniform films as they are highly sensitive to small changes in process parameters.

A slot-die coating system consists of a solution reservoir, a slot-die head, and rollers on which the substrate moves (as shown in Figure 22a). The main controls happen with the slot-die head and the roller speed. Figure 22b shows a slot-die head consisting of two slots. The solution enters through the inlet, goes to the manifold, and passes through the bottom of the slot-die head. The entire slot-die coating system is divided into four sub-systems, namely:

- **Metering system:** It controls the solution flow-rate with determine coating thickness and homogeneity of the film
- **Distribution system:** It controls the uniform width of the film through adjustment of the internal cavity of the slot-die head.

- **Head positioning system:** Controls the distance between the bottom of the slot-die head and the substrate through motors
- **Substrate movement system:** Controls the speed at which the substrate moves across the slot-die head through rotors.

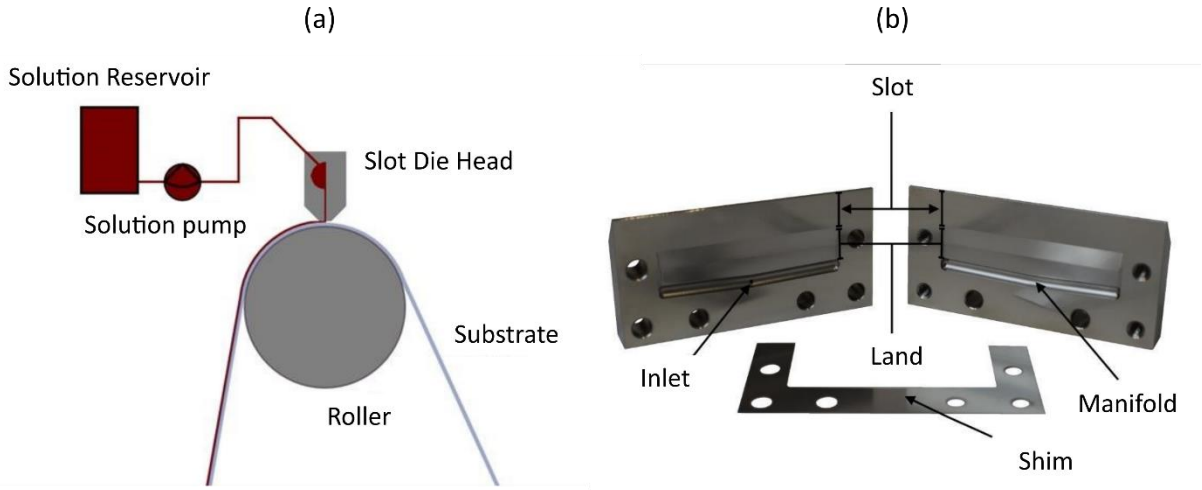

Figure 22: (a) Schematic of the slot-die coating system (b) Picture of a dismantled slot-die head [97]

The basic theory in slot die coating involves understanding the parameters that affect the flow of solution from the inlet to the wet film formation. The solution enters the inlet to the manifold of the slot-die head with pressure. Through gravitational forces, it moves to the bottom of the slot-die head. It causes a drop in pressure. The pressure drop is regulated to maintain the flow rate of the solution throughout the process. The pressure drop is given using the Pouiselle's flow equation:

$$\Delta p = \frac{12\mu LQ}{b^3} \qquad \textit{Eq 16}$$

where,

Δp = the drop in pressure (Pa)

μ = viscosity of solution (Pa.s)

Q = flow rate of solution (cm^3/s)

L = the channel length (mm)

b = the channel width (mm)

The pressure drop is regulated using shim, which determines the distance between the two slots in the slot-die head. When the solution comes out of the slot-die head (called lip), upstream and downstream are formed. They, in turn, form their corresponding menisci on the substrate. The continuous movement of the substrate creates a sheer force that forms the Couette flow. To obtain a high-quality thin-film, a balance should exist between the flow rate based on the pressure gradient (Pouisells's flow) and the shear stress through the movement of the substrate (Couette's flow). This balance in the flow makes both the menisci (upstream and downstream) pinned to the substrate (Figure 23a).

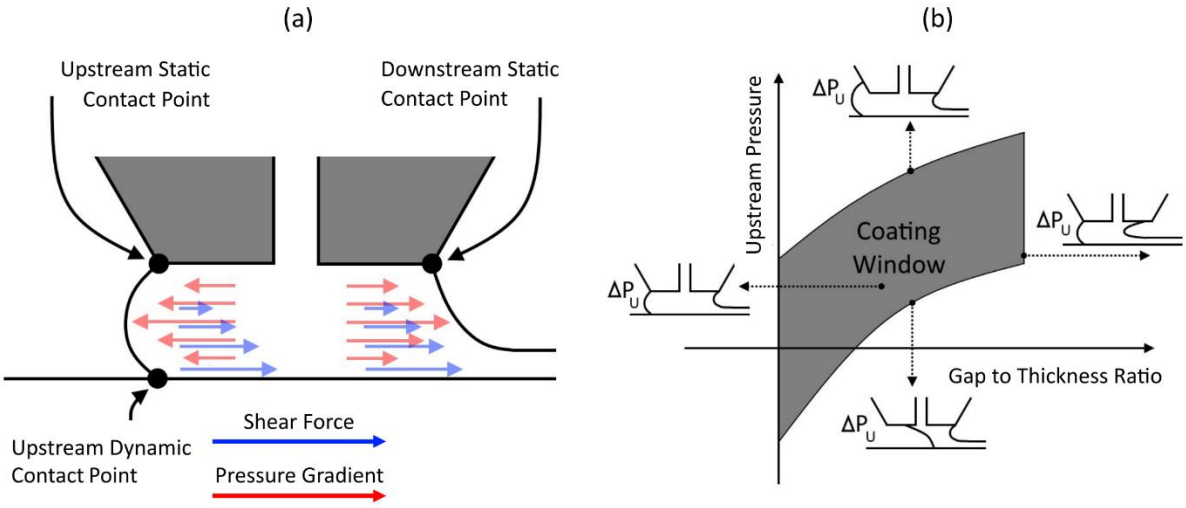

Figure 23: Maintenance of balance between the shear force and pressure gradient (b) Determination of coating window [97]

To obtain a stable coating, the coating window has to be determined. It is determined by finding a balance between the gap-to-thickness ratio and the upstream pressure where the gap-to-thickness ratio is varied by varying the critical process parameters. They are the flow rate of the solution, the bottom of slot-die to substrate height, and the speed at which the substrate moves. An example of the coating window determination is given in Figure 23b.

3.4.1 Slot-die coating parameters optimized for this thesis

The slot-die coating of SnO_2 is used as an electron transport layer (ETL) in planar perovskite solar cells shown in chapter 5. A home-made 3D printer turned slot-die coating system present at CSIRO was used. In this system, a stable substrate holder is used while the slot-die head is attached to a lever that moves. However, the basic principle governing the coating mechanism remains the same. All the process parameters (i.e., flow rate, menisci height, and

the speed of deposition) are controlled using the 3D designing software. Thus, the SnO_2 coating for the substrates used a coating speed of 10 mm/s, and a bed (substrate holder) temperature of 50 ^oC was maintained to have a homogeneous layer.

3.5 Screen-printing

The screen-printing technique exists for a long time now. It was first commercially developed in the 1850s for textile printing and further developed in the 1920s for printing posters and giant advertisements. Advantages such as low-cost fabrication and its flexibility in substrate independent application paved the way for its usage in electronic industries.

Figure 24 shows the necessary components involved in the screen-printer, and their functions in printing are as follows:

- **Screen** – The screen consists of a mesh and a polymer layer which is modified using a photo-stencil that replicates the required design. The mesh is stretched upon a frame with a tension such that the mesh peels away from the substrate soon after it passes over. Ideally, the mesh is stretched where its elongation limit is 1 %. They are attached to the frames such that the pressure given is spread to the corners preventing the screens from significant damages.
- **Squeegee** – Squeegee settings are essential to have a reproducible thickness of the resultant layer. The squeegee parameters, such as pressure, speed, and down-stop, are set. It is made sure that the squeegee always runs parallel to the substrate. Their size and thickness are selected based on the application and the viscosity of the paste to be printed. Widely, squeegees made from polyurethane are used.
- **Base** – The substrate is mounted on this base, which usually uses a vacuum to hold the substrate in place during the entire printing process.
- **Paste/ink** – The main element that needs to be transferred on to the substrate in a particular pattern. The viscosity of the paste also influences the printing parameters. The viscosity is selected such that they are not too viscous that it clogs the mesh and not less viscous that it is spread after printing.

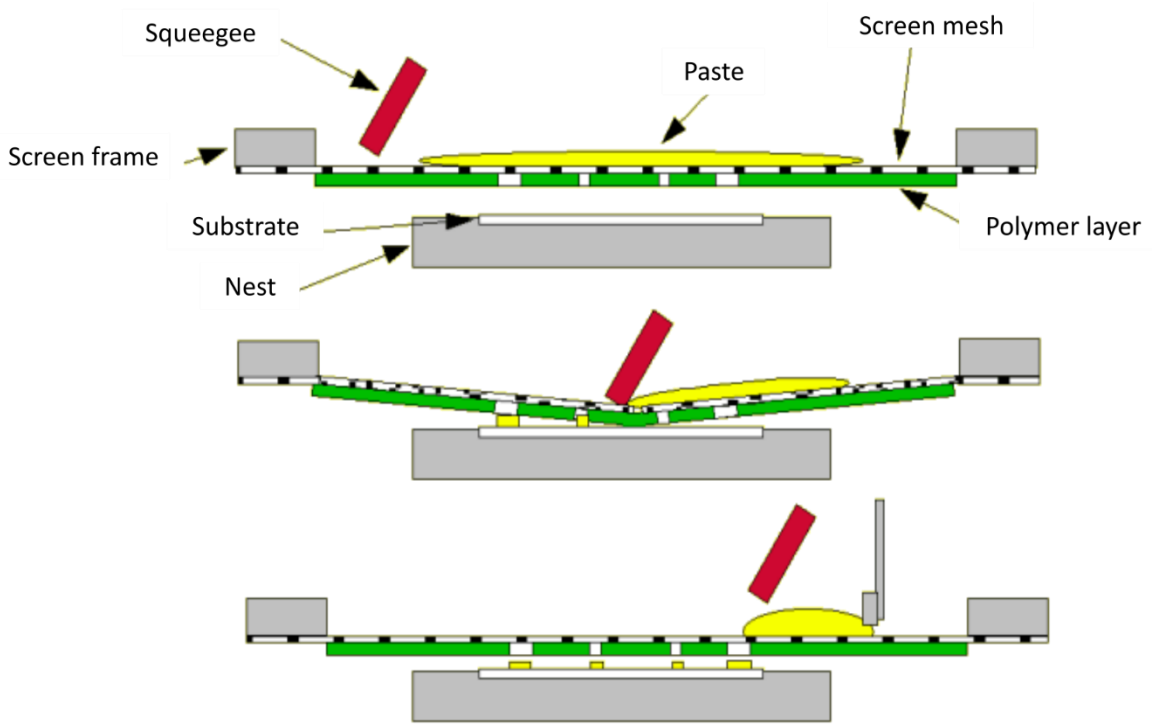

Figure 24: The basic printing process [98]

While screen-printing is widely used in the electronics industry, the print thickness plays a significant role in their performance. The mesh parameter determines the thickness of the print based on the thread thickness and the number of the mesh opening per cm^2. As a basic rule, the mesh opening should be three times the individual particle size used in the paste, and the minimum line of width is three times the mesh diameter.

For a reproducible printing of a particular paste, the following parameters should be optimized:

- **Squeegee pressure** – It is set such that the paste is pushed into the open area of the mesh precisely. Too much pressure leads to the reduced thickness, and too little pressure does not produce a uniform print.
- **Squeegee speed** – It is to set the speed such that the screen-mesh peels off from the substrate soon after the printing. Faster speed with low pressure will result in poor printing.
- **Snap-off** – it is the distance between the substrate and the screen. It is set such that the precise height-gap helps in peeling off.

It is to be noted that all these parameters are set based on the viscosity of the paste used.

3.5.1 Screen printing parameter optimized for this thesis

In this thesis, the devices prepared in chapter 6 and 7 has most of its layers fabricated through screen-printing. Ekra X4 screen printer located at Fraunhofer ISE was used. TiO_2 is screen-printed using the Dyesol DSL-18NRT paste mixed with terpineol in the weight ratio of 1:0.75. ZrO_2 is screen-printed using Solaronix Zr-Nanoxide ZT/SP paste. The parameters set for printing mp-TiO_2 and mp-ZrO_2 are a printing speed of 50 mm/s and a printing pressure of 50 N with a snap-off distance optimized to be 2 mm. The commercially bought carbon-graphite paste (Solaronix Elcocarb B/SP) is comparatively less viscous. Hence, less snap-off distance (1.25 mm) was used with a printing speed and pressure of 50 mm/s and 30 N, respectively.

Thereupon, in this section, the basic working principle of all the deposition techniques that have been used in device fabrication for this thesis was given. It also listed the specific process parameters that were optimized for the fabrication of different layers of the PSCs reported in this thesis.

Chapter - 4

Characterization Methods

4 Characterization Methods

This chapter provides a detailed explanation of all types of characterization techniques used in this thesis. It is divided into two sub-section. The first section, “morphology and crystallographic analysis,” specifies the techniques used for analyzing the layer morphology and its crystallographic details. It accounts for the working principle of various electron microscopy analysis such as SEM, TEM, EDX, roughness analysis through AFM, crystallographic analysis using XRD, Absorbance using UV-Vis and PL. The second sub-section details the shunt analysis with DLIT and other electrical characterizations used to interpret the performance of the PSCs. Detailed information is provided on the techniques used and the physics behind its data interpretation.

4.1 Morphology and crystallographic analysis

4.1.1 Scanning electron microscopy (SEM) and Energy dispersive X-ray (EDX) analysis

To fulfill the need to have a higher resolution than the optical microscope, an electron microscope (EM) came into existence. As the name says, these microscopes use accelerated electron to illuminate the source. Since the electrons are of high energy, resolution higher than the optical microscope is attained. Through SEM, topography, morphology, composition, and crystallographic information can be retrieved. It uses a focused electron beam to extract the structural information at the point of interest and collects the knocked-out electrons to recreate them as images. In 1935, a prototype of SEM was invented by Knoll in Germany, which was later released in the market in 1965 by Cambridge scientific instruments (UK) and Joel (Japan) separately.

Working Principle:

When the electron beam hits the sample, electrons or X-rays are emitted according to the depth of electron beam interaction with the sample (Figure 25).

- **Auger electrons:** These are electrons emitted with an interaction depth of 1 nm, which provides surface-sensitive information.
- **Secondary electrons (SE):** These are low energy electrons (< 50 eV) that results from the inelastic interaction between the electron beam and the sample. The interaction depth is the range of 5 – 50 nm. These electrons are detected by the Everhart-Thornley

detector, which consists of a scintillator inside a Faraday cage. The low energy SE is attracted to the surface of the cage that is at 10 kV. It is passed through the scintillator to produce light. They are amplified using a photon-multiplier tube (PMT) and are converted to electric signals to be given to the computer unit. SE provides information on the topography of the sample.

- **Backscattered electrons (BSE):** BSE are high energy electrons that result from elastic interaction between the electron beam and the sample. These are highly dependant on the atomic number of the sample. In this mode, the heavy elements appear brighter. The BSE are detected using a solid-state detector. They provide information on the atomic number and the topography information.
- **X-rays:** The electron beam that hits the sample knocks out an electron creating a hole. When electrons from the higher energy level fill this hole, the difference in the energy is emitted as X-ray. The energy of the X-rays depends on the atomic number of the element, making it a unique feature. Thus, X-rays are considered as a fingerprint of each element, which helps in their identification. A Silicon-drift detector (SDD) is used to capture the X-rays that provide information about the elements present in the sample. These X-rays are used for EDX analysis.

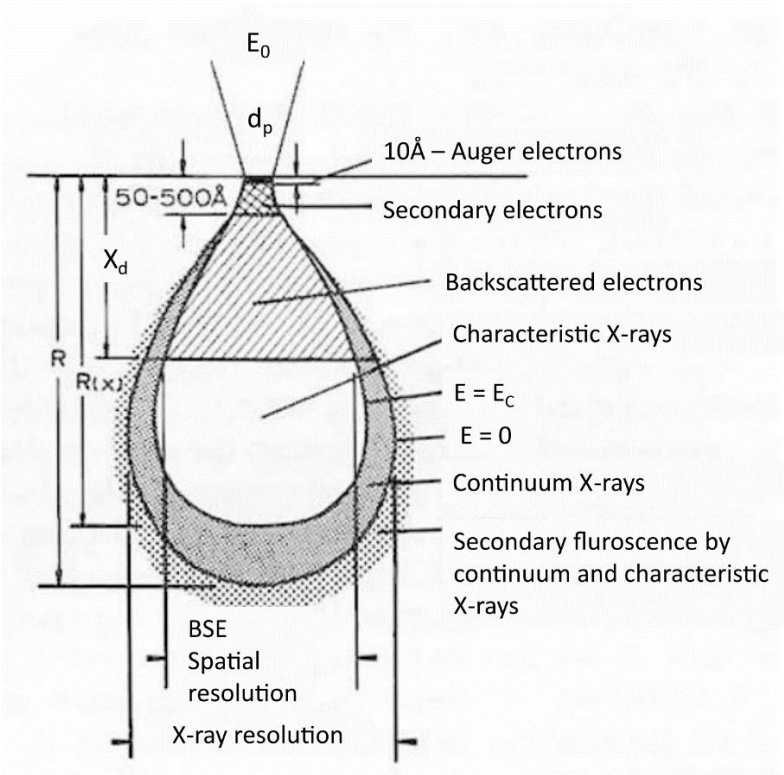

Figure 25: Signals from electron beam-sample interaction [99]

SEM Instrument:

The SEM instrument (Figure 26) consists of an electronic console, which stages the control knobs and an electron column that houses the source, lens, sample holder, and detectors. The details of the components in the electron column is given below:

1) **Electron gun:** It consists of a tungsten filament at 2700 K that produces the free electrons. Wehnelt, which houses the filament, controls the number of electrons that leave the gun. The acceleration of these electrons is controlled from 200 V to 30 kV.
2) **Condenser lens:** These lenses act as an anode. These are used to reduce the size of the incident to 1000 times its original size. It also adjusts the intensity of the beam that reaches the sample.
3) **Objective lens:** These lenses are used to determine the diameter or the spot size of the electron beam on to the sample. It is an important parameter that determines the resolution and the depth of the field produced in the sample. Lower the spot size higher is the resolution and deeper is the beam interaction in the sample.
4) **Scanning coils:** These coils are used to deflect the incident beam vertically or horizontally on the samples. It helps in focusing the beam on the region of interest (ROI). This vertical or horizontal deflection of the electron beam on the sample is called rastering.
5) **Detectors:** Various detectors such as solid-state detectors, Everhart-Thornley detector, and silicon-drift detectors are used to capture backscattered electrons, secondary electrons, and X-rays, respectively. All the detectors are connected to the computer unit that converts the signals to necessary output forms such as images, the elemental composition, which aids in quantitative and qualitative analysis.

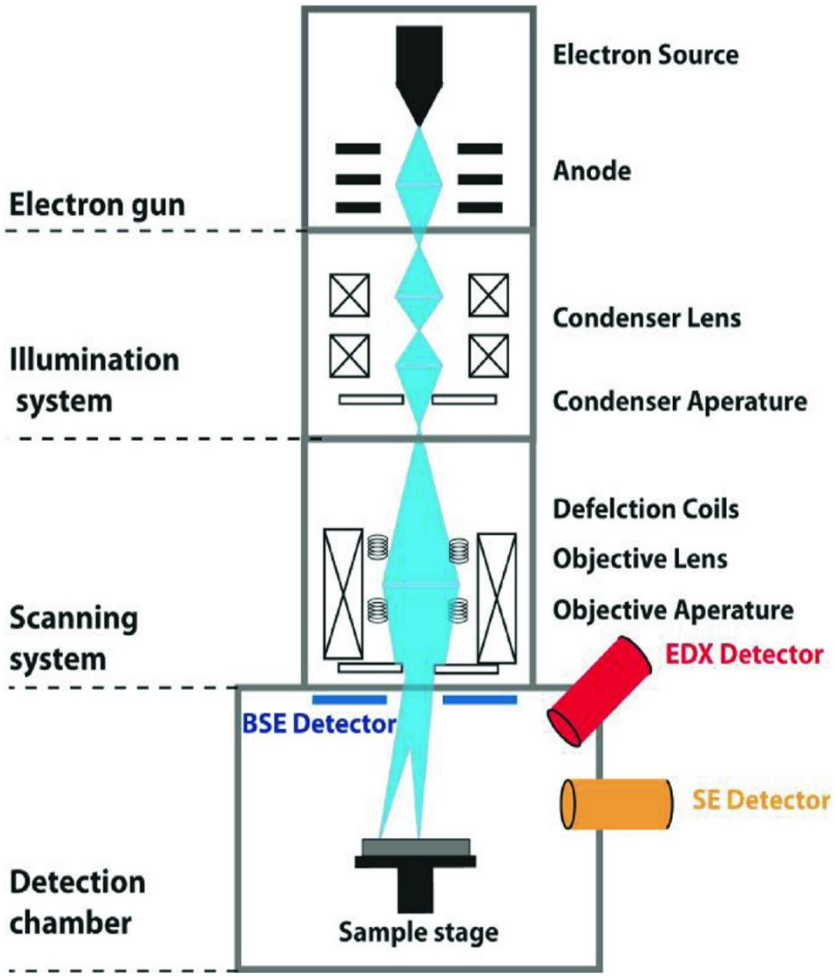

Figure 26: Schematic diagram of an SEM instrument [100]

Energy dispersive X-ray (EDX) analysis:

EDX is a non-destructive technique coupled with SEM that provides elemental information and supports its analysis. The EDX data consists of a spectrum of elements collected by the SDD. The software, coupled with it, marks each peak in the spectra to individual elements. These data then aid in qualitative and quantitative (percentage concentration of each element) analysis on the data.

Relation to this thesis

In this thesis, all the works reported in chapter 5, 6, and 7 has a standard SEM measurement that was carried out to analyze the crystallinity, crystal size, morphology and layer thickness of the corresponding architectures used. EDX analysis was used for precisely showing the ultra-thin sputtered Al_2O_3, as shown in Figure 83 and explained in section 7.3.3.1. For the results shown in chapter 5, SEM images were taken using the Zeiss Merlin field emission microscope in CSIRO. 5 kV and a working distance of 5-6 mm was used. The images were

captured using the InLens detector. For the results shown in chapters 6 and 7, Zeiss Aurigo 60 Dual Beam SEM present in Fraunhofer ISE was used. SEM images used 5 kV, and EDX analysis used 7 kV. Either InLens or SE2 detectors were used.

4.1.2 Transmission electron microscope (TEM)

A transmission electron microscope is also a microscopy technique that uses an electron beam as the source to illuminate the samples. Even though the basic principle is the same, TEM uses electrons at high acceleration voltages (enabling resolution of 0.2 nm) that passes through samples. The transmitted and diffracted electrons are captured onto a fluorescent screen. The captured image gives information on the crystallography and atomic position in the sample. 1n 1931, Max Knoll and Ernst Ruska from Germany built the first TEM, and it was later commercialized by the same group in 1939.

Working principle:

The highly accelerated electrons pass through a thin sample. The electrons are either transmitted or diffracted.

1) A **transmission beam** is formed by unscattered electrons that are not deflected while passing through the sample—the resulting image, as shown in Figure 27a. Dark region points to thicker regions, whereas bright areas are places where there is no element present.
2) The **diffraction pattern** results from the scattered electrons, which are sourced by two kinds of scattered electrons based on their interaction with the sample. Elastically scattered electrons are deflected by the atom's position but without any energy loss. It provides information about orientation, atomic arrangements, and its phases. Inelastically scattered electrons are deflected due to energy loss during the interaction of incident electron beam with the sample. As the energy losses are unique to each element, they are stored and analyzed in electron energy loss spectroscopy.

High resolution TEM (HRTEM):

It uses both the scattered and unscattered beam to produce an interference image (Figure 27b). It is capable of giving a contrast image of a unit cell, thereby giving a direct representation of the atomic structure.

Selected area electron diffraction (SAED):

Scattered electrons following Bragg's law $(\lambda = 2d \sin\theta)$ where a pattern of spots is formed corresponding to the plane and the atomic spacing in the element. Inset of Figure 27b is the result of selected area electron diffraction (SAED). By using the formula, $d = \frac{D}{\lambda L}$ where d is the spacing between the planes, D is the distance between the spots in SAED pattern, L is the camera length for the TEM machine, and λ is the wavelength of the electron beam. A pattern of spots is formed for single crystal, whereas a concentric ring of spots (Ewald sphere) is constructed for polycrystalline samples. No spots, but a halo bright spot is visible in case of an amorphous sample.

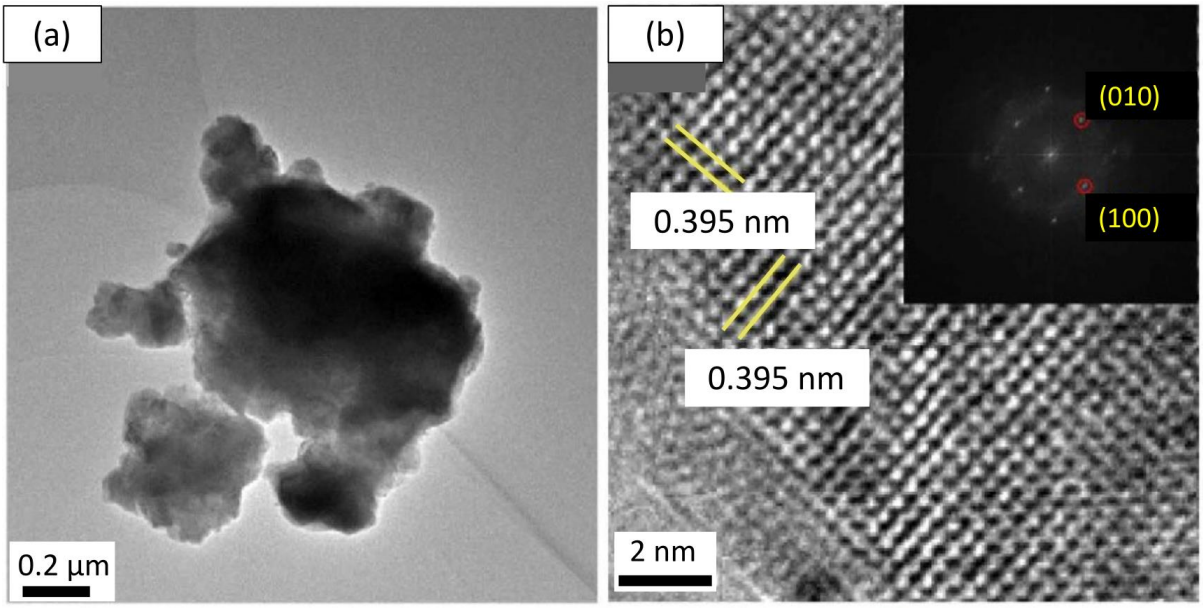

Figure 27: (a) TEM image of $Bi_{0.1}$BSCF - $Bi_{0.1}(Ba_{0.5}Sr_{0.5})_{0.9}Co_{0.8}Fe_{0.2}O_{3-\delta}$ perovskite (b) HRTEM and inset is the SAED analysis [101]

TEM instrument:

The TEM instrument (as shown in Figure 28) consists of the following components

1) **Electron gun:** A Wehnelt and a tungsten filament produces free electrons. The acceleration is controlled in the range of 40 to 100 kV.
2) **Condenser lens:** The free electrons are condensed to form a coherent beam and determine the spot size of the electrons beam onto the sample.
3) **Sample:** The holder for the sample is provided. The condensed electron beam passes through it.

4) **Objective lens:** It focuses on the transmitted electron and enhances its contrast to be formed into an image
5) **Intermediate lens:** The periodic diffraction of an electron can be studied by the user through adjusting this lens.
6) **Projector lens:** It projects the enhanced transmitted electron beam on to the screen.
7) **Fluorescent screen:** Forms the image pattern on a phosphor screen. When the electrons strike the screen, light is generated, which enables us to see the image.

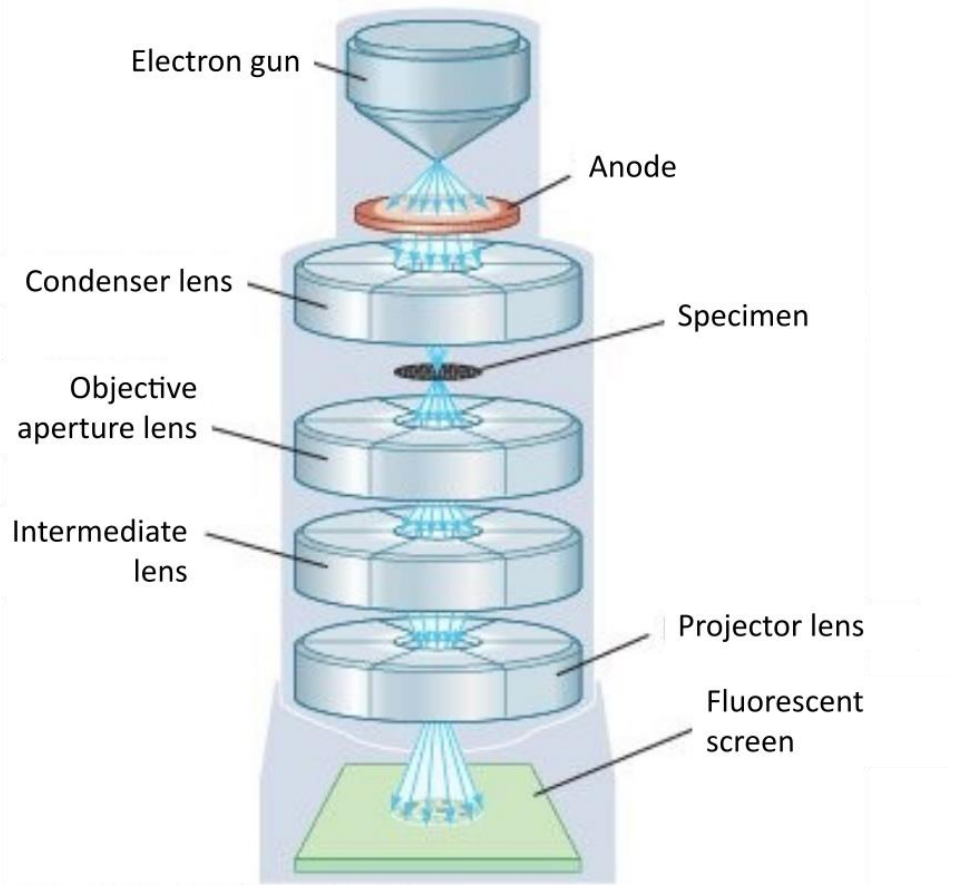

Figure 28: A schematic representation of a TEM instrument [102]

Relation to this thesis

In this thesis, HRTEM measurements were carried out for the devices reported in chapter 7. For our measurement, an instrument from JEOL present at the University of Strasbourg was used. It clearly shows the presence of an amorphous Al_2O_3 layer that surrounds the crystalline TiO_2 particles. The results are shown in Figure 78 and explained in section 7.3.1.1.

4.1.3 Atomic Force Microscopy (AFM)

Another technique to measure the topography of thin films is the AFM technique. It probes the surface in the atomic scale with a resolution of 0.2 nm. Its main advantage over SEM and TEM is that it gives a 3D magnification with a vertical resolution of 0.05 nm. It is used to analyze also non-conductive samples without any additional surface treatment. It was invented in 1986 by Gerd Binning, Christoph Gerber, and Calvin Quate [103]. One year later, Wickramasinghe *et al.* introduced a vibrating cantilever technique [104].

AFM instrument:

AFM measurement setup consists of a cantilever with a tip that moves over the sample as shown in Figure 29a. The force exerted over the tip is recognized by a photodiode that is sensitive to the position. A feedback system adjusts the new force according to the reference and gives a signal back to the scanner to maintain constant contact of the cantilever tip with the sample surface.

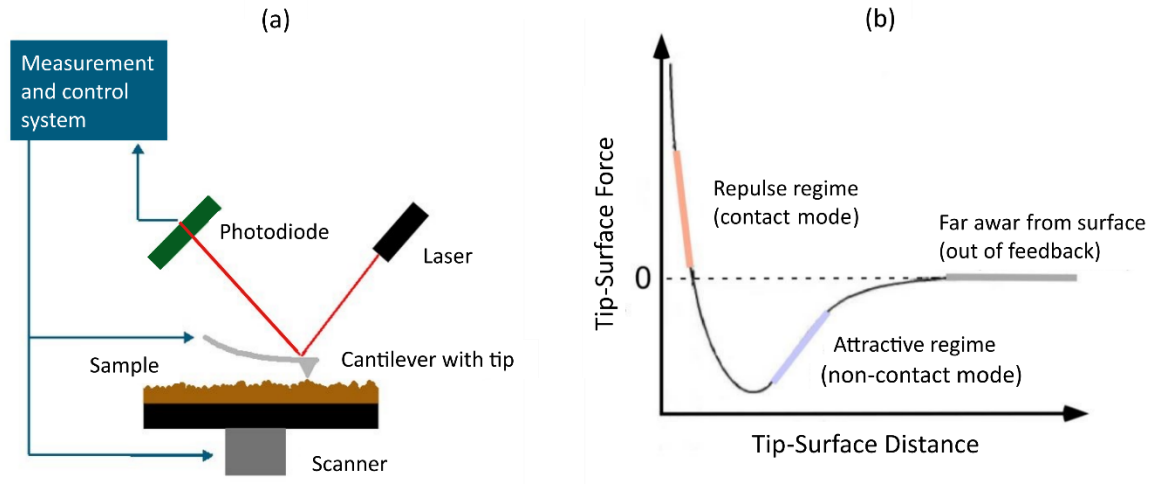

Figure 29: (a) Basic setup of AFM instrument [105] *(b) Different modes used in AFM* [106]

Modes of contact:

There are three types of scanning modes (Figure 29b)available. They are:

1. **Contact mode:** It works on the repulsion principle, where a minimal distance in angstrom is maintained between the tip and the sample. A strong repulsive force is exerted at the atomic level distances; thus, the tip-sample is considered to be in contact. The cantilever's deflection is maintained to sustain the tip-sample connection

consistently. High speed scan is possible in this mode; however, it damages the surface of the sample.

2. **Non-contact mode:** It works on the principle of attraction. Polarized atoms polarize its neighboring atoms, which creates a force of attraction. Thus, a sample-tip distance is maintained. Here the tip resonates at a constant frequency and maintains the amplitude. For this reason, only a low-resolution image is produced.
3. **Tapping mode:** The cantilever tip is continuously tapping on the surface of the sample (i.e., contact with the surface at constant intervals), and this it utilizes both the repulsive and attractive forces. In general, a frequency in the range of 50 – 500 kHz and the amplitude in the range of 20 – 200 nm can be maintained. Thus, the resulting image is of high resolution obtained without damaging the sample. However, it can be used only with slow scan speed.

Apart from the modes mentioned above, two other modes of scanning can be used—contact height mode and constant force mode. In contact height mode, the height of the scanner is fixed; thus, the deflection observed in the cantilever directly maps to the topographic image. The commonly used scanning mode is the constant force mode where the cantilever's deflection is given to the feedback system that controls the z (height) scan direction. Further, the phase lag between the surface-tip is recorded as phase image. It is also acquired together with the topography image to understand better surface morphology.

Relation to this thesis

AFM was used in this thesis to verify the roughness and morphology of the corresponding layers under investigation. In chapter 5, it is shown how to interpret the skewness factor in relation to the roughness. A negative skewness factor indicates the absence of big particles or agglomerates (section 5.3.2). In chapter 6 and chapter 7, AFM measurements showed a uniform layer of different HBL processing techniques on FTO and sputtered Al_2O_3 on mp-TiO_2, respectively. For the results shown in chapter 5, A Bruker FastScan atomic force microscope (present in CSIRO) with Icon scanning head along with Ultrasharp silicon nitride tips and NanoScope 9.4 software was used. For the results shown in chapters 6 and 7, similar AFM machine and software present in the University of Strasbourg was used. The surface topology, in all cases, was analyzed using tapping mode.

4.1.4 X-ray diffraction (XRD) analysis

In 1912, it was discovered that when X-rays pass through a crystal lattice, it forms a three-dimensional diffraction grating similar to the spacing of phases in the crystal. It is a non-destructive technique used to study atomic spacing, phase identification and its orientation, structural properties such as strain and grain/crystal size.

Working principle:

When the incident X-ray beam hits the samples, the atoms in the crystal lattice absorbs this energy. Due to elastic scattering between the X-ray and the sample, X-rays are further emitted from the sample. By rotating the source and the detector, the intensity of the reflected X-rays is recorded. Generally, the source is rotated at angle θ, and the detector is rotated at an angle of 2θ. When the incident and the reflected rays follow Bragg's equation, $n\lambda = 2d \sin\theta$, diffraction pattern as a result of constructive interference occurs (Figure 30). They are unique for various elements like a fingerprint. Thus, they are recorded, *d* spacing values are calculated and compared with values in the shared file to identify the elements present.

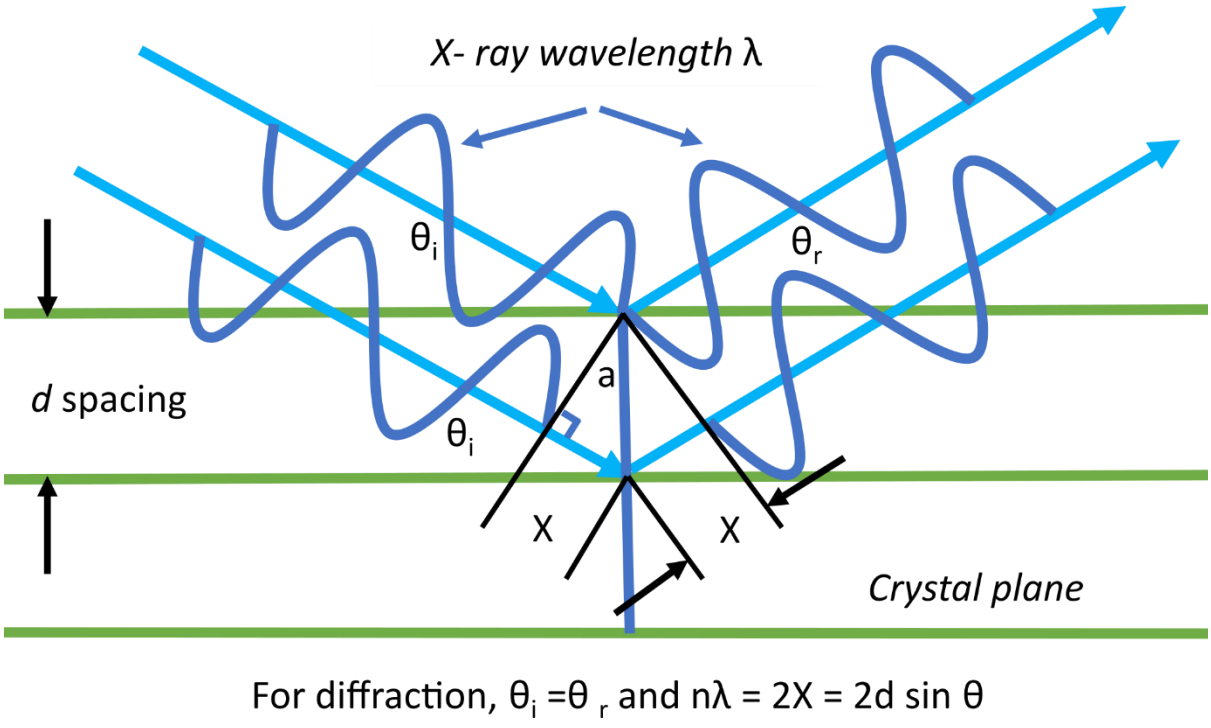

Figure 30: Diffraction according to Bragg's law [107]

XRD instrument:

A schematic diagram of an XRD instrument is shown in Figure 31. It consists of the following components:

1) **X-ray tube:** X-rays are created in a cathode ray tube by heating a filament. Free electrons produced are accelerated by applying voltage. They have the facility to be moved at different angles.
2) **Goniometer:** It consists of the sample holder that also can rotate.
3) **Detector:** The emitted characteristic X-rays from the sample is collected through the detector.

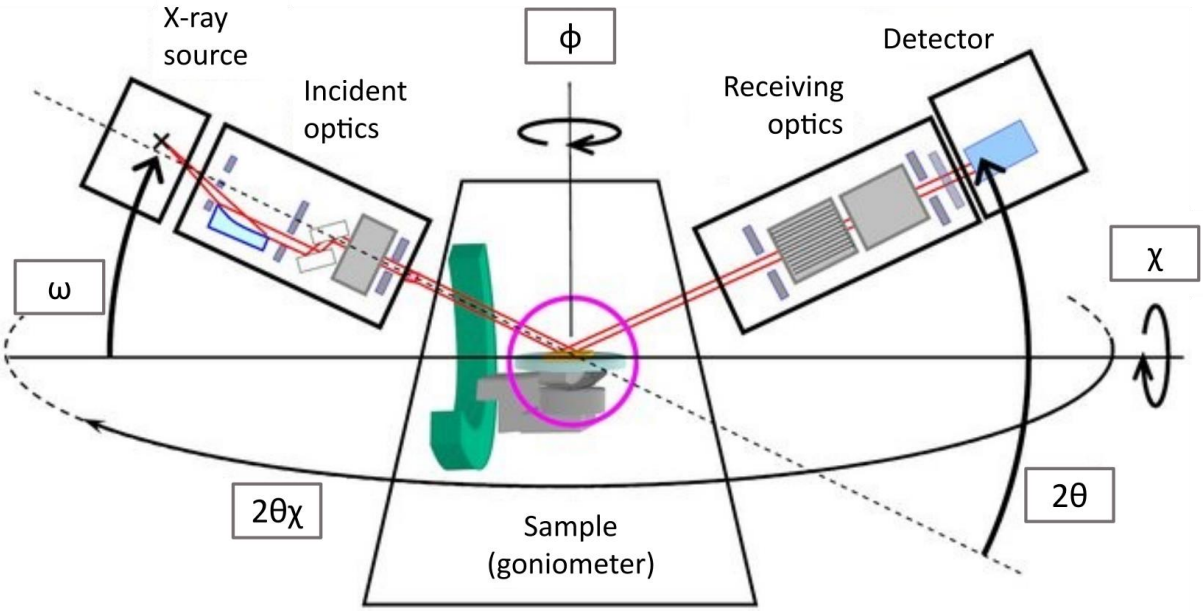

Figure 31: Schematic diagram of an XRD instrument [78]

Information from X-ray diffraction:

Informations that can be obtained from XRD are:

- **Phase identification:** The phase identification can be done quantitatively and also qualitatively. Qualitative analysis involves identifying the elements through *d* spacing calculation, and quantitative analysis is done commonly through the reference intensity ratio method (RIR). It identifies not only the crystalline phases but also its orientation.

- **Crystalline size:** When the size of the crystals is < 120 nm, the broadening of the diffraction peak occurs. Thus, using Scherrer's equation, the crystal size can be calculated.

$$\tau = \frac{k\lambda}{\beta \cos\theta} \qquad \textit{Eq 17}$$

where,

τ = Crystal or the crystallite size (nm)

k = shape factor, usually having a value close to 1

λ = X-ray wavelength (μm)

β = breadth at full-width half peak height

θ = Bragg angle (^{o})

- **Lattice strain:** It can be calculated while analyzing a thin film. The peak remains the same when there is no strain. The peak is shifted if there is a uniform strain present. However, the peak is broadened and also shifted in case of non-uniform strain caused by point defects, deformation, or poor crystallinity.

Relation to this thesis

In this thesis, all the results chapters 5, 6, and 7 consist of XRD results in grazing incidence mode. For the devices in chapters 6 and 7, it gives the crystallinity and its corresponding phase for the layers under investigation. In chapter 5, XRD results were interpreted uniquely. The results are shown in section 5.3.7. Here, the XRD diffractograms at various incidence angles were taken for sub-cells before and after UV treatment. The area under the main peak representing PbI_2 and perovskite was calculated, and the corresponding change in its value concerning the incidence angle was analyzed. An excess PbI_2 was observed on the surface of the sub-cell after UV treatment. Thus, a quantitative analysis of the sub-cells was made using XRD analysis. For the devices in chapter 5, A Rigaku SmartLab with a rotating anode CuKα source (45kV, 200mA) present in CSIRO, equipped with a Hypix 3000 detector, was employed to obtain grazing incidence XRD patterns. The analysis was performed on the collected XRD data using the Bruker XRD search match program EVA™5. For the results shown in chapters 6 and 7, a similar machine from the same manufacturer present in the University of Strasbourg was used.

4.1.5 UV-vis spectroscopy

Spectroscopy is the analysis of the interaction between the sample and the entire electromagnetic spectrum or with a particular wavelength.

UV-Vis spectroscopy involves measuring the absorbance of both UV (200 to 400 nm) and visible light wavelengths (400 nm to 750 nm) by the sample under investigation. When the molecule absorbs the light, the electrons in the highest energy occupied molecular orbital (HOMO) level are excited to the lowest energy unoccupied molecular orbital (LUMO) level. The distance between the HOMO and the LUMO level is the bandgap (E_g), and its values differ from various molecules. Thus, the absorption spectra produced is also distinct for individual molecules/elements.

The electronic interactions in the orbital level take places between n, π, σ, π* and σ* orbitals where, n is the non-bonding state, π and σ are bonding orbitals, and π* and σ* are non-bonding orbitals. Frequent electronic transitions are between n-π*, n- σ*, π- π*, π- σ* and σ-σ*orbitals (Figure 32). The peak wavelength absorbed is based on one or combined effect of these electronic transitions that differ based on the molecules.

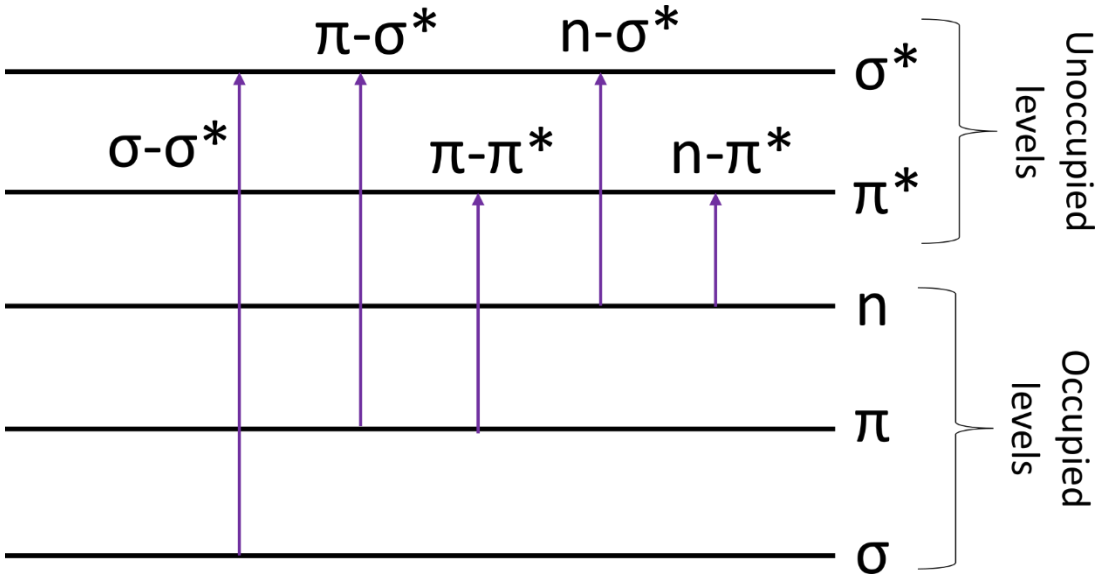

Figure 32: Frequent electronic transitions

UV-Vis spectroscopy instrument:

The UV-vis spectroscopy instrument (Figure 33) consists of the following components:

1) **Source:** Two lamps are used in this case, namely deuterium lamp for UV wavelength (170 to 375 nm) and tungsten filament lamp for visible wavelength (400 to 700 nm). Wavelengths longer than 700 nm are also possible to be obtained.
2) **Filter:** Focuses the light on to the monochromator
3) **Monochromator:** It consists of a prism and a slit. The prism diffracts the light and sends a spectrum of light through a slit that emits one wavelength at a time.
4) **Beam splitter:** The beam is split into two. One without any changes serves as reference intensity (I_0), and the other passes through the sample and its intensity changes after absorption (I).
5) **Data processing:** Photodiodes are reference, and the sample's intensities are compared and processed to give the absorption spectrum.

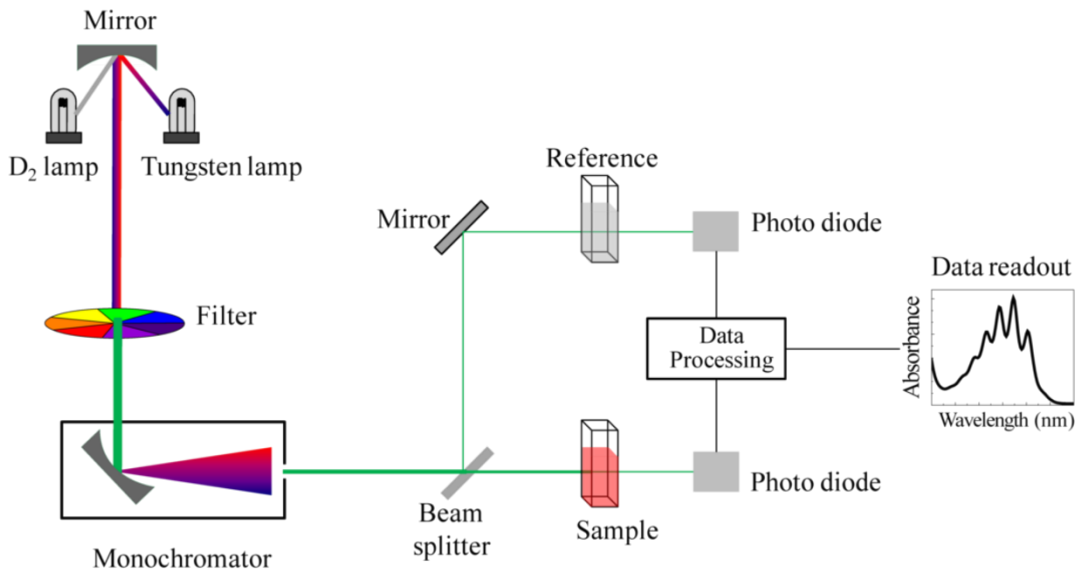

Figure 33: Schematic of UV-vis spectroscopy [108]

Working principle:

As explained, after the beam passes through the sample, it is compared with the reference. The ratio between them formulates the absorption spectrum and the peak wavelength that is observed (λ_{max}). They are calculated based on Beer-Lambert's law:

$$\log \frac{I_0}{I} = A = \varepsilon c l \qquad \textit{Eq 18}$$

where,

A = absorption

I_0 = Reference light intensity

I = light intensity after passing through the sample

ε = Molar extinction co-efficient (l mol^{-1} cm^{-1})

c = concentration of the sample (mol/l)

l = length of the light path (cm)

4.1.6 Fluorescence spectroscopy

The fluorescence spectroscopy is also sourced by a range of wavelengths; however, it provides information on the light emitted after the absorption.

Working principle:

The electrons in the HOMO level is excited to the LUMO level after absorbing light energy > bandgap of the molecule. It initially relaxes through its sub-levels by losing a few amounts of energy. This initial relaxation is named as vibrational relaxation. It is followed by the relaxation to back to the sub-levels of the HOMO level, which emits a photon. The process is described through a Jablonski diagram (Figure 34a). It is be noted that the energy of the emitted photon is lower than the incident light, and thus the peak is shifted to a higher wavelength (Figure 34b).

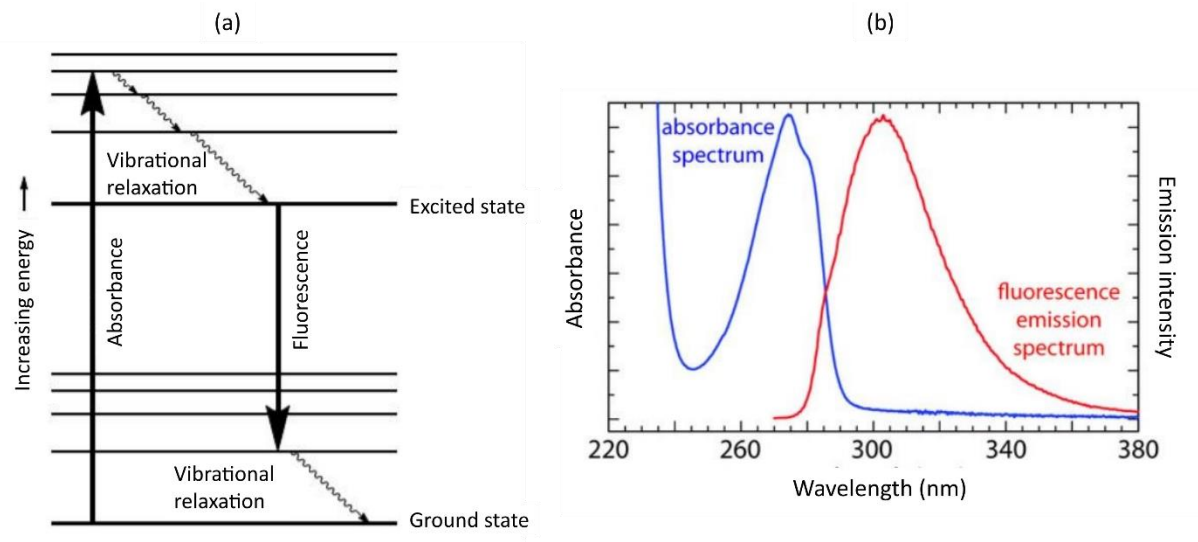

Figure 34: (a) Jablonski diagram showing fluorescence principle [109] *(b) Sample absorbance and emission spectrum* [110]

Relation to this thesis

In this thesis, the UV-vis spectroscopy was used to analyze the change in the transmittance of ITO/SnO_2/perovskite sub-cell before and after UV treatment in chapter 5 (section 5.3.6). UV-vis spectrophotometer from Hewlett-Packard/Agilent 8453 equipped with an integrated sphere in CSIRO was used. It was also used in chapter 6 to analyze the transmittance of HBL processed through various deposition techniques (section 6.3.2). Lower transmittance was observed for SPD-HBL owing to small distributed particles in their layers.

Fluorescence spectrometer instrument:

The components found in the instrument setup for fluorescence spectroscopy (Figure 35) is as follows:

1) **Source:** The necessary wavelength of light is produced similar to the source of a UV-vis spectroscopy setup.
2) **Monochromator:** Individual wavelengths are sent to the filter on to the sample
3) **Photomultiplier:** After passing through the sample, the emitted light is captured and sent to the photomultiplier for amplifying the signal
4) **Data processing:** The amplified signals are sent to the data processing unit for analysis.

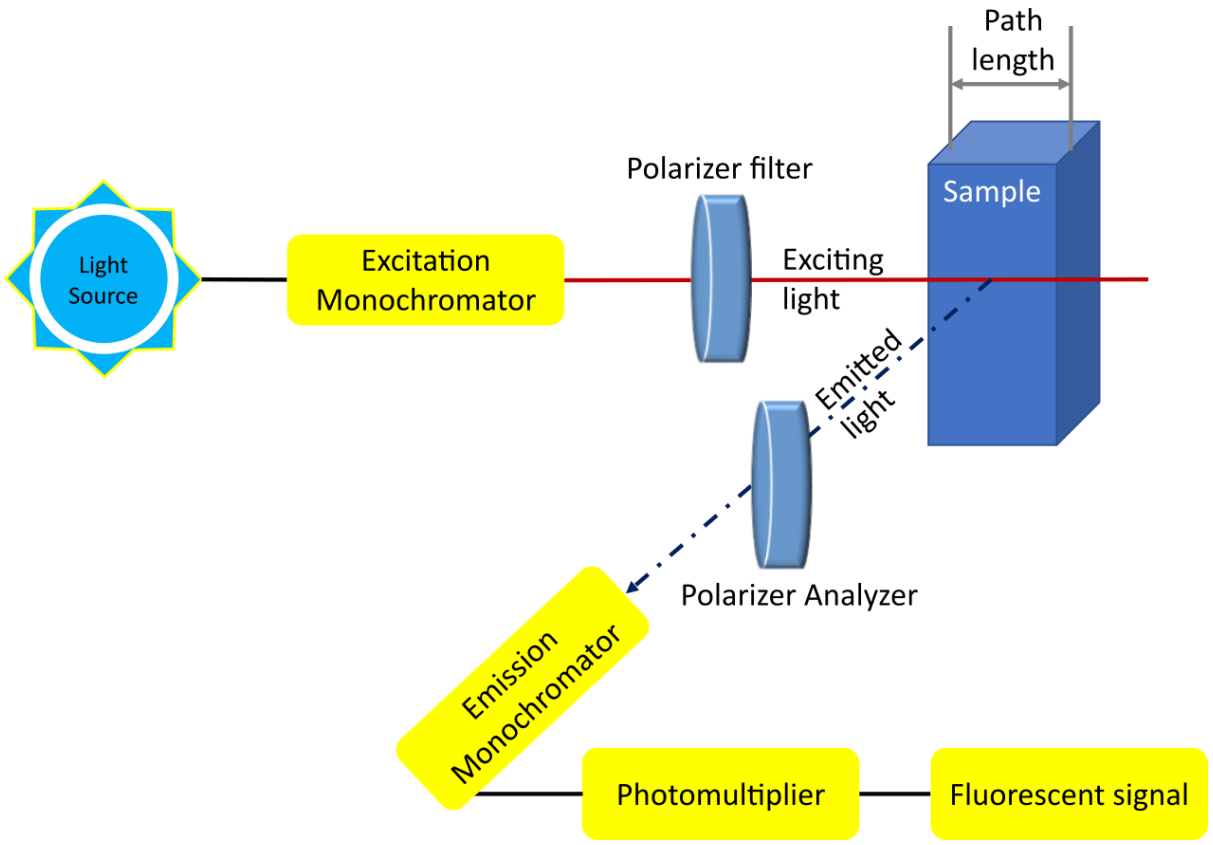

Figure 35: Schematic diagram of a fluorescence spectroscopy instrument [111]

Relation to this thesis

The fluorescence spectrometer was used to analyze the change in the PL for ITO/SnO_2/perovskite sub-cells before and after UV treatment in chapter 5 (section 5.3.6). The instrument from Perkin Elmer (model no. L5S5) present in CSIRO was used. The results show an increase in PL after UV stress owing to poor electron transfer to SnO_2.

4.1.7 X-ray photoelectron spectroscopy

X-ray photoelectron spectroscopy (XPS) is one of the surface characterization tools which is also used to determine the elements present. It was developed by Kai Siegbahn in the 1960s. It gives the data about the elements present in a sample and its bond with the neighboring elements.

Working principle:

When the energy of the incident X-ray is greater than the binding energy of an electron, then it is released from the atomic structure (Figure 36). The kinetic energy (KE) of this emitted electron depends on the photon energy and the binding energy of an electron. It can be given

by the formula, $KE = h\upsilon - BE$. Binding energy (BE) is defined as the energy required to remove an electron from the surface. These two energies are analyzed to obtain the details of the elements present in the sample's surface. The kinetic energy gives information on the element type, chemical state, and the binding energy. Further, the BE provides more in-depth information such as the orbital and chemical environment from which the electron is ejected. BE can be identified using the formula:

$$E_{binding} = E_{photon} - (E_{kinetic} + \Phi) \qquad \textit{Eq 19}$$

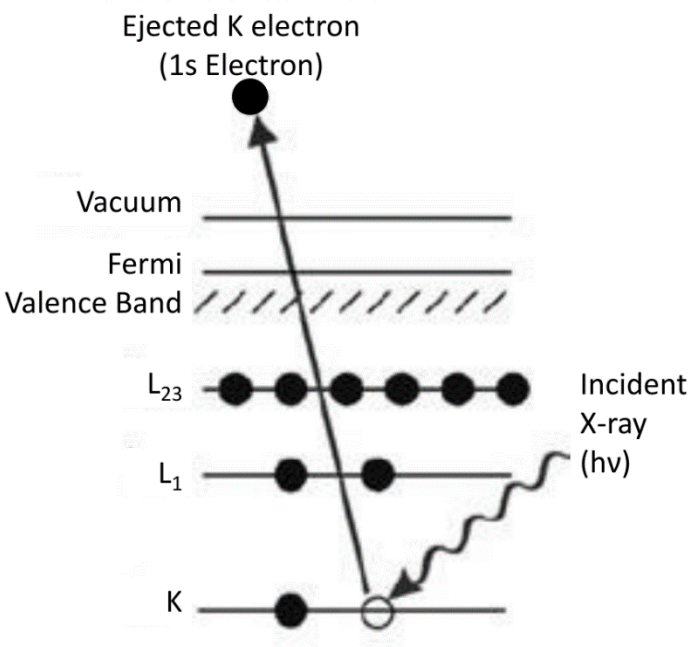

Figure 36: Working principle of XPS [112]

XPS instrument:

Schematic representation of an XPS instrument is shown in Figure 37.

1) **X-ray source:** Produces incident X-rays.
2) **Ultra-high vacuum (UHV) chamber:** The sample is housed inside the UHV chamber. It is kept in the pressure around 10^{-9} mbar. Such low pressure is required to prevent the sample from surface contaminations caused by atmospheric agents such as O_2, H_2O, etc. Even at pressures such as 10^{-6} mbar, the atmospheric gases can still interact with the surface, which might cause a discrepancy in the data later. Thus, the UHV chamber is used to prevent surface degradation resulting in accurate measurement.

3) **Lens system:** After the interaction with the X-ray, the electrons that escape from the sample's surface is caught by the lens system.
4) **Electron energy analyzer:** The amount of electron and its kinetic energy is analyzed in the electron analyzer.
5) **Electron multiplier:** The signal from the electron energy analyzer is further multiplied in the electron multiplier and given to the data processing unit. It formulates the XPS spectrum, which maps the intensity vs. the binding energy of all the emitted electrons.

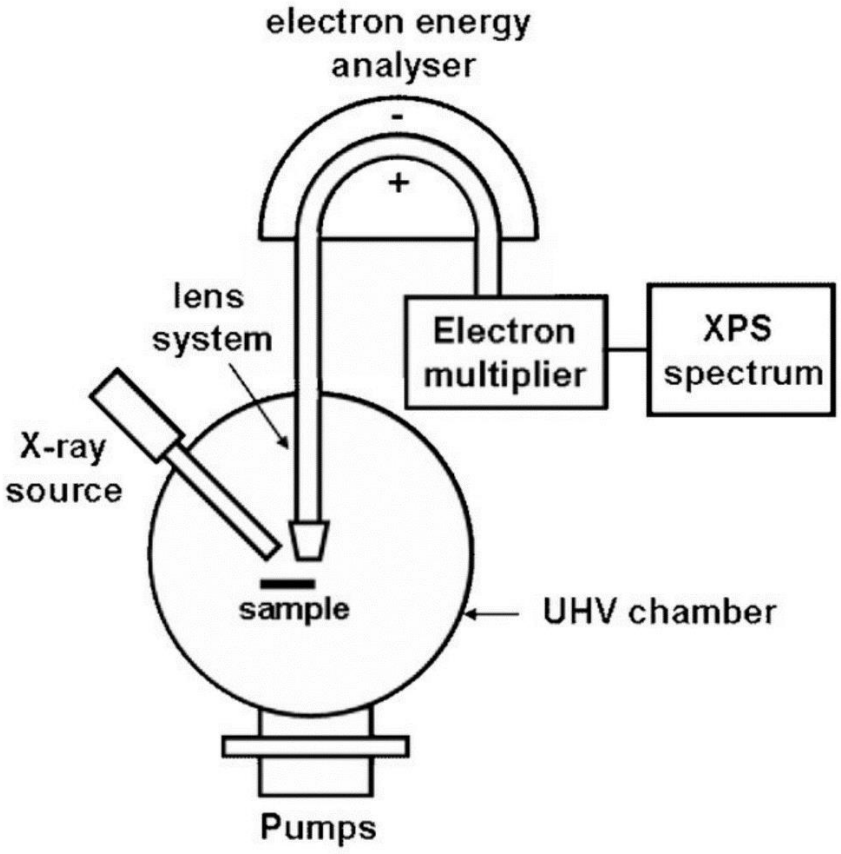

Figure 37: Schematic diagram of an XPS instrument [113]

Relation to this thesis

XPS measurements were conducted on devices that were used in chapter 5. The sub-cells (ITO/SnO_2/perovskite) used in chapter 5 utilized XPS measurement to investigate the elemental changes before and after the UV treatment. XPS data were acquired at various depths by etching the surface at intervals. By comparative analysis, excess Pb was detected in the samples after UV treatment (section 5.3.8). The changes in the Sn:O ratio in an ITO/SnO_2 sample before and after UV were also analyzed, and the results are presented in section 5.3.8.

XPS analysis was performed using an AXIS Nova spectrometer present in CSIRO (Kratos Analytical Inc., Manchester, UK) with a monochromated Al Kα source at a power of 180 W (15 kV × 12 mA), a hemispherical analyzer operating in the fixed analyzer transmission mode, and the standard aperture (analysis area: 0.3 mm × 0.7 mm). The same setup with a He discharge UV lamp employing He I radiation (incident photon energy: 21.22 eV) was used for ultraviolet photon spectroscopy (UPS). They were used to identify the ionization potential of SnO_2 reported in chapter 5.

4.1.8 Contact angle measurement

Contact angle (CA) measurement is used to characterize the surface properties of the sample under investigation. It provides information about the surface energy, the wettability of the surface, adhesion, and cohesion forces in the liquid and at the solid/liquid interface, respectively.

Working principle:

When the liquid is dropped on the surface under investigation, a drop is formed. Based on the adhesion forces between the solid and the liquid, the contact angle is increased or decreased. At the point where the liquid comes in contact with the surface, a three-point contact line is formed. As shown in Figure 38, at the corner of the drop, a solid-liquid (SL), a liquid-gas (LG), and a solid-gas (SG) lines converge. The baseline of the drop is formed by the interaction of the solid and liquid. The contact angle is formed between the solid-liquid and liquid-gas line. The surface tension of the solid is calculated using a liquid with known surface tension by substituting its value in Young's equation:

$$\gamma_{SV} = \gamma_{SL} + \gamma_{LG} \cos\theta \qquad \textit{Eq 20}$$

where,

γ = surface tension (N/m)

θ = contact angle (°)

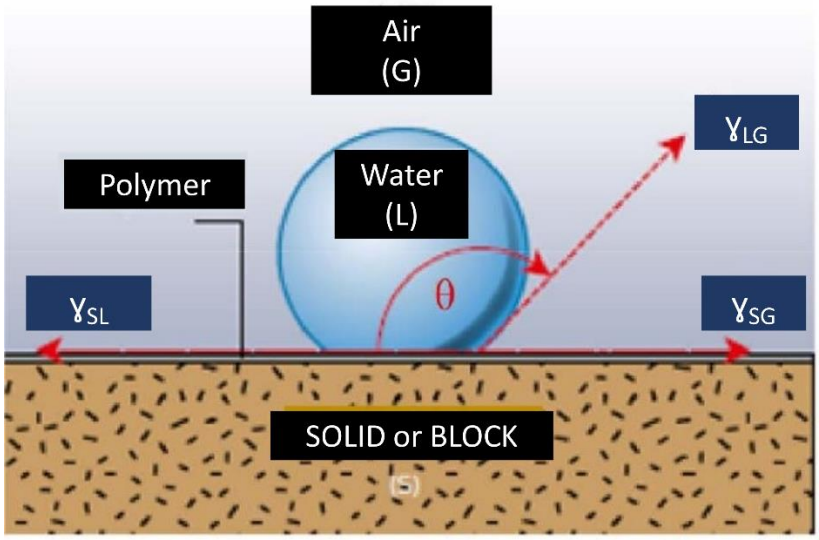

Figure 38: Formation of the drop on the sample film [114]

The nature of the surface under investigation can be understood through the contact angle and the surface tension values. Lower the contact angle, higher is the surface tension that results in good wetting and adhesion to the surface. Contaminants could also result in higher contact angle, which suggests different surface treatments based on the application.

Contact angle measurement instrument:

A schematic of a contact angle measurement is shown in Figure 39. It consists of a work station coupled with a stepping motor to control the pressure given to the syringe. The controls are also done through a user interface in software. The sample stage is well illuminated, and the CCD camera is used to record the bubble. Further calculations on the surface tension, height of the bubble, contact angle, etc. are calculated using the software.

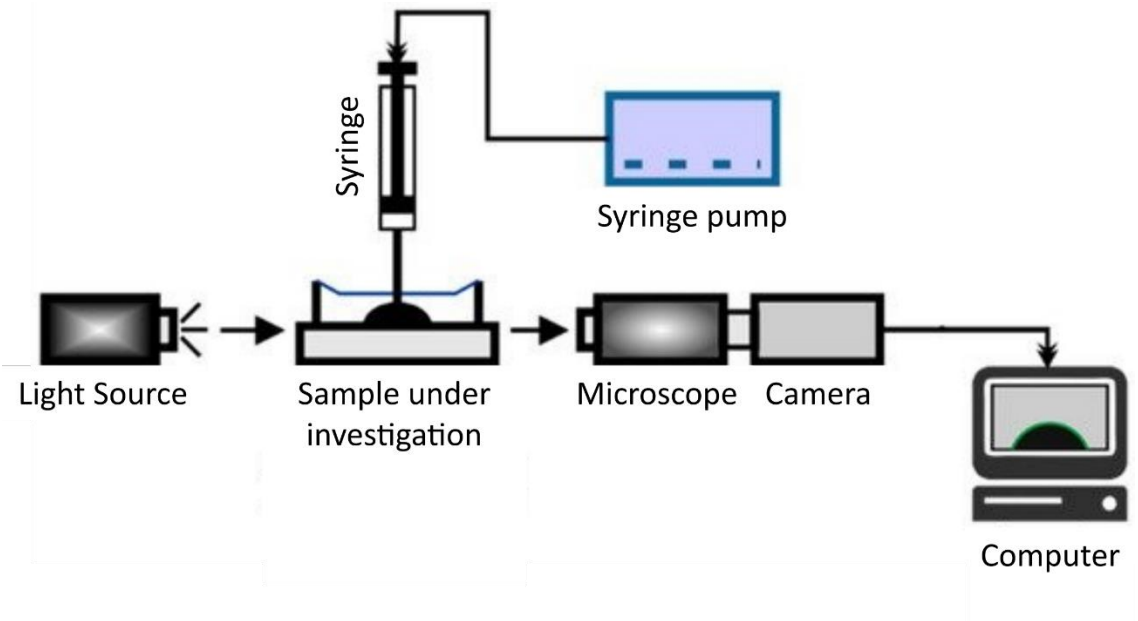

Figure 39: Contact angle measurement setup [115]

Relation to this thesis

Contact angle measurement was used to analyze the change in wettability when different additives were added to the SnO_2 solution (section 5.3.2) reported in chapter 5. The investigation was carried out in the CA instrument from Nanotechnology instruments present in CSIRO. Here, the perovskite solution itself was used as an investigating liquid. For the devices reported in chapter 7, the contact angle measurement was carried out to analyze the wetting properties of different thicknesses of Al_2O_3 sputtered on mp-TiO_2. Here, the corresponding drop height over time was plotted (Figure 81). Thus, the CA measurements not only provided an idea on the wettability of the sputtered Al_2O_3 layer but also provided an impression on the infiltration of the liquid through these layers. This knowledge will give an opinion on the penetration of perovskite solution into the CG-PSCs (because in CG-PSCs, perovskite drop coating is the last step in device fabrication).

4.2 Electrical characterization

This chapter discusses the electrical characterization that was carried out in this thesis.

4.2.1 Dark Lock-in Thermography (DLIT)

DLIT follows the camera-based thermal imaging technique. It is a non-intrusive technique to study the shunt points in a solar cell. It is an effective, easy to use quality control method where the shunt points are detected using an infrared (IR) camera.

Lock-in principle:

The mathematical expression of a lock-in principle is:

$$R(t) = \frac{1}{T}\int_0^T F(t).G(t)\,dt \qquad \textit{Eq 21}$$

where, R(t) is the resultant temperature signal from the solar cell, F(t) is the reference signal, and G(t) is the temperature signal. A phase-sensitive detection is carried out through the lock-in process to eliminate the noise signal. Therefore, the signal received at reference frequencies and frequencies in phase with reference is considered. Signals from all other frequencies are discarded.

Consider, sinusoidal input signal,

$$G(t) = G\sin(\omega_g t + \varphi) \qquad \textit{Eq 22}$$

And the reference signal,

$$F(t) = F\sin(\omega_f t + \Theta) \qquad \textit{Eq 23}$$

Applying G(t) and F(t) in R(t),

$$R(t) = \frac{GF}{2}\cos\left[\left(\omega_g - \omega_f\right)t + \varphi - \Theta\right] - \frac{GF}{2}\cos\left[\left(\left(\omega_g + \omega_f\right)t + \varphi + \Theta\right]\right. \qquad \textit{Eq 24}$$

If $\omega_g = \omega_f$,

$$R_1(t) = \frac{GF}{2}\cos(\varphi - \Theta) \qquad \textit{Eq 25}$$

$$R_1(t) \sim G\cos\delta \qquad \textit{Eq 26}$$

Where $\delta = \varphi - \Theta$ is the phase difference between the sinusoidal input and the reference signal.

Therefore,

$$f_g = f_f = f_{lock-in} \quad \textit{Eq 27}$$

If only one channel is considered, we have a signal at δ = 0 but not at δ = 90. Thus 2-channel lock-in preferred where the reference signal is phase-shifted for 90° and then multiplied with G(t) to get R(t).

$$R_2(t) = \frac{GF}{2}\sin(\varphi - \theta) \quad \textit{Eq 28}$$

$$R_2(t) \sim G \sin\delta \quad \textit{Eq 29}$$

Thus,

$R_1(t) = R(0^o)$ → in-phase component

$R_2(t) = R(90^o)$ → phase shifted component

Amplitude 'G' of R(t) is given by, $G = \sqrt{[R\ (0^o)]^2 + [R\ (90^o)]^2}$

Phase is given by, $\delta = \arctan\frac{R(90^o)}{R(0^o)}$

The frequency of lock-in ($f_{lock-in}$) is based on the frame rate of the camera. If the frame rate of the IR camera is given by f_s (in Hz), then according to the Nyquist sampling theorem (NST) $f_{lock-in}$ (in Hz) is:

$$f_{lock-in} = \frac{f_s}{n} \quad \textit{Eq 30}$$

where, n is the number of frames evaluated in each lock-in period. Thus, for a 2-channel lock-in, n should greater than or equal to 4. In other words, a minimum of one-fourth of the frame rate should be used as the lock-in frequency [116]. The IR camera obtains the thermal output for each lock-in period. For a 2-channel lock-in process, two images are obtained—one channel for 0° image and another channel for 90° image. For analog to digital conversion before being fed to the computer, the images are multiplied by weighing factor (K). Thus, the process of obtaining 0° image and 90° image and processing it with the weighing factor is defined as a lock-in process.

The resultant four images give essential information. 0° image provides the sine with correlation function, 90° image provides the phase-shifted image. It shows the dissipated heat from the shunt position. The amplitude image gives the magnitude of the leakage current that flows through the shunt point, and the phase image shows all the local shunt points.

DLIT instrument:

The schematic of a lock-in thermography system is shown in Figure 40. A frequency generator is used to produce a reference signal F(t) and trigger pulse. It triggers a pulsed voltage to the solar cell, thereby creating periodic thermal output signals G(t). The system is coupled with a computer to determine the period of pulses - R(t). An analog to digital conversion is done by multiplying with the weighing factor 'K.' In the end, four types of images are obtained using a two-channel lock-in process.

1) 0^o image
2) 90^o image
3) Amplitude image
4) Phase image

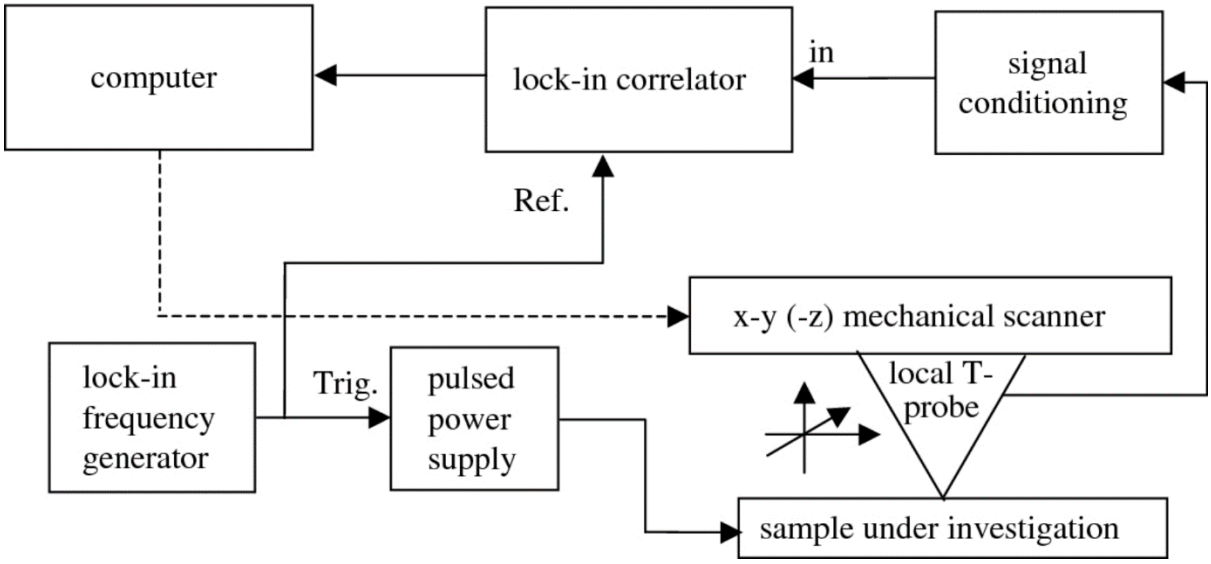

Figure 40: Schematic of a lock-in thermography system [116]

Relation to this thesis

The DLIT setup used for sample measurements reported in this thesis (in chapter 6) uses a custom-made state-of-the-art system developed by IRCAM GmBH in collaboration with Fraunhofer ISE. The infrared camera used in the setup has an InSb (Indium Antimonide) based Mid-wave Infrared (MWIR), Focal Plane Array (FPA) detector, which is sensitive to IR radiations between 1.5 µm to 5 µm. It has a Noise Equivalent Temperature Difference, NETD < 20 mK, and a sterling motor as the cooler for an enhanced signal-to-noise ratio. The measurements in this work are performed using the IR SM 50 lens with a focal length of 50

mm. The detector resolution was set to 512 x 512-pixel images that are used to obtain square-shaped images. The samples were measured at different voltage biases for integrated on 90 seconds at 30 Hz frequency. The electrical voltage bias is supplied by a Toellner TOE7621 four-quadrant power supply. The current at a given bias voltage is measured at the beginning and end of every measurement by two Agilent 34450S multi-meters. All the measurements are conducted at room temperature. As the typical open-circuit voltage V_{oc} value of the complete monolithic graphite-based solar cells considered in this work is ~0.90 V, all DLIT measurements presented in this work were done at ±1 V. All DLIT images are -90° images and have been normalized to the same brightness, contrast and color scale. For the local J-V analysis of shunt spots using DLIT signal intensity values, the signal intensity value at 0 V has been considered as the noise value and deducted from all other signal values.

DLIT analysis was carried out for sub-cells FTO/HBL/µ-graphite in chapter 6. Here, DLIT was used to detect HBL layer quality, mainly ohmic shunts. Additionally, the local J-V curve of a hot spot in the DLIT image obtained at forward bias provided more information on the nature of defects. Detailed results are presented in sections 6.3.3, 6.3.4, 6.3.5, and 6.3.6.

4.2.2 Current-voltage characteristics

Current-voltage (I-V) characteristics are the commonly used parameters to determine and analyze the performance of a solar cell. They are carried out in standard test conditions using 1000 W/m^2, AM 1.5 G spectrum, and at a cell temperature of 25 ^{o}C. They are used to analyze device performance under various load conditions. The current generated in an ideal solar cell follows a single-diode circuit model, as shown in Figure 41. The light generated in a p-n junction diode is given by:

$$I = I_0 \left[\left(exp \frac{V - IR_s}{nV_T} \right) - 1 \right] + \frac{V - IR_s}{R_{sh}} - I_L \qquad \textit{Eq 31}$$

where,

I = Net current flowing through the solar cell (A)

I_L = light generated current (A)

I_0 = dark saturation current (A)

R_s – Series resistance (Ω)

R_{sh} – Shunt resistance (Ω)

V = Voltage across the terminals (V)

V_T = Thermal voltage given by kT/q (V)

q = Charge of an electron (1.602 x 10^{-19} C)

k = Boltzmann's constant (1.38 x 10^{-23} J/K)

T = Absolute temperature (K)

n = Ideality factor → denotes the ideal shape of the I-V curve. The value ranges between 1 and 2. For an ideal solar cell, n = 1.

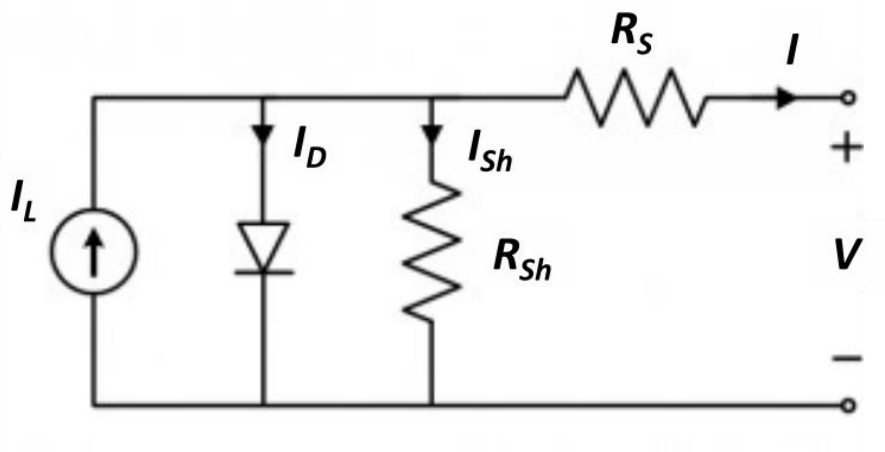

Figure 41: Equivalent circuit of a single-diode model of a solar cell [117]

Figure 42 shows the dark I-V curve and illuminated I-V curve. In the absence of light, the I-V curve shows the leakage current in the solar cell. This value gets higher with the decrease in the shunt resistance. The I-V curve is shifted downwards based on the current generated with respect to the illumination intensity.

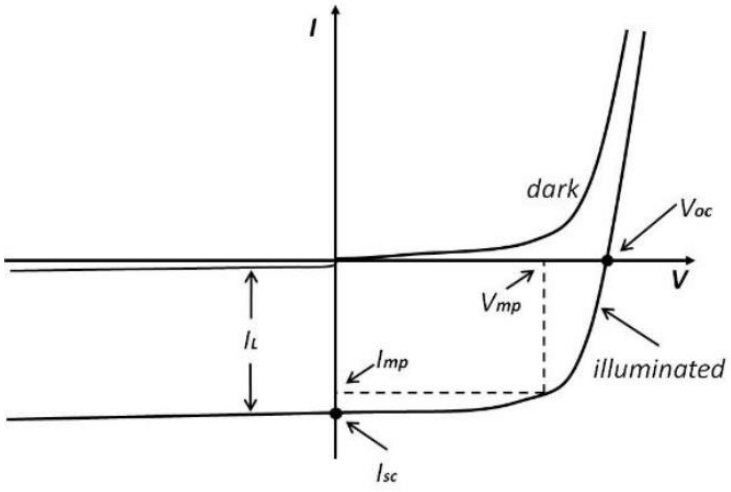

Figure 42: Characteristeristic I-V curve of a solar cell under dark and illuminated condition [118]

An ideal I-V curve and the same marked with the defect and loss mechanisms are shown in Figure 43, where for easy understanding, the I-V curve is shown in the 1st quadrant.

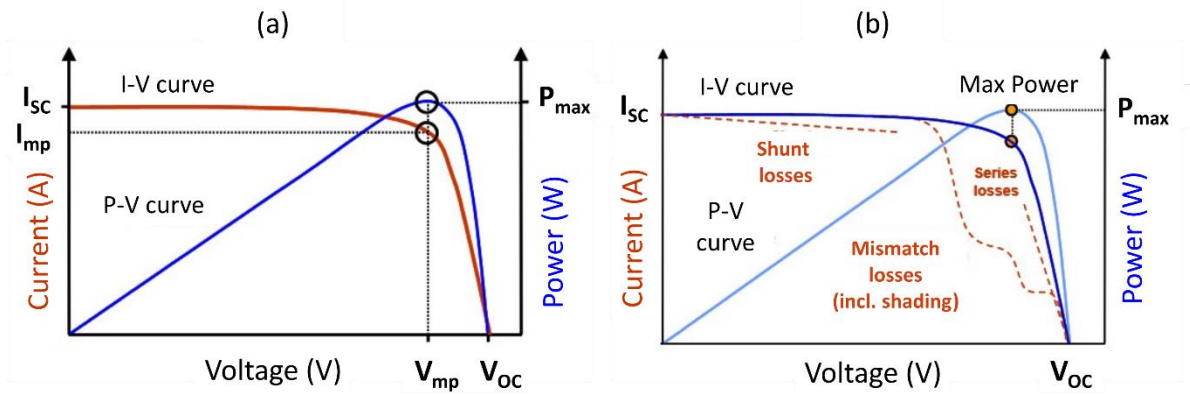

Figure 43: (a) Ideal I-V curve of a solar cell (b) I-V curve with loss mechanisms [119]

The important parameters in the I-V curve are given below:

1) V_{OC} → At this point, the light generated carriers forward bias the junction, which leads to the increase in the diffusion current. Since this current is opposite to the drift current, the net current inside the cell is zero. Thus, the maximum voltage that can be extracted from the solar cell is at $V_{OC,}$ where the current is zero.
2) I_{SC} → At this instant, the minority carrier concentration is increasing on both the n-type and p-type side of the cell. The current that depends on the minority charge carriers is called the drift current. As the minority charge carriers increases, the drift current also increases, which hinders the path to the majority charge carriers. Thus, I_{SC} is the maximum current that can be extracted from the cell where the voltage is zero.
3) Fill Factor (FF) →FF is an important performance indicator of the cell. It is a measure of the squareness of the curve. The fill factor is the ratio of the product of V_{OC} and I_{SC} to the voltage and current at the maximum power point. The performance of 2 cells having the same V_{OC} and I_{SC} might vary with their FF.
4) P_{max} → At V_{OC} and I_{SC}, the power extracted from the cell is zero as either voltage or current is zero [120]. The maximum power is extracted from the cell when the characteristic resistance of the cell is equal to the load resistance. The voltage and current corresponding to the maximum power point are less than the V_{OC} and $I_{SC,}$ respectively.
5) V_{MPP} → Voltage at the maximum power point

6) I_{MPP} → Current at the maximum power point

I-V curves are measured from V=0 to V_{OC}. The majority of losses are contributed by the series resistance and/or the shunt resistance. For an ideal cell, the series resistance is very low, and the shunt resistance has a very high value. The shunt resistance has to be very high so that it doesn't provide an alternative pathway for the light-generated charge carriers. The existence of a shunt resistance causing a leakage pathway can be observed in the curve near the I_{SC} point. The higher the shunt resistance, the better and the more horizontal the curve near the I_{SC} point will be. The series resistance addition affects the curve near the V_{OC} point and flattens the curve in that region. The addition of series resistance substantially alters the FF, which in turn reduces the power conversion efficiency of the cell. A very high value of series resistance also disturbs the Isc values. I-V curves are also measured in the reverse direction (from V_{OC} to V=0) and under the dark condition for a detailed analysis of the performance of the solar cell[4].

Relation to this thesis

In this thesis, average electrical parameters have been reported for all the devices. Two different scenarios are mostly studied – (1) Under illumination and (2) under dark. Under illumination is the standard condition to see the device performance, whereas, under dark, an idea on the recombination mechanism can be gained from forward onset voltage. As lower the forward current, as lower is the recombination at the interface under investigation. A straight forward judgment if a device is shunted can be devised using dark I-V measurements by the occurrence of a superimposed linear curve.

In chapter 6, the dark I-V measurement of a sub-cell is showing high forward onset voltage for a device with low recombination at the FTO/perovskite interface (section 6.3.6). It also shows that a high forward current (in the range of 100 µA) is observed for a shunted device (section 6.3.3). Apart from the I-V measurement under light and dark, a unique measurement is shown in section 7.3.2 in chapter 7. As all the electrodes and CTLs are present before the infiltration of perovskite in CG-PSCs, it facilitates the electrical characterization of the electrode stack before filling with photo absorber. To better understand the influence of different thicknesses of the isolation layer at the mp-TiO_2/graphite interface in the absence of perovskite, the mp-TiO_2 (E_g = 3.2 eV) was photoactivated using a UV light (365 nm with a max power of 320 mW illuminating 0.4 cm^2 of the active area placed at a distance of 10 cm). The result shows a high

barrier potential (> 1 V) for the transport of electrons from mp-TiO_2 to CG for Al_2O_3 thicknesses higher than 40 nm, which is in agreement with the theoretically achievable photovoltage.

4.2.3 Maximum power point tracking (MPPT)

Even though V_{OC} and I_{SC} give the maximum achievable electrical parameter from the solar cell, in practical cases, the power extracted is the vital parameter as they depend on the load connected to it. Mostly, the reported values, even in cases of certified measurements or record efficiencies, are taken from the I-V measurement. This measurement is highly influenced by the hysteresis effect. In turn, it is affected by varying the scan rate, scan direction, preparation method, device architecture, and history of device measurement. These factors make I-V measurement not an efficient and comparable tool for analyzing device performances. Additionally, I-V measurement also does not represent the standard solar cell working conditions.

In general, for any thin-film solar technologies to be commercialized, it has to meet the IEC61646 test conditions. Owing to the differences in the device physics between Silicon and novel solar cells, in 2011, Krebs and team formulated the ISOS test conditions (Test protocols, outdoor, thermal cycling, humidity cycling, shelf storage, continuous illumination, etc.) for analyzing Organic photovoltaics (OPVs) [121]. The main test condition emphasized to compare the stability of the devices is $T_{80,}$ i.e., the time taken by the device to reduce to 80 % of its initial PCE value. A recent review by Antonio Urbina emphasis that these ISOS standard conditions are required to be followed [122] as IEC61646 test conditions were concentrating more on environmental aspects. These conditions are vital not only to assess the reliability of the produced devices for commercialization purposes but also for the better comparison between the efficiencies reached by different teams, different architectures, etc. This review provides a detailed table with different architectures along with their T_{80} and T_{50} values. A high T_{80} values > 1000 h under illumination has been reported for carbon-based PSCs.

For a reliable and comparable measurement in PSCs, Zimmermann *et al.* suggest analyzing stabilized power conversion efficiencies, by tracking it for at least 60 s [123]. Analyzing the stabilized values not only provides reliable efficiencies at standard working conditions but also provides information on the effects of light soaking and device degradation over continuous illumination conditions. Using this technique, the non-reliable PCE values

dependent on light soaking, trap filling, scan speed, etc. can be avoided. It is to be noted that the majority of the times when high certified efficiencies are reported in literature, they are non-stabilized values without following standard test conditions.

In this thesis, even though average electrical parameter values are reported, for better reliability, we mainly compare MPP measurements over a period of time. In chapter 5, a T_{80} value of 14 h under continuous illumination is reported, as shown in section 5.3.9. In chapter 6, stable PCE values have been reported for 100 s. In chapter 7, a clear discrepancy in the J-V parameters and the PCE measured by MPPT is shown in section 7.3.3.7. It complements the arguments made at the start of this section. Thus, even though T_{80} or other standard test conditions for commercial purposes has not been tested here, tracking the MPPT already gives a reliable value for comparison.

4.2.4 Interfacial recombination analysis

In PSCs, one of the major losses in the device performance is caused via interfaces. Unlike silicon solar cells, PSCs consists of multi-layered organic/inorganic materials as charge transport layers (CTL), which is filled with the organic photo absorber material. A direct impact on how the CTLs influence the device performance and stability can be seen in the report by Antonio Urbina [122]. The role of interfaces between perovskite and CTLs has already been discussed in chapter 2.3.

The difference between the Fermi level of electrons ($E_{F,e}$) and holes ($E_{F,h}$) in the perovskite absorber is the quasi-fermi level splitting (QFLS), which is the upper limit for the open-circuit voltage (V_{OC}) of a solar cell. However, other reports show that the externally measured V_{OC} can be lower than the QFLS [124]. This means that the charge carrier selectivity of the transport layers is not sufficient [5]. Therefore, it is important to analyze V_{OC} over various conditions such as dark, low sun intensities, etc., which gives us the possibility to understand the nature of shunts, non-radiative recombination mechanisms, and its corresponding pathways. The main factors that influence the V_{OC} are the energy alignment of the CTL with perovskite; trap-assisted recombination and carrier densities [124].

In this thesis, three characterization techniques were used in analyzing the recombination at the interface. They are:

1. Open circuit voltage decay (OCVD) measurement
2. Suns-Voc measurement
3. Transient PL measurement

4.2.4.1 Open circuit voltage decay analysis

OCVD analysis is a dark measurement technique. For this measurement, the device is initially under illumination under open-circuit. Thus, the external photocurrent is maintained at zero. After a few seconds, the illumination is switched off, and V_{OC} is monitored.

A typical OCVD curve is drawn with V_{OC} over time Figure 44a. It consists of three phases. The mechanism of recombination in the respective phases is given in Figure 44b.

- **Phase A:** V_{OC} under illumination. The values correspond to the number of photogenerated charge carriers produced under illumination and their separation at the HTL and ETL.
- **Phase B:** Instance the light is switched off. As soon the illumination is off, at high voltage region, the following recombinations take place:
  - Fast radiative and non-radiative (non-trapped/shallow traps) recombination in the perovskite
  - Fast non-radiative recombination between the non-trapped/shallow-trapped charge carriers in the CTL with the charges in the perovskite

  Hereafter, these recombination pathways are collectively referred to as primary charge carrier recombination.

- **Phase C:** Here the V_{OC} is measured under dark. The primary charge carrier recombination is followed by the slow secondary purely non-radiative charge carrier recombination. The slow recombination takes place between the charges in the deep traps states of the mesoporous CTL and the charges in the perovskite. Other literatures of OCVD measurements on PSCs also show similar behaviour of the devices under dark [125,126]. It is to note that research is still ongoing to find the exact reason of such a storage behaviour of PSC under dark in the OCVD measurements. Therefore,

the electron response time is analyzed. It is obtained by taking the derivative of the OCVD curve normalized by the thermal voltage [127,128]:

$$\tau_n = \frac{k_B T}{q} \left(\frac{dV_{OC}}{dt}\right)^{-1} \qquad \textit{Eq 32}$$

where,

τ_n = Electron lifetime (s)

k_B = Boltzmann's constant (1.38 x 10^{-23} J/K)

T = Absolute temperature (K)

q = Charge of an electron (1.602 x 10^{-19} C)

As the photovoltage in solar cells is logarithmic with charge concentration, the electron lifetime depends on the amount of photocharges present in the device during the V_{OC} decay.

In Figure 44a, OCVD analysis of two different conditions present in a PSC is shown. In the presence of ohmic shunts (red line), no secondary charge carriers are present under dark as all the photogenerated charges recombine at the shunt center. Thus, as soon as the illumination is switched off, the V_{OC} drops to zero. In the other case, the charges are not immediately recombined. De-trapping and recombination of the trapped (deep) charges occur slowly under dark based on the quality of the interface (black line). Thus, a longer lifetime of the electrons staying at higher potential is observed for PSCs.

(a)

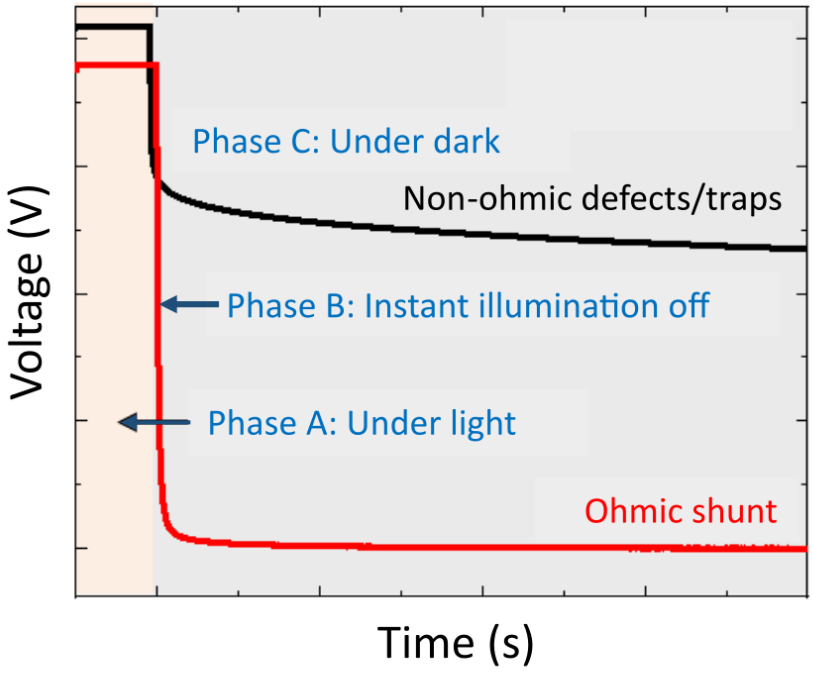

(b)

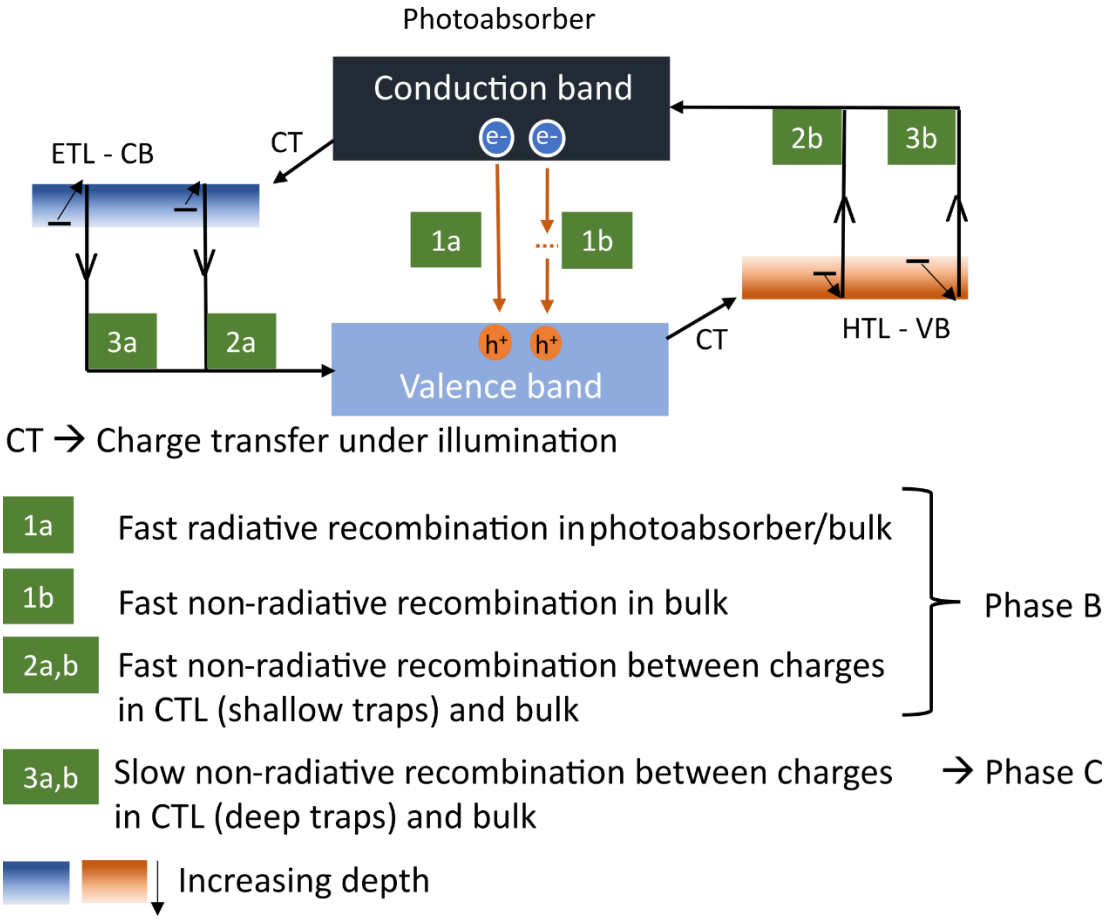

Figure 44: (a) Sample OCVD of a cell with ohmic shunt and cell with non-ohmic traps/defects (b) Mechanism of recombination under different phases.

Relation to this thesis

In this thesis, OCVD measurements were carried out for devices investigated in chapter 6 and 7. In the case of chapter 6, the influence of a hole blocking layer in preventing the recombination at the FTO/perovskite interface is studied. The results from the OCVD measurements (section 6.3.8) showed a higher electron lifetime at comparatively higher voltages for SPD-HBL and lower for sputtered-HBL. The observation was well in agreement with the DLIT results, where distributed non-linear defects were observed in the case of sputtered-HBL. Following the curve at times < 20 s, a voltage of 50 mV for a no HBL device is noticed. It shows in the absence of an HBL layer, more backtracking of electrons from FTO to perovskite is detected, and the effect is suppressed by the introduction of a thin, compact, dense HBL.

In the case of chapter 7, the influence of a sputtered isolation layer thickness on suppressing the interfacial recombination at the mp-TiO_2/CG interface is studied. A curious observation was made in section 7.3.3.4 for a device without an isolation layer. By theory, it is believed that when the mp-TiO_2 contact graphite counter electrode, it results in an ohmic shunt. However, in a perovskite filled device, voltage close to 300 mV after 1 min being under dark shows that the mp-TiO_2/CG is prone to more recombination in the absence of an isolation layer. However, it doesn't result in a linear shunt. A 1 kΩ resistor was connected in parallel to confirm it. The immediate drop to 0 V in < 50 µs as soon as the illumination was switched off confirmed that devices without isolation layer were not linearly shunted.

4.2.4.2 Suns-V_{OC} measurement

Another technique to analyze the recombination is the low illumination intensity measurement, where the V_{OC} is observed at varying illumination intensities. It was first introduced by Cuevas et al. for silicon solar cells[129] and has been well established in other solar cell technologies such as organic solar cells [130]. A typical suns-V_{OC} graph has the V_{OC} in the y-axis plotted against different sun intensities (usually plotted in log scale). With this measurement, the effects of series resistance over V_{OC} is eliminated as the net current is maintained at zero. Thus, only the effect of recombination on the V_{OC} values can be analyzed.

$$J_{light}(V = V_{OC}) = J_0\left[e^{\left(\frac{qV_{OC}}{n_{iD}k_BT}\right)} - 1\right] - J_G(I) = 0 \qquad \textit{Eq 33}$$

where,

J_0 = dark current density (mA/cm^2)

q = Charge of an electron (1.602 x 10^{-19} C)

n_{iD} = ideality factor

J_G (I) = generation current density with respect to illumination intensity (mA/cm^2)

For an ideal solar cell with only radiative recombination being present, at an absolute temperature of 300 K, there is a 60 mV decrease with per decade change in the sun intensity [131]. The slope is also denoted by the factor called the ideality factor (n_{iD}), given by the formula [132]:

$$n_{iD} = \frac{q}{k_B T} \frac{dV_{OC}}{d\ ln \frac{I}{1\ mW\ cm^{-2}}} \qquad \textit{Eq 34}$$

Tress *et al.* shows that,

n_{iD} = 1 only in the presence of surface recombination or band-to-band recombination.

1 < n_{iD} <2 in cases with SRH recombination as shown in Figure 45.

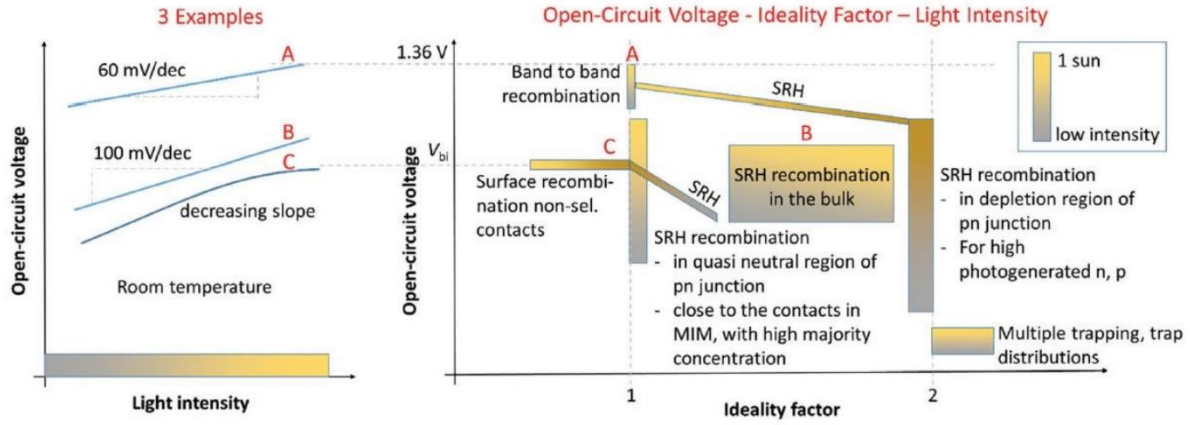

Figure 45: Suns-V_{OC} measurement and ideality factor explanations [132]

In other words, surface recombination is often referred to as bimolecular recombination leading to an ideality factor of n_{id} = 1 [124]. On the opposite, recombination solely from occupied trap states results in a higher ideality factor of 2 (n_{id} = 2). In real solar cells, both recombination types co-exist, resulting in an ideality factor between 1 and 2 [133].

The understanding of the ideality factor in perovskite solar cells is still under research. A high V_{OC} of 1 V with n_{iD} = 2 has been reported [132]. Also, low V_{OC} value < 1 V with the ideality factor was 1 has also been noticed [134]. It was attributed to the low built-in potential that limits the driving force for charge separation (i.e., the difference in work function because of the electrodes). The presence of the CTL is believed to be the reason for the vague understanding of the recombination with respect to the ideality factor. Bongiovanni *et al.* show that the recombination order can be different for electrons and holes. In case, one charge follows trap-assisted recombination (monomolecular recombination, n_{iD} = 2) another charge may follow bimolecular recombination (n_{iD} = 1). Thus, it is still under debate if lower or high ideality factor is beneficial in PSCs. However, it is interesting to note that, a combination of both recombination mechanism is considered, most perovskite solar cells report n_{iD} ~ 1.5 [135].

Relation to this thesis

In this thesis, Suns-V_{OC} measurement is carried out for devices investigated in the results chapter of 5 and 7. In all the measurements, the intensity was always ≤ 1 sun. The discrepancy in the ideality factor with the device performance was also observed in the results shown in this thesis. For the device in chapter 5, the suns-V_{OC} measurement helped to measure that the devices are free from ohmic shunts reliably.

In chapter 7, for the devices that resulted in high photovoltage, ~ 950 mV had a high ideality factor of 1.46. A time-dependant ideality factor was also observed, as suggested in Calado et al. [136]. For a device without an isolation layer, the ideality factor after stabilization (60 s) decreased to 0.92 from its unstabilized value (1.36). Thus, only stabilized values were considered later for observing the quality of an isolation layer based on its thickness. An illustration is provided to hypothesize the behavior seen. It is shown in Figure 86 for a device without the isolation layer; the probability of recombination comes from the fast detrapping of the shallow traps of mp-TiO_2 and less filled CB of perovskite. Thus, it resembles recombination from unoccupied shallow traps whose *n* value is 1. In the presence of an isolation layer, the fast detrapping of the shallow traps is prevented. It results in occupied shallow traps of mp-TiO_2 and CB of the perovskite thus, resembling an ideality factor *n* = 2. Thereby, an ideality factor of 1.4 shown is reliable for the cases achieving a high photovoltage > 950 mV.

4.2.4.3 Time-dependent PL measurements (In relation to thesis)

In general, photoluminescence (PL) in solar cells results from radiative recombination between the electrons in the conduction band and the holes in the valence band. It is, therefore a direct measure of the density of photoexcited primary charge carriers. In this thesis, a unique measurement technique was used where the PL images were taken toggling the sample between short circuit and open circuit conditions. While measuring each condition over a few seconds, and the reactions were monitored under a PL camera; charge generation, charge extraction, poor recombination centers were shown based on the set condition.

A completely filled device is connected electrically and controlled through a potentiostat. The device was illuminated using a red LED of 635 nm from Thorlabs, and Andor sCMOS camera was used to capture the PL signal from perovskite at 770 nm. It was toggled between two conditions, namely open circuit (OC) and short circuit (SC). MPP conditions can also be tested similarly. Each condition was monitored for a specific time frame (in s), and the change in the V_{OC}, $I_{SC,}$ and corresponding PL (as video) was recorded.

Condition 1: open circuit condition (I = 0 A) → The device was kept under open circuit condition for ~10 s while the V_{OC} was recorded parallelly with PL. V_{OC} values based on the charge generation is noticed, and a high PL was recorded over the entire time window.

Condition 2: Short circuit condition (V= 0 V) → As soon as the device is changed to short circuit condition, all the photogenerated charges are removed through the CTL to the external circuit. Thus, the V_{OC} value changed to zero, and I_{SC} values started to rise. The interesting phenomenon noticed is in the PL video. The entire PL window turned dark as soon as the condition was changed from open circuit to short circuit. In this thesis, this phenomenon is mentioned as "**PL quenching**" – reduction in PL when switched from V_{OC} to J_{SC} or V_{MPP}. Monitoring the device in SC condition over time, we noticed that, for devices with a good interface, the PL image was dark with comparatively high I_{SC} values monitored throughout the time window. However, for poor interface (with interfacial recombination), the PL slowly started to rise with the I_{SC} values decreasing. Later, both I_{SC} and PL stabilized over time (based on device architecture).

Thus, in open circuit conditions, the PL is only limited by the internal recombination. In contrast, under short circuit conditions, the electrons are drawn out, leading in an ideal case to a full quenching of the PL. The intensity of PL quenching (*i.e.,* the comparison between PL@V_{OC} and PL@V=0) is, therefore, a reciprocal measure of the current contributed by the primary charge carriers. Moreover, it is limited by the charge transport and the concentration of electrons in non-radiative traps (i.e., secondary charges). Thereby, measuring the PL quenching is an excellent method to check the charge transport in perovskite solar cells [137].

Dieter Neher and his team, also show similar technique and observation in their article [138], where PL quantum yield at V_{OC} and V_{MPP} were observed. Here they explain that there is a misconception of the term "PL quenching" reported for DSSCs or organic photovoltaics. In DSSCs, PL quenching of the bulk meant efficient electronic dissociation. However, in PSCs, low PL yield at V_{OC} could mean more interfacial recombination. Thus, high PL@V_{OC} and low PL@J_{SC} is desired.

Additional condition: For this, V_{MPP} from the I-V curve can be set, and the corresponding I_{SC} and PL can be recorded. Similar to SC condition, if the interface was well prevented from non-radiative recombination, low or no PL with high I_{SC} values will be observed.

Chapter 7 includes such a measurement (Figure 89) to investigate the quality of the insulation layer and its thickness. It helped to demonstrate the changes in the interfacial recombination dependent on the layer quality. The image below shows the example of the changes in the PL according to their interface quality when switched from OC to SC.

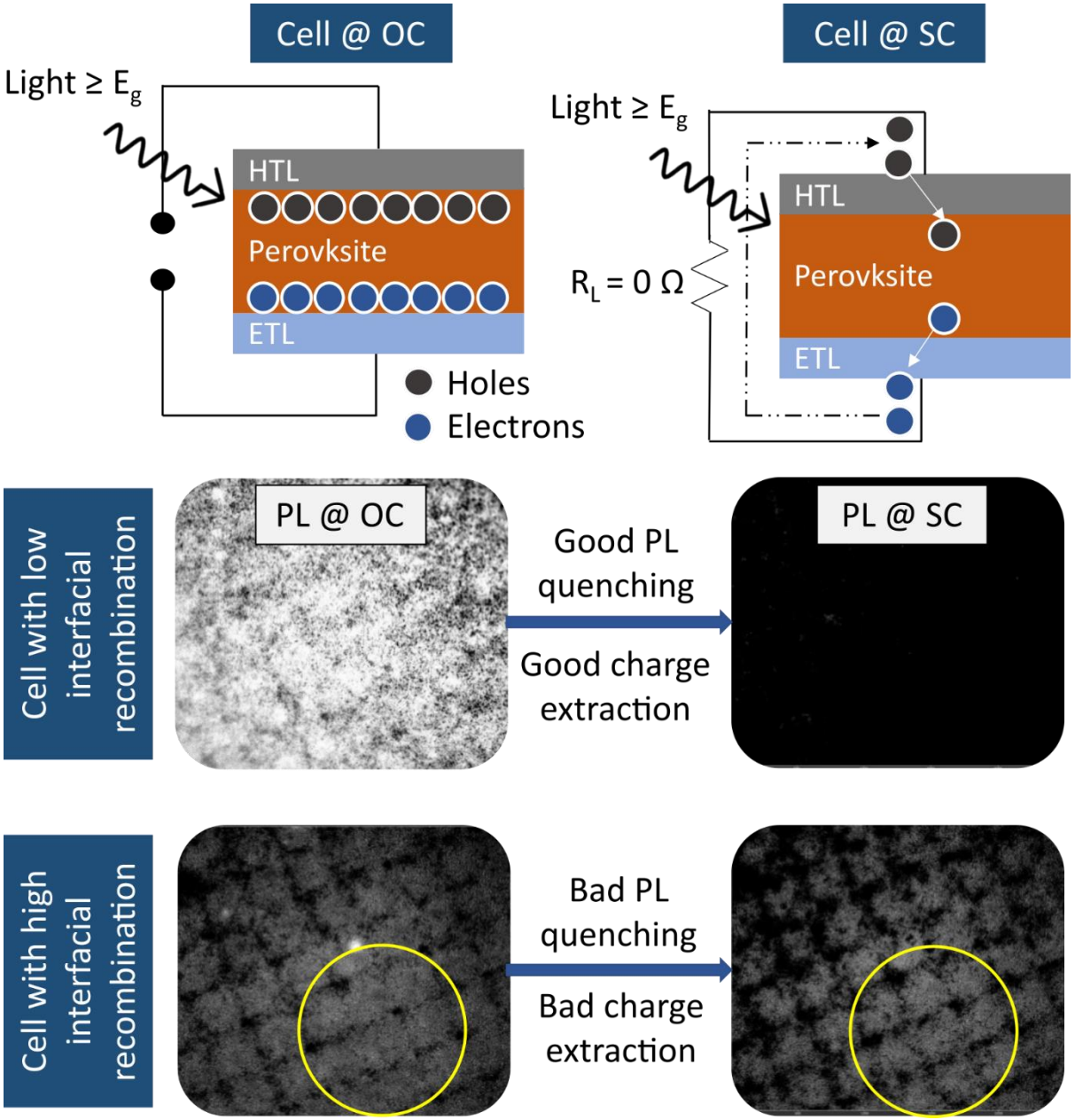

Figure 46: PL quenching in a perovskite solar cell with a good interface and a bad interface after toggling from the open circuit to the short circuit condition.

Therefore, this chapter firstly detailed the working principle of all the morphology and crystallographic analysis that was used to analyze the devices reported in the thesis. Apart from the working principle, the general measurement setup involved is explained. At the end of each sub-section, specific details on the instrument and parameters used to investigate the devices shown in this thesis are also provided. The second half of this chapter dealt with the electrical characterizations that were used to analyze the performance, stability, and special characterization techniques to investigate the non-radiative recombination present in the devices.

Chapter - 5

Sub-cell characterisation of SnO_2/perovskite interface and stability analysis on complete planar perovskite solar cell

5 Sub-cell characterisation of SnO_2/perovskite interface and stability analysis on complete planar perovskite solar cells

This chapter investigates the role of slot-die coated SnO_2 on air-processed planar PSCs by analyzing sub-cells (ITO/SnO_2/perovskite) under UV-exposure. The optical, morphological, and crystallographic analysis shows that UV treatment of ITO/SnO_2/perovskite has led to a reduced electron transfer to the SnO_2 layer and a gradual increase in the amount of PbI_2 towards the perovskite surfaces. Subsequently, the hole transporting layer (HTL) and electrodes were applied on SnO_2/perovskite interfaces (UV-treated and non-UV treated), and complete devices were fabricated. Device performance was compared and analyzed through J-V curves and maximum power point (MPP) tracking. Results show that devices built on a UV-treated SnO_2/perovskite interface show better stability, which is attributed to the presence of excess PbI_2 resulting in a passivation effect. Challenges in uniform film formation of slot-die coated SnO_2 and potential solutions using a polymeric additive is also highlighted.

The results shown in this chapter are based on the article published by the author of this thesis in Solar RRL under the title "Improving the stability of ambient processed, SnO_2-based, perovskite solar cells by the UV-treatment of sub-cells" [139]. This chapter documents my work during my half a year exchange term at Commonwealth scientific and industrial research organization (CSIRO), Melbourne, Australia.

5.1 Introduction

Commercializing PSCs requires not just an impressive PCE, but also capitalizing on their solution-processability, and low-cost materials and production to achieve an unprecedented cost breakthrough. However, for the cost benefits of high-throughput production methods on plastic substrates such as polyethylene terephthalate to be realized, post-deposition thermal treatment steps are limited to 140 ^oC to avoid degradation of the substrate. SnO_2 has emerged as the most promising ETL in planar PSCs with the highest certified efficiency of 23.32% PCE. With this achievement, it is increasingly important to rigorously test and understand the implications of SnO_2 on the stability of PSCs.

The stability of SnO_2-containing devices has been studied under varied test conditions, such as dark storage [140], 1 sun illumination [141], and under UV exposure [142]. However, conflicting

conclusions have been drawn on the role of SnO_2 in perovskite degradation. It is partly due to the lack of standardized testing protocols and vast differences in material and fabrication procedures. In specific tests, devices are stored in air or nitrogen environment [38], and intermittent [140] J-V measurements under standard 1 sun conditions (1000 W/m^2, AM 1.5 G) were carried out. Such tests qualify as dark storage tests at room temperature. Perovskite stability in dark storage tests is significantly higher compared to its operational stability under 1 sun test conditions, as the devices experience no long-term bias stress. For example, Chen *et al.* studied the stability of ITO/ETL/CsFAMA/Spiro-OMeTAD/Au devices in which the ETL was either SnO_2 or graphite carbon nitride doped SnO_2 [37], with the devices processed in nitrogen. The devices with undoped SnO_2 retained over 80% of the initial PCE after 1000 hours, which was significantly improved with doped SnO_2.

In contrast to the dark storage test, a steady decline in PCE is reported when devices are subjected to constant 1 sun illumination, and the performance is monitored by intermittent J-V measurements or maximum power point tracking (MPP) [141]. In other studies, UV tests are conducted and have shown varying results depending on the UV wavelength. For example, glass/ITO/SnO_2/$MAPbI_3$/Spiro-OMeTAD/Au devices showed negligible PCE degradation with UV-B (370 nm) irradiation over 1750 hours; however, significant degradation occurred with UV-A (311 nm) exposure due to degradation of the perovskite [142].

Chapter 2.3.2 explained PSC instability also in the presence of SnO_2 and reported solutions via its doping. Nonetheless, all n-i-p devices show steady degradation regardless of the use of doped or undoped SnO_2. The overall impact of SnO_2 cannot be easily discerned, as additional instability may also be attributed to the ubiquitously-used hole transport material (HTM), Spiro-OMETAD [143]. Additionally, the use of an inert processing environment limits the implications of these studies in real-world devices, as maintaining an inert atmosphere is costly and impractical in an industrial roll-to-roll manufacturing scenario.

Herein, the stability of devices incorporating SnO_2 produced by an industrially-compatible slot-die coating method is studied. Firstly, the use of a slot-die coated SnO_2 layer and its device optimization is examined as this coating technique presents several challenges to uniform film formation. An investigation on the role of SnO_2 on the stability of ambient-processed PSC devices under UV irradiation is performed.

Sub-cell configurations (glass/ITO/SnO_2/perovskite) before and after 500 hours of UV (365 nm) irradiation under open circuit in a nitrogen-filled glovebox (< 1 ppm H_2O, < 1 ppm O_2) is studied. By doing so, the effect of the hole transport layer (HTL) and the electrode that typically fail first has been eliminated. It previously limited investigation into the role that other layers and interfaces, play in device failure. Further results are compared with TiO_2 and ZnO to discern the relative differences among the three metal-oxides. Complete devices are built on the sub-cells (UV-treated and non-UV treated), and their performance and stability are analyzed. Thus, importance of analyzing the sub-cell configurations is shown to understand the specific interface kinetics, and also show that the stability of complete devices may not replicate the results from a sub-cell configuration. Unexpectedly, evidence has been found that the SnO_2/perovskite interface may not be stable under storage; however, UV irradiation can improve interfacial stability.

5.2 Experimental section

5.2.1 Precursor solution preparation:

The SnO_2 solution was prepared by the procedure defined by Wei *et al.* [144]. 225 µl of SnO_2 solution (2.25 ml of Sn_2O 15% in H_2O colloidal dispersion liquid from Alfa Aesar dissolved in 10 ml DI water) was added to 1.5 ml of $LiCl_2$ solution (17 mg/4 ml DI water). The mixture is stirred for 10 min @ room temperature (RT), and 5 mg of polyethylene glycol (PEG from Sigma Aldrich with molecular weight 8000K) was added and stirred overnight.

1 м of $MAPbI_3$, $FAPbI_3$, and $MAPbBr_3$ using DMF (as solvent was prepared. Additionally 0.85 м of $CsPbI_3$ in DMF:DMSO (4:1 v/v) was also prepared.. The precursor solutions were prepared in a glove box and stirred at 70 °C overnight. For the final CsMAFA solution, $MA_{0.61}FA_{0.37}Cs_{0.02}PbI_{2.96}Br_{0.074}$ was mixed with 2.5 mol% of $PbCl_2$ together with 10 ppm of L-α-phosphatidylcholine (Sigma Aldrich) as a surfactant. The recipe was optimized from previously reported by Tang *et al.* [145]. This solution was further stirred at 70 °C for 2 h.

5.2.2 Device fabrication:

Pre-patterned indium tin oxide (ITO) coated glass substrates (Shenzhen Display, 5 Ω sq $^{-1}$) were used for the fabrication of devices. The substrates were sequentially cleaned in an ultrasonic bath using a detergent solution (5 vol% Deconex 12 PA), twice with deionized water, acetone, and propan-2-ol for 5 minutes each, with drying under a nitrogen stream

between each step. The substrates were UV-ozone treated using Novascan PDS-UVT for 20 min before slot-die coating the SnO_2.

The process parameters of the slot-die coating of SnO_2 is given in section 3.4.1. Further steps are diagrammatically shown in Figure 47. The samples were annealed for 20 min at 200 ^oC, resulting in a 70 nm thick SnO_2 layer. 100 µl of the perovskite solution was spin-coated with a two-step spin speed of 2000 RPM for 5 s and 3500 RPM for 35 s. 500 µl of ethyl acetate as anti-solvent was deposited onto the surface of the perovskite 7 s after the start of 2^{nd} spin speed setting. Samples were then annealed at 100 ^oC for 2 min resulting in a 350 nm thick perovskite layer. 75 µl of the PEDOT: PSS was spin-coated at 5000 RPM for 30 s to give an 80 nm HTL layer. All the solution-based deposition until the HTL layer is performed in the air under ambient room conditions.

Samples were then transported to an evaporator (Angstrom) in a glovebox to evaporate 10 nm MoO_3 as an interlayer and 100 nm of Ag (99.9% pure, Kurt J. Lesker Company) or Au as the counter electrode. 10^{-7} Torr vacuum condition was used. The active area of the devices was defined as $0.1cm^2$ using an evaporation mask and cross-checked with laser-beam induced imaging.

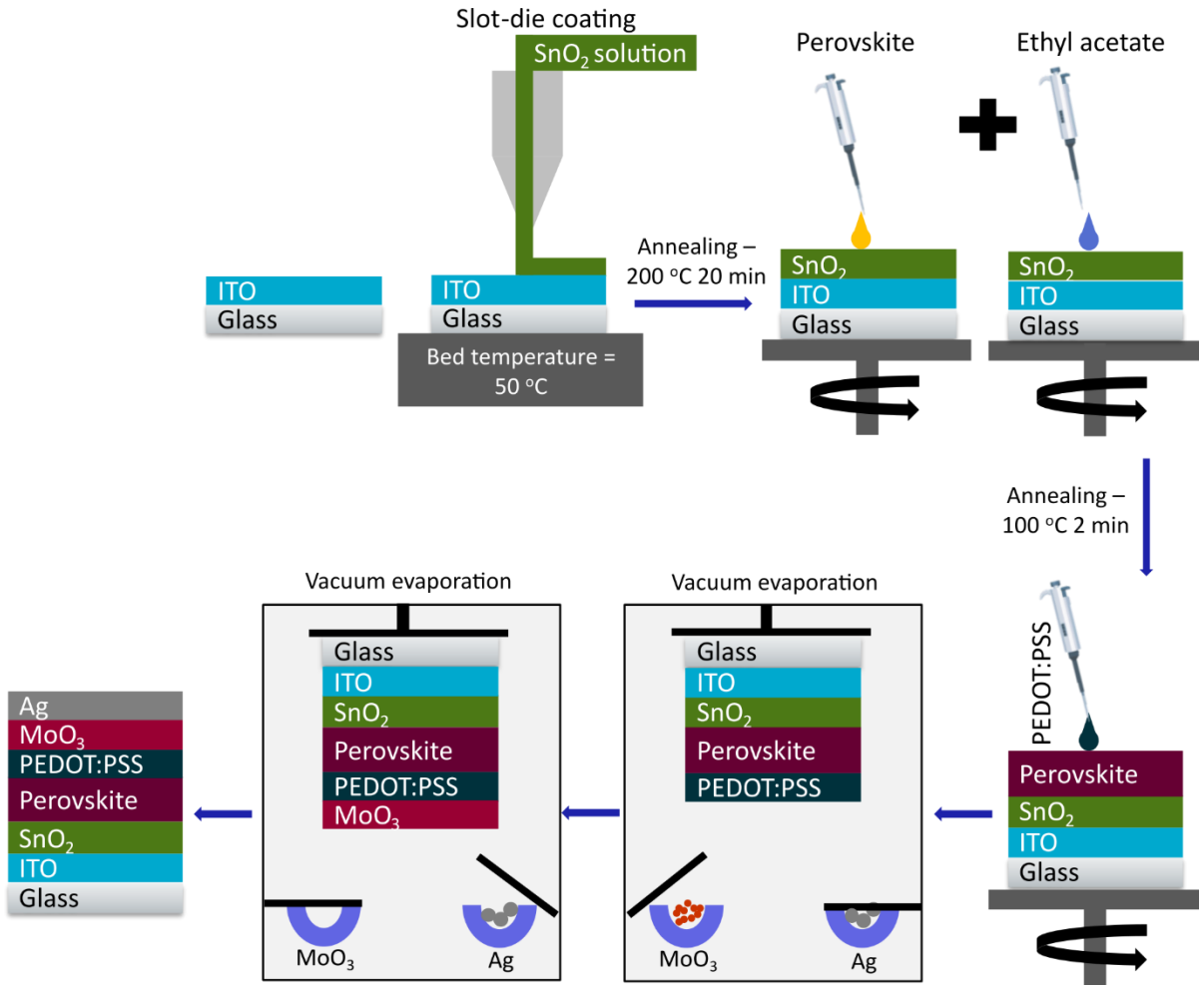

Figure 47: Device preparation for samples in Chapter 5.

5.3 Results and discussion

5.3.1 Device Architecture

Figure 48 shows a schematic representation of the charge transport layers and the electrodes in the n-i-p planar PSCs that are used in this chapter. The basic working of PSCs has already been explained in Chapter 2.2.2. Here, SnO_2 is the ETL and PEDOT: PSS is the HTL.

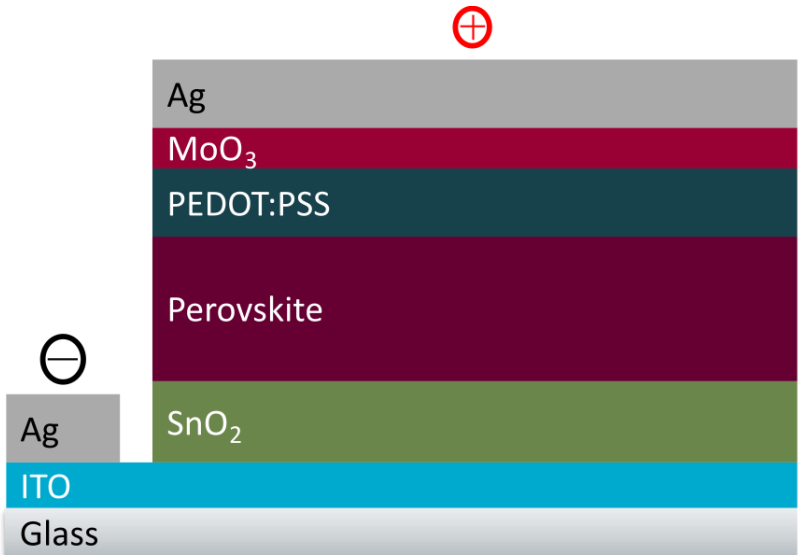

Figure 48: Schematic representation of n-i-p planar perovskite solar cells.

5.3.2 AFM and Contact angle measurement of SnO_2 and perovskite films

An as-received nanoparticle solution of SnO_2 was slot-die coated on glass/ITO substrates. It is observed that slot-die coating leads to the formation of SnO_2 agglomerates, even after 20 minutes of UV ozone treatment of the substrate. SnO_2 agglomeration during film formation is undesirable for optimal device performance as the agglomerates can create shunt pathways in the device [144]. This agglomeration occurs in slot-die films because it is a passive deposition process in which deposition and drying/evaporation are discrete sequential processes with the lag time between deposition and drying, facilitating nanoparticles movement leading to agglomeration. In contrast, such agglomerations are not observed in spin-coated films with UV-treatment of the substrates, because spin-coating is a dynamic process in which deposition and evaporation are concurrent mechanisms, leading to rapid drying of the film. In addition to the agglomeration challenge, perovskite precursors have poor wetting on the SnO_2 layer. As such, SnO_2 films are treated with UV-ozone before the deposition of perovskite precursor [36].

In literature, surface modification through improved interface modification has been achieved by adding elements such as Li [146], Mg [147], Y [148], Sb [149], and Nb [150] as dopants in SnO_2. To prevent agglomeration in the SnO_2 film and also to provide better wetting to the perovskite solution, this chapter studied several additives, including polyethylene glycol (PEG), polyvinyl

acetate (PVA), ethylene glycol (EG). Among these, PEG addition gave the best film with slot-die coating while also improving the wettability of the perovskite solution.

Figure 49 shows the Atomic Force Microscopy (AFM) image of SnO_2 layers with and without PEG, fabricated on an ITO-coated glass substrate. A clear difference in the layer morphology can be observed by comparing the AFM results. While roughness values (R_q) are similar ca. 4 nm, the PEG-SnO_2 layer has a negative skewness factor of -0.376 in comparison to the positive skewness of the commercial SnO_2 (com-SnO_2) films, the PEG-added SnO_2 film is uniform without any big particles or agglomerates.

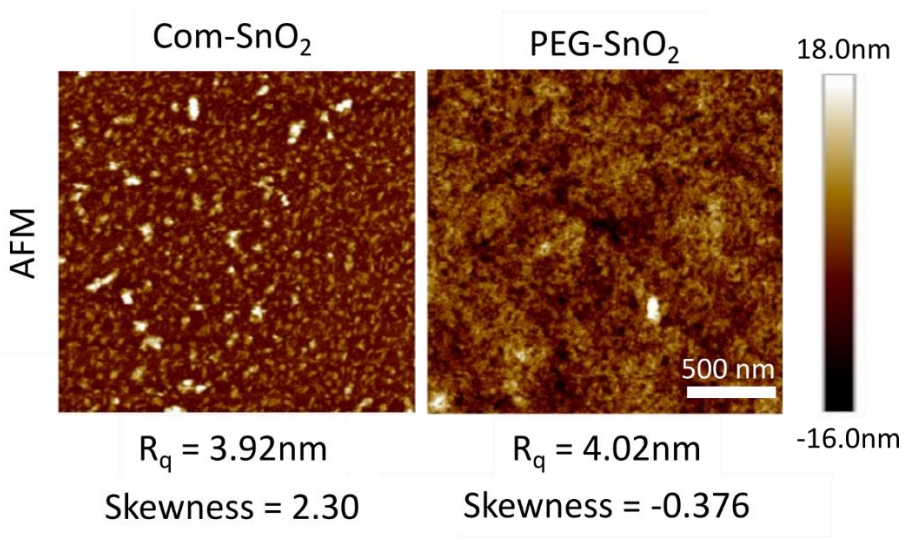

Figure 49: AFM comparing the commercial SnO_2 (Com-SnO_2) and SnO_2 with PEG (PEG-SnO_2). A bar scale of 500 nm is used for both the images. Figure reproduced from publication [139].

Figure 50 shows the CA measurement for layers fabricated using SnO_2 with different additives; the lowest CA was measured for SnO_2 with PEG. This improved SnO_2 morphology is ascribed to the hydrogen bonding of PEG with SnO_2, which has improved the layer wettability [144]. Thus, all the devices reported hereafter contain SnO_2 with PEG and referred to as SnO_2.

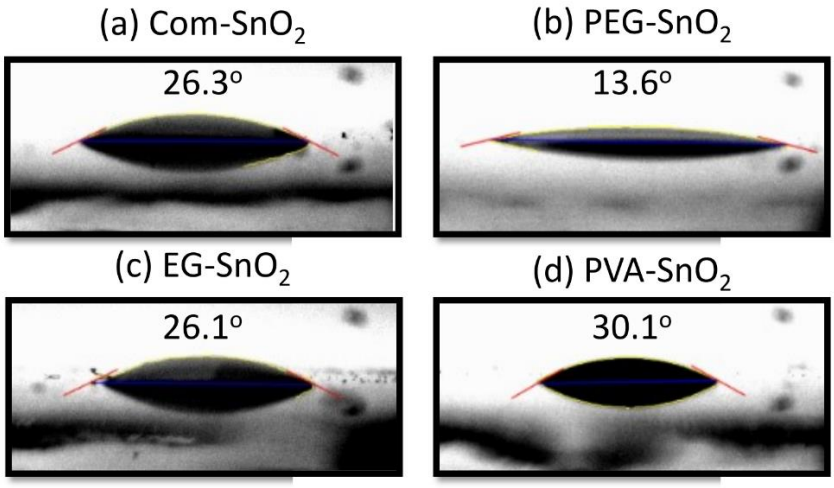

Figure 50: Contact angle measurements of SnO_2 with various additives. (a) Commerical SnO_2 (b) SnO_2 with PEG (c) SnO_2 with EG and (d) SnO_2 with PVA. Figure reproduced from publication [139].

5.3.3 SEM analysis of SnO_2 and perovskite films

The morphology of the SnO_2 and perovskite layers was investigated using scanning electron microscopy (SEM). Figure 51a and Figure 51b shows the SEM images of slot-die coated SnO_2 and the perovskite layer, respectively. Confirming the AFM results, no agglomeration of SnO_2 was observed, and a pinhole-free homogeneous layer is present in the investigated area, as seen in Figure 51a. The SEM image in Figure 51b shows the perovskite layer is conformally coated on the SnO_2 layer and is pin-hole free. As a comparison, an SEM image of a perovskite layer spin-coated on glass is shown as an inset in Figure 51b to show no difference to the perovskite layer when coated on SnO_2. Figure 51c and Figure 51d illustrate the X-ray diffractograms of SnO_2 and perovskite, respectively. The diffractogram of SnO_2 shows that it has a tetragonal phase and belongs to the P42/mnm (136) space group (matched to PDF# 04-014-0193). The absence of sharp peaks in the diffractogram indicates the slot-die coated SnO_2 layer is nanocrystalline. With the crystallite size calculated to be in the range of 2.5 ± 0.8 nm. Similar particle sizes of SnO_2 and its nano crystallinity/amorphous property in the resultant layer for a solution-processed technique has also been observed in other reports [36]. The XRD diffractogram of a perovskite film is shown in Figure 51d. The peaks, indexed in Figure 51d, correspond to cubic phase perovskite {space group Pm-3m (matched to PDF# 01-085-6374)}. A peak at 12.6° is also present, which corresponds to the (0 0 1) plane of PbI_2 (matched to PDF# 04-009-6453).

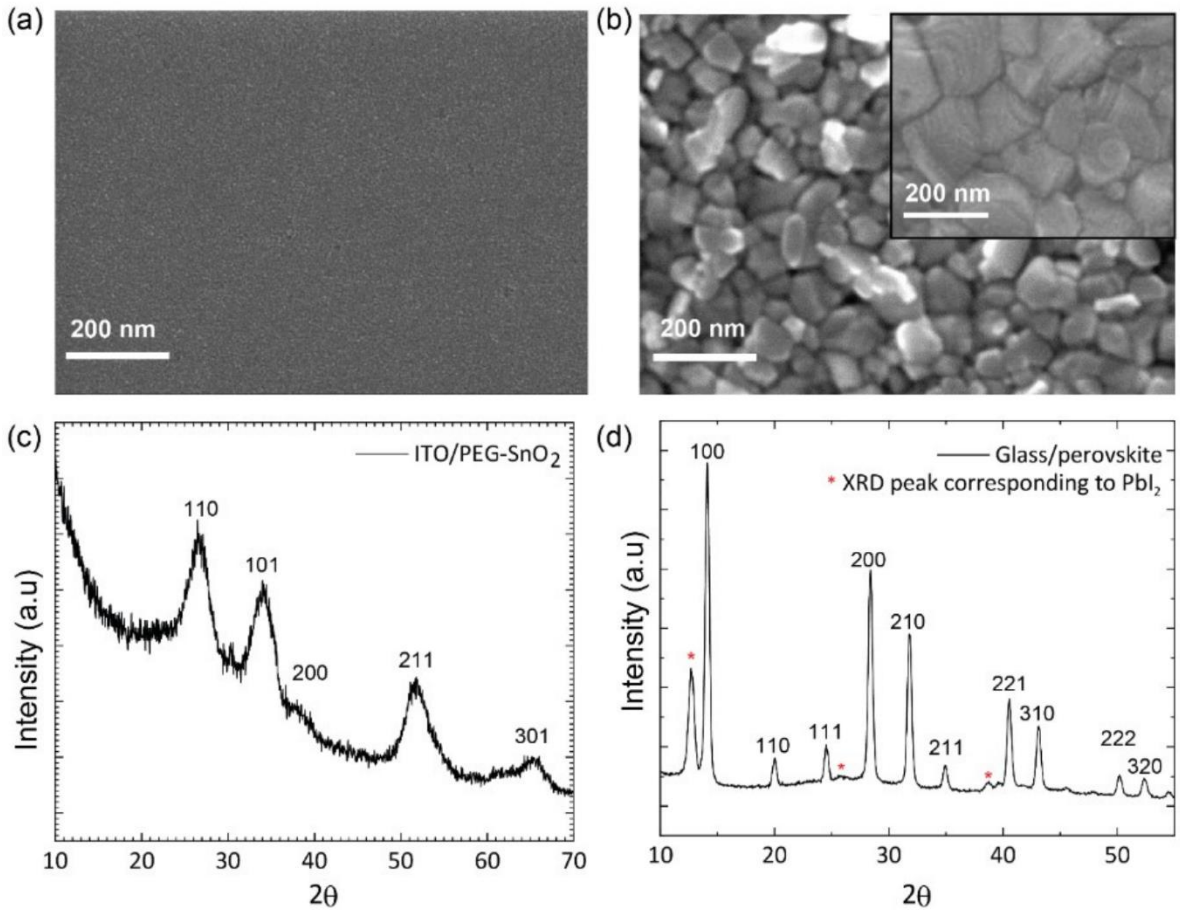

Figure 51: (a) Top-view SEM image of slot-die coated SnO_2 layer, (b) Top-view SEM image of spin-coated perovskite fabricated on SnO_2. Inset shows the top-view SEM image of the perovskite layer on glass (c) XRD pattern of the SnO_2 layer (d) XRD pattern of the perovskite layer. Figure reproduced from publication [139].

5.3.4 Average device performance

After optimization of the SnO_2 and perovskite layers, the devices are completed by depositing anhydrous poly(3,4-ethylene dioxythiophene) polystyrene sulfonate (PEDOT: PSS). Above it, MoO_3 is evaporated to improve hole injection [151] and, in the end, the counter electrode (Ag). The film thickness of SnO_2, perovskite, PEDOT: PSS, MoO_3, Ag were 70 nm, 350 nm, 80 nm, 10 nm, and 100 nm, respectively. The histogram of 133 complete devices is shown in Figure 52 to demonstrate the reproducibility of the devices reported in this article. The average electrical performances of these devices are V_{OC} of 920 mV, J_{SC} of 17.54 mA/cm^2, FF of 57.60 %, and PCE of 9.32 %.

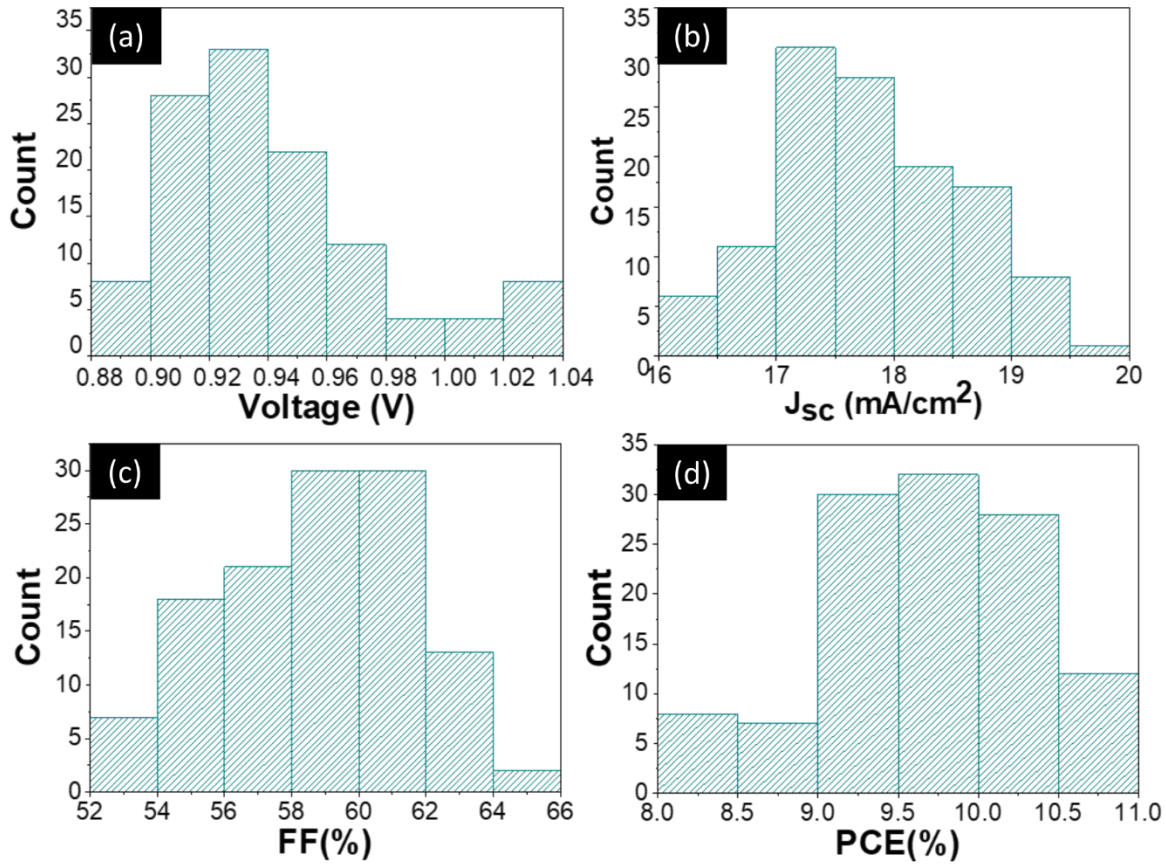

Figure 52: Histogram of 133 devices with architecture ITO/SnO_2/perovskite/PEDOT/MoO_3/Ag (a) V_{OC} (b) J_{SC} (c) FF and (d) PCE. Figure reproduced from publication [139].

5.3.5 Champion device, Suns-V_{OC} measurement, and Energy band diagram

Figure 53a illustrates the J-V curve of the champion device, where V_{OC} of 960 mV, 18.34 mA/cm^2 J_{SC}, 61.5% FF, and 10.82% PCE were achieved. Device performance is lower compared to literature values due to devices being fabricated under ambient conditions, as well as the non-optimal hole transport layer [152]. The PCE is, however, comparable to other reports on ambient-processed PSCs [153,154]. Despite the lower PCE, we confirmed that the films were compact and that no shunt pathways (pin-holes) were present by studying its V_{OC} under different light intensities (Figure 53b). The results show that all devices studied here retained V_{OC} at low sun intensity, confirming that the devices are shunt-free. It is important to confirm this point as the presence of shunts accelerates the degradation and can interfere with the interpretation of results [155].

Figure 53c shows the energy level diagram where a higher conduction band level of SnO_2 (-3.67 eV) was observed when compared to the values (-3.9 to -4.5 eV) shown most times in

literature [37,39,146,156]. It causes a mismatch at the SnO_2/perovskite interface. It could have been caused by the slot-die coating of SnO_2 and requires further investigation beyond the current scope of this work. The ionization potential (IP) of SnO_2 was calculated through ultraviolet photoelectron spectroscopy (UPS) measurement. The IP of perovskite and PEDOT: PSS was obtained through photoelectron spectroscopy in air (PESA) measurement.

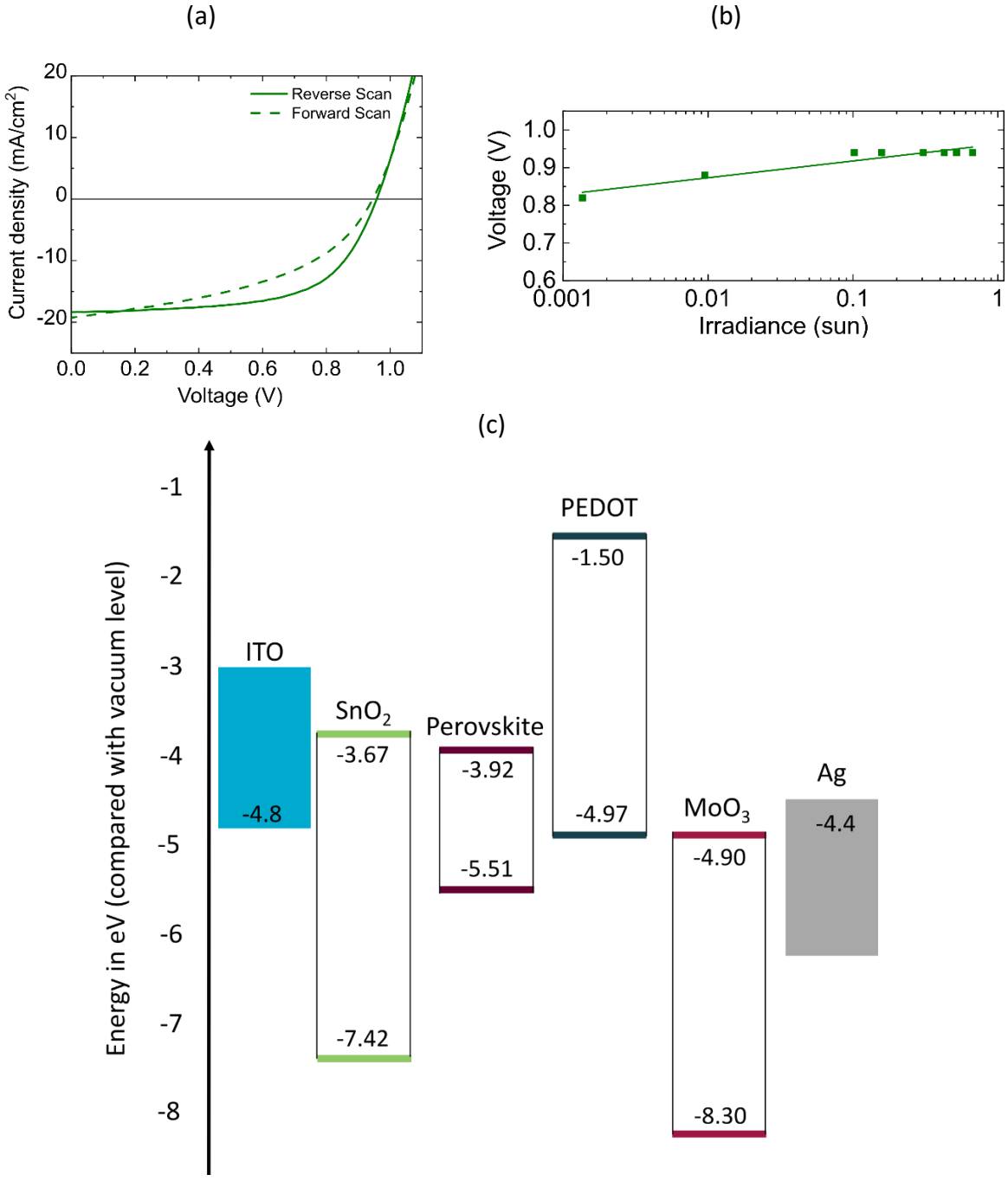

Figure 53: (a) J-V curve of the champion device presenting a PCE of 10.82 % whose active area was 0.1 cm² measured under AM 1.5 G at a scan rate of 100 mV/s (b) Suns-V_{OC} measurement and (c) Energy band diagram. Figure reproduced from publication [139].

5.3.6 Optical characterization of sub-cells before and after UV stress

Both internal and external factors contribute to a solar cell's instability. Light, heat, oxygen, and moisture are four key external degradation factors. UV is the most prominent degradation-causing components in light due to its high energy. To study the effect of UV light exposure, sub-cells comprising glass/ITO/SnO_2/perovskite photoelectrode was exposed to a UV lamp (λ = 365 nm with a power of 6 W). UV light was emitted through two windows, each comprising an area of 31.95 cm^2, placed at a distance of 21 cm for 500 h from the glass side. It leaves the perovskite layer openly exposed to the N_2 environment. Figure 54a shows the experimental setup. By using a sub-cell configuration, any additional effects from the perovskite/HTL and HTL/electrode interfaces present in a complete cell was eliminated. Thereby, problems related to ion migration and incompatibility of the perovskite with the metal electrode are avoided [155]. Tests were carried out inside a glove box with oxygen and moisture levels of less than 1 ppm and at room temperature to eliminate competing degradation agents, as perovskite layers tend to degrade in the presence of oxygen and moisture rapidly [157,158]. Ingress of moisture and oxygen can be avoided by the development of encapsulation. The sub-cells were characterized using photoluminescence (PL) spectroscopy and UV-vis spectroscopy before and after UV exposure.

Figure 54b shows the light absorption spectra of sub-cells before and after 500 hours of UV exposure. The light absorption through the 300 to 1000 nm range decreased slightly for UV-treated sub-cells in comparison to non-UV-treated fresh sub-cells, which indicates degradation upon UV irradiation [159,160]. It could arise due to degradation within the bulk perovskite or the perovskite/SnO_2 interface, or a combination of both. Degradation within the perovskite layer is probed by studying Glass/Perovskite films under similar experimental conditions. Figure 54c shows the light absorption spectra of glass/perovskite films before and after 500 hours of UV-treatment, and glass/perovskite film before and after 500 hours of storage in the same glovebox but without any UV-treatment. The spectra reveal absorption has decreased to a similar extent in both the stored and the UV-treated sample, which suggests perovskite degrades, and UV-treatment does not exacerbate or alleviate the rate of degradation of the perovskite film itself. However, the decrease in absorption of the sub-cells shown in Figure 54b is comparatively lower than the reduction in absorption of perovskite

only films in Figure 54c, which indicate that UV-treatment of sub-cells may indeed reduce the degradation of perovskite.

Figure 54d shows the PL measurement of a freshly prepared sub-cell and a UV-treated sub-cell. The PL intensity significantly increased after UV exposure, which suggests a reduced electron transfer from the photo-generated electron-hole pair of the perovskite to the SnO_2 layer when compared to samples without UV exposure. The reduced electron transfer, therefore, indicates changes at the SnO_2/perovskite interface or of the bulk perovskite after the UV exposure. To find out whether the degradation is due to the bulk perovskite or due to its interface with SnO_2, a glass/Perovskite film was exposed to UV light for 500 hours to probe the bulk perovskite as a reference. The PL spectra of glass/perovskite films with and without UV-treatment are shown in Figure 54e. UV-treatment of the glass/perovskite indeed decreased the PL intensity, indicating bulk perovskite degradation under the UV light, in accordance with UV-vis results. It might be because the longer-lived electron-hole pair charges are not extracted in the absence of electrode, which can lead to adverse side reactions [22,161].

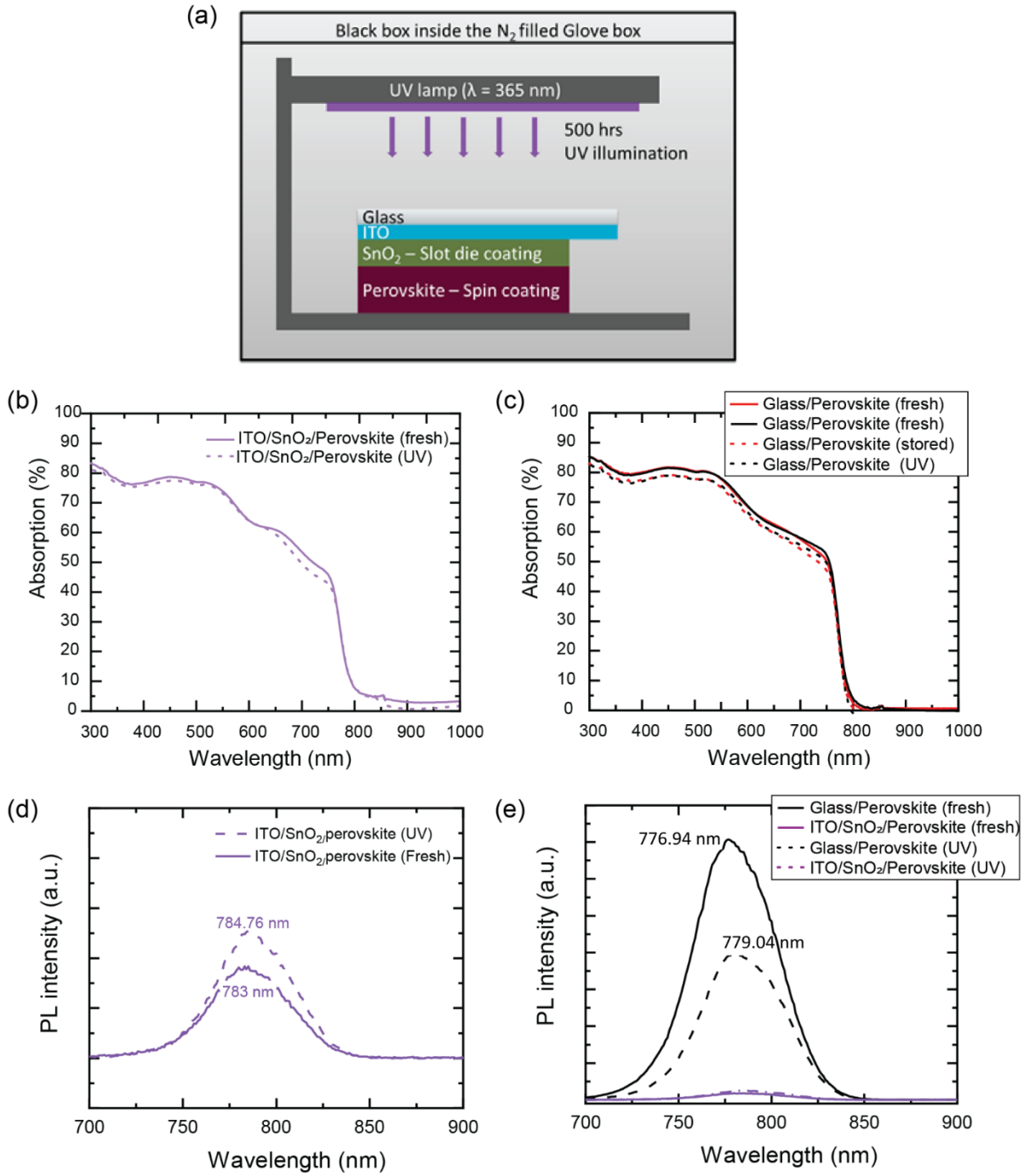

Figure 54: (a) Schematic representation of the experimental setup for UV stress for 500 h inside a glove box where sub-cells (glass/ITO/SnO_2/perovskite) were illuminated from the glass side using a UV lamp of 365 nm with 6W power source (b) UV-vis spectrum of a glass/ITO/SnO_2/perovskite sub-cell before and after UV stress for 500 h (c) UV-vis spectrum of a glass/perovskite before and after UV stress for 500 h and before and after storage in the glovebox for 500 h (d) PL spectrum of a glass/ITO/SnO_2/perovskite sub-cells before and after UV stress for 500 h and (e) PL spectrum of a glass/perovskite before and after UV stress for 500 h. Figure reproduced from publication [139].

To further attest whether the presence of SnO_2 can alleviate the degradation of the perovskite, the PL before and after UV-exposure of glass/ITO/SnO_2/perovskite with other metal-oxides, such as ZnO, and TiO_2 was compared. The samples were fabricated on the same day, and the measurements were done on a similar day. Figure 55 shows that the PL peak intensity of both glass/ITO/SnO_2/perovskite and glass/ITO/TiO_2/perovskite increased after 48 h of UV exposure. In contrast, the peak PL intensity of ZnO/perovskite decreased significantly after UV exposure. It suggests that the perovskite has degraded substantially in the presence of ZnO. It is also known that the TiO_2/perovskite interface is adversely affected in the presence of UV [162], which caused the reduced charge-transfer efficiency upon UV irradiation. Nevertheless, SnO_2 shows a similar trend as TiO_2.

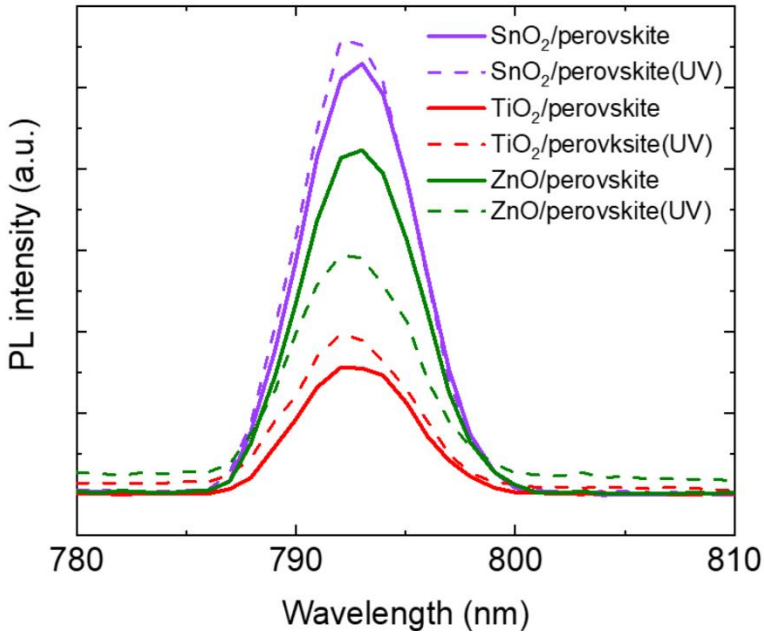

Figure 55: PL of sub-cells (ITO/ETL/perovskite) with TiO_2, SnO_2, or ZnO as the ETL. The solid and dashed lines compare the PL acquired before and after 48 h of UV stress, respectively. Figure reproduced from publication [139].

5.3.7 GIXRD analysis on sub-cells before and after UV stress

Figure 56 shows grazing incidence X-ray diffractograms taken at 0.25 degrees to study the influence of UV at the surface. Glass/ITO/ZnO/perovskite film shows the highest evolution of the PbI_2 phase, as evident in the peak at $2\Theta = 12.6^{o,}$ which corresponds to PbI_2 (0 0 1) phase. The relative peak intensities of the PbI_2 (0 0 1) phase with respect to the perovskite (1 0 0) phase are similar for both glass/ITO/SnO_2/Perovskite and glass/perovskite indicating that SnO_2 does not increase the degradation of perovskite at the surface.

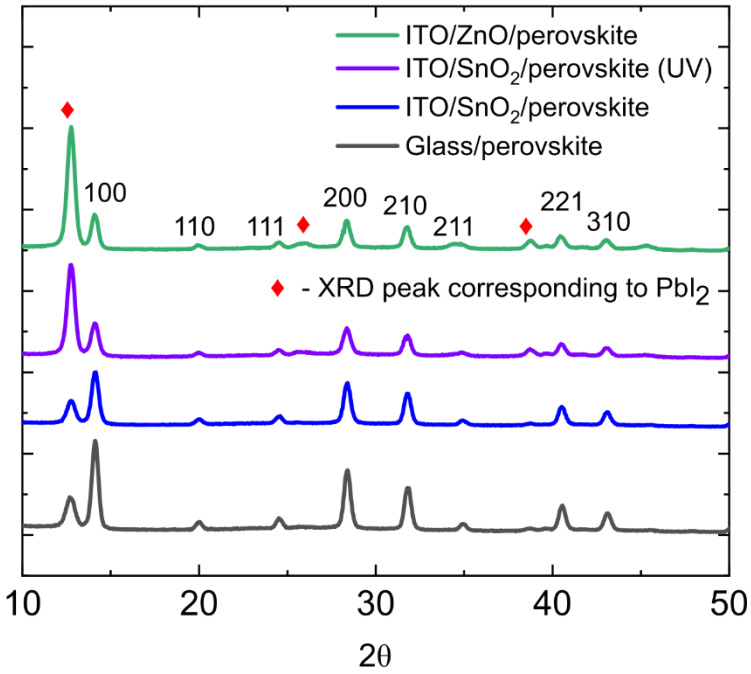

Figure 56: GIXRD diffractograms taken at an incidence angle of 0.25° of freshly prepared glass/ITO/ZnO/perovskite, glass/ITO/SnO_2/perovskite, and glass/perovskite compared with glass/ITO/SnO_2/perovskite – UV stressed for 500 h. Figure reproduced from publication [139].

To probe deeper into the bulk of the perovskite and the SnO_2/perovskite interface, XRD was carried out in grazing incidence mode (GIXRD) at several incidence angles ranging from 0.25° to 1.3° for glass/ITO/SnO_2/perovskite sub-cells before and after 500 h UV stress. The results were further compared with glass/ITO/ZnO/perovskite and glass/perovskite. The low incidence angle grazes the surface while higher angles probe into the bulk perovskite towards the ETL/perovskite interface.

The bar graphs in Figure 57 summarise the phase composition of PbI_2 and perovskite seen in the four samples at various GIXRD incidence angles by plotting the relative ratio of the integrated peak intensity for the (0 0 1) PbI_2 peak located at 12.6° with respect to the integrated intensity of the main perovskite (1 0 0) peak at 14°. The comparison of glass/perovskite and glass/ITO/SnO_2/perovskite reveals similar results (37% and 38% of PbI_2 respectively) at the surface. However, the relative proportion of PbI_2 increases in the glass/ITO/SnO_2/perovskite sample as one probe deeper into the bulk towards the interface in comparison to glass/perovskite films, indicating the possibility of enhanced interfacial degradation due to the presence of SnO_2 (Figure 57a and Figure 57b).

Comparing the UV-treated and non-UV treated sub-cells, it is observed that a relatively higher proportion of PbI_2 (72%) is present at the surface of the UV-treated sub-cell, as shown in Figure 57c. It could be induced by photo-oxidative reaction at the perovskite surface with residual oxygen and water, which may be present in the glovebox leading to a loss of iodine. A similar observation has been reported by Ouyang *et al*. [163,164].

In the case of the glass/ITO/ZnO/perovskite configuration (Figure 57e), a high proportion of PbI_2 (78%) at the surface has been observed with a uniform PbI_2 amount being present throughout the bulk of the film. The PL also shows that there is a much faster degradation of the perovskite occurring in the presence of ZnO as the reaction can be observed in a few minutes when ZnO is deposited under ambient atmospheric conditions. The degrading effect of ZnO on the perovskite has been attributed to photocatalytic reactions [165] due to the presence of hydroxyl groups. Thus, our results show that the degradation of perovskite in the presence of SnO_2 is much less pronounced.

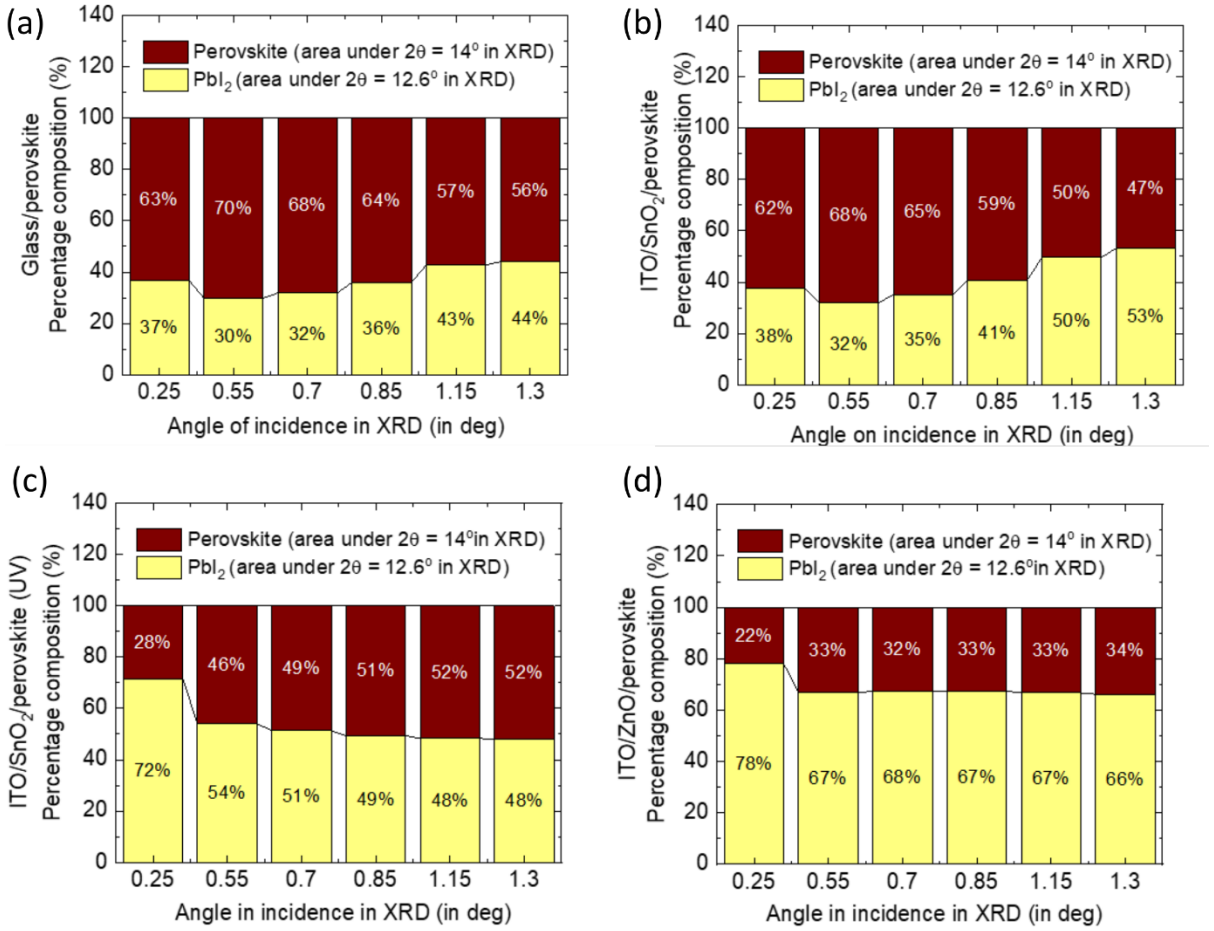

Figure 57: Percentage composition of the area under the curve of 2Θ = 12.6° (for PbI_2 phase 0 0 1) and 2Θ = 14° (for perovskite phase 1 0 0) for various GIXRD incidence angles for (a) glass/perovskite (b) glass/ITO/SnO_2/perovskite (d) glass/ITO/SnO_2/perovskite– UV stressed for 500 h (d) glass/ITO/ZnO/perovskite. Figure reproduced from publication [139].

5.3.8 X-ray photoelectron spectroscopy (XPS) of sub-cells

Figure 58 shows the compositional depth profiles generated by XPS. In consists of two sub-cells that had both been stored for 500 hours, one sub-cell receiving UV-treatment throughout storage (referred to as UV-treated sub-cell) and one sub-cell without UV-treatment (referred to as non-UV-treated-stored sub-cell). The graphs are acquired by repeatedly sputter-etching the sample surface for a short period (effective etch time). It is followed by reanalyzing the freshly exposed surface to capture atomic concentrations of all elements. Thus, the graphs show the evolution of the atomic concentration of elements into the depth of the layers starting with the perovskite top exposed surface. It should be noted that XPS depth profiling is not a straightforward or well-controlled experimental technique.

Several complicating factors, such as preferential sputtering, can potentially affect results and add significant uncertainty to any interpretation. With this in mind, the following is offered as a qualitative discussion of our results based on a relative comparison between the two sub-cells. It is noted that both sub-cells were prepared on the same day, using the same perovskite solution, and XPS was conducted on the same day as well.

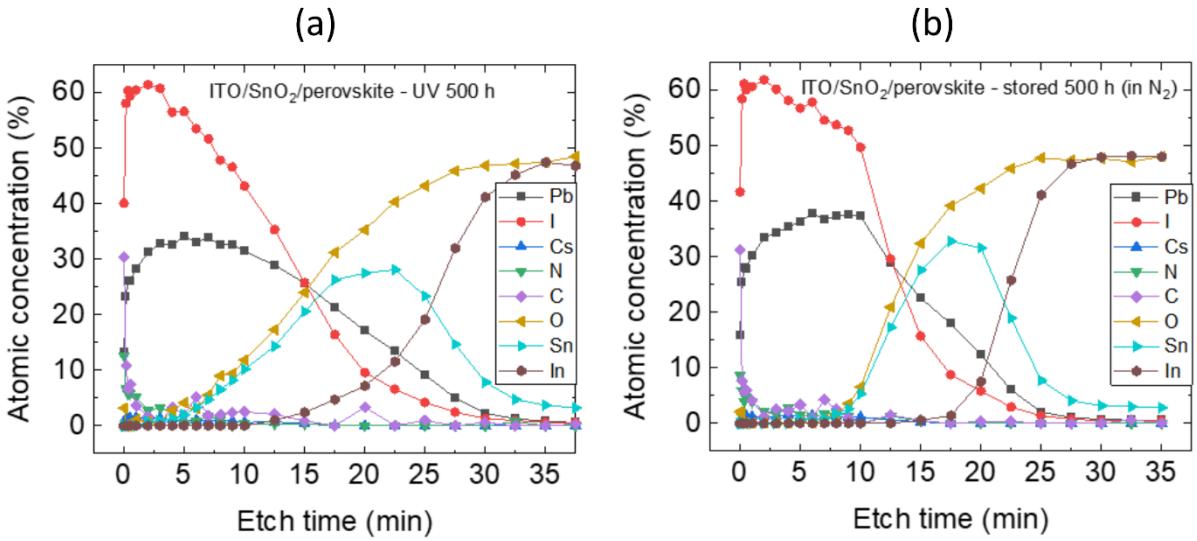

Figure 58: X-ray photoelectron spectroscopy (XPS) for (a) UV-treated sub-cell and (b)non-UV-treated-stored sub-cells. Figure reproduced from publication [139].

At the top surface, all samples show a relatively higher concentration of C, N, and some O, which is attributed to surface contamination as it is commonly observed. It is evidenced in the sudden drop in C and N levels and the absence of oxygen within less than a minute of etching. After that, only elements comprised in the perovskite, including C, N, Cs, I, and Pb, are observed. Br is not detected, which is due to the low atomic content in the perovskite formulation combined with the low sensitivity of XPS to Br. The composition of the perovskite appears to change with depth, which is due to the poor stability of perovskite, making it susceptible to decomposition as a result of the sputtering process itself.

Nevertheless, the comparison of the two samples can indicate the relative stability of the samples. Table 1 shows the relative composition of various elements at three different points of interest. Firstly, it compares multiple elements of the top surface layer before etching has started. The relative ratio of I to Pb is also shown in Table 1. The lower amount of iodine suggests higher relative degradation as perovskite degradation leads to release $CH_3NH_2^+$ and HI in the gaseous form [166]. Pb provides a reference point as the Pb remains in the sample even

after degradation. The UV-treated sub-cell has the highest relative ratio of I to Pb compared to the non-UV-treated-stored sub-cell. However, the I/Pb ratio may also be affected by the migration of Iodide ions in perovskite films [155].

The comparison of the relative ratio of C to Pb can further attest to the relative stability between the sub-cells while overcoming the uncertainty associated with Iodine migration. This comparison of C to Pb ratio is performed after 0.33 min and 0.17 min of etching for non-UV-treated-stored and UV-treated sub-cells, respectively, which is the first instance when oxygen is no longer detected. This is assumed to be the contamination-free perovskite surface, and thus, an overestimation of the concentration of carbon due to the surface layer of adventitious carbon is avoided. Like in the case of I, higher relative C content indicates relatively higher stability; however, C as a non-ionic is not associated with any known elemental migration in perovskites. Again, the UV-treated sub-cell demonstrates a higher relative ratio of C compared to Pb.

Lastly, the table also compares the elemental composition at the interface point between the perovskite and SnO_2 layer. It is taken at the etch time corresponding to the full-width at a half-maximum point towards the perovskite side, which occurs at ca. 12.5 minutes for both sub-cells. Again, the UV-treated sub-cell shows higher iodine and carbon relative to the non-UV-treated-stored sub-cell in agreement with XRD depth profiling.

Sub-cell	Etch time (min)	Pb	I	Cs	N	C	O	Sn	I/Pb	C/Pb
Non-UV-treated-stored	0.00	15.8	41.6	0.4	8.6	31.2	2.1	0.0	2.6	*
UV-treated	0.00	13.1	40.1	0.6	12.6	30.3	3.2	0.0	3.0	*
Non-UV-treated-stored	0.33	27.9	61.1	1.2	3.9	5.7	0.0	0.0	2.2	0.21
UV-treated	0.17	23.1	58.0	1.3	6.6	10.8	0.0	0.0	2.5	0.47
Non-UV-treated-stored	12.50	28.7	29.6	0.6	1.2	1.4	20.9	17.3	1.0	0.05
UV-treated	12.50	28.9	35.3	0.7	0.3	2.1	17.3	14.3	1.2	0.07
*Adventitious carbon makes the surface data relating to carbon unreliable										

Table 1: Raw data from XPS for UV-treated and non-UV-treated-stored sub-cell. Reproduced from publication [139].

The elemental composition at the interface point between perovskite and SnO_2 layer can be taken from Figure 58 at ca. 12.5 minutes. It is noted that the relative ratio of Sn:O is not 1:2 because the etching process preferentially removes O from certain metal oxide films. To confirm this, an XPS depth profile on a SnO_2 only film is conducted, which showed a ratio of ca. 1:2 on the surface without any etching. It gradually changes to 1:1 with increasing etch time (Table 2).

Etch Time	XPS Atomic%			Atomic ratio
(s)	Sn	O	C	O/Sn
0	21.20	49.89	25.44	2.353
10	26.27	48.51	21.60	1.847
20	29.01	47.75	19.02	1.646
30	31.13	47.21	17.31	1.517
60	35.55	46.60	13.15	1.311
120	39.17	46.41	9.84	1.185
300	43.30	45.31	6.67	1.046
600	43.21	45.65	6.65	1.056

Table 2: Atomic concentration of ITO/SnO_2 sub-cell obtained from X-ray photoelectron spectroscopy (XPS). Reproduced from publication [139].

Thus, as the sub-cells were fabricated in ambient room conditions, the surface of the films and the grain boundaries are likely to contain a higher concentration of adsorbed oxygen and moisture, which triggers degradation upon UV illumination [158]. It is evident in the XRD depth profiling, which revealed a higher relative presence of PbI_2 on the film surface of the UV-treated sub-cell compared to the non-UV treated sub-cell (Figure 57b and Figure 57c). Complementing to XRD results, XPS depth profiling also indicates a gradient of PbI_2 concentration for the UV-treated sub-cells.

5.3.9 Maximum power point tracking of complete devices

To investigate the effect of UV-treatment on the operational stability of planar n-i-p PSCs, the cells were completed by depositing PEDOT: PSS as the HTL, MoO_x, and Ag on top of the UV-treated (500 h) glass/ITO/SnO_2/perovskite. MoO_x was used to create a barrier against Ag, and I reacting, which can lead to degradation of the contact [155]. For comparison, the devices were also fabricated on the non-UV treated glass/ITO/SnO_2/perovskite sub-cell with PEDOT: PSS, MoO_x, and Ag. Hereafter, for simplification, glass/ITO/SnO_2/perovskite is referred to as the sub-cell. The average electrical parameter is given in Figure 59. It can be noticed that the large variation is found within the non-UV treated stored samples (light grey box). However, such

an effect has been suppressed through UV treatment and the effect has been maintained also in the UV-treated,stored devices (light blue box).

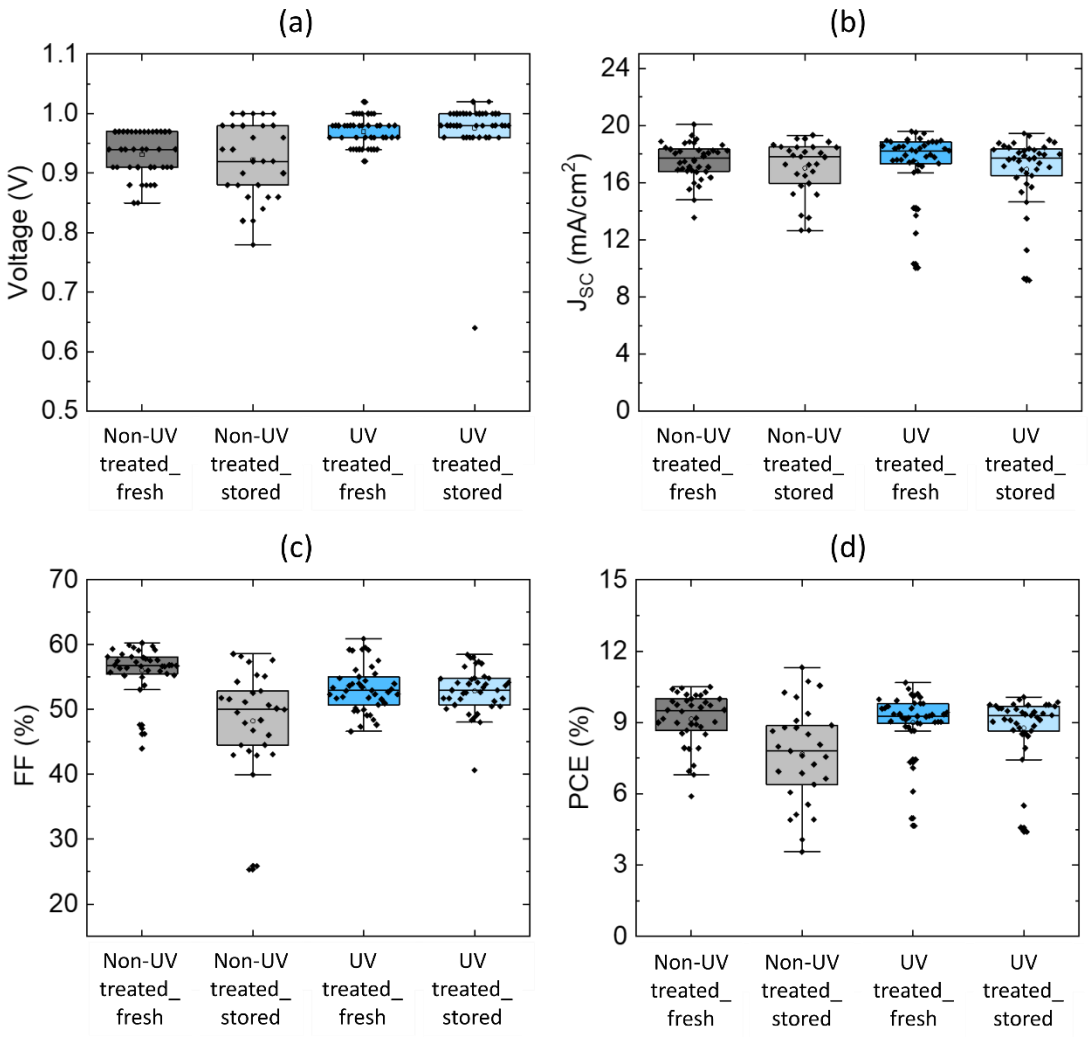

Figure 59: Electrical parameter comparison (a) V_{OC} (b) J_{SC} (c) FF and (d) PCE of devices containing UV-treated and non-UV treated sub-cells. Figure reproduced from publication [139].

Figure 60 shows the normalized maximum power point (MPP) of devices made from a UV-treated sub-cell and a non-UV treated sub-cell after 500 h of full cell fabrication, acquired for 14 h under continuous 1 sun illumination in an N_2-filled glove box. The MPP of the device made from a UV-treated sub-cell shows an abrupt initial decay with a loss of only 20% of initial MPP value within 3-4 hours, followed by a stabilized trend. The degradation is similar to that observed in organic solar cell devices where the initial rapid degradation is known as the "burn-in" [167]. As has been shown for $MAPbI_3$ films [168], oxygen can substantially be trapped inside the perovskite, which might lead to a similar effect in the initial stability.

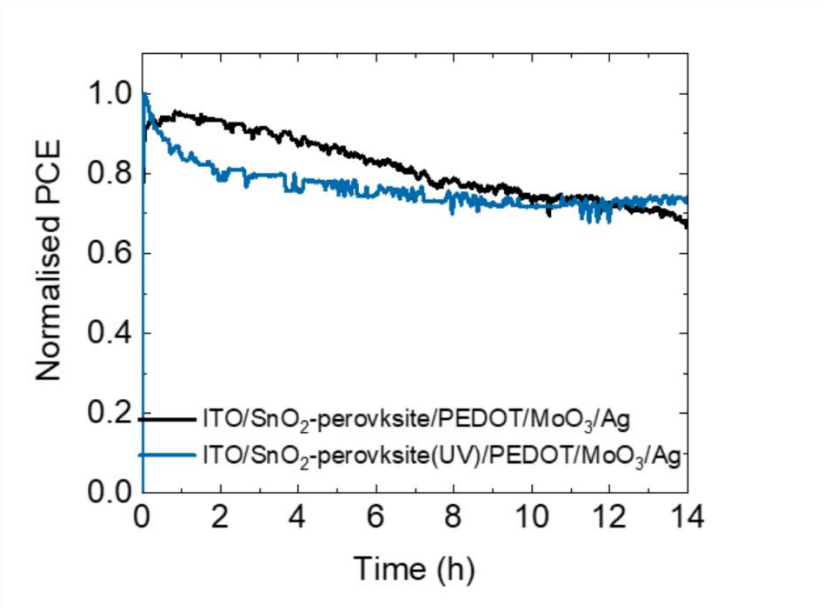

Figure 60: Comparison of normalized MPP of devices whose glass/ITO/SnO_2/perovskite interface is UV-treated with devices whose glass/ITO/SnO_2/perovskite is not UV-treated. Figure reproduced from publication [139].

Figure 61a and Figure 61b compares the J-V curves before and after the MPP measurement. Figure 61c and Figure 61d shows the normalized photovoltaic parameters acquired from the J-V curves. The devices with a non-UV treated sub-cell undergo a linear reduction in all photovoltaic parameters, particularly V_{OC} and J_{SC}. It suggests a degradation in bulk and interfaces, whereas devices with UV-treated sub-cells have similar Jsc and Voc with somewhat reduced FF, which could be due to contact issues trigged by a high concentration of PbI_2 on the surface. This accumulation of additional PbI_2 at the perovskite/electrode interfaces will induce a passivation effect by reduction of defect states [169], ion defect migrations [170], and recombination sites [171], which would lead to the stabilization of MPP in the devices made of UV-treated sub-cells.

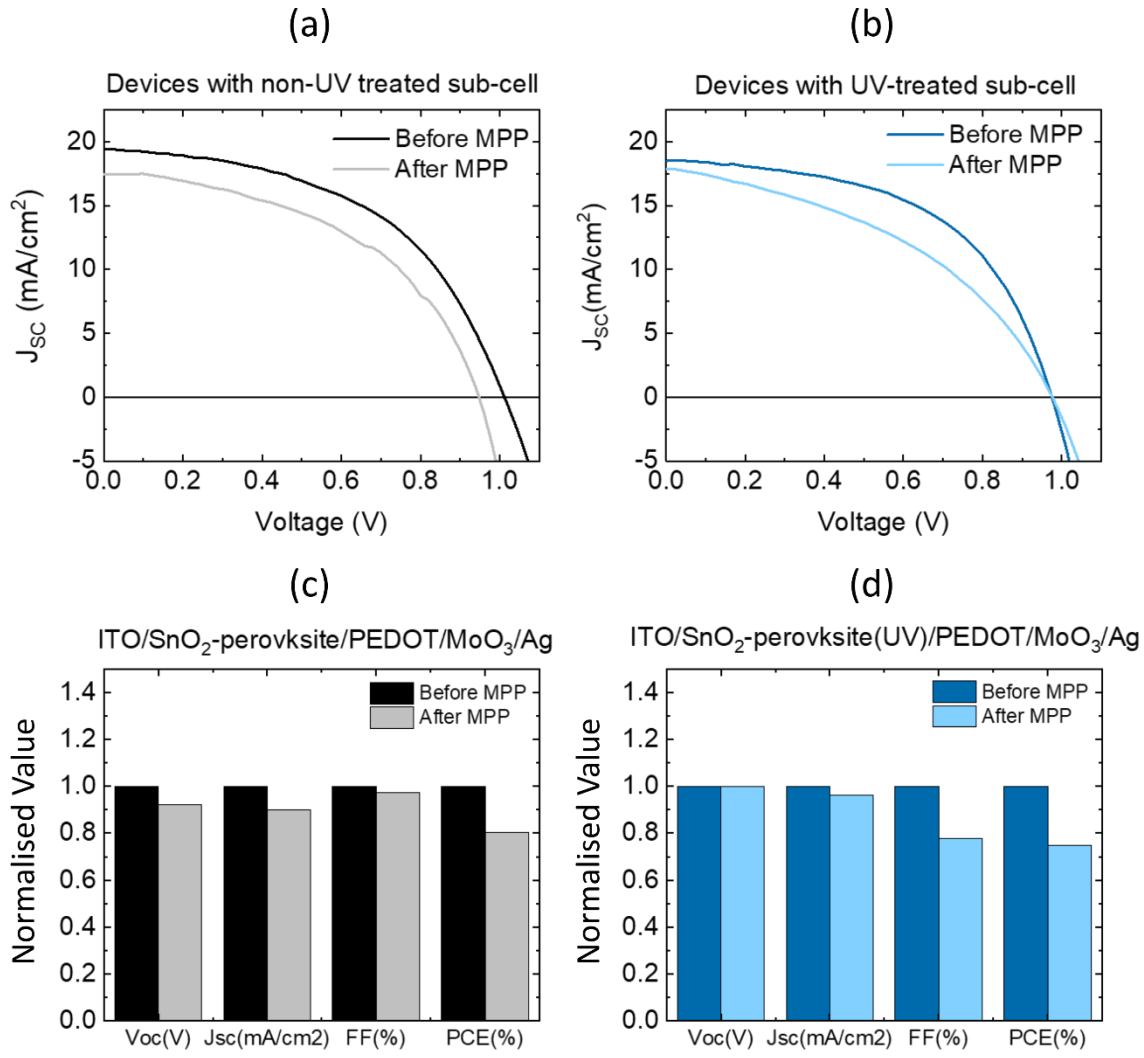

Figure 61: J-V curves (a) before and after maximum power point tracking (MPP) of a device containing a non-UV treated sub-cell and (b) before and after MPP of a device containing UV-treated sub-cell. Comparison of normalized electrical parameters taken from J-V curves acquired before and after MPP for (c) devices made from non-UV treated sub-cells (d) devices made from UV-treated sub-cells. Figure reproduced from publication [139].

5.4 Conclusion

The effect of slot-die coated SnO_2 on the UV stability of perovskite films was investigated. The challenges of forming a uniform film with slot-die coating SnO_2 is demonstrated. The problem of agglomeration is solved by adding polyethylene glycol (PEG) as a polymeric additive. The formed SnO_2 electron transport layer (ETL) is characterized by using XRD and found that the layer is nanocrystalline in nature. In comparison to the literature, a significant positive shift in the range of 0.2 - 0.8 eV in the conduction band level of SnO_2 (-3.67 eV) is observed using UPS. It might originate from film formation differences owing to slower solvent evaporation in a slot-die coating process compared to the often-used spin-coating.

To particularly investigate the SnO_2/perovskite interface's contribution to device stability, the glass/ITO/SnO_2/perovskite sub-cells before and after 500 h continuous UV illumination under an N_2 environment from the glass side was characterized. Perovskite films on glass alone as control samples were also investigated to rule out the influence of bulk degradation. Absorption spectra of all perovskite films and sub-cells showed little change after UV treatment. However, higher photoluminescence (PL) intensity was observed after the UV treatment, which could indicate a lower electron injection rate into the electron-accepting SnO_2 layer. Additionally, GIXRD measurements show the presence of excess PbI_2, which formed at the surfaces of perovskite photo absorber after the UV-treatment. Confirming observations showing the change in perovskite surfaces was also seen in XPS measurements. Subsequently, devices were completed from sub-cells to full devices through a hole transport layer (HTL) and electrode deposition. During the maximum power point (MPP) tracking, unlike the constant drop of PCE observed in the case of the device with non-UV treated sub-cell, 80% of the initial PCE was retained for 10 h after the initial decrease in a device with UV-treated sub-cell. It is attributed to the passivation effect from the presence of excess PbI_2 at the HTL/perovskite interface.

In conclusion, detrimental effects have been noticed in the sub-cells after long UV illumination. However, surprisingly, complete devices fabricated from UV-treated sub-cells showed stable performance. Therefore, to understand further the device stability under UV, the importance of also analyzing a specific interface in a sub-cell is shown. Analyzing a sub-cell can, therefore, be a powerful tool to probe layers and interfaces across a plethora of

characterisation tools. While UV treatment of sub-cells shows unexpected improvement in the full device stability, future work should explore stability over the different duration and the impact of hole transporting layers other than PEDOT:PSS. Additionally, this study indicates that the UV-treatment of sub-cells may be an effective passivation tool. For this, various parameters, including UV intensity, wavelength, and duration of exposure, requires further investigation.

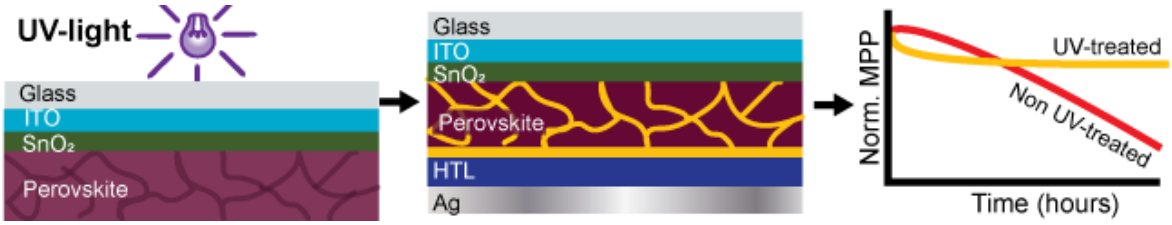

Figure 62: Summary diagram for chapter 5 showing the result of UV treatment of sub-cell and the final stabilized device performance. Figure reproduced from publication [139].

Chapter - 6

Sub-cell analysis and optimization of FTO/perovskite interface with different hole blocking layer deposition techniques in carbon-based perovskite solar cells

6 Sub-cell analysis and optimization of FTO/perovskite interface with different hole blocking layer deposition techniques in carbon-based perovskite solar cells

In perovskite solar cells, the compact hole-blocking layer (HBL) governs the transport resistance, as well as the rates for electron-transfer and the recombination at the FTO-perovskite interface and hence significantly affects the solar cell efficiency. For the work in this chapter, compact-TiO_2 (c-TiO_2) as HBLs were processed using different techniques (screen-printing, atomic layer deposition (ALD), sputtering and spray pyrolysis deposition (SPD)) to attain very thin (<30 nm) and uniform layers for enhanced performance of perovskite solar cells (PSC). Results from SEM and AFM show that all the deposition techniques can successfully result in a conformal coating of the c-TiO_2. Even though layer morphology and thickness can be seen through SEM and AFM, they are destructive techniques, and only micrometer-sized area can be analyzed. Additionally, the electrical quality (i.e defects, shunts, current distribution) of the layers cannot be explained.

In this chapter, an FTO/c-TiO_2/µ-graphite sub-cell was used to analyze the electrical quality of c-TiO_2 using a camera-based imaging technique - Dark Lock-in Thermography (DLIT). DLIT is a reliable, fast thermal imaging tool for shunt detection and to examine the distribution of the current flux in solar cells. DLIT has been used not only to identify defects/irregularities in the investigated layer but also to determine the local current-voltage characteristics of these weak spots, facilitating the distinction of linear/ohmic from non-linear defects. DLIT helps for the identification of the causes for defects and aids towards optimization of the cell. From the analyses, the ALD-TiO_2 film proves to be the most efficient, pin-hole free HBL for carbon-graphite based PSCs (CG-PSCs). It offers an efficient layer to prevent the backtracking of electrons from c-TiO_2 to perovskite. Thereby, the charge recombination at the FTO/perovskite interface is reduced. The results show high power conversion efficiency of stable efficiency of 10.1 %.

Part of the results shown in this chapter are based on the framework of a master thesis from Mrs. Shanmugam Lakshmi Subramaniam for which I was her immediate supervisor. She contributed to the DLIT measurements and analysis. I participated in further analyzing the complete devices.

6.1 Introduction

The understanding of the charge transfer mechanisms [35] and physical processes at the layer interfaces has led to the optimization of charge selective layers. Thanks to this, numerous papers have been reported to enhance cell performance by reducing interfacial recombination [72,128] and improving the properties of electron and hole blocking layers. The role and importance of HBL have already been explained in Chapter 2.3.3. One way to enhance HBL property is by adding a buffer layer (Sb_2S_3 [41], Al_2O_3 layer [85], etc.). By adding a buffer layer above HBL, claims a passivation effect at the c-TiO_2/perovskite interface [41]. Another solution is given by using different HBL or EBL materials [49,65,172,173].

On the other hand, to ease large scale production, faster processing, and in the aim of knowledge transfer towards flexible PSCs, steps attempting elimination of charge selective layers in the device structures have also proven successful [21,174,175]. In general, charge transport layer (CTL)-free PSCs undergo many challenges such as energy misalignment, poor surface finish, and coverage of TCO, hysteresis, and lack of permanent built-in potential [176,177]. However, power conversion efficiencies (PCE) > 19% has been reported for the electron transfer layer (ETL) -free and hole transfer layer (HTL) -free devices. Huang et al. published an article where surface modification of ITO with tetramethylammonium hydroxide (TMAH) is shown. Such a treatment is claimed to modify the surface of ITO. Thereby, the recombination and defects at the ITO/perovskite interface are reduced. Conductivity in the perovskite grain boundaries is also increased. It led to a high efficiency of 20.1 % for an ETL-free architecture [176]. In an HTL-free device, the main drawback is the mismatch of the perovskite and ITO energy levels. W.Q. Wu and his team reports a $MAPbI_3$ perovskite doped with p-type organic 2,3,5,6-tetrafluoro-7,7,8,8-tetracyanoquinodimethane (F4TCNQ). Better energy alignment, favorable band bending has led to the reduction of series resistance at the ITO/perovskite interface. The article claims that the F4TCNQ increases the charge extraction also in the grain boundaries. Thus, achieving a stable PCE of 20.2 % for 75 s [178]. Therefore other works show that the thickness of HTL and ETL can be surprisingly low as reported by Lunt and team [179]. In this report, they show an architecture where hole extraction is enhanced from perovskite to ITO using 1.6 nm PEDOT. Electron extraction is enhanced from perovskite to Ag also through 1 nm of vacuum evaporated C_{60}. The high efficiency is attributed to the reduced space charge accumulation at interfaces. However, irrespective of the device configuration, controlling the

nature of the charge selective layers and their interfaces with the perovskite absorber is indispensable to maximize the cell performance.

One of the proven camera-based thermal imaging tool for shunt imaging and examining current distribution in solar cells is Dark Lock-in Thermography (DLIT) [116,180–182]. The thermal behavior of the cell varies based on different applied voltages. Lock-in frequencies set ensures to capture even the weakest thermal loss, which helps in identifying the smallest defect/shunts present in the solar cell. Thus, this imaging technique makes it a quick, reliable quality control tool that can be adapted to the manufacturing of large-area solar cells, as well. DLIT, as a control tool, has already been used in Si, CdTe, and organic solar cells [180,182,183]. More details on the working principle of DLIT has been provided in section 4.2.1.

In this work, a sub-cell configuration FTO/c-TiO_2/μ-graphite is employed for studying the quality of the HBL processed through different deposition techniques. Various optical, crystallographic, and morphological tools have been used to analyze its physical quality. However, the electrical quality (i.e., shunt detection, defect detection, current distribution) of a specific layer cannot be investigated through the techniques mentioned above. For this purpose, this work uses the non-intrusive DLIT technique to investigate shunts, defects, and non-uniformity of the HBL in specific. Results from the sub-cells showed SPD and ALD techniques produce smooth and defect-free HBL. When compared with the electrical parameters of complete devices, SPD shows a high voltage > 900 mV. However, owing to improved current density and FF, the high average efficiencies were achieved for devices with ALD - c-TiO_2, reaching an average PCE of 10.7 %.

6.2 Experimental section

6.2.1 Preparation of sub-cells for DLIT measurement

100 x 100 mm^2 FTO TEC 7 glass plates were patterned using in-house class III, Nd-Yag laser machine, to create both electrodes on a single glass to be used as a monolithic cell. These plates were then cleaned in an ultrasonic bath containing 3% Deconex OP153 at 60°C for 2 min and rinsed with DI water to remove the soap residues. Further, they were ultrasonically treated in the bath for 1 min at 60° C in DI water, rinsed, and dried with dry nitrogen. The samples are deposited with compact TiO_2 as HBLs using different techniques and sintered at

500°C for 30 mins in air. The sintering process has been performed to have a direct comparison with complete PSCs, where the mesoporous layers need to be treated at T>400°C. To deposit the μ-graphite film, a 1:7 ratio graphite-water solution (Aquadag colloidal graphite) is prepared and manually sprayed on the samples at 140° C with compressed air at 2.5 mbar. The spraying is done using a metal mask to result in an active cell area of 0.4 cm^2. The plates are then cut into substrates of 25 x 25 x 2.2 mm^3 dimensions, and electrical contacts are established with silver paint (G3692 Acheson silver DAG 1415) on the TCO patches.

6.2.2 HBL deposition methods

The sputtering process details for c-TiO_2 are given in section 3.1.2.2, and ALD details are provided in section 3.2.1. Spray Pyrolysis Deposition (SPD) was carried out manually, and the corresponding process parameters are given in section 3.3.1. Screen-printing was carried out using Dyesol TiO_2 paste using a metal mesh screen. These layers were air-dried at 150 ^oC before its sintering process.

6.2.3 Device Fabrication

For full device fabrication, the same steps until the manufacturing of c-TiO_2, as mentioned in section 6.2.1, is used. It is followed by the screen printing of mesoporous layers of TiO_2 and ZrO_2, whose thickness is 900 nm and 1600 nm, respectively. These layers are sintered together at a temperature of 500 ^oC for 30 min. The carbon-graphite counter electrode of 9 μm is screen printed and sintered at 400 ^oC for 30 min. The process parameters for screen printing is defined in section 3.5.1. For perovskite infiltration, 1 M 1-step perovskite solution was prepared by mixing 0.6675 g of PbI_2, 0.2186 g of MAI, and 0.0177 g of 5-AVAI in 2 ml GBL. 4.5 μl of the solution was drop casted onto each device. After 20 min of wait time, the devices were annealed at 50 ^oC for 60 min.

6.3 Results and discussion

6.3.1 SEM and AFM characterizations of c-TiO_2 films processed on FTO

In this section, the morphology and the surface features of TiO_2 films have been studied using scanning electron microscopy (SEM) and atomic force microscope (AFM) images. The SEM images of TiO_2 films deposited on FTO through ALD, SPD, and sputtering have been compared with bare FTO as a reference in Figure 63. From the cross-sectional analysis, all TiO_2-HBLs

appear conformal with the bare FTO Figure 63a, indicating a uniform coverage of the FTO's peaks and valleys. The top-view images in the inset suggest that ALD-TiO_2 (Figure 63b) and sputtered-TiO_2 (Figure 63c) both produce a smooth layer, slightly rounding off the FTO peaks. In contrast, the TiO_2 deposited through SPD (Figure 63d) is comparatively rougher with smaller particles distributed across the layer. However, very thin layers (≤ 30 nm) of TiO_2 can be effectively deposited on FTO substrates through ALD, SPD, and sputtering processes to produce uniformly thin HBLs with good coverage on large areas.

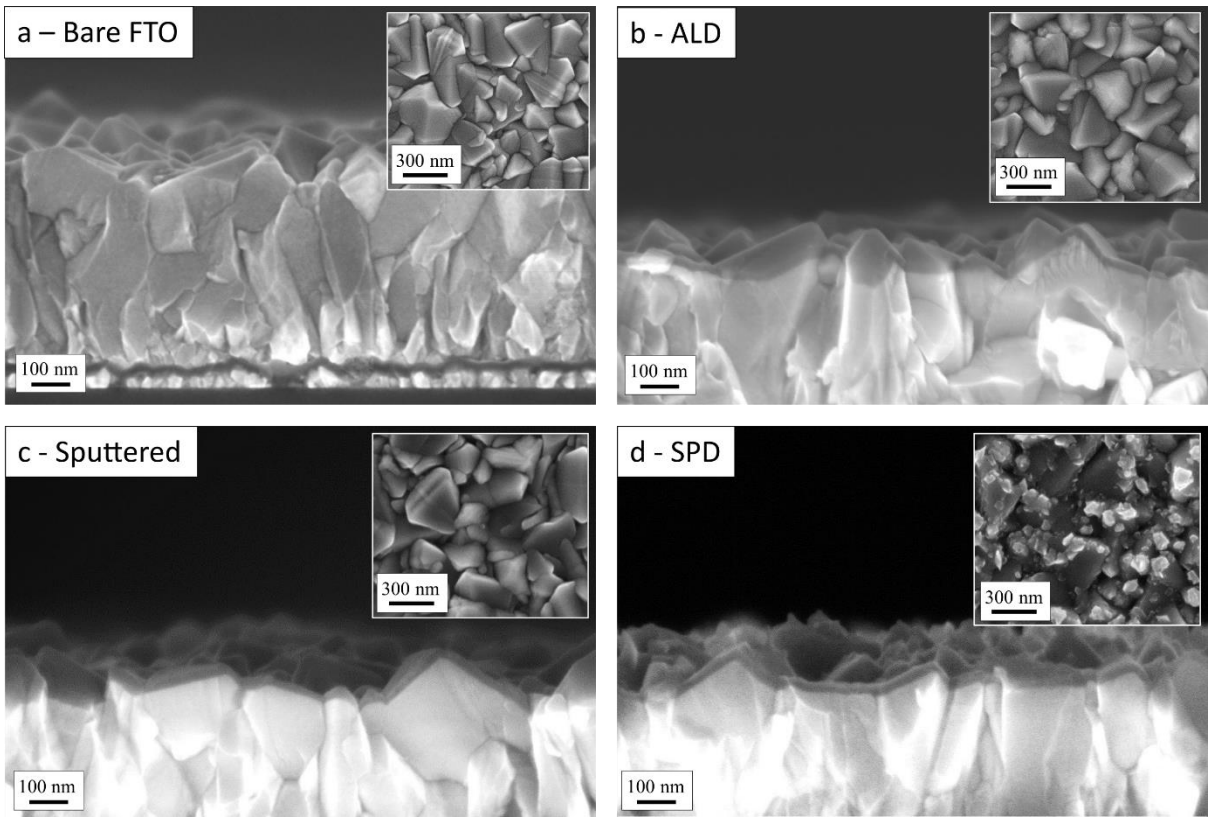

Figure 63: Cross-sectional and top-view (inset) SEM images of (a) bare FTO glass substrate, (b) 20 nm TiO_2-HBL deposited through ALD, (c) 20 nm sputtered TiO_2-HBL and (d) 30 nm TiO_2-HBL deposited through SPD. All TiO_2 films were treated at 500° C before measurement.

Further investigations on the layer roughnesses are presented in Figure 64. The root-mean-squared (RMS) roughness values of these layers, determined on an area of 5 μm^2, are presented. The TiO_2-HBLs deposited through ALD, and sputtering processes (Figure 64b and Figure 64c) gives the smoothest layers supporting the information obtained from SEM measurements. The roughest layer is obtained through SPD processing, as shown in Figure 64d. A higher resolved AFM image of the SPD films is given in Figure 64e to highlight tiny distributed particle-like structures, causing a rougher surface.

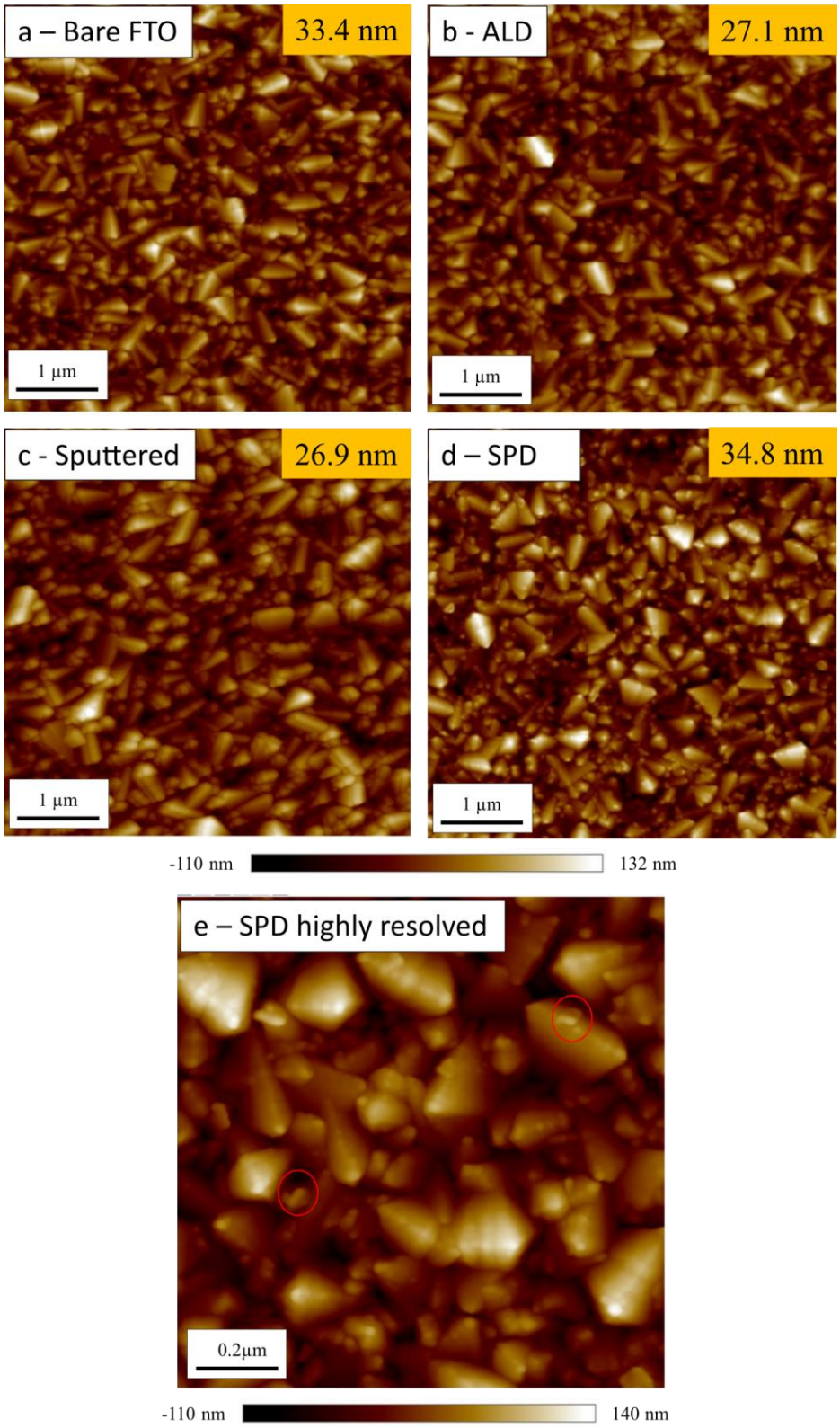

Figure 64: Tapping mode AFM top-view images of (a) bare FTO glass substrate, (b) 20 nm TiO_2-HBL deposited through ALD, (c) 20 nm sputtered TiO_2-HBL, and (d) 30 nm TiO_2-HBL deposited through SPD. The values on the top-right corner of the images are the RMS roughness values determined through AFM on an area of 5 µm² and (e) Highly resolved top-view AFM image of TiO_2 deposited through SPD. Encircled are the tiny distributed particle-like structures on the film.

SEM and AFM are widely used optical characterization tools for thickness and morphology investigation. However, they are destructive and micrometric-localized analysis tools. Even though reliable morphology measurements can be made using SEM and AFM, it is difficult to precisely identify defect points and have a bigger picture of the entire active area.

6.3.2 Transmittance, UV-vis and XRD measurements of c-TiO_2 - HBL layers

Figure 65a and Figure 65b displays the transmissivity curves of FTO/c-TiO_2 samples in the 300 – 1000 nm wavelength range. As expected from SEM measurements, it is observed that the SPD-TiO_2 has a lower transmittance of (69.67% at 550 nm) differing from the sputtered-TiO_2 having a transmissivity of 75.4% (at 550 nm). The energy band gap values (E_g) of the different HBLs derived from the Tauc plots obtained from UV-spectroscopy measured on the same day are presented in Figure 65c. The E_g values for SPD and ALD blocking layers are found at 3.19 eV, and 3.27 eV, respectively, close to the values stated for anatase-TiO_2 in literature [184]. The E_g value for sputtered TiO_2-HBL, however, deviates considerably from the other two samples and is measured to be 3.38 eV. From the spectroscopy measurements above and the analogous/comparable values found in the literature[184], it can be stated that the TiO_2 films deposited using ALD and SPD methods (and annealed at 500°C) is in the anatase phase. However, to verify the crystallinity of the TiO_2 layers, X-ray diffraction measurements (XRD) have been carried out on a Si substrate. Although the E_g is higher, the XRD results reveal that the sputtered TiO_2-HBL layer is also in the anatase phase.

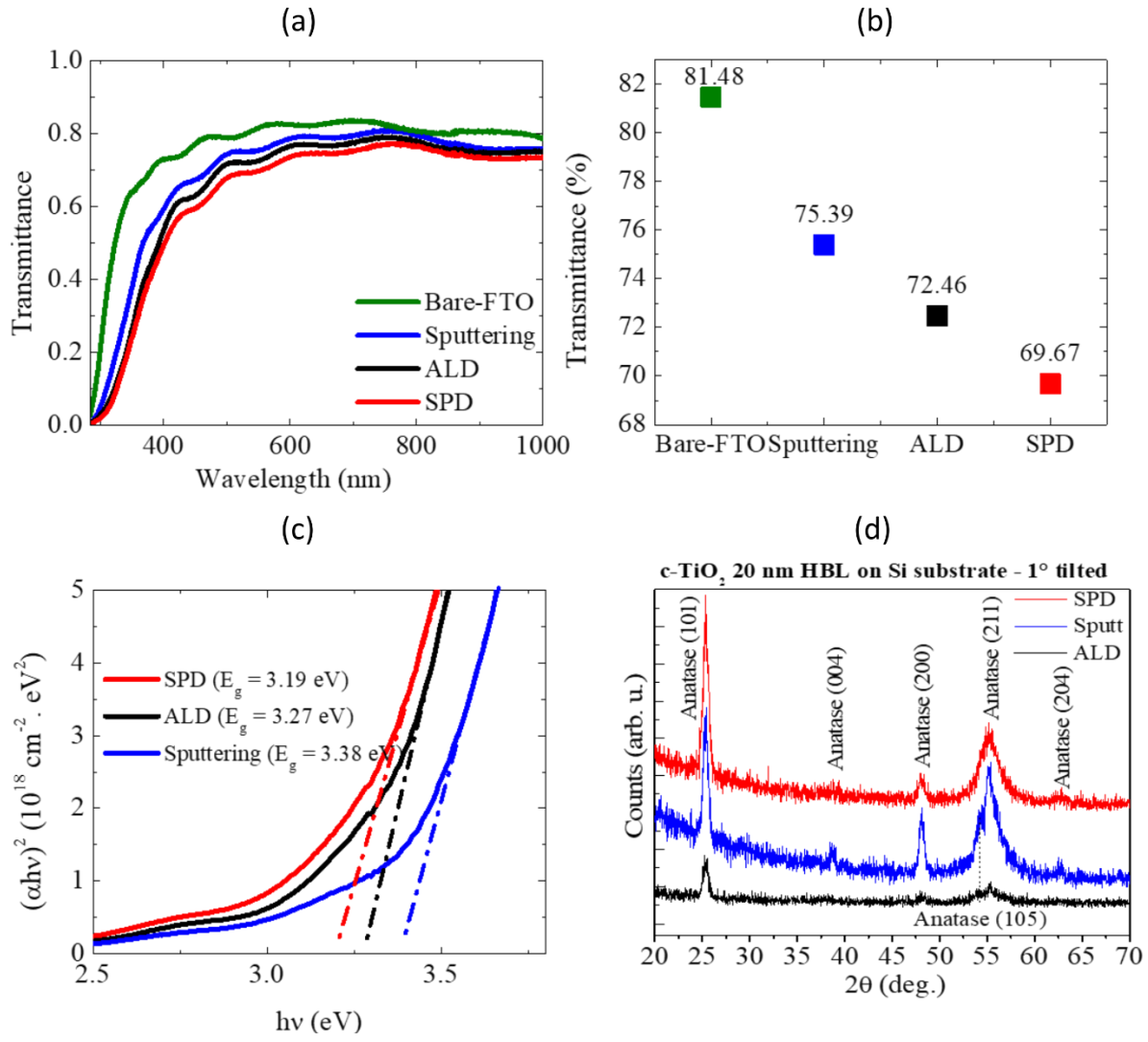

Figure 65: (a) Transmittance of c-TiO_2 processed through various deposition techniques on glass substrate (b) Transmittance value at 550 nm plotted from (a), (c) UV-vis spectroscopy measurement and (d) XRD measurements of c-TiO_2 processed through various deposition techniques on Si substrate

6.3.3 Understanding DLIT images of sub-cells FTO/c-TiO_2/µ-graphite

The introduction and basic working principle of the DLIT have already been discussed in section 4.2.1. By following the lock-in principle, the IR signal in the investigated sample is periodically modulated through an external source (i.e., an applied voltage), and the lock-in is applied to every temperature signal from every pixel of the image of the sample. Practically, increased thermal radiation will occur in areas with high localized heat, such as shunts and non-radiative recombination points. These spots are defined as high emission regions/points in the DLIT image of the sample under investigation: the mean power dissipated (P_{mean}) at

every voltage is proportional to the mean of the DLIT signal intensity (I_{DLIT}) [183]. It can be equated as following to determine the current density J at the corresponding voltage.

$$P_{mean} \propto I_{DLIT} \propto J^2 \quad \textit{Eq 35}$$

$$J \propto \sqrt{I_{DLIT}} \quad \textit{Eq 36}$$

The HBL material (TiO_2) investigated in this work is a nano-thin film having low emissivity and thus low radiated power, making the distinction of defects challenging. Hence, the compact HBL film deposited on the FTO substrate is homogeneously covered by spraying a 4-5 µm thick micronized graphite (µ-graphite) having emissivity in the MWIR region > 0.92 (1.0 is for a blackbody). This process results in a conductive highly emitting conformal coating with low heat conductivity able to finely follow the morphology of the underlying FTO/HBL layer. Thus, the resulting FTO/HBL/µ-graphite layer effectively radiates the local heat after the application of a bias to the test sample.

Figure 66a and sample Figure 66b show a top-view photograph, a cross-sectional schematic, and an SEM image of the sub-cell (FTO/HBL/µ-graphite) with a compact and uniform appearance. It demonstrates the achievement of high-quality interfacial contact between the compact HBL and the µ-graphite. This FTO/HBL/µ-graphite sub-cell was measured through DLIT using a bias voltage of 1 V. The resultant DLIT image is shown in Figure 66c (with the active area outlined). It displays the presence of hot-spots (bright spots/regions), which indicate shunt paths, defects, or non-uniformity in the hole-blocking layer.

Generally, the work function of the conductive µ-graphite matches with the work function of Gold (metal) and can be considered similar to metal contact. Since the HBL is an n-type semiconductor, it is important to note that this sub-cell configuration HBL/µ-graphite forms a Schottky diode (semiconductor/metal contact) and hence should show a rectification behavior by theory [185,186]. Thus, this prominent feature of the sub-cell configuration additionally helps in qualitatively analyze the HBL. It is done by analyzing the voltage-dependent intensity of the resulting DLIT image.

In this direction, the DLIT signal is acquired at voltage-steps, and the I_{DLIT} obtained is then equated using Eq 36 to calculate the corresponding current in the active area. The dark J-V curve, thus obtained, is compared with the dark J-V curve of the sample measured with a potentiostat in Figure 66d. The dark J-V from the potentiostat shows a diodic behavior of the

sub-cell. The active area current, thus calculated from a voltage-dependent DLIT image, also follows a similar pattern. Thereby, it indicates that the voltage vs. DLIT intensity curve can provide supplementary information on the quality of the HBL in addition to the indication of shunt spots in the DLIT image.

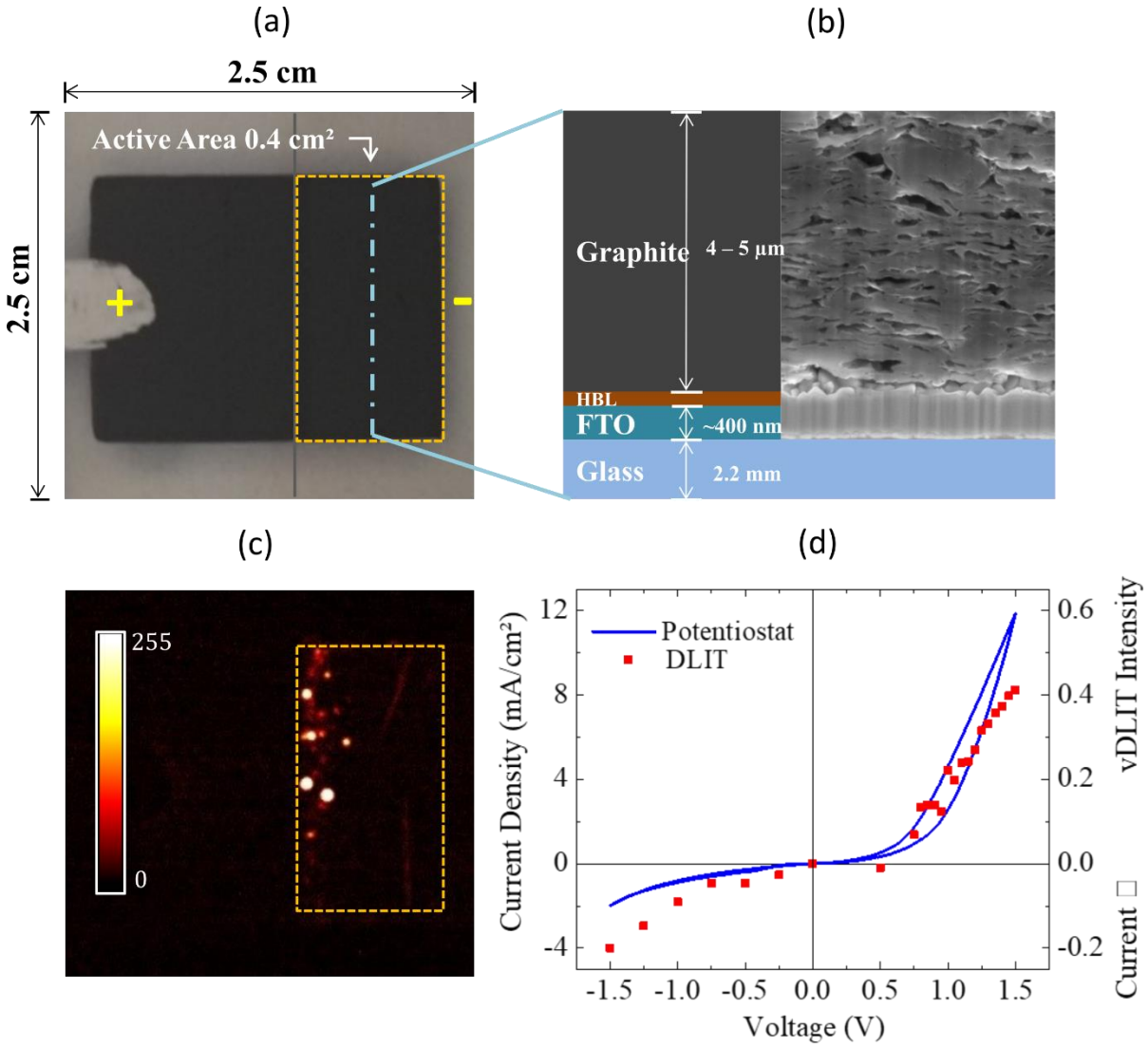

Figure 66: (a) Photograph (top-view) of an FTO/HBL/µ-graphite sample prepared for DLIT measurements with a defined active area of 0.4 cm². (b) Schematic cross-sectional image and FIB-SEM image of an FTO/HBL/µ-graphite sample prepared for DLIT measurements. (c) DLIT image acquired at +1 V of an FTO/HBL/ µ-Graphite sample indicating bright spots and (d) Dark J-V curves of the measured sample obtained from standard J-V measurements and qualitatively determined from DLIT images. Max. shunt detection resolution = 20 µm.

6.3.4 Reverse and forward bias of the sub-cell

By having a voltage-dependent analysis, the sub-cell can be put under reverse bias and forward bias. In the case of a reverse-biased sub-cell, the electrons are passed through the graphite towards FTO. Even though this is the desired direction in which the HBL should allow the electrons to pass through in a PSC, the property is changed because of its interface with graphite. Thus, in a reverse bias condition, an electron depletion region is created at the HBL/ µ-graphite interface. Thereby, blocking behavior is observed. Hence, only in the presence of a linear/ohmic shunt, electrons pass through HBL and produce a bright spot in the resultant DLIT image.

In the case of a forward-biased sub-cell, the electrons are pushed through the HBL from FTO (Figure 67b). It is the undesired direction in which an HBL should not conduct. However, the electrons find their way toward the µ-graphite through various non-linear Schottky type interfaces, defects (i.e., non-uniformity in the layer, dust, etc.) and linear ohmic shunts (graphite in contact with FTO). It results in high forward current, as shown in Figure 67a. The corresponding DLIT images in a forward-biased condition is shown in Figure 67c. For a non-linear defect, its forward current is lower in the range of 1 µA (more moderate DLIT intensity), whereas the current through an ohmic/linear shunt point is in the range of 100 µA (high DLIT intensity). Therefore, by comparing the DLIT image at forward bias and the DLIT image at reverse bias, ohmic shunts can be identified.

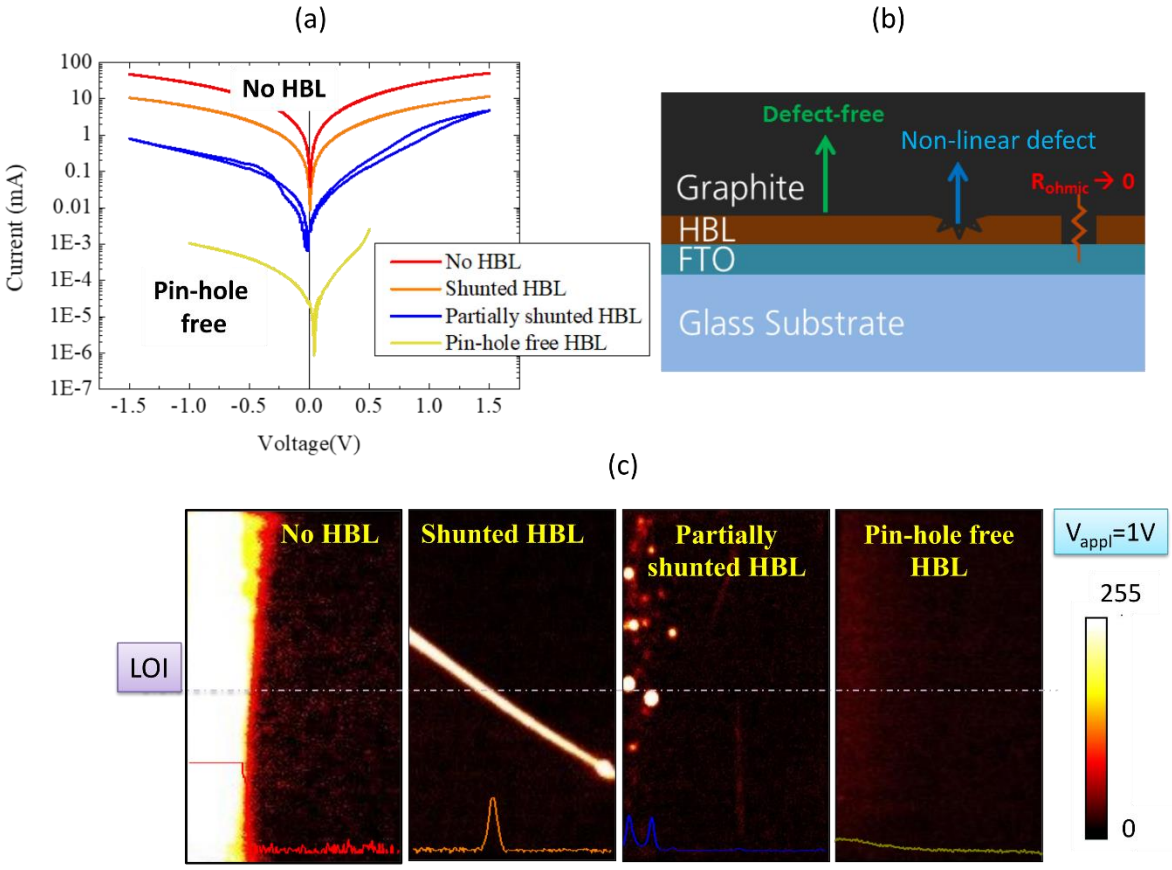

Figure 67: (a) dark J-V curve of HBL having different defects (b) schematic diagram of a sub-cell under forward bias marked with the layer inhomogeneities and (c) Corresponding DLIT images of conditions mentioned in (a) at a bias voltage of 1 V. LOI is the line of interest (dashed line). Max. shunt detection resolution = 20 µm.

6.3.5 Local J-V curve analysis of shunt spots for defect detection

As introduced in the previous section, the defects studied in this work have been classified into two categories – linear shunts and non-linear shunts or defects. Classifying the shunts and defects can aid better optimization of the HBLs through the deposition processes. The proportionality analysis mentioned in section 6.3.3 has been applied to local hot-spots to plot the local J-V curves of the shunts observed in the sample shown in Figure 68. The qualitatively fitted J-V curves of the three local regions of interest (ROIs) hence obtained, are presented in Figure 68b-d.

The non-linear shape of the J-V curve and the onset voltage in the forward bias (~0.6 V) of ROI1 (Figure 68b) exhibit non-linear exponential behavior of the spot and hence can be stated as a non-ohmic diodic type shunt. This spot could be a result of non-uniformity in the TiO_2 film or foreign dirt-particles. The perfectly linear shape of the J-V curve of ROI2 (Figure 68c),

on the other hand, indicates a pure ohmic behavior of the spot, hence an ohmic shunt. The ohmic shunt is a result of direct contact of the FTO and µ-graphite, suggesting a pin-hole in the deposited TiO_2 HBL film, which would be detrimental in this case for complete cells, aiding direct electron-hole recombination. A hot-spot-free third region ROI3 was analyzed, whose local J-V curve is presented in Figure 68d. As explained in section 6.3.3, the diode-like shape of this curve is based on the Schottky diode configuration of the sub-cell. The J-V curve of ROI3 represents the desired behavior expected from a uniform, compact TiO_2 film. This local J-V curve analysis method can be used to determine the contribution of each individual shunt spot on the behavior of the whole sample. Thus, apart from straight-forward detection of the presence of shunts in the HBL through reverse bias, DLIT can be importantly used to identify the type of shunts. Thus, more profound knowledge of the HBL structure, presenting partially shunted or defected areas are given.

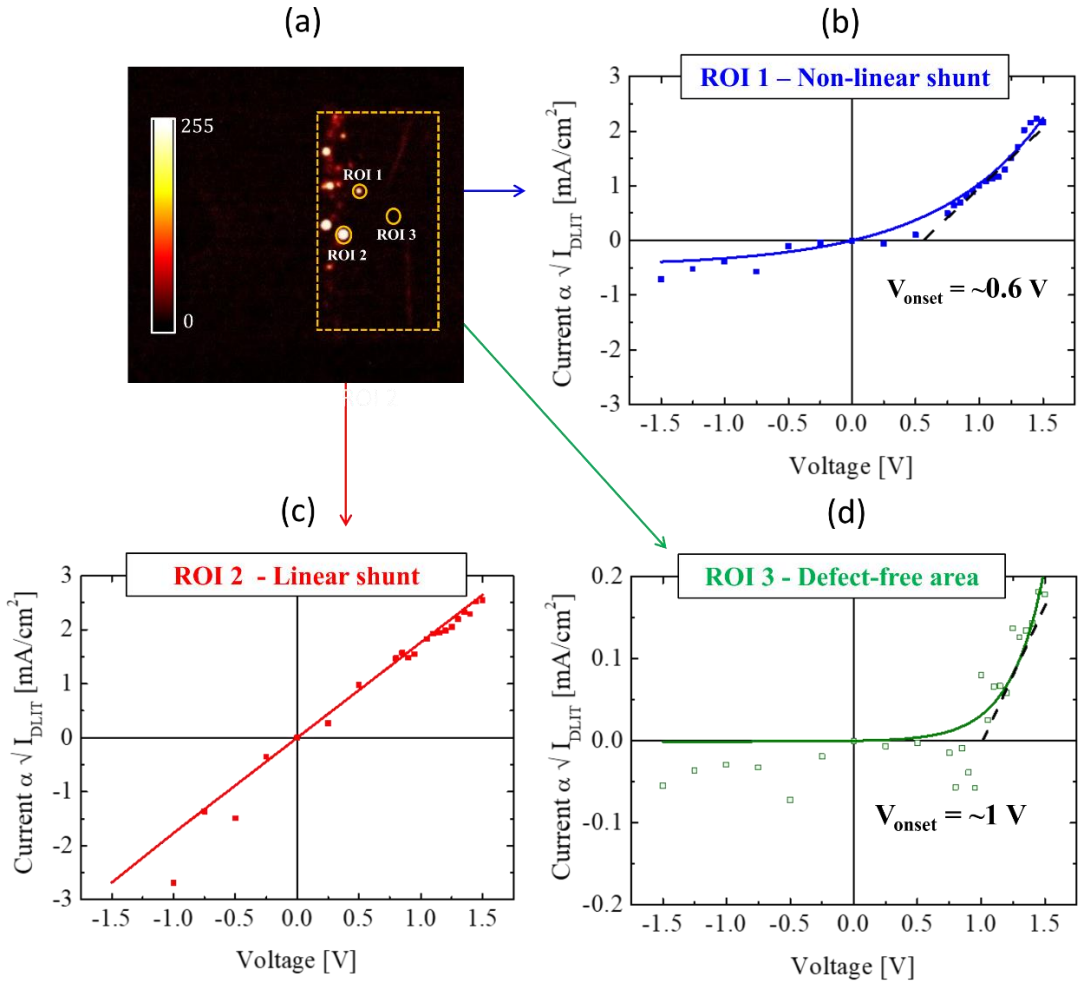

Figure 68: (a) DLIT image of an FTO/HBL/ µ-Graphite sample measured at 1V. Qualitative local I-V curves of the shunt spots derived from DLIT for three ROIs, (b) ROI 1 (c) ROI 2 and (d) ROI 3. Max. shunt detection resolution = 20 µm.

6.3.6 Sub-cell analysis of different HBLs through DLIT

To identify a reliable (pin-hole free) technique for deposition of TiO_2 hole blocking layers, FTO/HBL/ μ-graphite structured samples with different HBL deposition typologies - ALD, SPD, and Sputtering - have been fabricated and characterized using DLIT. The DLIT results of a reference sample in each typology are presented in Figure 69a-d. For each typology, DLIT images in reverse bias (- 1 V) and forward bias (+ 1 V) is shown. As explained in the section 6.3.4, linear/ohmic shunt points are displayed both in -1 V and +1 V DLIT image. Additionally, the non-linear defects in the layer are also shown in +1 V DLIT. Here, the bias voltage of 1 V is chosen, such that a bright DLIT intensity is obtained. Bias voltage and integration time determine the right quality image with a high signal-to-noise ratio. The selected values should not either be too low as the intensity of the DLIT also will be low or too high that it damages the sub-cell. For the measurements shown here, an integration time of 2 min was chosen.

Although the DLIT image at reverse bias displays purely ohmic shunts, it does not entirely represent the shunt behavior of the sample. However, from DLIT images at a reverse bias (shown in Figure 69a-d), it is inferred that the ohmic shunt densities in all the three typologies are negligible. The DLIT images at a forward bias(Figure 69a-d) gives us additional information about the non-linear shunts in the HBL. The ALD-TiO_2 film (Figure 69c) displays absolutely no singularly shunt spots denoting a very uniform, pin-hole free HBL. The signal gradient across the active area is attributed to uniform heat dissipation due to a forward current onset at voltage < 1 V (Figure 69e). The sputtered-TiO_2 film (Figure 69b) displays distributed defect spots in the forward bias but no shunts on the revere bias. It is suggestive of the fact that the sputtered HBL has a pin-hole free coverage, which is, on the contrary, a non-uniform film revealed by the DLIT image at forward bias. The SPD-TiO_2 film can also be said to be uniform with almost negligible pin-holes (Figure 69d). On the whole, it is deduced that the ALD and SPD processes produce a more uniform TiO_2-HBL as compared to the sputtering method.

The DLIT images are compared with the corresponding dark J-V curves shown in Figure 69e. High forward current density or a lower current onset voltage means back-flow of electrons from the FTO to the graphite via the HBL or holes from the μ-graphite to the FTO, which defeats the function of the HBL and is undesirable. From the J-V curves in Figure 69e, higher values of forward onset voltage for SPD and Sputtered TiO_2 films indicate better blocking properties than of the ALD-TiO_2 film [57].

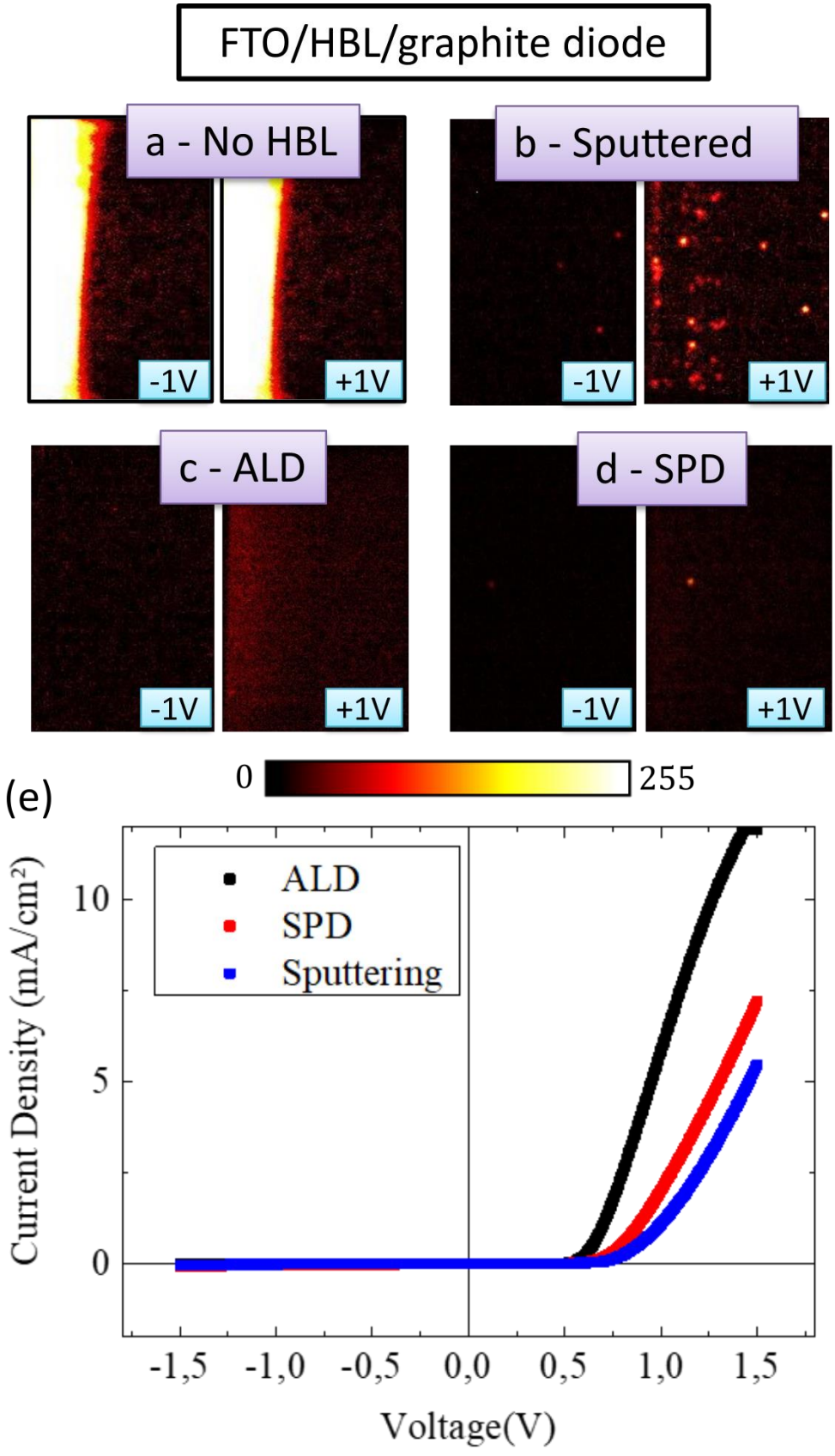

Figure 69: Reverse bias and forward biased DLIT images of sub-cell FTO/HBL/ µ-graphite (a) No HBL (b) Sputtered (c) ALD and (d) SPD and (e) Dark J-V curves of the sub-cells shown in (b), (c) and (d). Max. shunt detection resolution = 20 µm.

Three sub-cells from each HBL processing technique were accessed to see the dependency of defects with the processing techniques. The result shown in Figure 70 shows that the densities of errors in all typologies seem to be independent of the deposition process.

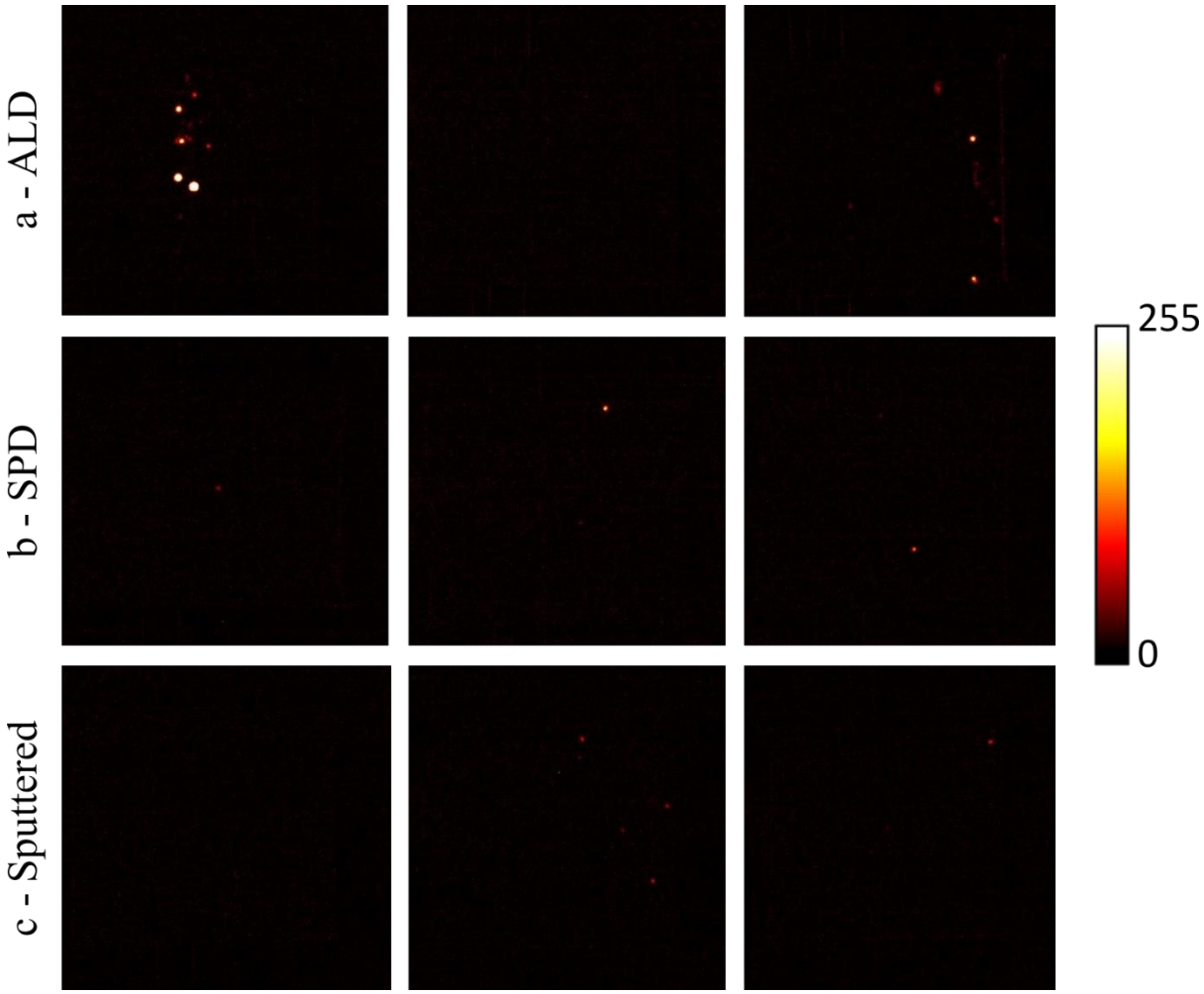

Figure 70: DLIT images at 1V for sub-cells (FTO/HBL/µ-graphite) processed from different HBL processing techniques. Three sub-cells were analyzed in each sub-cell category (a) ALD, (b) SPD, and (c) Sputtered HBL. Max. shunt detection resolution = 20 µm.

Thus, the results from the sub-cell analysis show that all the deposition technique works well as HBL with no linear shunt points. However, more non-linearities were found in the sputtering technique owing to the non-uniformity of the nano-thin layer on FTO. Surprisingly, a high forward onset voltage was observed for the sputtering technique, and the undesired low forward onset voltage was found for the ALD process.

6.3.7 Complete device fabrication with c-TiO_2 processed with various deposition techniques

Complete devices were fabricated with steps, as described in section 6.2.3. The average electrical parameters are compared in Figure 71. An average high voltage of 907 mV is observed in SPD. However, with high Jsc and FF, the average device performance of the ALD is shown to be better with average PCE of 10.7 %.

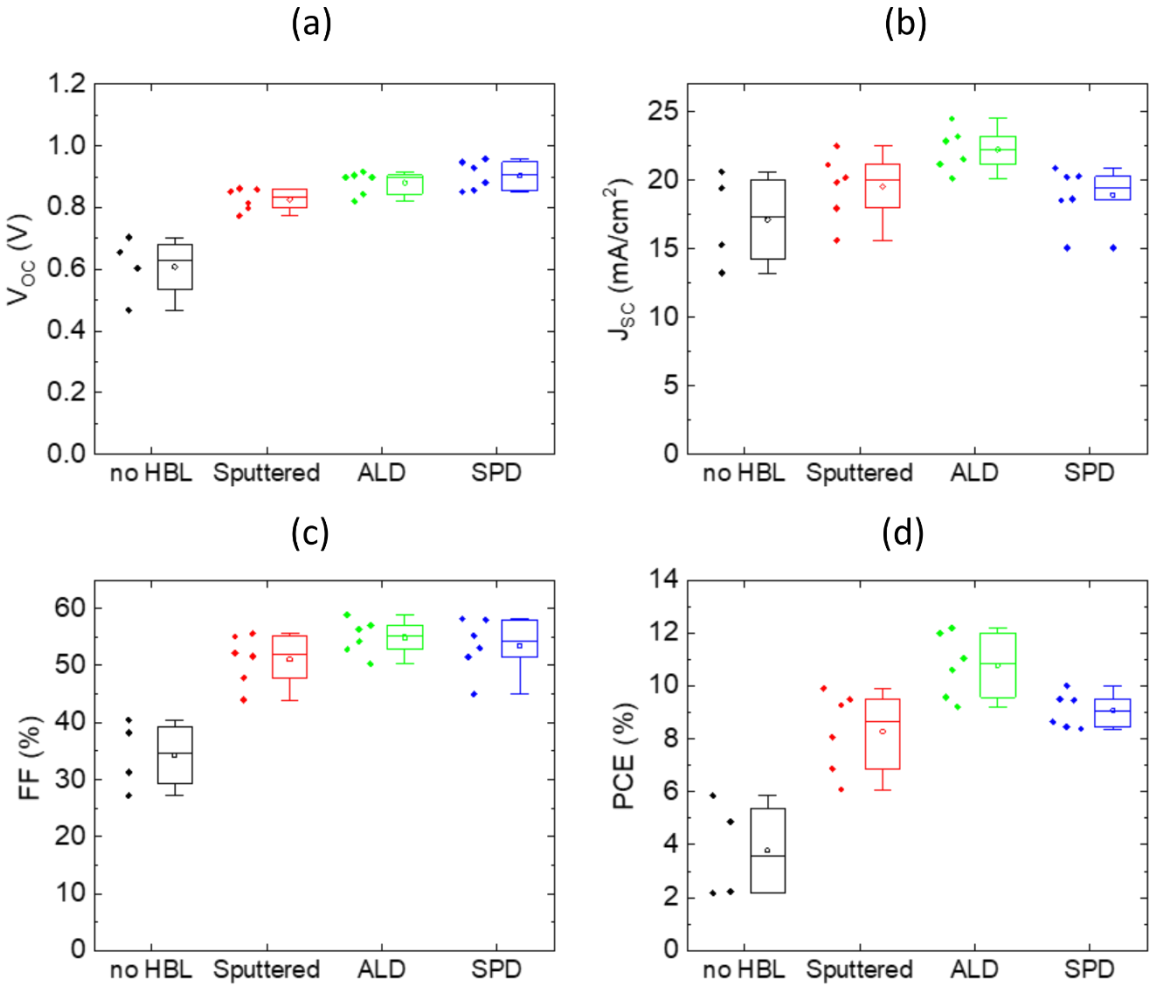

Figure 71: Average electrical parameters of complete devices with HBL processed using various deposition techniques (a) V_{OC} (b) J_{SC} (c) FF and (d) PCE.

6.3.8 Stable Voltage and open-circuit voltage decay (OCVD) measurement

To further understand the recombination at the FTO/perovskite interface, the stable voltage, along with OCVD measurements, were investigated. A high stable voltage of 925 mV was observed for devices with SPD processed c-TiO_2. It can be noticed that there is a difference between the initial and the final voltage in the stabilized voltage measurements in PSCs. It was also observed in other PSC architectures (as shown in section 7.3.3.2). The low stable

voltage for a sputtered c-TiO_2 is well in agreement with the result from DLIT. As predicted, the backflow of electrons from FTO to the VB of perovskite is higher in the absence of an HBL with a low voltage of 747 mV (Figure 72a).

A similar trend has been observed in the OCVD measurements. The basic interpretation of OCVD analysis for PSCs is discussed in section 4.2.4.1. Figure 72b shows the OCVD measurement for 10 min. Comparatively, the charges in the sputtered HBL recombine faster, as also seen from DLIT results. It is to note that it took around 50 s for the voltage to reach 0 V in a no HBL device. Analyzing in the range of few tens of seconds (< 20 s), the device without HBL does not reach 0 V as soon as the illumination is off. It shows that without HBL, there are no ohmic shunts. Still, their absence evolves to a high amount of non-radiative recombination due to the backtracking of electrons toward the perovskite. And this recombination has been suppressed with a thin conformal coating of c-TiO_2.

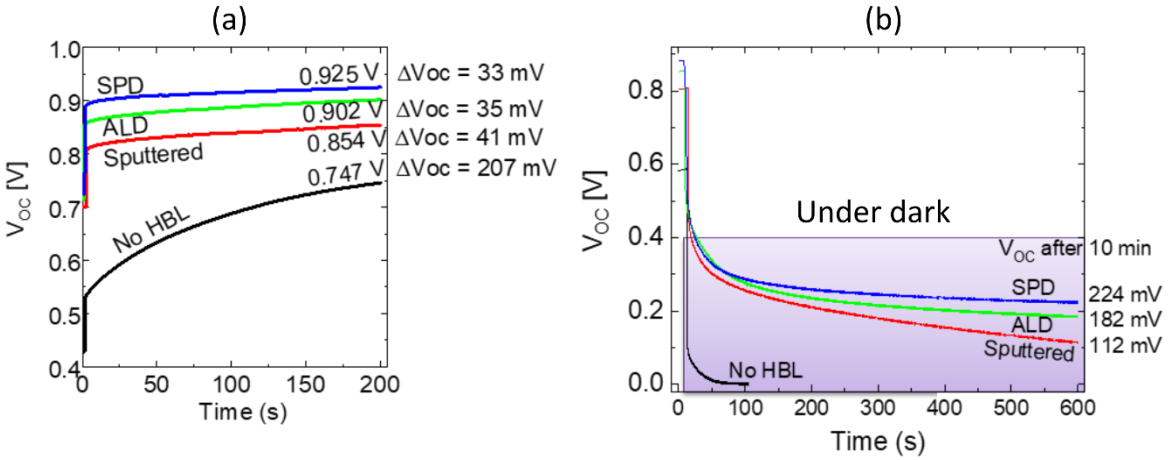

Figure 72: Stable V_{OC} measurement and (b) OCVD measurement

6.3.9 Stable device performance

After analyzing the recombination at the FTO/perovskite interface, the complete device performances are analyzed through stable MPP measurements. A high stable PCE of 10.1 % has been achieved for the devices with ALD c-TiO_2 (Figure 73). With high forward current and low onset voltage (Figure 69e) in an ALD processed sub-cell, its complete device was thought to perform poorly. However, considering the interface change of the ALD processed HBL from µ-graphite (in case of sub-cell) to mp-TiO_2/perovskite (in complete devices) could mean that

ALD of a nano-thin HBL has a uniform low series resistance with enhanced charge extraction. The same has been reflected in the average electrical parameters through high J_{SC} and FF.

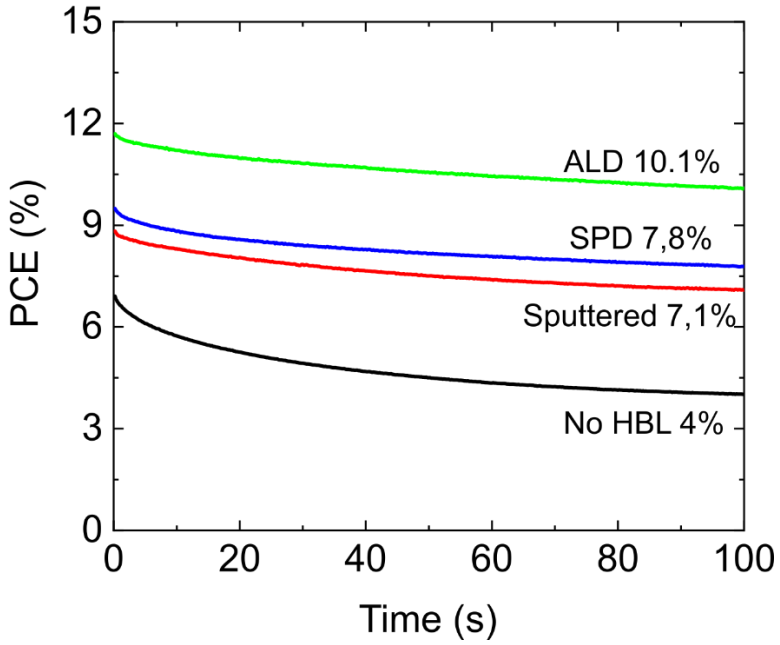

Figure 73: Stable PCE of complete devices whose HBL is processed with different deposition techniques.

6.4 Conclusion

To conclude, compact TiO_2 films deposited using different methods, including Atomic Layer Deposition, Spray Pyrolysis Deposition, and sputtering have been investigated. A sub-cell configuration (FTO/c-TiO_2/ μ-graphite) was used to analyze the physical and electrical quality of the HBL layer. The results were also compared with devices having no HBL. Notably, a Dark Lock-in Thermography tool has been used for shunt identification and analysis of the qualitative local J-V curves of the shunt spots to determine the linear and non-linear attributes of the defects present in the HBL layer.

Sub-cell analysis from SEM and AFM show that a conformal coating of HBL was achieved with all the investigated deposition techniques. Additionally, shunt detection through the DLIT image under reverse bias also revealed the same. The forward biased DLIT analysis showed a lot of non-linear defects in a sputtered HBL layer. Thus, the TiO_2-films formed by ALD and SPD methods are more uniform and reliable in comparison to the sputtered HBL. Dark J-V curve of the sub-cells revealed that ALD has a low onset voltage, which is an undesired quality of an HBL.

Surprisingly, complete perovskite solar cells fabricated with ALD resulted in a highly stable efficiency of 10.1 % owing to high J_{SC} and FF. Even though better recombination resistance at FTO/perovskite interface was observed for SPD processed HBL through OCVD measurements, the device performance was higher for the device with ALD processed c-TiO_2.

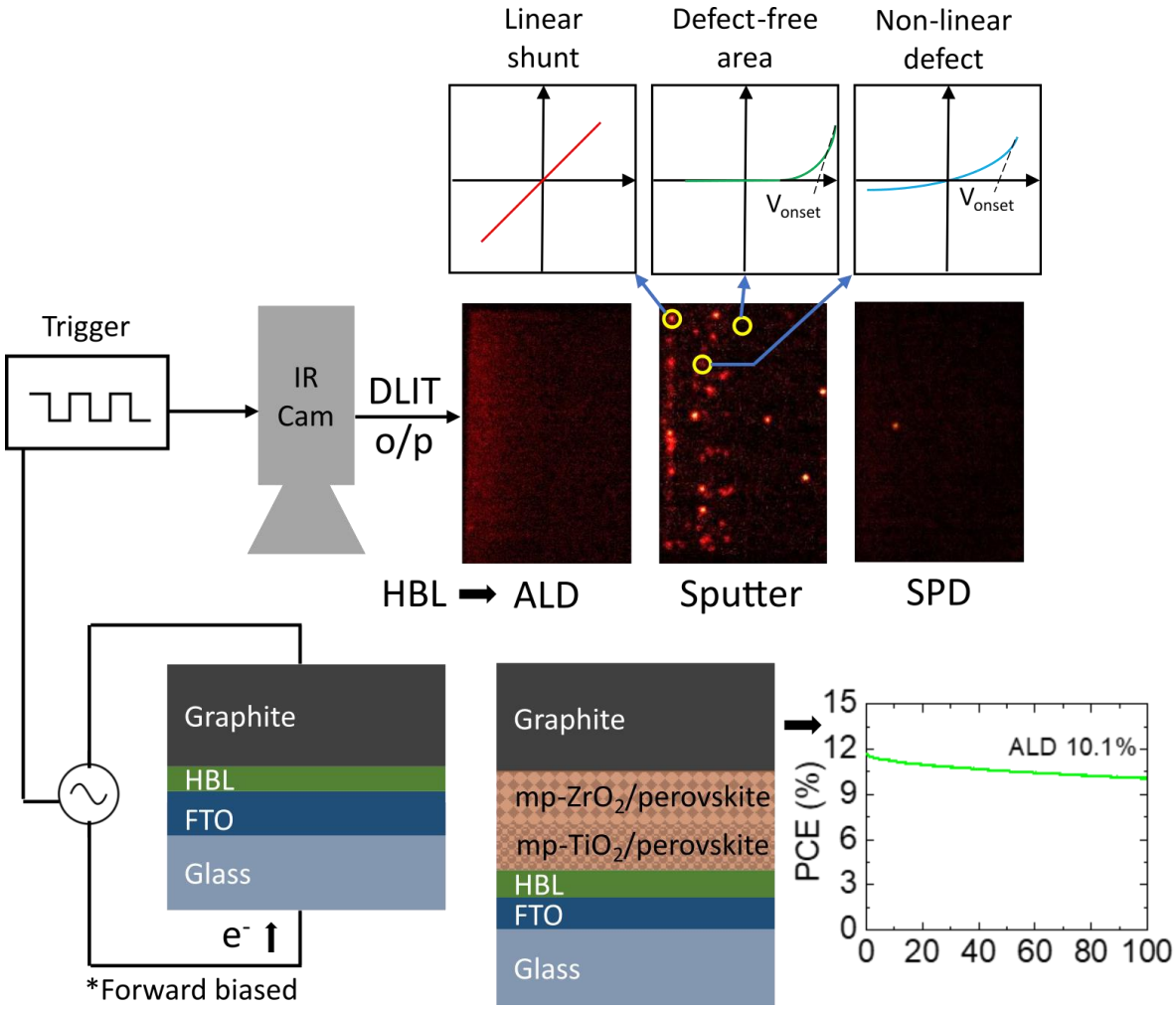

Figure 74: Summary diagram for Chapter 6 showing the sub-cell configuration that was measured under DLIT and its interpretation that led to suppression of non-radiative recombination at FTO/perovskite interface.

Chapter - 7

Analysis and optimization of mp-TiO_2/carbon-graphite interface with sputtered Al_2O_3 ultra-thin insulation layer in carbon-based perovskite solar cells

7 Analysis and optimization of mp-TiO_2/carbon-graphite interface with sputtered Al_2O_3 ultra-thin insulation layer in carbon-based perovskite solar cells

The electrically insulating space layer takes a fundamental role in monolithic carbon-graphite based perovskite solar cells (PSCs), and it has been established to prevent the charge recombination of electrons at the mp-TiO_2/carbon-graphite (CG) interface. Thick 1 µm printed layers are commonly used for this purpose in the established triple-mesoscopic structures to avoid ohmic shunts and to achieve a high open circuit voltage. In this work, a reproducible large-area procedure was developed to replace this thick space layer with an ultra-thin dense 40 nm sputtered Al_2O_3, which acts as a highly electrically insulating layer preventing ohmic shunts. Herewith, transport limitations related so far to the hole diffusion path length inside the thick mesoporous space layer have been omitted by concept. It will pave the way towards the development of next generation double-mesoscopic carbon-graphite based PSCs with high efficiencies.

Scanning electron microscope (SEM), energy dispersive x-ray analysis (EDX), and atomic force microscopy (AFM) measurements show the presence of fully oxidized sputtered Al_2O_3 layer forming a pseudo-porous covering of the underlying mesoporous layer. The thickness has been finely tuned for the achievement of both electrical isolation and optimal infiltration of the perovskite solution allowing full percolation and crystallization. Photo voltage decay, light-dependent, and time-dependent photoluminescence measurements showed that the optimal 40 nm thick Al_2O_3 not only prevents ohmic shunts but also efficiently reduces the charge recombination at the mp-TiO_2/CG interface and, at the same time, allows efficient hole diffusion through the perovskite crystals embedded in its pseudo-pores. Thus, a stable V_{OC} of 1 V using $CH_3NH_3PbI_3$ perovskite has been achieved under full sun AM 1.5 G with a stabilized device performance of 12.1%.

The results shown in this chapter are based on the article published by the author of this thesis in ACS Applied Nano Materials under the title "Double-mesoscopic Hole-Transport-Material-Free Perovskite Solar Cells: Overcoming Charge-Transport Limitation by Sputtered Ultra-Thin Al_2O_3 Isolating Layer" [187]. The results are based on the devices that I produced at Fraunhofer ISE.

7.1 Introduction

The necessity of replacing Spiro-OMeTAD with CG as a counter electrode to reduce production cost and improve stability has been introduced in section 2.2.4. This change in architecture leads to the introduction of the insulation layer. Its role, details regarding the commonly used mesoporous thick insulation layer (ZrO_2), and other developing insulation layer material (Al_2O_3) have been already discussed in chapter 2.2.4 and 2.3.4. Further status-quo on the stability analysis of this architecture was also included in those sections.

In this work, for the first time a cell architecture is presented in which a thick mesoscopic space layer is avoided by using an ultra-thin sputtered Al_2O_3 as an insulator to prevent direct electrical contact between ETL and CG, giving rise to double-mesoscopic PSCs. Figure 75a shows the focused ion beam cut cross-sectional scanned electron microscope (FIB-SEM) image of this new device architecture before the filling of the perovskite and the magnified cross-section of the mp-TiO_2/Al_2O_3 interface is shown in Figure 75b. The energy level alignment of the material stack is depicted through the energy band diagram in Figure 75c [79,83,85].

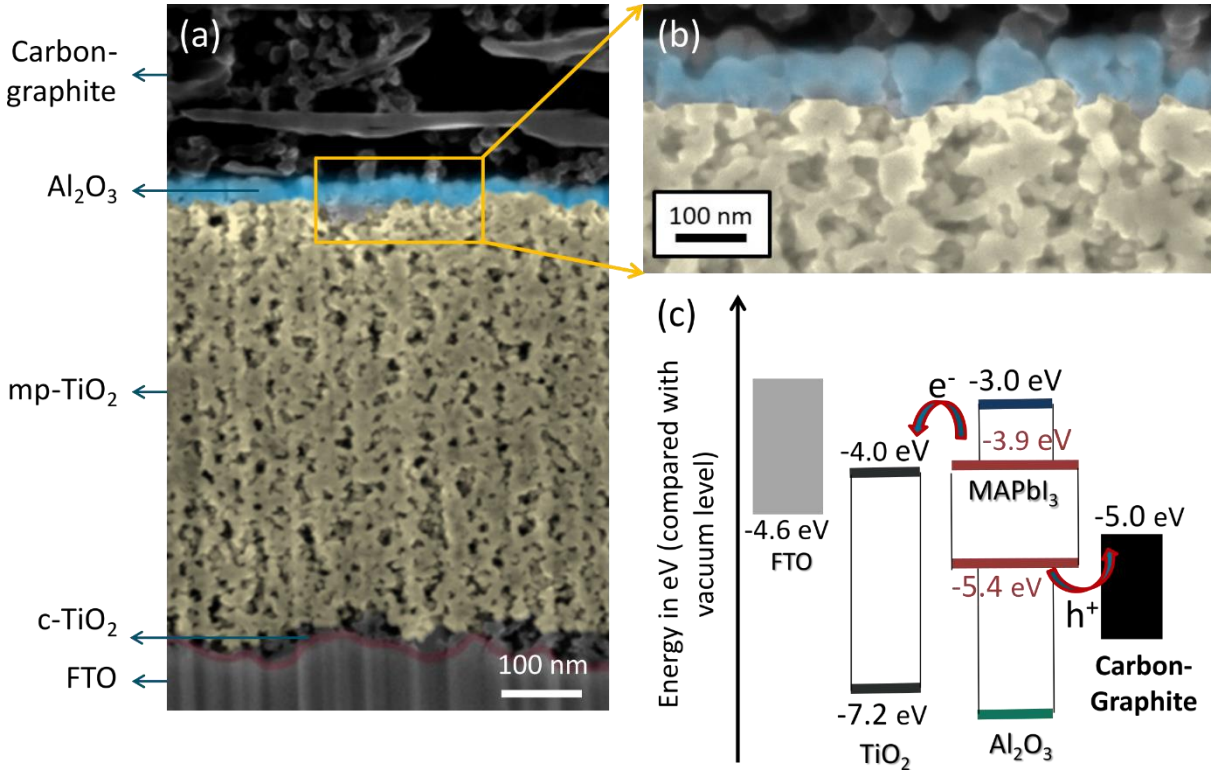

Figure 75: (a) FIB-SEM image of an unfilled double-mesoscopic carbon-graphite CG-PSC developed in this work (b) Magnified image of an mp-TiO_2/Al_2O_3/CG interface (c) Energy band diagram. Figure reproduced from publication [187].

As explained, the function of the thin insulating Al_2O_3 layer is to prevent the electrical connection of electrons in the mp-TiO_2 to the CG that creates direct shunt and recombination pathways. To differentiate from the widely used triple-mesoscopic architecture in the literature (mesoporous ETL, thick mesoporous isolation layer, mesoporous counter electrode), hereafter, we refer to our structure as double-mesoscopic PSCs (mesoporous ETL, sputtered thin isolation layer, mesoporous counter electrode). Pictorial representation showing the architectural difference of a triple-mesoscopic CG-PSCs compared to a double-mesoscopic CG-PSCs is shown in Figure 76.

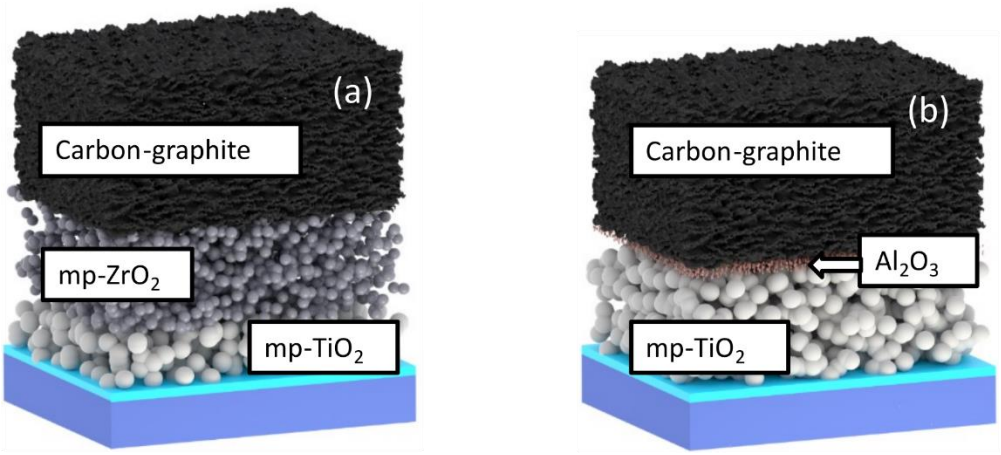

(a) Triple-mesoscopic CG-PSCs with µm-thick isolation layer (ZrO_2)

(b) Double-mesoscopic CG-PSCs with nm-thin isolation layer (Al_2O_3)

Figure 76: (a) Schematic representation of a triple-mesoscopic CG-PCSs with a micrometer thick screen printed mesoporous ZrO_2 sandwiched between mesoporous TiO_2 and carbon-graphite layer and (b) Schematic representation of a double-mesoscopic CG-PCSs with a nanometer thin sputtered pseudo-porous Al_2O_3 sandwiched between mesoporous TiO_2 and carbon-graphite layer. Figure reproduced from publication [187].

Results from optimizing the isolation layer thickness in the range between 10 nm and 100 nm show that 40 nm already guarantees optimal film quality to avoid any ohmic shunt. It achieves a high and stabilized V_{OC} of 1 V and stabilized power conversion efficiency (PCE) of 12.1%, thanks to the control of charge recombination at the mp-TiO_2/CG interface. A new technique to investigate the electrical properties of the isolation layer in an unfilled device is illustrated. Further investigation on the charge extraction ability of a filled device was observed by space resolved photoluminescence (PL) quenching. The combination of these two techniques provides new insight about ohmic shunt detection in unfilled devices and recombination suppression at the mp-TiO_2/CG interface in perovskite filled devices. Conclusively, through this section, a discussion is opened if a thick space layer (*i.e.*,> 0.5 µm) is detrimental for the efficient performance of CG-PSCs, and the new double-mesoscopic CG-PSC architecture is introduced.

7.2 Device fabrication

The FTO glasses were cleaned, as mentioned in section 6.2.1. A compact layer of TiO_2 (c- TiO_2) of 20 nm was sputtered, as given in section 3.1.2.2. 1.5 µm of mp-TiO_2 was screen printed and sintered at 500°C for 30 min. Different thicknesses of Al_2O_3 were sputtered using the parameters mentioned in section 3.1.2.3 and sintered at 500°C for 30 min. Then, a carbon-

graphite (CG) counter electrode of a thickness of 8 µm was screen printed and sintered at 400°C for 30 min. The process parameters for screen printing TiO_2 and CG were already defined in section 3.5.1. Finally, 1.2 M 1-step perovskite solution was prepared by mixing 1.106 g of PbI_2, 3.624 g of MAI, and 0.0294 g of 5-AVAI in 2 ml GBL. 4.5 µl of the solution was drop casted into each device. The devices were kept in an enclosed space by covering using a glass lid during its wait time at room temperature for 30 min. It is then transferred to a hot plate of 50° C. The cells are still kept closed within the glass lid on the hot plate for 30 min. The lid is then opened, and the cells are further annealed for 1 h at 50° C. Keeping the cells in a closed space at RT allows efficient spreading and percolation of the precursor solution into the stacks. Further, annealing in a closed space prevents fast perovskite crystallization. It additionally facilitates enhanced pore filling of the thick mesoporous TiO_2 layers.

7.3 Results and discussion

7.3.1 Sub-cell characterization of ultra-thin sputtered Al_2O_3 layer

The sub-cell characterization involves analyzing the Al_2O_3 sputtered layer either on the Si wafer or on the mp-TiO_2 layer. Various characterizations such as SEM, AFM, TEM, and contact angle measurements are shown to identify the crystalline nature, roughness, and porosity of the sputtered layer. The comparison between sputtering Al_2O_3 on Si wafer and mp-TiO_2 shows that the sputtered layer adapts to the morphology of the underlying layer. This section also shows the importance of the sintering of the Al_2O_3. It is also analyzed using a sub-cell configuration for a strong understanding.

7.3.1.1 SEM, AFM and TEM analysis comparison of sputtered 10 nm Al_2O_3 on Si wafer and mp-TiO_2

In this work, sputtered Al_2O_3 as the isolating layer in CG-PSCs was chosen to achieve ultra-thin and conformal covering for the fabrication of an insulation layer in carbon-graphite based perovskite solar cells (CG-PSCs). Thus, a manufacturing technique that can allow the transition to larger-scale production was chosen. Many literature reports show that the layers achieved using the sputtering technique is compact in nature [72,188,189]. However, it is demonstrated here that the compactness for a very thin layer is governed by the underlying layer onto which they are sputtered. A sputtered layer on a flat substrate and on a mesoscopic layer was examined to study the difference in morphology. Figure 77 shows the top-view scanned electron

microscope (SEM) image of a 10 nm Al_2O_3 sputtered on top of Si substrate (Figure 77a) and on mp-TiO_2 (Figure 77c). Their corresponding atomic force microscopy (AFM) images are shown in Figure 77b and Figure 77d. Both SEM and AFM reveal that the Al_2O_3 sputtered on a mesoporous layer is less dense, mirroring/adapting to the morphology of the underlying mp-TiO_2 layer. Thus, as observed, a pseudo-porous layer is formed when a compact layer adapts to the porosity of the underlying porous layer. The change in the morphology of the sputtered layer facilitates the infiltration of the perovskite precursor solution that is drop casted as the last step in the CG-PSCs production.

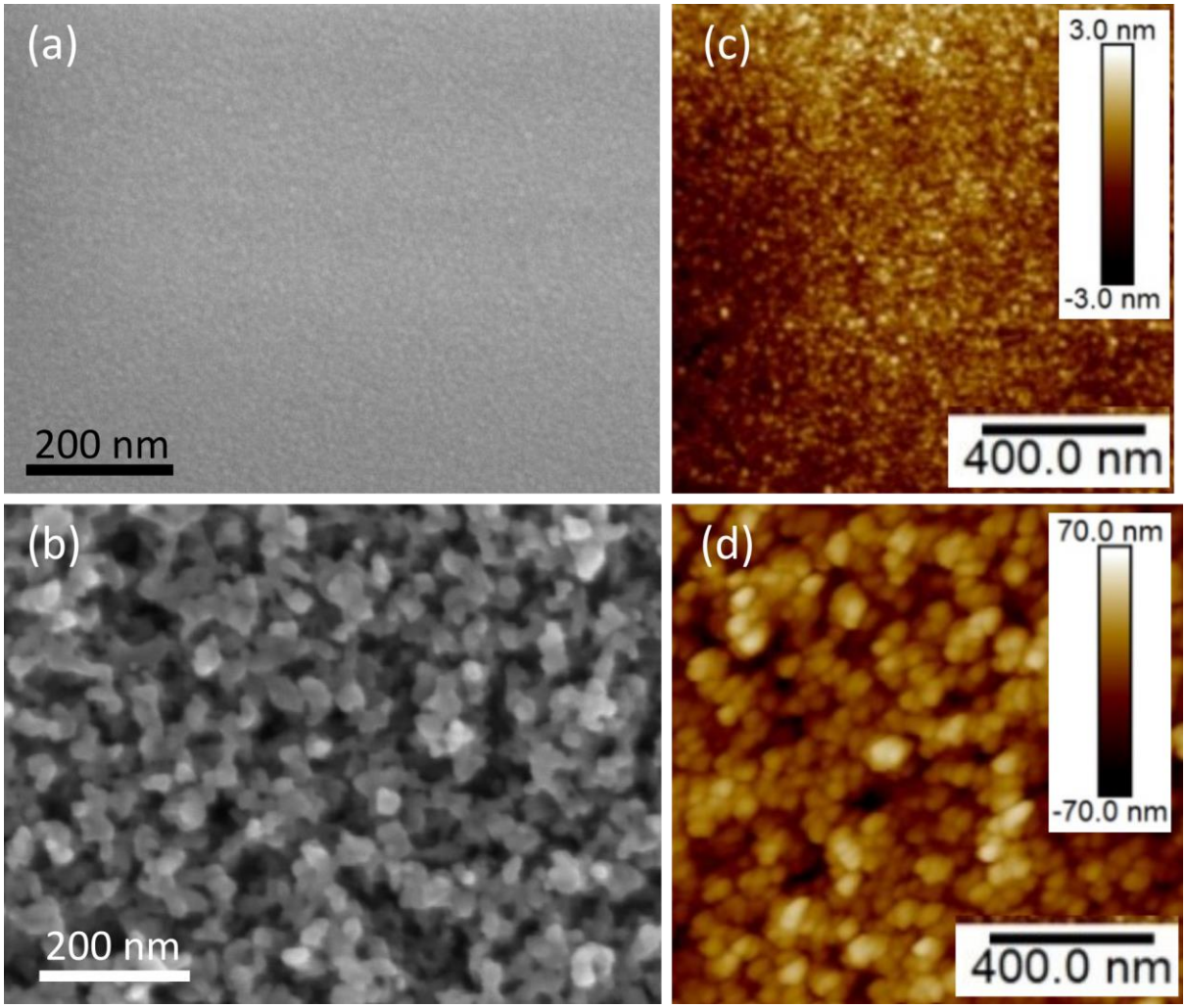

Figure 77: (a) Top-view SEM image of sputtered 10 nm Al_2O_3 on a flat Si-wafer surface (b) AFM of sputtered 10 nm Al_2O_3 on Si with color scale ± 3 nm (c) Top-view SEM image of sputtered 10 nm Al_2O_3 on mp-TiO_2 (d) AFM of sputtered 10 nm Al_2O_3 on mp-TiO_2 with color scale ± 70 nm. Figure reproduced from publication [187].

The crystalline property of the sputtered Al_2O_3 was investigated through a transmission electron microscope (TEM) and X-ray diffraction in grazing incidence mode (GIXRD). The TEM image in Figure 78a shows the surface facets of the TiO_2 nano-crystals (as parallel lines), indicating the presence of crystalline TiO_2 layer. A non-defined layer surrounding the parallel lines defines the presence of an amorphous Al_2O_3 layer. The elements present in the layer are shown in Figure 78b through the energy dispersive x-ray (EDX) analysis. The presence of an Al_2O_3 layer is confirmed by the presence of an Al peak (as seen in Figure 78b). Additional Al_2O_3 property analysis was carried out using GIXRD. No sharp peak present in the GIXRD mapping (Figure 78c) confirms that the sputtered Al_2O_3 is amorphous. Interesting to note is that this thin and conformal covering layer is enough to isolate the TiO_2 nanoparticle from the electrical contact with the flaky nature of the carbon-graphite electrode.

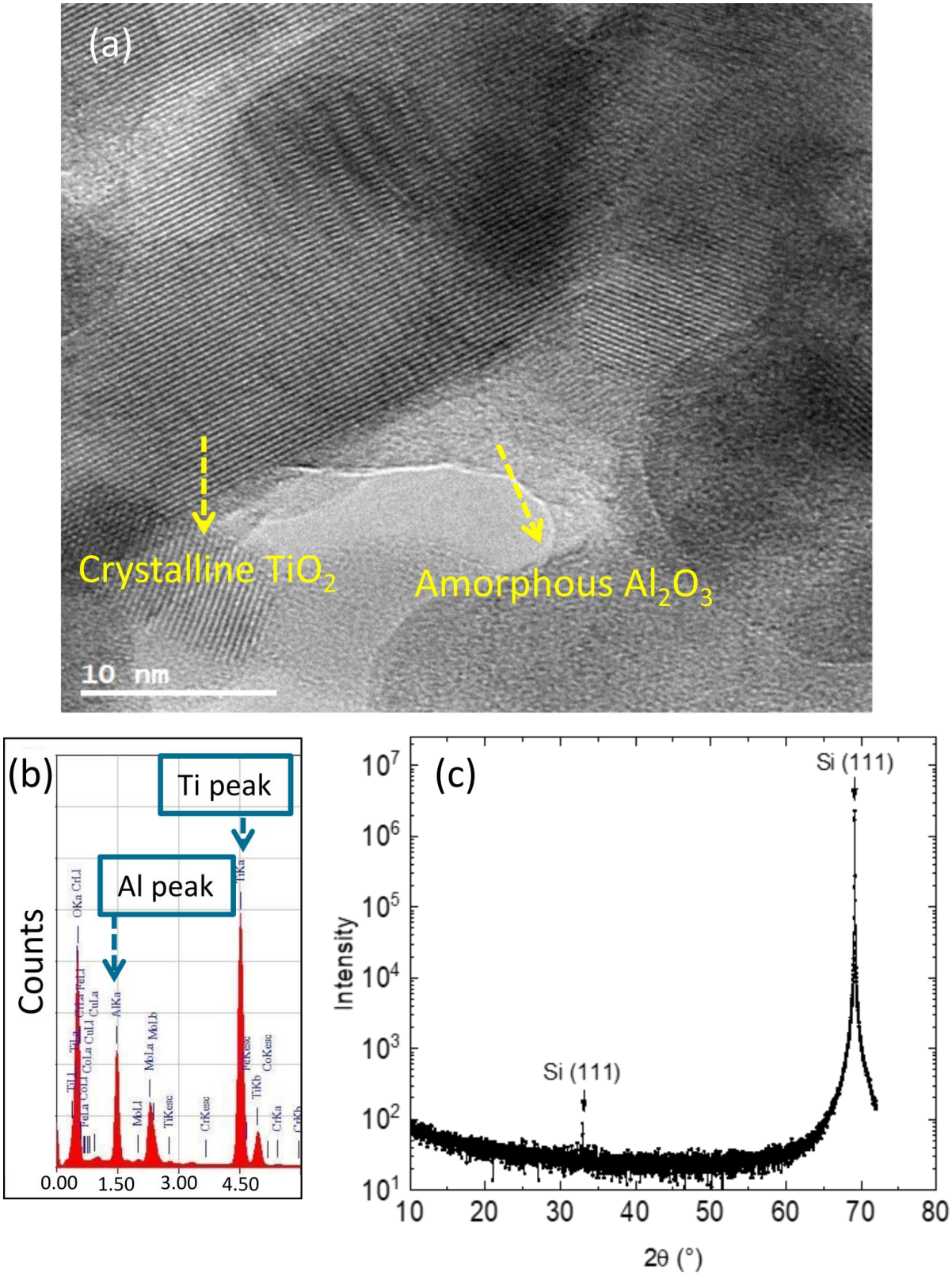

Figure 78: (a) TEM image of mp-TiO_2/10 nm Al_2O_3 (b) Elemental analysis using EDX in TEM (c) GIXRD of Si/100 nm Al_2O_3. Figure reproduced from publication [187].

Sintering effects in sputtered Al_2O_3

To achieve insulating properties and for better light absorption, it is essential to fabricate a transparent and completely oxidized Al_2O_3 layer. Thus, to ensure complete oxidation, the sputtered layers were sintered at 500° C for 30 min. To compare the surface topology of the sintered and non-sintered layers, Atomic force microscopy (AFM) and SEM images were captured for 100 nm Al_2O_3 sputtered on a Si wafer. The resulting images from the optical measurements (AFM and SEM) show the increase in particle size after sintering. Qiang *et al.* show that this increase in the size of crystals with low surface energy is a result of decreased internal strain caused during sintering [190]. The cross-section SEM images, together with its AFM images in the inset, are shown in Figure 79a and Figure 79c for non-sintered and sintered Al_2O_3 layers, respectively. These, along with its corresponding magnified specific spot image in Figure 79b and Figure 79d, shows that the layer properties have visibly changed after sintering, showing pseudo-porous Al_2O_3 layer.

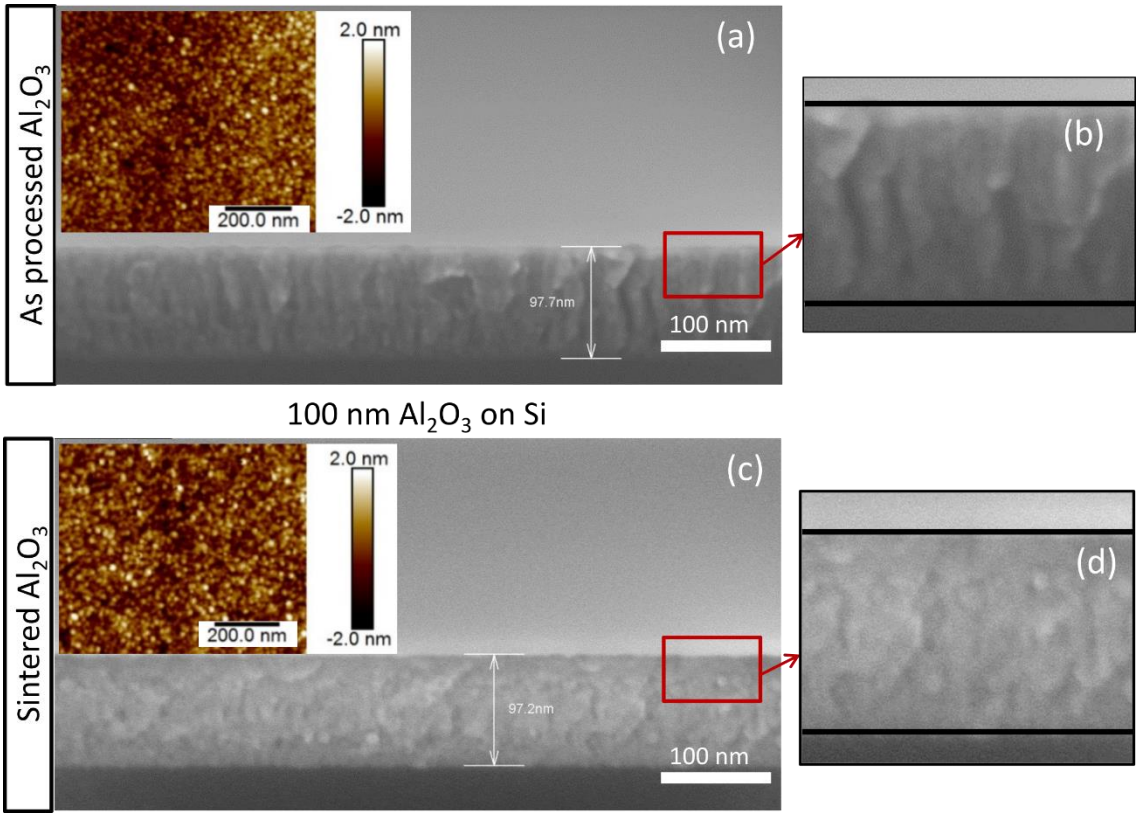

Figure 79: (a) Cross-section SEM image of as processed 100 nm Al_2O_3 sputtered on Si wafer. Inset shows the top view of the AFM image. (b) Magnified image of a section in (a). (c) Cross-section SEM image of sintered 100 nm Al_2O_3 sputtered on Si wafer. Inset shows the top view of the AFM image. (d) Magnified image of a section in (c). Figure reproduced from publication [187].

7.3.1.2 Thickness optimization of sputtered Al_2O_3 layer on mp-TiO_2

SEM images of the different Al_2O_3 thicknesses on mp-TiO_2 in tilted and cross-sectional view are shown in Figure 80. The porosity of the mp-TiO_2 layer is noticeable in the SEM of the layer stack without Al_2O_3 (w/o SL) (Figure 80a). Additionally, it is clearly visible in Figure 80b-d that the sputtering leads to the formation of an Al_2O_3 layer with high open porosity at 10 nm and nearly closed particle boundaries at 100 nm as a result of the dense Al_2O_3 structure growth. It is important to allow complete infiltration and homogenous crystallization of the perovskite solution in the cell stack. It ensures efficient light-harvesting and efficient charge transfer thanks to the electrical coupling of perovskite crystals with the cathode. Therefore, it is expected that the Al_2O_3 thickness increase will hinder the infiltration of the perovskite precursor solution from filling the underlying mesoporous layer and thereby resulting in lower photocurrent.

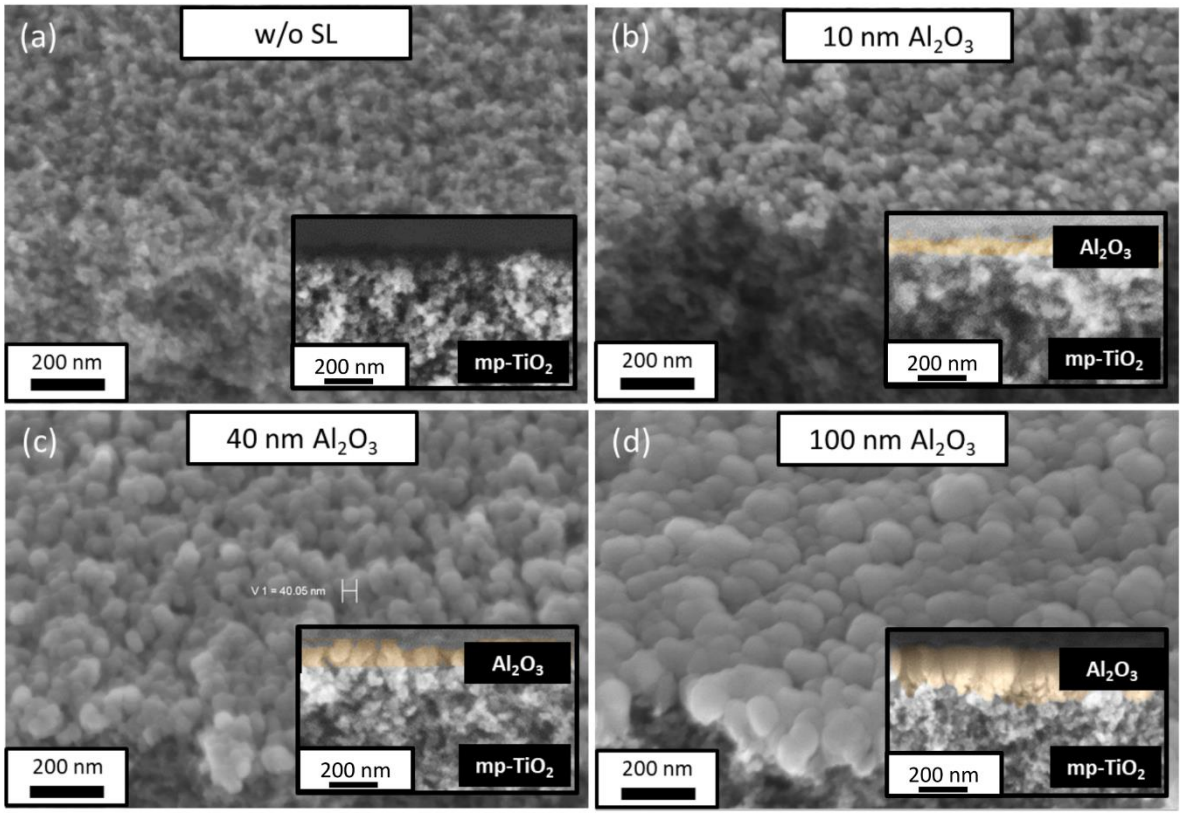

Figure 80: Tilted SEM images of different Al_2O_3 thicknesses sputtered on 1.5 µm of mp-TiO_2 (a) No Al_2O_3– referred to as w/o SL (b) 10 nm Al_2O_3 (c) 40 nm Al_2O_3 and (d) 100 nm Al_2O_3. Corresponding cross-sectional images are seen in the inset. Figure reproduced from publication [187].

Detailed information on CA measurements on different thicknesses of Al_2O_3 is shown in Figure 81. Figure 81a shows the representative image captured under a CA setup where CA is the contact angle, H is the height of the droplet formed on the layer under inspection, and BD is the base diameter of the droplet. The graph in Figure 81b shows the height of the droplet formed on the mp-TiO_2/Al_2O_3 layer measured over time, where DI water is used as the testing liquid. Figure 81c shows the series of images taken over time while the DI water is percolating in the mp-TiO_2/40 nm Al_2O_3 layer. No change was observed in the droplet's base diameter, indicating that the difference in droplet height (H) is not due to the spreading of the liquid but due to the liquid percolation into the underlying layer. This possibility of liquid infiltration through a sputtered layer is attributed to the pseudo-porosity formed when it is sputtered on a mesoporous underlayer, as explained under section 7.3.1.1. Lowest height of 0.17 mm and the fastest percolation time of 30 s are observed in the absence of a sputtered insulation layer (w/o SL). Introducing an ultra-thin 10 nm sputtered layer increases the bubble height to 0.32 mm, which has the lowest value comparing to other sputtered layer thicknesses.

Further increase in thickness affects the wetting and the liquid percolation (droplet height of 0.38 mm for 100 nm of sputtered Al_2O_3). The results indicate that devices with 100 nm Al_2O_3 could present with percolation difficulties due to their increased particle size. However, the possibility of percolation through these layers cannot be denied due to the observed droplet height decrease over time. Similar difficulties in percolation were also observed by Xiong *et al.,* where they had optimized their Al_2O_3 interlayer to 10 nm (real set thickness is 60 nm) vacuum evaporated between mp-TiO_2 and 1 µm ZrO_2 [85].

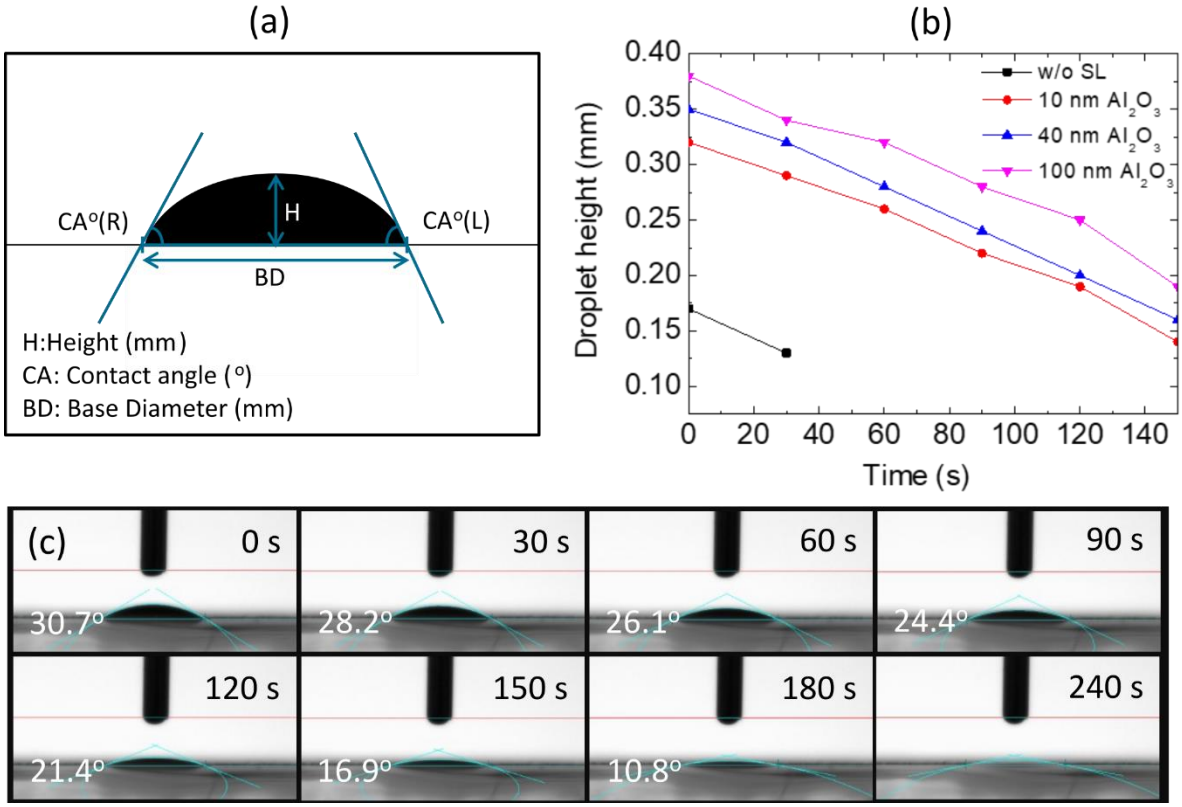

Figure 81: (a) Schematic representation of an image captured with the droplet on the layer of interest. (b) Graph showing the trend in decreasing the height of the droplet on different thicknesses of Al_2O_3 sputtered on 1.5µm mp-TiO_2 describing the solution percolation into the mp-TiO_2 layer. As expected, a fast solution percolation is observed in the absence of Al_2O_3 (w/o SL) (c) Series of photos of the contact angle measured for every 30 s for mp-TiO_2/40 nm Al_2O_3. Figure reproduced from publication [187].

7.3.2 Characterization of double-mesoscopic CG-PSC prior to perovskite infiltration

As explained before, perovskite infiltration is the last step in PSC fabrication. Thus, analyzing the electrical isolation over the mp-TiO_2/CG interface as a function of the thickness of the isolation layer independent of the interaction with perovskite was possible. For this purpose, the mp-TiO_2 layer itself had to be made conductive by direct photoexcitation over the bandgap of TiO_2 (3.2 eV) using UV light. Stevanovic et al. have recently explained the mechanism of such TiO_2 conduction. They are originating from the hopping of photoexcited electrons from illuminated to non-illuminated TiO_2 particles leading to electron diffusion as a result of an electron density gradient [191].

According to the varying thickness of Al_2O_3, our devices are named as 10 nm Al_2O_3, 20 nm Al_2O_3, 40 nm Al_2O_3, and 100 nm Al_2O_3. The unfilled electrode stack (c-TiO_2/mp-TiO_2/Al_2O_3/CG) with different thicknesses of Al_2O_3 was illuminated from the glass side using a UV-LED (365

nm). All devices shared the same structure with thicknesses as follows: 20 nm c-TiO_2/1.5 µm mp-TiO_2/Al_2O_3/8µm CG. Linear-scale J-V curves and the scheme of the experimental setup are shown in Figure 82a and Figure 82b, respectively. Figure 82c shows the absolute current in log scale plotted to its corresponding voltage to determine the points of lowest current at the respective photovoltage. For Al_2O_3 thicknesses above 40 nm, the current density over the space charge region at the mp-TiO_2/CG interface at V_{OC} is only in the range of a few nano amperes as a result of pin-hole free and an efficient isolating layer. Therefore, a high barrier potential against electron transfer to the CG counter electrode larger than 1.3 V is observed for Al_2O_3 thickness of more than 40 nm. It is similar in value to the theoretically achievable photovoltage of 1.34 V for the $CH_3NH_3PbI_3$ (MAPI) perovskite absorber [192] to be applied later in the full device.

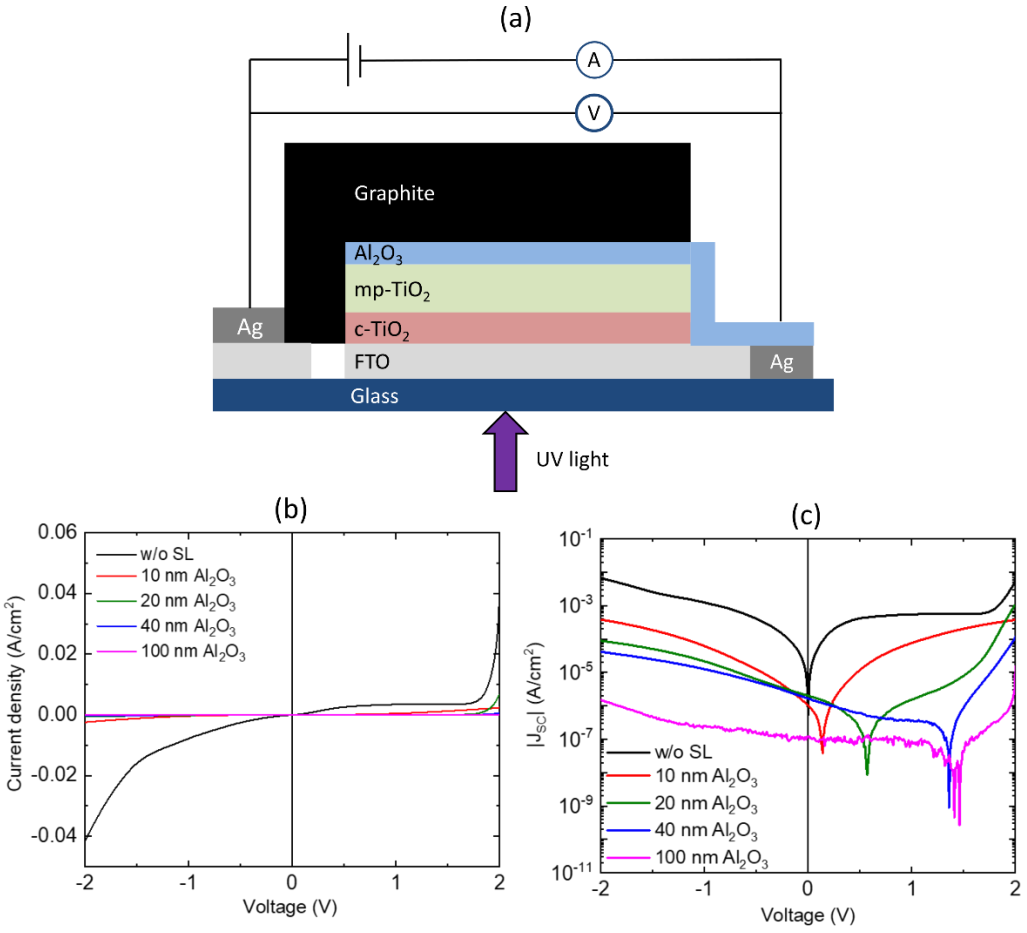

Figure 82: Shunt detection by analyzing the perovskite independent UV, induced photocurrent at the mp-TiO_2/CG interface. The current-voltage characteristics (J-V) curve of unfilled CG-PSCs (c-TiO_2/mp-TiO_2/Al_2O_3/CG) with varying thickness of Al_2O_3 illuminated under UV-LED (365 nm) is plotted. (a) Experimental setup (b) Resultant J-V curve (c) corresponding log plot of (b) measured at a scan rate of 5 mV/s. Figure reproduced from publication [187].

7.3.3 Characterization of perovskite filled complete device

Elemental characterization, such as EDX analysis and various electrical characterizations such as stable V_{OC}, OCVD, suns-V_{OC} measurement, and I-V curves, are shown for complete devices filled with perovskite. All the devices shown in this section will have 20 nm of c-TiO_2, 1.5 µm of mp-TiO_2, and 8 µm of CG. Above mp-TiO_2, various thicknesses of Al_2O_3 are sputtered.

7.3.3.1 EDX analysis

Focused ion beam - scanned electron microscopy (FIB-SEM) image and energy dispersive X-ray (EDX) analysis of a perovskite filled double-mesoscopic HTM-free CG-PSCs are shown in Figure 83. A defined presence of Al_2O_3 on top of mp-TiO_2 is noticed along with a good pore filling of the mp-TiO_2 with the perovskite. It shows that thin Al_2O_3 layers have not hindered the percolation of the precursor solution.

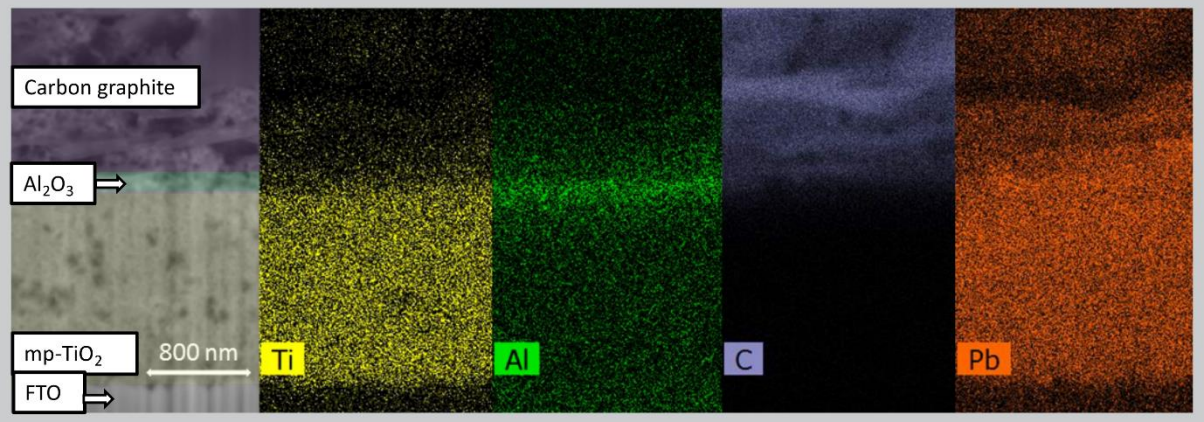

Figure 83: EDX analysis of perovskite filled double-mesoscopic CG-PSC with 1.5 µm mp-TiO_2 and thin Al_2O_3 after crystallization. Figure reproduced from publication [187].

7.3.3.2 Stable V_{OC} measurement

The results from stabilized photovoltage measurements of the complete cells (c-TiO_2/mp-TiO_2/Al_2O_3/CG) with different Al_2O_3 thicknesses are shown in Figure 84. By just adding a very thin 10 nm Al_2O_3 to the mp-TiO_2/CG interface, already a 130 mV increase in photovoltage was observed. On further optimization, stabilized 1 V for devices with 40 nm Al_2O_3 has been reached.

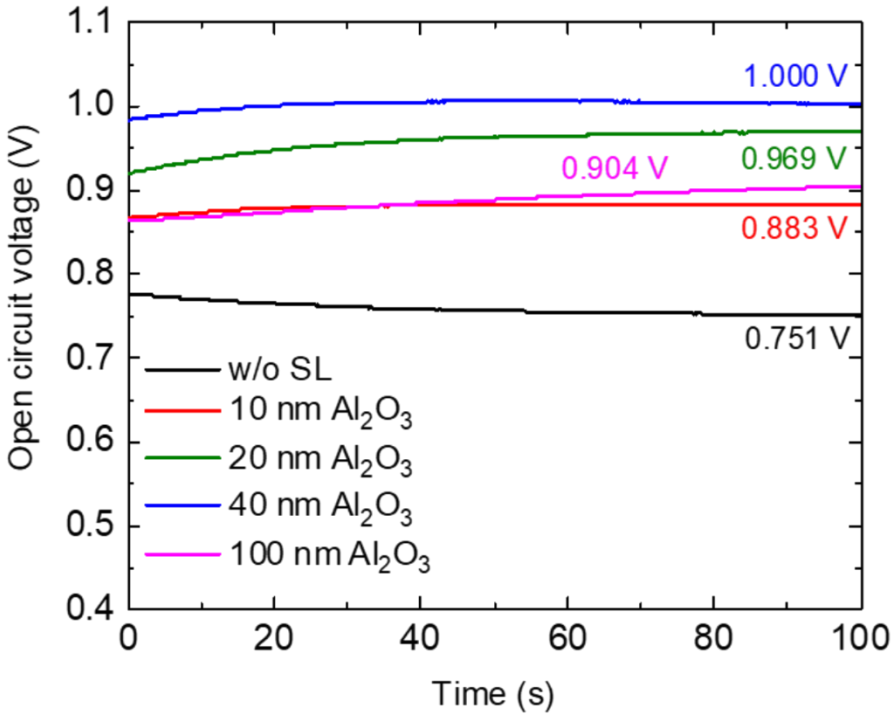

Figure 84: Stabilized V_{OC} of complete perovskite-filled devices for 100 s at 1000 W/m² AM 1.5 G. Figure reproduced from publication [187].

7.3.3.3 Suns-V_{OC} measurement

V_{OC} vs. light intensities of Figure 85a gives additional information on the nature of shunts and diode ideality factor present in the cells under investigation. In literature, it has been reported that the *n* value of PSCs varies with the V_{OC} stabilization time [136]. It also agrees with our measurements. To illustrate this effect, Figure 85b shows the suns-V_{OC} measurement for devices without Al_2O_3 at two-time intervals, namely 0 s (V_{OC} unstabilized) and 60 s (V_{OC} stabilized over 60 s). The slope from these values was used to calculate the ideality factor, *n*. An ideality factor of 0.92 was observed in devices without Al_2O_3. Calado *et al.* show that the ideality factor varies with time as the V_{OC} is influenced over time for different illumination intensities, e.g., by ion movement [136]. To investigate the same condition in our cells, the ideality factor with V_{OC} values taken from the initial time and with the values after stabilizing for 60 s was compared. Unstabilized values are observed at 0 s (denoted as w/o SL_unstabilised), which, when plotted, results in higher slope and *n* values. 32 % decrease in the slope values when plotted with stabilized photovoltage at 60 s (denoted as w/o SL_stabilised) is observed. Thus, the comparison shows a high *n* value (1.36) for unstabilized V_{OC} (at 0 s) due to the overestimation of the dominant order recombination [136]. Thus, only stabilized V_{OC} values (after 60 s) have been considered for Figure 85a.

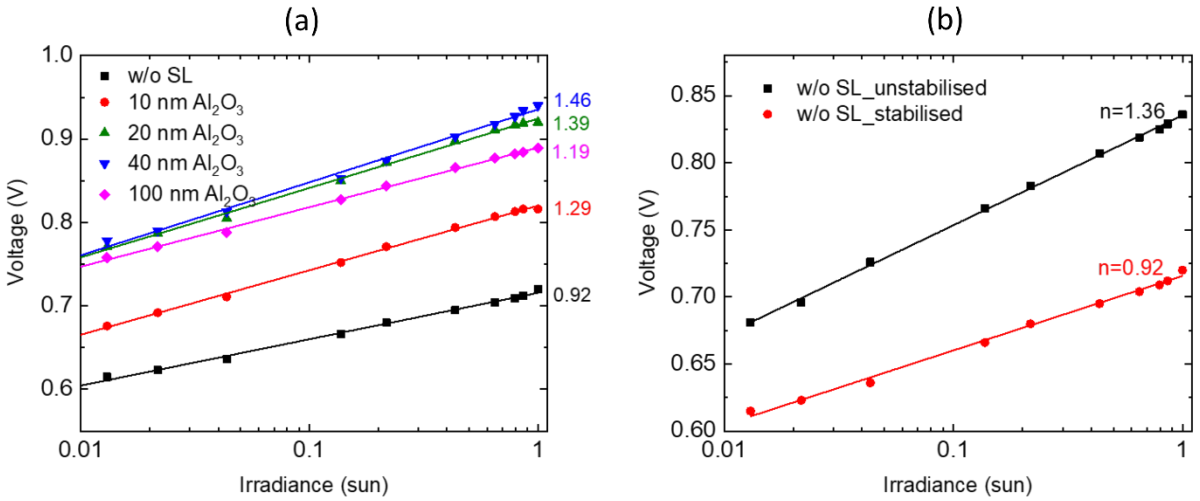

Figure 85: (a) V_{OC} measured at various sun intensities using an LED array for complete perovskite-filled devices with different thicknesses of Al_2O_3 (b) V_{OC} measured at various sun intensities using an LED array for a device without space layer (c-TiO_2/mp-TiO_2/CG) – measured at two different time intervals: before V_{OC} stabilization (black line) and after 60 s stabilization (red line). Figure reproduced from publication [187].

Interpretation of suns-V_{OC} measurement for an ideal and real solar cell has been explained in section 4.2. Devices without Al_2O_3 show the *n* value of 0.92, pointing to a situation with unoccupied traps. The observation of the low photovoltage of 750 mV at 1 sun indicates that there is a low density of photoexcited charges present in the perovskite. It leads us to the conclusion that electrons from the conduction band of the TiO_2 are pulled away by the carbon-graphite leading to a strong and fast emptying of shallow trap states in the mp-TiO_2. However, with the increase in Al_2O_3 thickness, the electrons in the mp-TiO_2 become now well isolated from the CG. It means that traps are currently occupied, leading towards an n = 2 type recombination behavior. At the same time, the charge carrier density in the conduction band of the mp-TiO_2 and the perovskite is high, leading to a high photovoltage. A similar observation has also been recently reported and interpreted by Tress *et al.* [132]. The pictorial representation of the recombination pathway mechanisms and its corresponding *n* factor is shown in Figure 86.

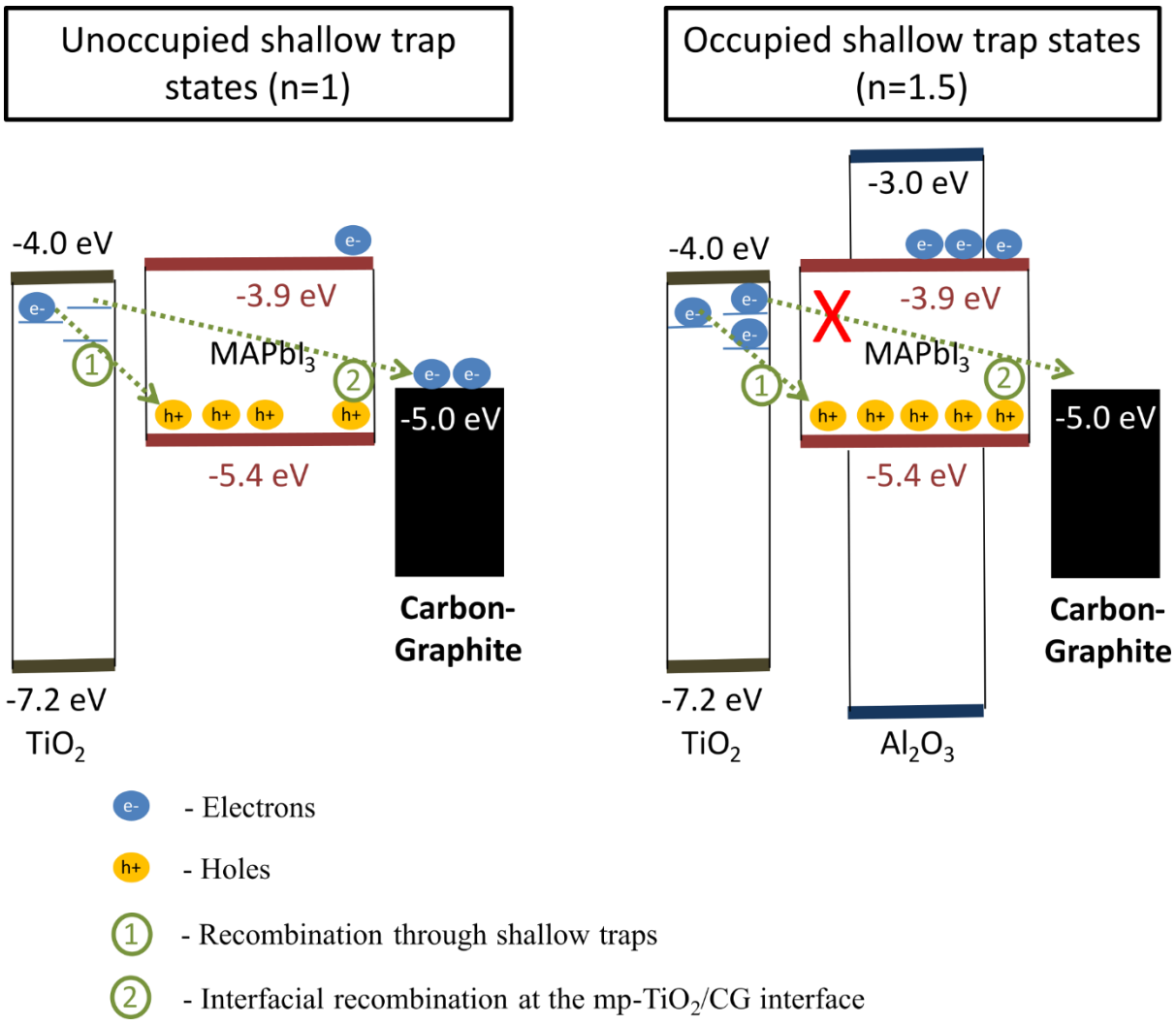

Figure 86: Schematic representation of recombination mechanisms in a device without Al_2O_3 and for c-TiO_2/mp-TiO_2/Al_2O_3/CG. Figure reproduced from publication [187].

7.3.3.4 Open circuit voltage decay measurement

Under open circuit conditions, the external photocurrent in a solar cell is zero by definition. It means that the photovoltage is determined by the equilibrium between the photogenerated charges and the charge recombination. The graph in Figure 87a shows the voltage decay from the stabilized V_{OC} of the cells under illumination after the light is switched off. As explained in section 4.2.4.1, the sharp decrease in the V_{OC} decay as soon as the illumination is switched off is caused by the fast recombining primary charge carriers and the recombination from shallow traps. In the time frame of seconds (Figure 87b), the voltage value is determined by the very slowly recombining secondary charges (i.e., deep trapped charges in mp-TiO_2). The upward shift in the voltage with respect to increasing Al_2O_3 thickness up to 40 nm shows that the thin isolation layer efficiently prevents the recombination of electrons at the mp-TiO_2/CG

interface. Thus, the impact of fast recombination at the interface (mp-TiO_2/CG) is reduced by introducing Al_2O_3 of 40 nm (or thicker), resulting in higher photovoltages and long-living charges. Interestingly, the voltage decay even for devices without Al_2O_3 is slow in the seconds range. It indicates that the decay from the deep traps is eligible in all cases and shows the absence of ohmic shunts.

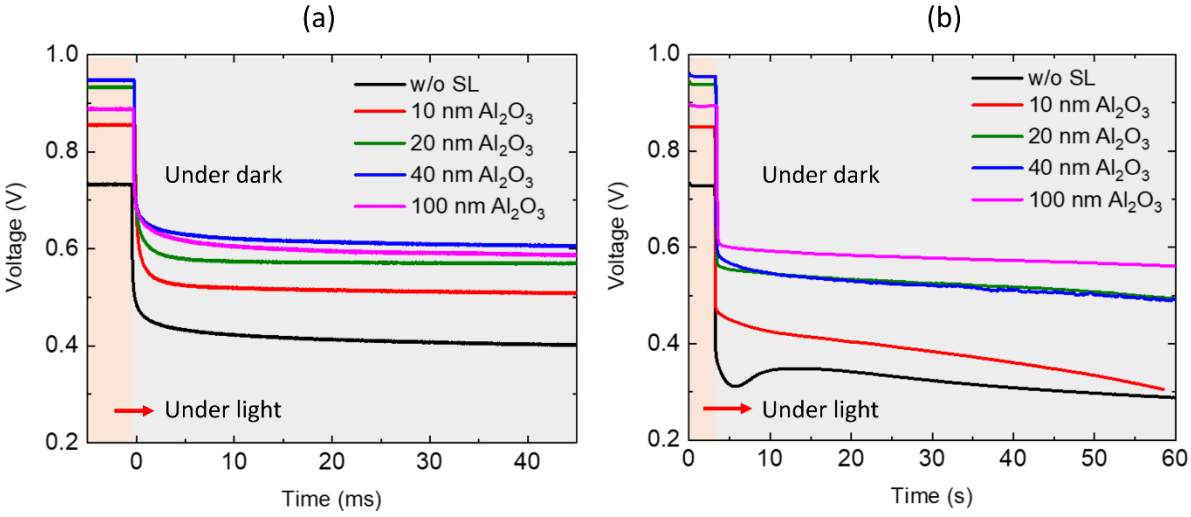

Figure 87: V_{OC} decay measurement with cells illuminated using red LED as the light source with a constant current of 5650 mA (approx. 1 sun intensity) (a) for 45 ms and (b) for 60 s. Figure reproduced from publication [187].

The absence of ohmic shunts has been studied in more detail for the case of devices without Al_2O_3. An external 1 kΩ resistor was connected in parallel for the voltage decay measurements. As shown in Figure 88, the voltage drops to zero in less than 50 µs, demonstrating the absence of an internal ohmic shunt. The observation of the fast decay (i.e., a small amount of trapped charge) also validates the mechanism of emptying the shallow traps through the mp-TiO_2/CG interface, as described in the explanation for Figure 86.

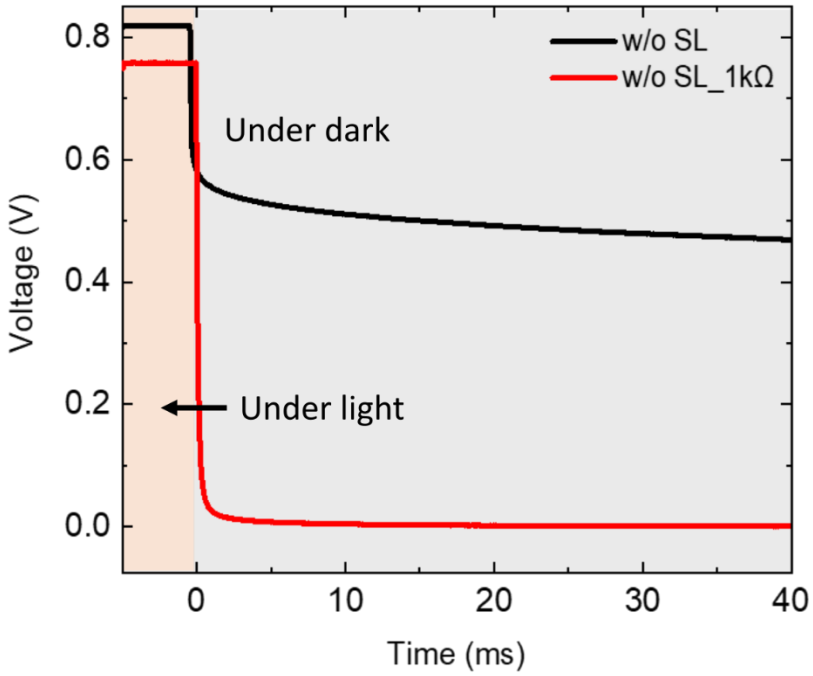

Figure 88: Open-circuit voltage decay measurements (OCVD) for a device w/o SL (c-TiO_2/mp-TiO_2/CG) with and without a resistor. Figure reproduced from publication [187].

7.3.3.5 Time-dependent PL imaging

Voltage, current, and averaged PL signal as derived from time-dependent PL imaging was recorded under constant illumination when the devices were switched between open circuit (OC) and short circuit (SC) conditions. The graph in Figure 89a shows the corresponding results for devices from the same batch with 10 nm Al_2O_3, 40 nm Al_2O_3, 100 nm Al_2O_3, and without Al_2O_3 (w/o SL). The quenching in PL intensity and the increase in the current while switching from V_{OC} to V = 0V (short-circuit condition) shows the charge extraction ability of the devices, as explained in section 4.2.4.3. At least a double exponential behavior in quenching of the PL intensity is observed for the devices with Al_2O_3, which stabilizes at the same low values after 20 s. This behavior corresponds to efficient non-limited charge transport. It is confirmed by the high J_{SC} values of these devices (as shown in Figure 90). The PL images corresponding to the 9th s and the 30th s are compared in Figure 89b, which evidently shows the efficient and uniform PL quenching in the monitored area in devices with Al_2O_3.

In contrast, devices without Al_2O_3, after switching to SC conditions, show an initial fast quenching of the average PL, followed by a slow recovery of the PL towards the initial value under V_{OC}. The initially high photocurrent drops to half of its initial value after stabilization, also indicating charge transport problems. As PL is a measure of the number of primary charge

carriers, this could mean, in case of devices without space layer; primary charge carriers are mainly not contributing to the current, leaving the current to be driven mostly by long-living secondary charge carriers. The reason for this is not fully understood. Still, it anyway indicates that the electron transport over the mp-TiO_2/CG interface creates a recombination center and that the presence of the thin Al_2O_3 layer is sufficient to solve this issue.

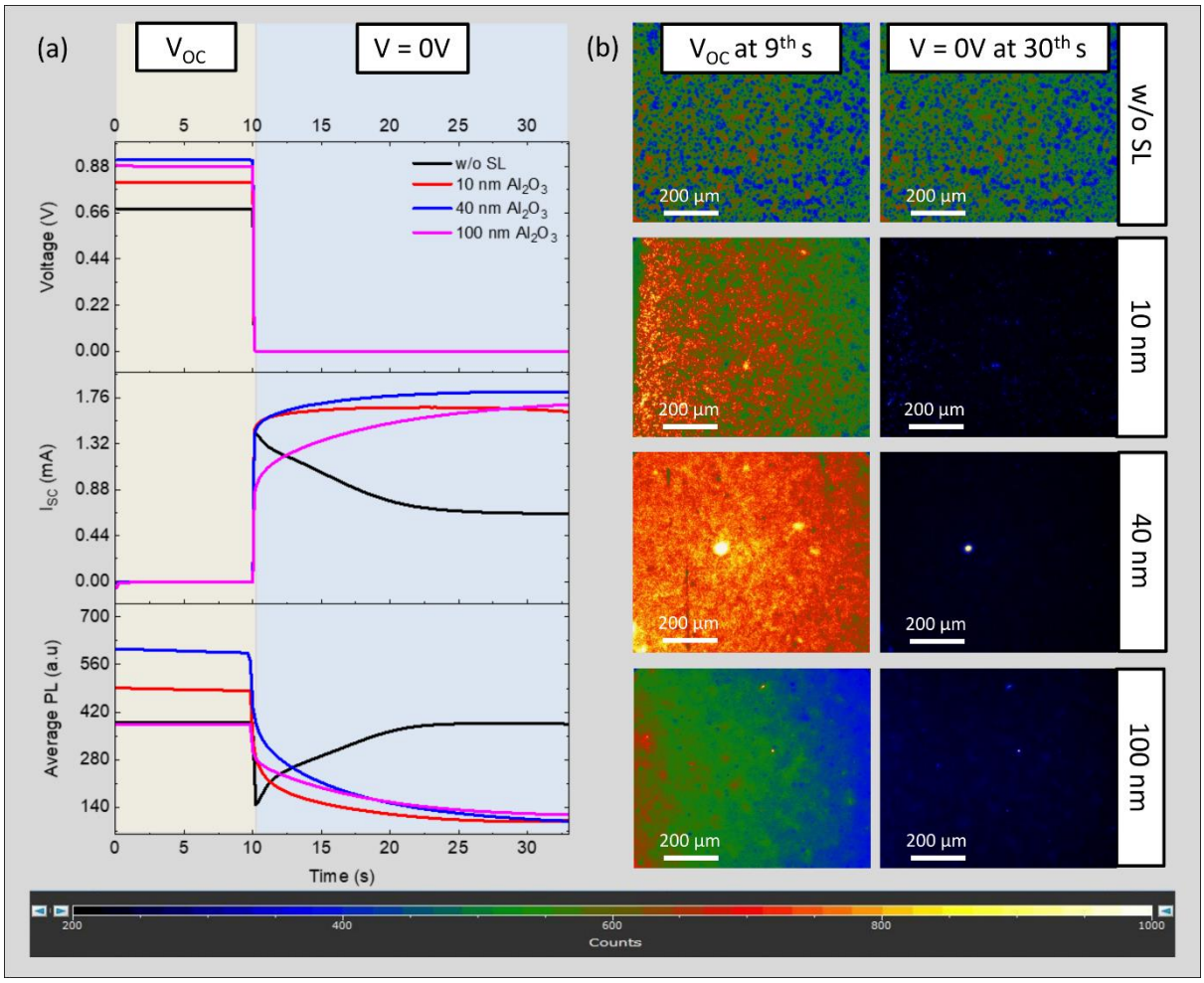

Figure 89: Differentiating between primary charge carrier transport by observing space resolved photoluminescence (PL) after switching from open circuit conditions to short circuit conditions: at constant illumination (a) The graph shows the voltage, current and PL measured while switching between two conditions, namely open circuit condition (V_{OC}) and short circuit condition (V = 0 V). The measurements were carried out using a red LED as the light source with a constant current of 1413 mA whose spot diameter 2 mm was resulting in an intensity of approx. 1 sun (b) PL images of all device at 9th and 30th s (i.e., stabilized in open circuit and short circuit conditions) which show an efficient and improved charge extraction for devices with Al_2O_3 with maximum voltage, current and PL quenching observed in devices with 40 nm Al_2O_3 as the insulation layer. Figure reproduced from publication [187].

7.3.3.6 Average electrical parameters

Upon investigating the photovoltage and charge extraction ability of the devices, the reproducibility of the described enhancements is observed through analyzing the average electrical parameters. It is extracted by the J-V characteristics and stabilized measurements for devices without SL, Al_2O_3, and also 1 µm thick ZrO_2 as SL. Four to six devices from each cell condition/typology are considered for statistics. The average electrical parameters, such as V_{OC}, J_{SC}, FF, and PCE, are shown in Figure 90, respectively. Devices with 40 nm Al_2O_3 as the isolation layer achieved the highest average photovoltage, thereby achieving a high PCE of 11.11% with a V_{OC} of 983 mV with 19.28 mA/cm^2 J_{SC}, 59% FF an active area mask of 0.4 cm^2.

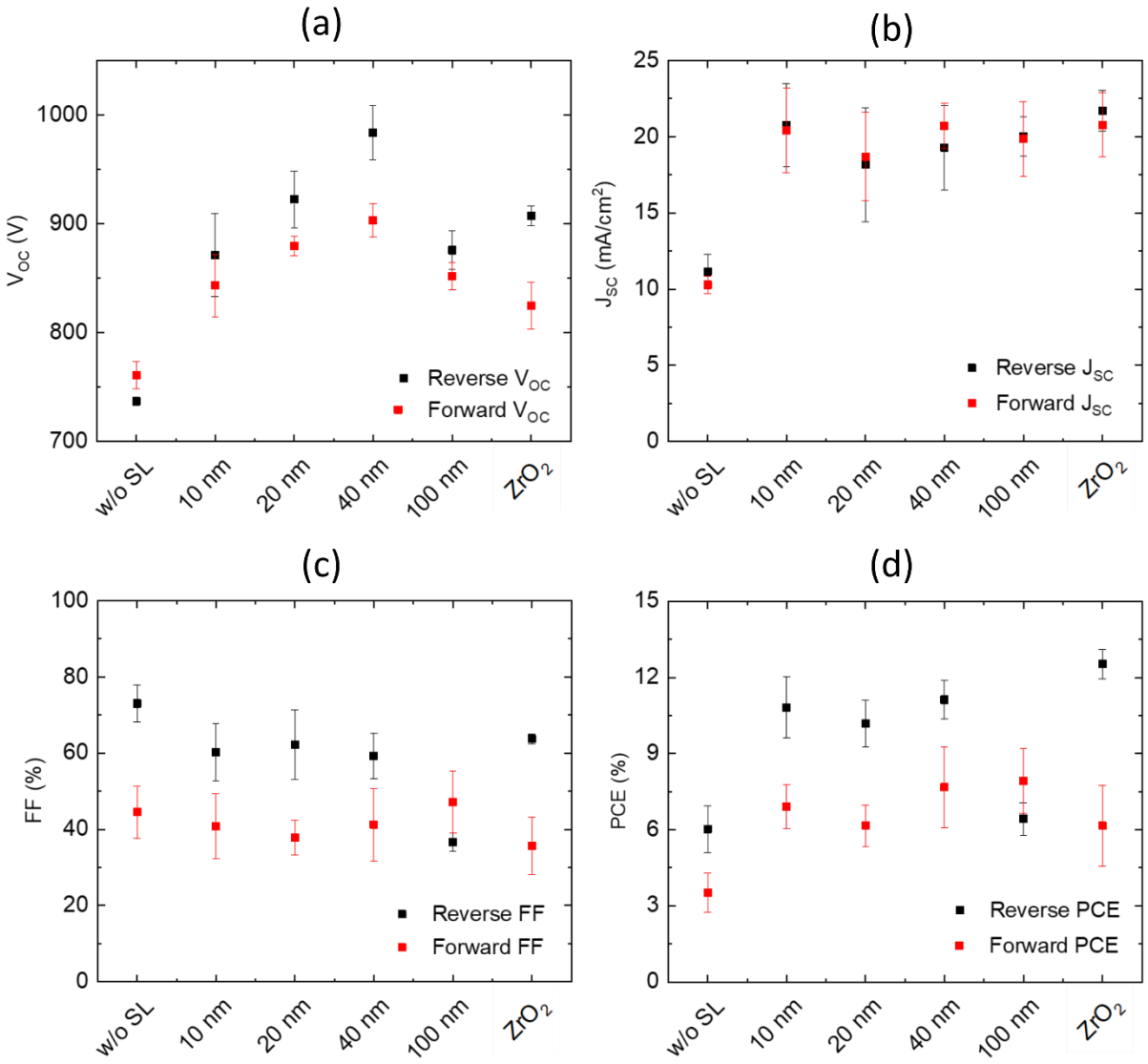

Figure 90: Average electrical parameters comparing devices with various spacer layers and also different thicknesses of Al_2O_3 (a) V_{OC} (b) J_{SC} (c) FF and (d) PCE. Figure reproduced from publication [187].

7.3.3.7 J-V curves and stabilized PCE of best devices

The J-V curves of the best devices from each condition are presented in Figure 91a and their stabilized PCE values are shown in Figure 91b. When compared, ZrO_2 cells have a higher average reverse PCE of 12.52 % (Figure 90d) but present a significantly lower stabilized PCE of 8.31% (Figure 91b). The average V_{OC} from the reverse J-V curve and the stabilized V_{OC} for the ZrO_2 based devices is 907 mV and 911 mV, respectively. It can be noticed that these values are ~10 % lower compared to the 40 nm Al_2O_3 devices where the average V_{OC} measured from the reverse J-V scan is 984 mV (Figure 90a), whereas the stabilized values are 1002 mV (Figure 84). It can be noticed that the shape of the IV curves does not represent the ideal curve. Discrepancies are also found between IV and stabilized values. Hence, the importance of relying on stabilized values has already been explained in section 4.2.3.

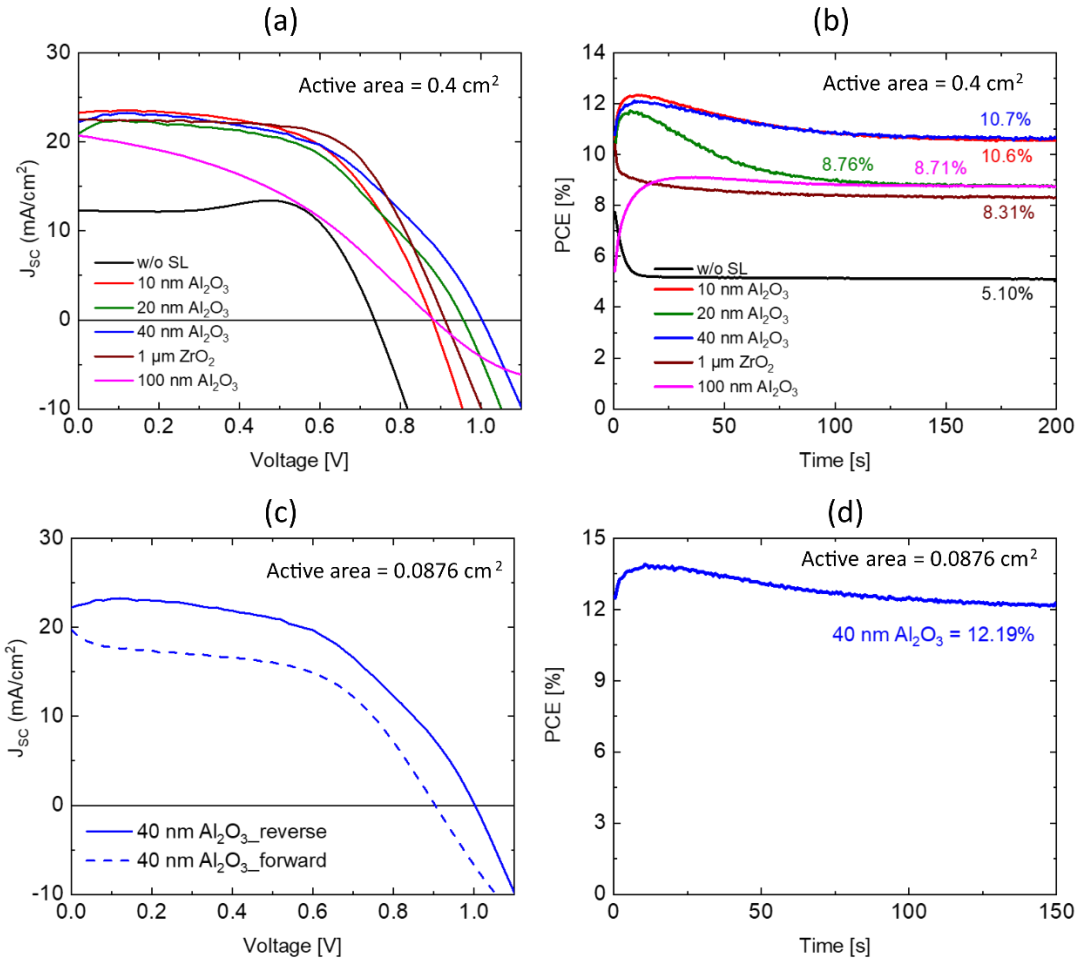

Figure 91: (a) J-V cures of the best devices from all the device conditions (b) Stabilized PCE of the best devices from all the device conditions compared with an active area of 0.4 cm² (c) J-V of the champion device with an active area (d) stabilized PCE of the champion device with active area 0.0876 cm². Figure reproduced from publication [187].

A stable PCE of 12.1% for the champion device was measured with a masked area of 0.0876 cm^2(Figure 91d). Its corresponding J-V curve is shown in Figure 91c. To further demonstrate the reproducibility of Al_2O_3 devices, Figure 92a and Figure 92b show the histogram of V_{OC} and PCE from J-V curves for 28 devices with 10 nm Al_2O_3 that were produced over a period of 1 year.

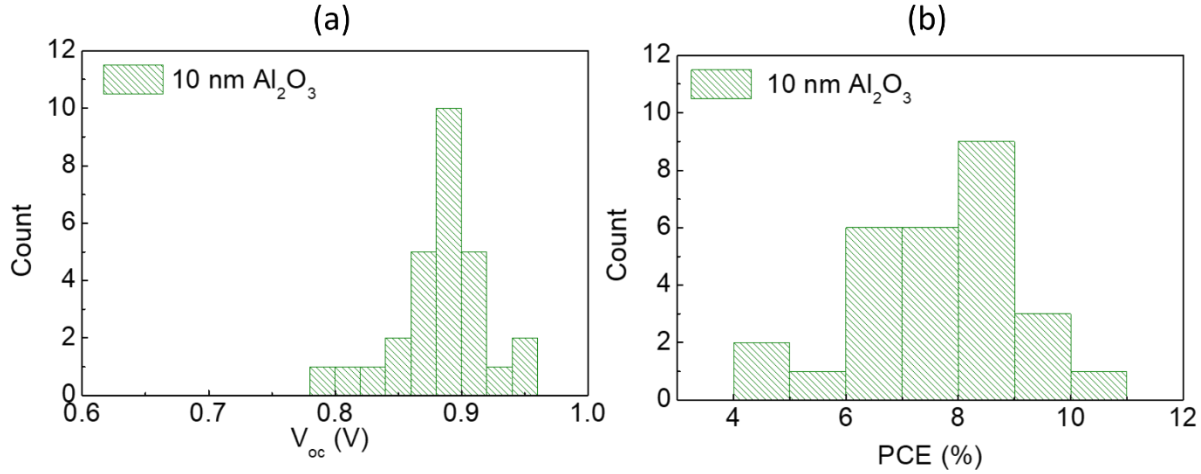

Figure 92: Histogram of 23 devices with 10 nm Al_2O_3 (a) V_{OC} (b) PCE. Figure reproduced from publication [187].

Thus, a successful replacement of the thick spacer layer (ZrO_2 or Al_2O_3) with an ultra-thin isolation layer provides a reduction of the transport limitations of such PSC architecture. Results show the capability and true potential of double-mesoscopic HTM-free CG-PSCs and bring to the conclusion that the state-of-the-art thick space layers limit the performance of CG-PSCs.

7.4 Conclusion

In this chapter, a new double-mesoscopic architecture has been introduced for hole conductor (HTM)-free carbon-graphite (CG) perovskite solar cells (PSCs), favoring more efficient charge transport compared to existing triple-mesoscopic CG-PSCs. A thin 40 nm sputtered pseudo-porous Al_2O_3 layer can compensate the need for a conventional micrometer thick (> 1µm) mesoporous insulating space layer in triple-mesoscopic CG-PSCs. By concept, this allows a smaller diffusion path length for holes inside perovskite photo absorber. With this new configuration, a high photovoltage of 1.0 V and a stabilized solar efficiency of 12.1% have been reached for $CH_3NH_3PbI_3$ (MAPI) perovskites. It already

outperforms the results reported for high temperature processed triple-mesoscopic CG-PSCs using standard MAPI perovskite by others.

SEM, TEM, EDX, and AFM measurements from the sub-cells show that the fully oxidized sputtered Al_2O_3 layer covers the underlying mesoporous TiO_2 (mp-TiO_2) layer. The pseudo-porosity of Al_2O_3 is therefore governed by the roughness of the underlying layer. The Al_2O_3 thicknesses have been finely tuned between 10 nm and 100 nm for an optimal infiltration of the perovskite solution and allow full perovskite crystallization inside the mp-TiO_2 electrode layer. The absence of pure ohmic shunts in the presence of Al_2O_3 has been shown prior to the infiltration of perovskite using direct photoexcitation of the TiO_2 layer with UV. Light-dependent photovoltage and photovoltage decay, as well as time-dependent photoluminescence measurements, showed that the optimal 40 nm thick Al_2O_3 efficiently reduces the charge recombination at the mp-TiO_2/CG interface and, at the same time, allows efficient hole diffusion through the perovskite crystals embedded in its pseudo-pores.

The outcome of this work opens the discussion that an ultra-thin space layer efficiently isolates the CG counter electrode from electrons, which have been transferred from the perovskite to the mp-TiO_2. The thickness of the isolation layer has been optimized to achieve a high stable V_{OC} by preventing the interfacial recombination of free electrons from the illuminated perovskite region at the CG interface.

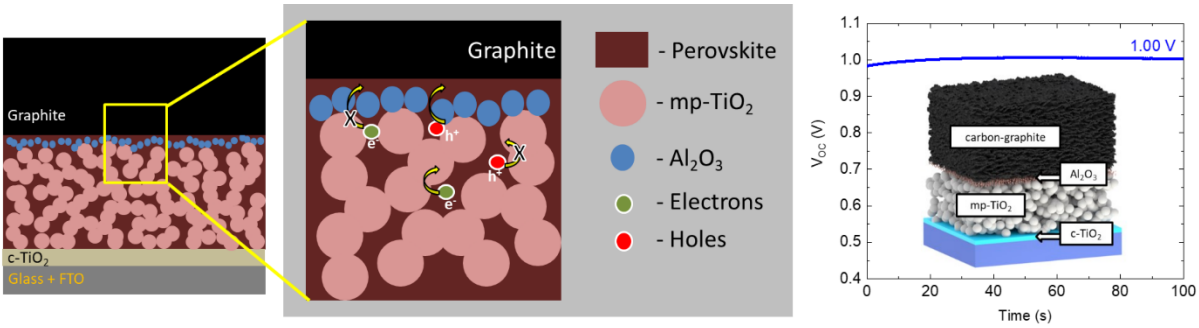

Figure 93: Summary diagram for Chapter 7 showing that the recombination at mp-TiO_2/CG interface is suppressed. Figure reproduced from publication [187].

Chapter - 8

Conclusions and Outlook

8 Conclusions and outlook

8.1 Conclusions

The analysis of interfaces in perovskite solar cells is of increasing importance due to the excellent bulk properties of the perovskite absorber material. It is essential to improve the stability of the devices without comprising its performance for the PSCs to be commercialized. For this purpose, not only the study of the material is critical but also its property changes when it is in contact with the photo absorber or any other charge transport layer. Even though various interfaces influence the overall performance of the device, it is vital to understand each interface separately. Deeper understanding then helps in realizing specific functions of the interfaces, which, in turn, aids in finding methods to improve them. In this direction, this doctoral thesis shows a way to establish the **interfacial analysis using sub-cell configuration**.

For this thesis, three different interfaces in two different cell architectures were studied. For each interfacial analysis, suitable sub-cell configuration and its investigation methods were decided. Results from the sub-cells improved the understanding of the individual interface. Then complete PSCs were fabricated. A comparison of results from sub-cells and complete devices provided an understanding of the specific interface and the way it is influenced in a complete device due to the presence of other interfaces. It also provided information on how the interface analyzed in the sub-cell influences the complete device performance.

Analyzing the quality of ETL/perovskite interface:

The first interface that was analyzed and reported in this thesis (Chapter 5) was the **ETL/perovskite interface in an n-i-p planar perovskite architecture**. The aim here was to study the stability of the ETL/perovskite interface against UV illumination. All the processes except counter electrode fabrication were done under a room ambient atmosphere. A suitable sub-cell, FTO/SnO_2/perovskite, was subjected to 500 h of continuous UV illumination to study the influence of SnO_2 on perovskite under UV, where SnO_2 is often reported to be UV stable. The results of the sub-cells from XRD, XPS, absorbance, and PL spectroscopy measurements showed the formation of excess PbI_2 in the cell after the UV treatment. However, surprisingly, the complete devices fabricated on this UV-treated sub-cell showed impressive stability where 80 % of the initial PCE was maintained after 14 h under continuous

AM 1.5 G illumination. The improved stability of the complete device could be attributed to the passivation effect due to excess PbI_2 at the HTL/perovskite interface.

- **PSC architecture:** Ambient processed planar PSC
- **Cell configuration:** Glass/ITO/SnO_2/perovskite/PEDOT:PSS/MoO_3/Ag
- **Focus:** To investigate the effect of slot-die coated SnO_2 at the SnO_2/perovskite interface
- **Sub-cell:** ITO/SnO_2/perovskite
- **Outcome:** The UV-treatment of sub-cell improved device stability. 80 % of the initial PCE remained after 14 h of continuous AM 1.5 G illumination.
- **Published article:** This work has been published in Solar RRL under the title "Improving the Stability of Ambient processed, SnO_2-Based, Perovskite Solar Cells by the UV-treatment of Sub-Cells". DOI: 10.1002/solr.202000262

Analyzing the quality of the hole blocking layer (HBL) at FTO/perovskite interface:

The second interface that was analyzed and reported in this thesis (Chapter 6) was the **FTO/perovskite interface in an n-i-p mesoporous HTL-free carbon-graphite based perovskite cell architecture.** Here also all the processes, including counter electrode fabrication, were done in an ambient room atmosphere. The compact hole blocking layer (HBL) is an already established solution to prevent the backtracking of electrons from FTO to perovskite. In this work, dark lock-in thermography (DLIT), as a non-intrusive, large area technique, is developed to study the stand-alone interface. The quality of the TiO_2-HBL processed through various deposition techniques such as sputtering, spray pyrolysis deposition (SPD), and atomic layer deposition (ALD) has been studied. For this purpose, an FTO/c-TiO_2/μ-graphite sub-cell was analyzed using DLIT. The importance of using DLIT for shunt detection and other defects was shown. The local J-V curve of the hot spots in DLIT provides more information other than linear shunts. The sub-cell analysis showed that all HBL processing techniques produced a conformal coating upon FTO; however, the density of shunts was not related to the processing technique. DLIT showed SPD and ALD helped in uniform film deposition.

Even though conformal and pinhole-free coating was established using ALD, the dark J-V curves of the sub-cell showed low forward onset voltage. Complete devices were fabricated and compared. Stabilized voltage and open-circuit voltage decay (OCVD) measurements inferred the presence of less shallow trap states in SPD, resulting in a storage type effect

showing 224 mV of voltage 10 min after switching off the illumination. A stable voltage of 925 mV was observed for the SPD layer. However, contrary to the analysis from the dark J-V of the sub-cell, a device with ALD processed HBL showed a high stable PCE of 10.1 % owing to high J_{SC} and FF.

- **PSC architecture:** Ambient processed mesoporous HTL-free PSC
- **Cell configuration:** Glass/FTO/c-TiO_2/mp-TiO_2/mp-ZrO_2/carbon-graphite (CG) where mesoporous layers are filled with perovskite
- **Sub-cell:** FTO/c-TiO_2/ μ-graphite
- **Focus:** To investigate the quality of HBL - compact-TiO_2 (c-TiO_2) and its role in preventing recombination at the FTO/perovskite interface
- **Outcome:** The quality of the c-TiO_2 was analyzed using dark lock-in thermography (DLIT). Various HBL deposition technique was analyzed. Atomic layer deposition (ALD) proved to produce pin-hole free, shunt-free HBL thereby reducing the recombination at c-TiO_2/perovskite interface achieving photo-voltage higher than 900 mV

Analyzing the quality of the insulation layer at mp-ETL/cathode interface:

The third interface that was analyzed in this thesis (Chapter 7) was the **mp-TiO_2/carbon-graphite (CG) interface in an n-i-p mesoporous HTL-free carbon-graphite based perovskite architecture**. Also, here also all the processes, including counter-electrode fabrication, were done in an ambient room atmosphere. Using a thick 1 μm mp-ZrO_2 or mp-Al_2O_3 layer as an insulation/spacer is the established technique to prevent the recombination at the mp-TiO_2/CG interface. The novelty in this work involved replacing this thick mesoporous spacer layer with a sputtered ultra-thin Al_2O_3 layer. A sub-cell configuration of FTO/mp-TiO_2/sputtered Al_2O_3 was used to study the properties of the layer and also to optimize it. SEM, AFM, and TEM measurements show the pseudo-porosity of an ultra-thin sputtered layer up to 40 nm when fabricated on a mesoporous layer. Contact angle measurements were carried out to show the wetting properties of the layer. J-V curves measured before perovskite infiltration by photoactivation of the mp-TiO_2 using UV light showed low forward current density for the 40 nm pseudo-porous Al_2O_3 layer proving its isolation property. Complete devices fabricated resulted in a highly stable voltage of 1 V with a stable PCE of 12.1 % for devices with 40 nm ultra-thin sputtered Al_2O_3 layer. Thus, it is shown that a 40 nm Al_2O_3 layer is sufficient to prevent the charge recombination at the mp-TiO_2/CG interface.

- **PSC architecture:** Ambient processed mesoporous HTL-free CG-PSC
- **Cell configuration:** Glass/FTO/c-TiO_2/mp-TiO_2/Al_2O_3/CG where mesoporous layers are filled with perovskite
- **Sub-cell:** FTO/c-TiO_2/ mp-TiO_2/Al_2O_3
- **Focus:** To investigate the quality of sputtered Al_2O_3 and its role in preventing recombination at the mp-TiO_2/CG interface
- **Outcome:** An ultra-thin 40 nm sputtered Al_2O_3 is enough to prevent the recombination at the mp-TiO_2/CG interface. A stable photo-voltage of 1 V and power conversion efficiency (PCE) of 12.1 % was achieved.
- **Published article:** This work has been published in ACS Applied Nano Materials under the title "Double-Mesoscopic Hole-Transport-Material-Free Perovskite Solar Cells: Overcoming Charge-Transport Limitation by Sputtered Ultra-Thin Al_2O_3 Isolating layer". DOI: 10.1021/acsanm.9b02563.

In conclusion, this doctoral thesis shows that stand-alone interfaces can be studied, allowing a deeper understanding of an individual interface. For this purpose, suitable sub-cells were fabricated and analyzed. The results of the sub-cells and complete devices were compared to understand the specific interface's influence on the complete devices. Thereby, new techniques can be found to improve the interface that eventually results in improved device performance and stability.

8.2 Outlook

The thesis proposed a method (to identify and utilize a sub-cell characterization) through which the role of interfaces, individually, without the influence from interfaces, can be studied. The proposed method was applied to study three specific interfaces in PSCs. Two different architecture were also involved.

The first interface studied was the **ETL/perovskite interface,** using a sub-cell involving only this interface. A planar PSC was used in this case. Continuous **UV exposure for 500 h** led to excess PbI_2 being found on the perovskite surface. When device fabrication was completed, it led to the device optimization attributed to the passivation of the HTL/perovskite interface. In this case, the sub-cell was subjected to 500 h of UV stress from a particular UV wavelength. **Future work could involve various parameters, including UV intensity, wavelength, and duration of exposure** to define in detail the effects of UV treatment in PSC. The impact of the HTL/perovskite interface can also be studied using the sub-cell technique, and the performances of various other HTLs can be investigated.

The second interface studied was **the FTO/perovskite** interface in a carbon-graphite (CG) based PSC. The recombination at this interface was suppressed using the fabrication of compact hole blocking layer (HBL). In this case, c-TiO_2. **The dark lock-in thermography technique** was used to study the **electrical quality of the HBLs** processed using various fabrication techniques**. In the future, DLIT analysis using the studied method of applying graphite layer could be made for investigating each layer involved in the PSC fabrication**. It will give us the idea of how the quality of each layer plays a role in preventing/contributing to the ohmic shunts in the device. Additionally, non-ohmic diodic type defects can also be identified.

The third interface studied was the **mp-ETL/cathode** interface in a CG-PSC. Here, the recombination at the mp-TiO_2/CG interface was prevented using a **sputtered ultra-thin 40 nm Al_2O_3 layer**. The thickness of the Al_2O_3 layer was optimized. However, the mp-TiO_2 thickness was consistently 1.5 µm. **Future work could involve optimizing the thickness of mp-TiO_2 for the double-mesoscopic CG-PSC architecture** to find optimum between recombination losses vs gain in photoabsorption.

This work demontstrated the effects of strong UV exposure on a ETL/perovksite . Thus, a technique to study the interface of interest by subjecting the specific interface to environmental stress is suggested. Different stress conditions, such as UV, moisture, and temperature with a gradient of exposure times, can be considered in future. The results will help to have an in-depth knowledge of specific interfaces. Eventually, the goal towards long term stable and efficient PSCs can be reached.

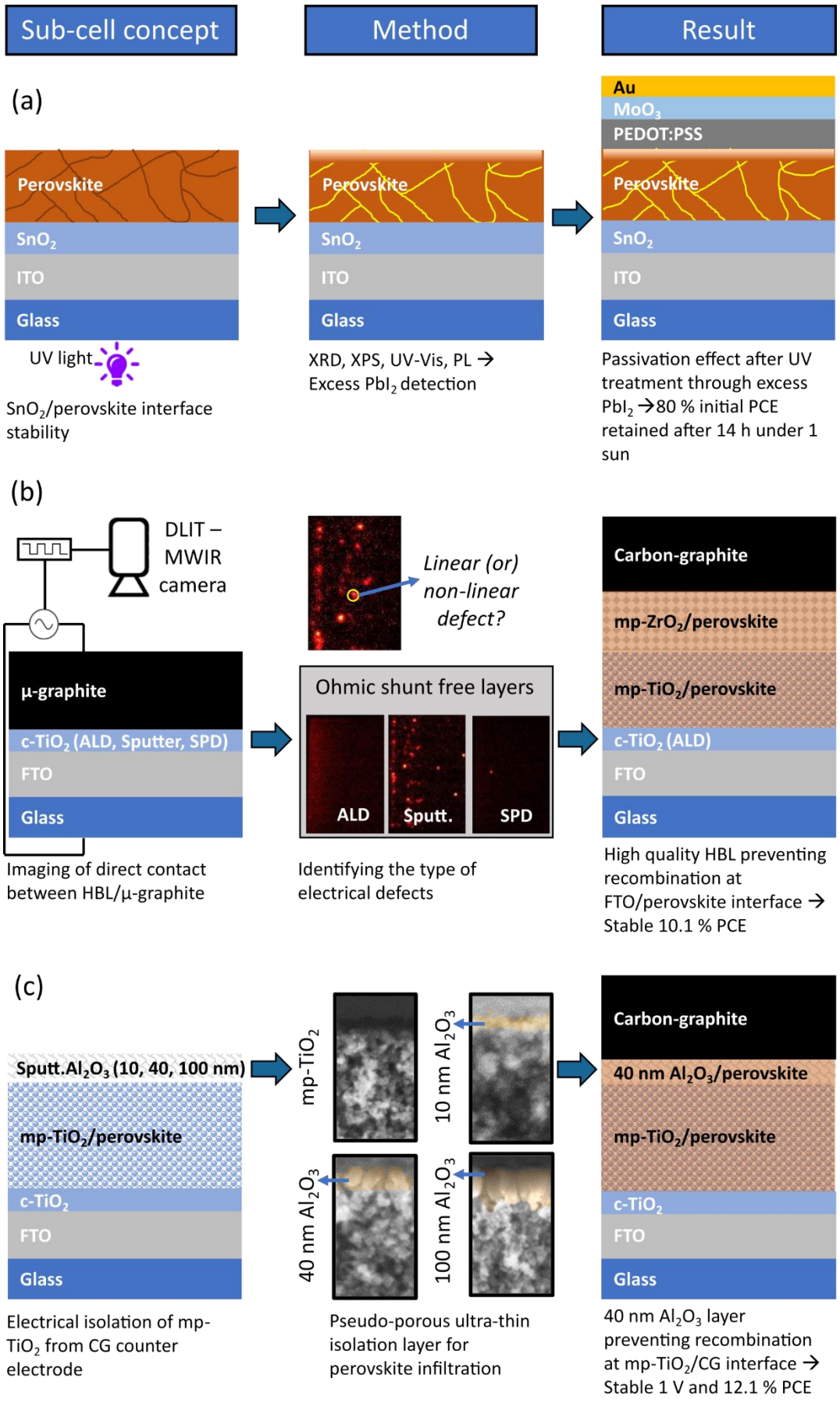

Figure 94: Graphical conclusion showing the sub-cell concept, method and the main results.

Publications and Conferences

Publications

Peer-reviewed journal publication as first author

1) **G. Mathiazhagan,** L. Wagner, S. Bogati, K. Y. Unal, D. Bogachuk, T. Kroyer, S. Mastroianni, and A. Hinsch, "Double-Mesoscopic Hole-Transport-Material-Free Perovskite Solar Cells: Overcoming Charge-Transport Limitation by Sputtered Ultra-Thin Al_2O_3 Isolating Layer". DOI: 10.1021/acsanm.9b02563.
2) **G. Mathiazhagan,** A. Seeber, T. Gengenbach, S. Mastroianni, D. Vak, A. Chesman, M. Gao, D. Angmo, and A. Hinsch, "Improving the Stability of Ambient processed, SnO_2-Based, Perovskite Solar Cells by the UV-treatment of Sub-Cells". DOI: 10.1002/solr.202000262.

Peer-reviewed journal publication as co-author

1) L. Wagner, S. Chacko, **G. Mathiazhagan**, S. Mastroianni, and A. Hinsch, "High Photovoltage of 1 V on a Steady-State Certified Hole Transport Layer-Free Perovskite Solar Cell by a Molten-Salt Approach". DOI: 10.1021/acsenergylett.8b00293
2) L. Wagner, L. E. Mundt, **G. Mathiazhagan**, M. Mundus, M. C. Schubert, S. Mastroianni, U. Würfel, A. Hinsch, and S. W. Glunz, "Distinguishing crystallization stages and their influence on quantum efficiency during perovskite solar cell formation in real-time." DOI: 10.1038/s41598-017-13855-6

Contribution to International conferences

1) Won Sustainable Energy and Fuels **poster award** for the poster titled "Double-Mesoscopic HTM-Free Perovskite Solar Cells: Overcoming Charge-Transport Limitation by Sputtered 40 nm Al_2O_3 Isolating Layer" at The Asia-Pacific International Conference on Perovskite, Organic Photovoltaic and Optolectronics (IPEROP20) held in January 2020, Tsukuba, Japan
2) Presented a poster on the title " Ultra-thin Space Layer for Graphite Based Perovskite Solar cells" at the 10^{th} International Conference on Hybrid and Organic Photovoltaics in May 2018, Benidorm, Spain

3) Presented a poster on the title “Monitoring of Crystallization Kinetics in Graphite based Perovskite Solar Cells” at the 9th International Conference on Materials for Advances Technologies in June 2017, Singapore.

Acknowledgments

குறள் 102:
காலத்தி னாற்செய்த நன்றி சிறிதெனினும்
ஞாலத்தின் மாணப் பெரிது.

-திருவள்ளுவர்

Kural 102:
Kaalaththi naarseydha nandri siridheninum
Nyaalaththin maanap peridhu

-Thiruvalluvar

Meaning:
A favor conferred in the time of need, though it be small (in itself), is (in value) much larger than the world.

Acknowledgments

My mother – A single word of gratitude is not enough to acknowledge the support she has given all through my life. I am grateful and blessed to be her daughter; without her, I am not here.

My sincere thanks to my first supervisor Prof. Dr. Stefan Glunz, for supporting me throughout the thesis period. Discussions with him always gave me enlightenment in subject matters or on general topics. Like others, I was also influenced by his positive attitude and a dose of it whenever I met him, pushed me to work harder. I thank my second supervisor Prof. Dr. Aziz Dinia, for his immense support from Uni Strasbourg. His positive acknowledgments on my work helped me to keep myself motivated. To my scientific supervisor, Dr. Andreas Hinsch, I am immensely grateful to him for hiring me as a HiWi at Fraunhofer ISE and introducing me to the world of Perovskite solar cells. I thank him - for the wonderful ideas, discussion, and suggestions that improved the quality of my work. I thank my scientific supervisor in Australia, Dr. Dechan Angmo, for providing me an excellent opportunity to work with her for six months in CSIRO, Melbourne. Without her support, my work in CSIRO wouldn't be complete.

To my mentor, Dr.Simone Mastroianni, thank you is not enough for the support, confidence, and for all the things he has taught me since the time I joined Fraunhofer ISE as a HiWi. He has been a pillar of support, personally and professionally. I am always grateful for his incredible listening whenever I had confusion about various topics. The way he made me look at my own experiences gave me a positive perspective that I had never thought of. He always

helped me to see the best in the not so good experiences I had. I am forever grateful to him for leading me from behind.

I thank my wonderful OPP team – Lukas Wagner, Kubra Yasaroglu, Dmitry Bogachuk, Salma Zouhair, Soyul Kang, Jaekeun Lim, Karima Saddedine, Bin Luo, Nico Glissmann, Jutta Zielonka, Konrad Fischer, Kevin Eble, Lakshmi Subramaniam, Arvind Prasanna, Welmoed Veurmann, Natalia Krochmal, Inez Skran, Mohammed Elshamy, Julius Glissner, Vita Megner, Peter Hirner and Benedickt Szabo for their support in the experiments, organizations, analysis, unique ideas and particularly for the huge amount of laughter. I thank them for the funny and memorable discussions on various crazy topics that I will always cherish. I thank Shankar Bogati and Tom Kroyer for their valuable suggestions and for their help in sputtering layers. I appreciate all the members in the characterization team from Fraunhofer ISE, CSIRO, and Uni Strasbourg for their help. I also thank all my colleagues with whom I have worked with for their support in various aspects.

I also acknowledge the support by the scholarship funds from the State Graduate Funding Program of Baden-Württemberg

I thank my friends Luis Esteban Guerra, Soundarya Palaniswamy, Anu Sajith, Hemalalitha Murugesan, Dhanya, Vittoria Sacchetto, Bhavana Khola, and Abhishek Arora for patiently listened to my laments and to have always been there to support me when I was at the lowest. Distance never played a role for these people to be there for me.

Last but not the least, to my Sundar, I thank him for his love, affection, support, and understanding that helped to keep my enthusiasm alive.

Bibliography

Bibliography

1. NREL. Efficiency chart. https://www.nrel.gov/pv/assets/images/efficiency-chart.png.
2. Dr. Xiaoxi He. Perovksite photovoltaics 2018-2028 Technologies, Markets, Players. https://www.idtechex.com/en/research-report/perovskite-photovoltaics-2018-2028/541.
3. Shockley W, Queisser HJ. Detailed Balance Limit of Efficiency of p--n Junction Solar Cells. *J Appl Phys*. 1961;32(3):510-519. doi:10.1063/1.1736034
4. A A M Sayigh. *Comprehensive Renewable Energy*. Elsevier; 2012.
5. Wurfel U, Cuevas A, Wurfel P. Charge Carrier Separation in Solar Cells. *IEEE J Photovoltaics*. 2015;5(1):461-469. doi:10.1109/JPHOTOV.2014.2363550
6. Kojima A, Teshima K, Shirai Y, Miyasaka T. Organometal halide perovskites as visible-light sensitizers for photovoltaic cells. *J Am Chem Soc*. 2009;131(17):6050-6051. doi:10.1021/ja809598r
7. Gao P, Grätzel M, Nazeeruddin MK. Organohalide lead perovskites for photovoltaic applications. *Energy Environ Sci*. 2014;7(8):2448-2463. doi:10.1039/C4EE00942H
8. Giorgi G, Yamashita K. Organic--inorganic halide perovskites: an ambipolar class of materials with enhanced photovoltaic performances. *J Mater Chem A*. 2015;3(17):8981-8991. doi:10.1039/C4TA05046K
9. Mitzi DB. Synthesis, Crystal Structure, and Optical and Thermal Properties of (C 4 H 9 NH 3) 2 MI 4 (M = Ge, Sn, Pb). *Chem Mater*. 1996;8(3):791-800. doi:10.1021/cm9505097
10. Nethercot AH. Prediction of Fermi Energies and Photoelectric Thresholds Based on Electronegativity Concepts. *Phys Rev Lett*. 1974;33(18):1088-1091. doi:10.1103/PhysRevLett.33.1088
11. Choi W, Choudhary N, Han GH, Park J, Akinwande D, Lee YH. Recent development of two-dimensional transition metal dichalcogenides and their applications. *Mater Today*. 2017;20(3):116-130. doi:10.1016/j.mattod.2016.10.002
12. Chen Y, Sun Y, Peng J, Tang J, Zheng K, Liang Z. 2D Ruddlesden-Popper Perovskites for Optoelectronics. *Adv Mater*. 2018;30(2). doi:10.1002/adma.201703487
13. Ortiz-Cervantes C, Carmona-Monroy P, Solis-Ibarra D. Two-Dimensional Halide Perovskites in Solar Cells: 2D or not 2D? *ChemSusChem*. 2019;12(8):1560-1575. doi:10.1002/cssc.201802992
14. J. Burschka. Sequential deposition as a route to high-performance perovskite-sentisized solar cells. 2013.
15. Stranks SD, Eperon GE, Grancini G, et al. Electron-hole diffusion lengths exceeding 1 micrometer in an organometal trihalide perovskite absorber. *Science*. 2013;342(6156):341-344. doi:10.1126/science.1243982

16. Tress W, Marinova N, Inganas O, Nazeeruddin MK, Zakeeruddin SM, Graetzel M. The role of the hole-transport layer in perovskite solar cells - reducing recombination and increasing absorption. In: Conference IPS, ed. *IEEE 40th Photovoltaic Specialists Conference (PVSC), 2014*. Piscataway, NJ: IEEE; 2014:1563-1566. doi:10.1109/PVSC.2014.6925216

17. Liu M, Johnston MB, Snaith HJ. Efficient planar heterojunction perovskite solar cells by vapour deposition. *Nature*. 2013;501(7467):395-398. doi:10.1038/nature12509

18. Hinsch A, Mastroianni S, Brandt H, Heinz F, Schubert MC, Veurman W. Introduction to in-Situ Produced Perovskite Solar Cells; a New Concept towards Lowest Module Manufacturing Costs: 5 pages / 29th European Photovoltaic Solar Energy Conference and Exhibition; 1493-1497 / 29th European Photovoltaic Solar Energy Conference a. 2014. doi:10.4229/EUPVSEC20142014-3BO.8.5

19. Kim H-S, Lee C-R, Im J-H, et al. Lead iodide perovskite sensitized all-solid-state submicron thin film mesoscopic solar cell with efficiency exceeding 9%. *Sci Rep*. 2012;2:591. doi:10.1038/srep00591

20. Lee MM, Teuscher J, Miyasaka T, Murakami TN, Snaith HJ. Efficient hybrid solar cells based on meso-superstructured organometal halide perovskites. *Science*. 2012;338(6107):643-647. doi:10.1126/science.1228604

21. Laban WA, Etgar L. Depleted hole conductor-free lead halide iodide heterojunction solar cells. *Energy Environ Sci*. 2013;6(11):3249. doi:10.1039/c3ee42282h

22. Jiang Q, Zhao Y, Zhang X, et al. Surface passivation of perovskite film for efficient solar cells. *Nat Photonics*. 2019;13(7):460-466. doi:10.1038/s41566-019-0398-2

23. Jeng J-Y, Chiang Y-F, Lee M-H, et al. CH3NH3PbI3 perovskite/fullerene planar-heterojunction hybrid solar cells. *Adv Mater*. 2013;25(27):3727-3732. doi:10.1002/adma.201301327

24. Tang J, Jiao D, Zhang L, et al. High-performance inverted planar perovskite solar cells based on efficient hole-transporting layers from well-crystalline NiO nanocrystals. *Sol Energy*. 2018;161:100-108. doi:10.1016/j.solener.2017.12.045

25. Zheng X, Hou Y, Bao C, et al. Managing grains and interfaces via ligand anchoring enables 22.3%-efficiency inverted perovskite solar cells. *Nat Energy*. 2020;5(2):131-140. doi:10.1038/s41560-019-0538-4

26. Heo JH, Im SH, Noh JH, et al. Efficient inorganic--organic hybrid heterojunction solar cells containing perovskite compound and polymeric hole conductors. *Nat Photonics*. 2013;7(6):486-491. doi:10.1038/nphoton.2013.80

27. Giordano F, Abate A, Correa Baena JP, et al. Enhanced electronic properties in mesoporous TiO2 via lithium doping for high-efficiency perovskite solar cells. *Nat Commun*. 2016;7:10379. doi:10.1038/ncomms10379

28. Meng L, You J, Yang Y. Addressing the stability issue of perovskite solar cells for commercial applications. *Nat Commun*. 2018;9(1):5265. doi:10.1038/s41467-018-07255-1

29. Kim S, Bae S, Lee S-W, et al. Relationship between ion migration and interfacial degradation of CH3NH3PbI3 perovskite solar cells under thermal conditions. *Sci Rep*. 2017;7(1):1200. doi:10.1038/s41598-017-00866-6

30. Ito S, Kanaya S, Nishino H, Umeyama T, Imahori H. Material Exchange Property of Organo Lead Halide Perovskite with Hole-Transporting Materials. *Photonics*. 2015;2(4):1043-1053. doi:10.3390/photonics2041043

31. Kay A, Grätzel M. Low cost photovoltaic modules based on dye sensitized nanocrystalline titanium dioxide and carbon powder. *Sol Energy Mater Sol Cells*. 1996;44(1):99-117. doi:10.1016/0927-0248(96)00063-3

32. Mei A, Li X, Liu L, et al. A hole-conductor-free, fully printable mesoscopic perovskite solar cell with high stability. *Science*. 2014;345(6194):295-298. doi:10.1126/science.1254763

33. Liu T, Liu L, Hu M, et al. Critical parameters in TiO2/ZrO2/Carbon-based mesoscopic perovskite solar cell. *J Power Sources*. 2015;293:533-538. doi:10.1016/j.jpowsour.2015.05.106

34. Samiee Esfahani M. *Device Physics of Organic and Perovskite Solar Cells*.; 2015. doi:10.31274/etd-180810-4563

35. Marchioro A, Teuscher J, Friedrich D, et al. Unravelling the mechanism of photoinduced charge transfer processes in lead iodide perovskite solar cells. *Nat Photonics*. 2014;8(3):250-255. doi:10.1038/NPHOTON.2013.374

36. Jiang Q, Zhang X, You J. SnO2 : A Wonderful Electron Transport Layer for Perovskite Solar Cells. *Small*. 2018:e1801154. doi:10.1002/smll.201801154

37. Chen J, Dong H, Zhang L, et al. Graphitic carbon nitride doped SnO 2 enabling efficient perovskite solar cells with PCEs exceeding 22%. *J Mater Chem A*. 2020;8(5):2644-2653. doi:10.1039/c9ta11344d

38. Roose B, Johansen CM, Dupraz K, et al. A Ga-doped SnO 2 mesoporous contact for UV stable highly efficient perovskite solar cells. *J Mater Chem A*. 2018;6(4):1850-1857. doi:10.1039/C7TA07663K

39. Yang D, Yang R, Wang K, et al. High efficiency planar-type perovskite solar cells with negligible hysteresis using EDTA-complexed SnO2. *Nat Commun*. 2018;9(1):3239. doi:10.1038/s41467-018-05760-x

40. Zuo L, Dong S, de Marco N, et al. Morphology Evolution of High Efficiency Perovskite Solar Cells via Vapor Induced Intermediate Phases. *J Am Chem Soc*. 2016;138(48):15710-15716. doi:10.1021/jacs.6b09656

41. Ito S, Tanaka S, Manabe K, Nishino H. Effects of Surface Blocking Layer of Sb 2 S 3 on Nanocrystalline TiO 2 for CH 3 NH 3 PbI 3 Perovskite Solar Cells. *J Phys Chem C*. 2014;118(30):16995-17000. doi:10.1021/jp500449z

42. Anaraki EH, Kermanpur A, Steier L, et al. Highly efficient and stable planar perovskite solar cells by solution-processed tin oxide. *Energy Environ Sci*. 2016;9(10):3128-3134. doi:10.1039/C6EE02390H

43. Correa Baena JP, Steier L, Tress W, et al. Highly efficient planar perovskite solar cells through band alignment engineering. *Energy Environ Sci*. 2015;8(10):2928-2934. doi:10.1039/C5EE02608C

44. Kumar MH, Yantara N, Dharani S, et al. Flexible, low-temperature, solution processed ZnO-based perovskite solid state solar cells. *Chem Commun (Camb)*. 2013;49(94):11089-11091. doi:10.1039/c3cc46534a

45. Dong X, Hu H, Lin B, Ding J, Yuan N. The effect of ALD-Zno layers on the formation of CH$_3$NH$_3$PbI$_3$ with different perovskite precursors and sintering temperatures. *Chem Commun (Camb)*. 2014;50(92):14405-14408. doi:10.1039/c4cc04685d

46. Liu D, Kelly TL. Perovskite solar cells with a planar heterojunction structure prepared using room-temperature solution processing techniques. *Nat Photonics*. 2014;8(2):133-138. doi:10.1038/nphoton.2013.342

47. Zhao D, Ke W, Grice CR, et al. Annealing-free efficient vacuum-deposited planar perovskite solar cells with evaporated fullerenes as electron-selective layers. *Nano Energy*. 2016;19:88-97. doi:10.1016/j.nanoen.2015.11.008

48. Wang JT-W, Ball JM, Barea EM, et al. Low-temperature processed electron collection layers of graphene/TiO2 nanocomposites in thin film perovskite solar cells. *Nano Lett*. 2014;14(2):724-730. doi:10.1021/nl403997a

49. Hwang I, Yong K. Novel CdS Hole-Blocking Layer for Photostable Perovskite Solar Cells. *ACS Appl Mater Interfaces*. 2016;8(6):4226-4232. doi:10.1021/acsami.5b12336

50. Huang A, Zhu J, Zheng J, et al. Room-temperature processible TiO2 electron selective layers with controllable crystallinity for high efficiency perovskite photovoltaics. *Sol Energy Mater Sol Cells*. 2017;163:15-22. doi:10.1016/j.solmat.2017.01.006

51. Juarez-Perez EJ, Wu\textgreekbler M, Fabregat-Santiago F, et al. Role of the Selective Contacts in the Performance of Lead Halide Perovskite Solar Cells. *J Phys Chem Lett*. 2014;5(4):680-685. doi:10.1021/jz500059v

52. Zardetto V, Williams BL, Perrotta A, et al. Atomic layer deposition for perovskite solar cells: research status, opportunities and challenges. *Sustain Energy Fuels*. 2017;1(1):30-55. doi:10.1039/c6se00076b

53. Yang D, Yang R, Zhang J, Yang Z, Liu S, Li C. High efficiency flexible perovskite solar cells using superior low temperature TiO 2. *Energy Environ Sci*. 2015;8(11):3208-3214. doi:10.1039/C5EE02155C

54. Gao Q, Yang S, Lei L, et al. An Effective TiO 2 Blocking Layer for Perovskite Solar Cells with Enhanced Performance. *Chem Lett*. 2015;44(5):624-626. doi:10.1246/cl.150049

55. Zardetto V, Di Giacomo F, Lucarelli G, Kessels WMM, Brown TM, Creatore M. Plasma-assisted atomic layer deposition of TiO2 compact layers for flexible mesostructured perovskite solar cells. *Sol Energy*. 2017;150:447-453. doi:10.1016/j.solener.2017.04.028

56. Wu Y, Yang X, Chen H, et al. Highly compact TiO 2 layer for efficient hole-blocking in perovskite solar cells. *Appl Phys Express*. 2014;7(5):52301. doi:10.7567/APEX.7.052301

57. Chandiran AK, Yella A, Mayer MT, Gao P, Nazeeruddin MK, Grätzel M. Sub-nanometer conformal TiO$_2$ blocking layer for high efficiency solid-state perovskite absorber solar cells. *Adv Mater*. 2014;26(25):4309-4312. doi:10.1002/adma.201306271

58. Cojocaru L, Uchida S, Sanehira Y, Nakazaki J, Kubo T, Segawa H. Surface Treatment of the Compact TiO 2 Layer for Efficient Planar Heterojunction Perovskite Solar Cells. *Chem Lett*. 2015;44(5):674-676. doi:10.1246/cl.150068

59. Rajmohan GD, Huang FZ, d'Agostino R, Du Plessis J, Dai XJ. Low temperature reactively sputtered crystalline TiO2 thin film as effective blocking layer for perovskite solar cells. *Thin Solid Films*. 2017;636:307-313. doi:10.1016/j.tsf.2017.06.037

60. Peng B, Jungmann G, Jäger C, Haarer D, Schmidt H-W, Thelakkat M. Systematic investigation of the role of compact TiO2 layer in solid state dye-sensitized TiO2 solar cells. *Coord Chem Rev*. 2004;248(13-14):1479-1489. doi:10.1016/j.ccr.2004.02.008

61. Kment S, Krysova H, Hubicka Z, Kmentova H, Kavan L, Zboril R. Very thin thermally stable TiO2 blocking layers with enhanced electron transfer for solar cells. *Appl Mater Today*. 2017;9:122-129. doi:10.1016/j.apmt.2017.05.008

62. Kim DH, Woodroof M, Lee K, Parsons GN. Atomic layer deposition of high performance ultrathin TiO$_2$ blocking layers for dye-sensitized solar cells. *ChemSusChem*. 2013;6(6):1014-1020. doi:10.1002/cssc.201300067

63. Dong Q, Wang M, Zhang Q, et al. Discontinuous SnO 2 derived blended-interfacial-layer in mesoscopic perovskite solar cells: Minimizing electron transfer resistance and improving stability. *Nano Energy*. 2017;38:358-367. doi:10.1016/j.nanoen.2017.05.058

64. Li W, Jiang Q, Yang J, et al. Improvement of photovoltaic performance of perovskite solar cells with a ZnO/Zn2SnO4 composite compact layer. *Sol Energy Mater Sol Cells*. 2017;159:143-150. doi:10.1016/j.solmat.2016.09.007

65. Fernandes SL, Véron AC, Neto NFA, et al. Nb2O5 hole blocking layer for hysteresis-free perovskite solar cells. *Mater Lett*. 2016;181:103-107. doi:10.1016/j.matlet.2016.06.018

66. Tu Y, Wu J, Zheng M, et al. TiO2 quantum dots as superb compact block layers for high-performance CH3NH3PbI3 perovskite solar cells with an efficiency of 16.97. *Nanoscale*. 2015;7(48):20539-20546. doi:10.1039/C5NR05563F

67. Cao J, Wu B, Chen R, et al. Efficient, Hysteresis-Free, and Stable Perovskite Solar Cells with ZnO as Electron-Transport Layer: Effect of Surface Passivation. *Adv Mater*. 2018;30(11). doi:10.1002/adma.201705596

68. Song J, Li SP, Zhao YL, et al. Performance enhancement of perovskite solar cells by doping TiO2 blocking layer with group VB elements. *J Alloys Compd*. 2017;694:1232-1238. doi:10.1016/j.jallcom.2016.10.106

69. Li H, Zheng B, Xue Y, Liu S, Gao C, Liu X. Spray deposited lanthanum doped TiO 2 compact layers as electron selective contact for perovskite solar cells. *Sol Energy Mater Sol Cells*. 2017;168:85-90. doi:10.1016/j.solmat.2017.04.027

70. Wang J, Qin M, Tao H, et al. Performance enhancement of perovskite solar cells with Mg-doped TiO 2 compact film as the hole-blocking layer. *Appl Phys Lett*. 2015;106(12):121104. doi:10.1063/1.4916345

71. Shalan AE, Narra S, Oshikiri T, et al. Optimization of a compact layer of TiO 2 via atomic-layer deposition for high-performance perovskite solar cells. *Sustain Energy Fuels*. 2017;1(7):1533-1540. doi:10.1039/C7SE00220C

72. Ke W, Fang G, Wang J, et al. Perovskite solar cell with an efficient TiO$_2$ compact film. *ACS Appl Mater Interfaces*. 2014;6(18):15959-15965. doi:10.1021/am503728d

73. Zhang C, Luo Y, Chen X, et al. Influence of different TiO2 blocking films on the photovoltaic performance of perovskite solar cells. *Appl Surf Sci*. 2016;388:82-88. doi:10.1016/j.apsusc.2016.03.093

74. Li S, Zhao Y, Gu X, Qiang Y, Tan N. Improved performance of perovskite solar cells by optimizing deposition parameters of TiO2 compact layers. *J Mater Sci Mater Electron*. 2017;28(18):13626-13632. doi:10.1007/s10854-017-7203-0

75. Vivo P, Ojanperä A, Smått J-H, et al. Influence of TiO2 compact layer precursor on the performance of perovskite solar cells. *Org Electron*. 2017;41:287-293. doi:10.1016/j.orgel.2016.11.017

76. Su T-S, Hsieh T-Y, Wei T-C. Electrodeposited TiO 2 Film with Mossy Nanostructure for Efficient Compact Layer in Scaffold-Type Perovskite Solar Cell. *Sol RRL*. 2018;2(3):1700120. doi:10.1002/solr.201700120

77. Hong S, Han A, Lee EC, et al. A facile and low-cost fabrication of TiO2 compact layer for efficient perovskite solar cells. *Curr Appl Phys*. 2015;15(5):574-579. doi:10.1016/j.cap.2015.01.028

78. Inaba K, Kobayashi S, Uehara K, Okada A, Reddy SL, Endo T. High Resolution X-Ray Diffraction Analyses of (La,Sr)MnO_3/ZnO/Sapphire(0001) Double Heteroepitaxial Films. *Adv Mater Phys Chem*. 2013;03(01):72-89. doi:10.4236/ampc.2013.31A010

79. Liu T, Rong Y, Xiong Y, et al. Spacer improvement for efficient and fully printable mesoscopic perovskite solar cells. *RSC Adv*. 2017;7(17):10118-10123. doi:10.1039/c6ra25347d

80. Zimmermann I, Gratia P, Martineau D, et al. Improved efficiency and reduced hysteresis in ultra-stable fully printable mesoscopic perovskite solar cells through incorporation of CuSCN into the perovskite layer. *J Mater Chem A*. 2019;7(14):8073-8077. doi:10.1039/c9ta00669a

81. Wagner L, Chacko S, Mathiazhagan G, Mastroianni S, Hinsch A. High Photovoltage of 1 V on a Steady-State Certified Hole Transport Layer-Free Perovskite Solar Cell by a Molten-Salt Approach. *ACS Energy Lett*. 2018;3(5):1122-1127. doi:10.1021/acsenergylett.8b00293

82. Tsai C-M, Wu G-W, Narra S, et al. Control of preferred orientation with slow crystallization for carbon-based mesoscopic perovskite solar cells attaining efficiency 15%. *J Mater Chem A*. 2017;5(2):739-747. doi:10.1039/c6ta09036b

83. Zhang H, Wang H, Williams ST, et al. SrCl2 Derived Perovskite Facilitating a High Efficiency of 16% in Hole-Conductor-Free Fully Printable Mesoscopic Perovskite Solar Cells. *Adv Mater*. 2017;29(15):1606608. doi:10.1002/adma.201606608

84. Liu S, Huang W, Liao P, et al. 17% efficient printable mesoscopic PIN metal oxide framework perovskite solar cells using cesium-containing triple cation perovskite. *J Mater Chem A*. 2017;5(44):22952-22958. doi:10.1039/C7TA07660F

85. Xiong Y, Zhu X, Mei A, et al. Bifunctional Al 2 O 3 Interlayer Leads to Enhanced Open-Circuit Voltage for Hole-Conductor-Free Carbon-Based Perovskite Solar Cells. *Sol RRL*. 2018;2(5):1800002. doi:10.1002/solr.201800002

86. Fu Z, Xu M, Sheng Y, et al. Encapsulation of Printable Mesoscopic Perovskite Solar Cells Enables High Temperature and Long--Term Outdoor Stability. *Adv Funct Mater*. 2019;29(16):1809129. doi:10.1002/adfm.201809129

87. Bashir A, Lew JH, Shukla S, et al. Cu-doped nickel oxide interface layer with nanoscale thickness for efficient and highly stable printable carbon-based perovskite solar cell. *Sol Energy*. 2019;182:225-236. doi:10.1016/j.solener.2019.02.056

88. Grancini G, Roldán-Carmona C, Zimmermann I, et al. One-Year stable perovskite solar cells by 2D/3D interface engineering. *Nat Commun*. 2017;8:15684. doi:10.1038/ncomms15684

89. Kaur G. *Biomedical, Therapeutic and Clinical Applications of Bioactive Glasses*. Oxford: Woodhead Publishing; 2018. doi:10.1016/C2016-0-03487-3

90. Li Fan, Jiao Junkai, Luo Haiyun, Du Junan and Lin Feng. Preliminary study of glow discharge plasms on th static pressure measurement. 2014. https://gpps.global/documents/events/zurich17/papers/control-instrumentation/GPPF_2017_paper_107.pdf.

91. Hideaki Adachi KW. *Handbook of Sputtering Technology*. 2nd ed.; 2012.

92. He W. ALD: Atomic Layer Deposition, Precise and Conformal Coating for Better Performance. In: Nee A, ed. *Handbook of Manufacturing Engineering and Technology*. London: {Springer London} and {Imprint: Springer}; 2020:1-33. doi:10.1007/978-1-4471-4976-7{\textunderscore }80-1

93. Detavernier C, Dendooven J, Sree SP, Ludwig KF, Martens JA. Tailoring nanoporous materials by atomic layer deposition. *Chem Soc Rev*. 2011;40(11):5242-5253. doi:10.1039/c1cs15091j

94. Aliano A, Cicero G, Nili H, et al. Atomic Layer Deposition. In: Bhushan B, ed. *Encyclopedia of Nanotechnology*. Springer reference. Dordrecht and London: Springer; 2012:161-171. doi:10.1007/978-90-481-9751-4{\textunderscore }372

95. Perednis D, Gauckler LJ. Thin Film Deposition Using Spray Pyrolysis. *J Electroceramics*. 2005;14(2):103-111. doi:10.1007/s10832-005-0870-x

96. Moholkar A V. *Transparent Conductors*. [Place of publication not identified]: Lap Lambert Academic Publ; 2011.

97. Ossila. Slot-die coating:Theory, Design , and Applications. https://www.ossila.com/pages/slot-die-coating-theory).

98. Hobby A (DEK PML. No Title. http://www.gwent.org/gem_screen_printing.html.

99. Mochel ME, Dümler I, Greene A, Eades JA. Scanning electron microscopy, X-ray microanalysis, and analytical electron microscopy. A laboratory workbook, By Charles E. Lyman, Dale E. Newbury, Joseph I. Goldstein, David B. Williams, Alton D. Romig Jr., John T. Armstrong, Patrick Echlin, Charles E. F. *J Electron Microsc Tech*. 1991;19(3):379. doi:10.1002/jemt.1060190312

100. Jiang X, Higuchi T, Jinnai H. Scanning Electron Microscopy. In: Maeda M, Takahara A, Kitano H, Yamaoka T, Miura Y, eds. *Molecular Soft-Interface Science*. Tokyo, Japan: Springer; 2019:141-146. doi:10.1007/978-4-431-56877-3{\textunderscore }9

101. Sun J, Zhang Z, Gong Y, et al. Plasma engraved Bi0.1(Ba0.5Sr0.5)0.9Co0.8Fe0.2O3-\textgreek{d} perovskite for highly active and durable oxygen evolution. *Sci Rep*. 2019;9(1):4210. doi:10.1038/s41598-019-40972-1

102. Savile Bradbury, David C. Joy. Transmission electron microscope. https://www.britannica.com/technology/transmission-electron-microscope.

103. Binnig, Quate, Gerber. Atomic force microscope. *Phys Rev Lett*. 1986;56(9):930-933. doi:10.1103/PhysRevLett.56.930

104. Martin Y, Williams CC, Wickramasinghe HK. Atomic force microscope--force mapping and profiling on a sub 100--Åscale. *J Appl Phys*. 1987;61(10):4723-4729. doi:10.1063/1.338807

105. Michael Hirtz. Surface structuring by bottom-up and top-down approcahes. 2009.

106. Lecture notes. AFM. https://my.eng.utah.edu/~lzang/images/Lecture_10_AFM.pdf. Accessed June 16, 2020.

107. Wuhrer R, Moran K. A new life for the wavelength-dispersive X-ray spectrometer (WDS): incorporation of a silicon drift detector into the WDS for improved quantification and X-ray mapping. *IOP Conf Ser Mater Sci Eng*. 2018;304:12021. doi:10.1088/1757-899X/304/1/012021

108. Sobarwiki. Schematic of UV- visible spectrophotometer. https://commons.wikimedia.org/wiki/File:Schematic_of_UV-_visible_spectrophotometer.png.

109. University of Colorado at Boulder. UV-Visibile and Fluorescence spectroscopy. https://orgchemboulder.com/Labs/Handbook/UV-Vis.pdf.

110. Yuguo (Hugo) Zhang and Hang Li. Light absorption and photoluminescence (PL) spectroscopy. 2019. https://chem.libretexts.org/Courses/Franklin_and_Marshall_College/Introduction_to_Materials_Characterization_-_CHM_412_Collaborative_Text/Spectroscopy/Light_absorption_and_photoluminescence_(PL)_spectroscopy.

111. F. Al-Rawashdeh NA. Current Achievement and Future Potential of Fluorescence Spectroscopy. In: Uddin J, ed. *Identification, Quantitative Determination, and Antioxidant Properties of Polyphenols of Some Malian Medicinal Plant Parts Used in Folk Medicine*. INTECH Open Access Publisher; 2012. doi:10.5772/48034

112. Thermo scientific. What is X-Ray Photoelectron Spectroscopy (XPS)? https://xpssimplified.com/whatisxps.php#:~:text=XPS spectra are obtained by,range of electron kinetic energies.

113. Domenico Regonini. Anodised TiO2 Nanotubes: Synthesis, growth mechanisms and thermal stability.

114. Malbila E, Delvoie S, Toguyeni D, Attia S, Courard L. An Experimental Study on the Use of Fonio Straw and Shea Butter Residue for Improving the Thermophysical and Mechanical Properties of Compressed Earth Blocks. *J Miner Mater Charact Eng*. 2020;08(03):107-132. doi:10.4236/jmmce.2020.83008

115. Ogunlaja SB, Pal R. Effects of Bentonite Nanoclay and Cetyltrimethyl Ammonium Bromide Modified Bentonite Nanoclay on Phase Inversion of Water-in-Oil Emulsions. *Colloids and Interfaces*. 2020;4(1):2. doi:10.3390/colloids4010002

116. Breitenstein O, Warta W, Langenkamp M. *Lock-in Thermography: Basics and Applications to Functional Diagnostics of Electronic Components*. Vol 10. Berlin and London: Springer; 2011. doi:10.1007/978-3-662-08396-3

117. PV Performance Modeling Collaborative. Single Diode Equivalent Circuit Models. https://pvpmc.sandia.gov/modeling-steps/2-dc-module-iv/diode-equivalent-circuit-models/. Accessed June 16, 2020.

118. Sidi P, Sukoco D, Purnomo W, Sudibyo H, Hartanto D. Electric Energy Management and Engineering in Solar Cell System. In: Morales-Acevedo A, ed. *Solar Cells*. Rijeka: InTech; 2013. doi:10.5772/52572

119. Solmetric. Guide To Interpreting I-V Curve Measurements of PV Arrays. 2011. http://resources.solmetric.com/get/Guide to Interpreting I-V Curves.pdf. Accessed June 16, 2020.

120. Green MA. *Solar Cells: Operating Principles, Technology, and System Applications / Martin A. Green*. Englewood Cliffs and London: Prentice-Hall; 1982.

121. Reese MO, Gevorgyan SA, Jørgensen M, et al. Consensus stability testing protocols for organic photovoltaic materials and devices. *Sol Energy Mater Sol Cells*. 2011;95(5):1253-1267. doi:10.1016/j.solmat.2011.01.036

122. Urbina A. The balance between efficiency, stability and environmental impacts in perovskite solar cells: a review. *J Phys Energy*. 2020;2(2):22001. doi:10.1088/2515-7655/ab5eee

123. Zimmermann E, Wong KK, Müller M, et al. Characterization of perovskite solar cells: Towards a reliable measurement protocol. *APL Mater*. 2016;4(9):91901. doi:10.1063/1.4960759

124. Caprioglio P, Stolterfoht M, Wolff CM, et al. On the Relation between the Open--Circuit Voltage and Quasi--Fermi Level Splitting in Efficient Perovskite Solar Cells. *Adv Energy Mater*. 2019;9(33):1901631. doi:10.1002/aenm.201901631

125. Gao X, Li J, Baker J, et al. Enhanced photovoltaic performance of perovskite CH 3 NH 3 PbI 3 solar cells with freestanding TiO 2 nanotube array films. *Chem Commun*. 2014;50(48):6368-6371. doi:10.1039/C4CC01864H

126. Liu Z, Sun B, Shi T, Tang Z, Liao G. Enhanced photovoltaic performance and stability of carbon counter electrode based perovskite solar cells encapsulated by PDMS. *J Mater Chem A*. 2016;4(27):10700-10709. doi:10.1039/C6TA02851A

127. Zaban A, Greenshtein M, Bisquert J. Determination of the electron lifetime in nanocrystalline dye solar cells by open-circuit voltage decay measurements. *Chemphyschem*. 2003;4(8):859-864. doi:10.1002/cphc.200200615

128. Di Giacomo F, Zardetto V, Lucarelli G, et al. Mesoporous perovskite solar cells and the role of nanoscale compact layers for remarkable all-round high efficiency under both indoor and outdoor illumination. *Nano Energy*. 2016;30:460-469. doi:10.1016/j.nanoen.2016.10.030

129. Macdonald D, Sinton RA, Cuevas A. On the use of a bias-light correction for trapping effects in photoconductance-based lifetime measurements of silicon. *J Appl Phys*. 2001;89(5):2772-2778. doi:10.1063/1.1346652

130. Schiefer S, Zimmermann B, Glunz SW, Wurfel U. Applicability of the Suns-V$_{\rm OC}$ Method on Organic Solar Cells. *IEEE J Photovoltaics*. 2014;4(1):271-277. doi:10.1109/JPHOTOV.2013.2288527

131. Sze SM. *Semiconductor Devices: Physics and Technology / S.M. Sze*. New York: Wiley; 1985.

132. Tress W, Yavari M, Domanski K, et al. Interpretation and evolution of open-circuit voltage, recombination, ideality factor and subgap defect states during reversible light-soaking and irreversible degradation of perovskite solar cells. *Energy Environ Sci*. 2018;11(1):151-165. doi:10.1039/c7ee02415k

133. Sarritzu V, Sestu N, Marongiu D, et al. Optical determination of Shockley-Read-Hall and interface recombination currents in hybrid perovskites. *Sci Rep*. 2017;7:44629. doi:10.1038/srep44629

134. Tress W, Leo K, Riede M. Dominating recombination mechanisms in organic solar cells based on ZnPc and C 60. *Appl Phys Lett*. 2013;102(16):163901. doi:10.1063/1.4802276

135. Sarritzu V, Sestu N, Marongiu D, et al. Optical determination of Shockley-Read-Hall and interface recombination currents in hybrid perovskites. *Sci Rep*. 2017;7:44629. doi:10.1038/srep44629

136. Calado P, Burkitt D, Yao J, et al. Identifying Dominant Recombination Mechanisms in Perovskite Solar Cells by Measuring the Transient Ideality Factor. *Phys Rev Appl*. 2019;11(4). doi:10.1103/PhysRevApplied.11.044005

137. Mastroianni S, Heinz FD, Im J-H, et al. Analysing the effect of crystal size and structure in highly efficient CH3NH3PbI3 perovskite solar cells by spatially resolved photo- and electroluminescence imaging. *Nanoscale*. 2015;7(46):19653-19662. doi:10.1039/c5nr05308k

138. Stolterfoht M, Le Corre VM, Feuerstein M, Caprioglio P, Koster LJA, Neher D. Voltage-Dependent Photoluminescence and How It Correlates with the Fill Factor and Open-Circuit Voltage in Perovskite Solar Cells. *ACS Energy Lett*. 2019;4(12):2887-2892. doi:10.1021/acsenergylett.9b02262

139. Mathiazhagan G, Seeber A, Gengenbach T, et al. Improving the Stability of Ambient Processed, SnO 2 -Based, Perovskite Solar Cells by the UV-Treatment of Sub-Cells. *Sol RRL*. July 2020:2000262. doi:10.1002/solr.202000262

140. Zhao Y, Wei J, Li H, et al. A polymer scaffold for self-healing perovskite solar cells. *Nat Commun*. 2016;7:10228. doi:10.1038/ncomms10228

141. Roose B, Baena J-PC, Gödel KC, et al. Mesoporous SnO2 electron selective contact enables UV-stable perovskite solar cells. *Nano Energy*. 2016;30:517-522. doi:10.1016/j.nanoen.2016.10.055

142. Farooq A, Hossain IM, Moghadamzadeh S, et al. Spectral Dependence of Degradation under Ultraviolet Light in Perovskite Solar Cells. *ACS Appl Mater Interfaces*. 2018;10(26):21985-21990. doi:10.1021/acsami.8b03024

143. Hawash Z, Ono LK, Qi Y. Recent Advances in Spiro-MeOTAD Hole Transport Material and Its Applications in Organic-Inorganic Halide Perovskite Solar Cells. *Adv Mater Interfaces*. 2018;5(1):1700623. doi:10.1002/admi.201700623

144. Wei J, Guo F, Wang X, et al. SnO2 -in-Polymer Matrix for High-Efficiency Perovskite Solar Cells with Improved Reproducibility and Stability. *Adv Mater*. 2018;30(52):e1805153. doi:10.1002/adma.201805153

145. Tang S, Deng Y, Zheng X, et al. Composition Engineering in Doctor-Blading of Perovskite Solar Cells. *Adv Energy Mater*. 2017;7(18):1700302. doi:10.1002/aenm.201700302

146. Park M, Kim J-Y, Son HJ, Lee C-H, Jang SS, Ko MJ. Low-temperature solution-processed Li-doped SnO 2 as an effective electron transporting layer for high-performance flexible and wearable perovskite solar cells. *Nano Energy*. 2016;26:208-215. doi:10.1016/j.nanoen.2016.04.060

147. Xiong L, Qin M, Yang G, et al. Performance enhancement of high temperature SnO 2 -based planar perovskite solar cells: electrical characterization and understanding of the mechanism. *J Mater Chem A*. 2016;4(21):8374-8383. doi:10.1039/C6TA01839D

148. Yang G, Lei H, Tao H, et al. Reducing Hysteresis and Enhancing Performance of Perovskite Solar Cells Using Low-Temperature Processed Y-Doped SnO2 Nanosheets as Electron Selective Layers. *Small*. 2017;13(2). doi:10.1002/smll.201601769

149. Bai Y, Fang Y, Deng Y, et al. Low Temperature Solution-Processed Sb:SnO2 Nanocrystals for Efficient Planar Perovskite Solar Cells. *ChemSusChem*. 2016;9(18):2686-2691. doi:10.1002/cssc.201600944

150. Ren X, Yang D, Yang Z, et al. Solution-Processed Nb:SnO2 Electron Transport Layer for Efficient Planar Perovskite Solar Cells. *ACS Appl Mater Interfaces*. 2017;9(3):2421-2429. doi:10.1021/acsami.6b13362

151. Avigad E, Etgar L. Studying the Effect of MoO 3 in Hole-Conductor-Free Perovskite Solar Cells. *ACS Energy Lett*. 2018;3(9):2240-2245. doi:10.1021/acsenergylett.8b01169

152. Angmo D, Peng X, Seeber A, et al. Controlling Homogenous Spherulitic Crystallization for High-Efficiency Planar Perovskite Solar Cells Fabricated under Ambient High-Humidity Conditions. *Small*. 2019;15(49):e1904422. doi:10.1002/smll.201904422

153. Angmo D, Peng X, Cheng J, et al. Beyond Fullerenes: Indacenodithiophene-Based Organic Charge-Transport Layer toward Upscaling of Low-Cost Perovskite Solar Cells. *ACS Appl Mater Interfaces*. 2018;10(26):22143-22155. doi:10.1021/acsami.8b04861

154. Galagan Y, Di Giacomo F, Gorter H, et al. Roll-to-Roll Slot Die Coated Perovskite for Efficient Flexible Solar Cells. *Adv Energy Mater*. 2018;8(32):1801935. doi:10.1002/aenm.201801935

155. Besleaga C, Abramiuc LE, Stancu V, et al. Iodine Migration and Degradation of Perovskite Solar Cells Enhanced by Metallic Electrodes. *J Phys Chem Lett*. 2016;7(24):5168-5175. doi:10.1021/acs.jpclett.6b02375

156. Wang S, Zhu Y, Liu B, Wang C, Ma R. Introduction of carbon nanodots into SnO 2 electron transport layer for efficient and UV stable planar perovskite solar cells. *J Mater Chem A*. 2019;7(10):5353-5362. doi:10.1039/C8TA11651B

157. Ciccioli A, Latini A. Thermodynamics and the Intrinsic Stability of Lead Halide Perovskites CH3NH3PbX3. *J Phys Chem Lett*. 2018;9(13):3756-3765. doi:10.1021/acs.jpclett.8b00463

158. Bisquert J, Juarez-Perez EJ. The Causes of Degradation of Perovskite Solar Cells. *J Phys Chem Lett*. 2019;10(19):5889-5891. doi:10.1021/acs.jpclett.9b00613

159. Lee S-W, Kim S, Bae S, et al. UV Degradation and Recovery of Perovskite Solar Cells. *Sci Rep*. 2016;6:38150. doi:10.1038/srep38150

160. Wei D, Wang T, Ji J, et al. Photo-induced degradation of lead halide perovskite solar cells caused by the hole transport layer/metal electrode interface. *J Mater Chem A*. 2016;4(5):1991-1998. doi:10.1039/C5TA08622A

161. O'Mahony FTF, Lee YH, Jellett C, et al. Improved environmental stability of organic lead trihalide perovskite-based photoactive-layers in the presence of mesoporous TiO 2. *J Mater Chem A*. 2015;3(14):7219-7223. doi:10.1039/c5ta01221j

162. Leijtens T, Eperon GE, Pathak S, Abate A, Lee MM, Snaith HJ. Overcoming ultraviolet light instability of sensitized TiO$_2$ with meso-superstructured organometal tri-halide perovskite solar cells. *Nat Commun*. 2013;4:2885. doi:10.1038/ncomms3885

163. Ouyang Y, Shi L, Li Q, Wang J. Role of Water and Defects in Photo--Oxidative Degradation of Methylammonium Lead Iodide Perovskite. *Small Methods*. 2019;3(7):1900154. doi:10.1002/smtd.201900154

164. Ouyang Y, Li Y, Zhu P, et al. Photo-oxidative degradation of methylammonium lead iodide perovskite: mechanism and protection. *J Mater Chem A*. 2019;7(5):2275-2282. doi:10.1039/C8TA12193A

165. Verbakel F, Meskers SCJ, Janssen RAJ. Electronic memory effects in diodes from a zinc oxide nanoparticle-polystyrene hybrid material. *Appl Phys Lett*. 2006;89(10):102103. doi:10.1063/1.2345612

166. McLeod JA, Liu L. Prospects for Mitigating Intrinsic Organic Decomposition in Methylammonium Lead Triiodide Perovskite. *J Phys Chem Lett*. 2018;9(9):2411-2417. doi:10.1021/acs.jpclett.8b00323

167. Kong J, Song S, Yoo M, et al. Long-term stable polymer solar cells with significantly reduced burn-in loss. *Nat Commun*. 2014;5:5688. doi:10.1038/ncomms6688

168. Aristidou N, Sanchez-Molina I, Chotchuangchutchaval T, et al. The Role of Oxygen in the Degradation of Methylammonium Lead Trihalide Perovskite Photoactive Layers. *Angew Chem Int Ed Engl*. 2015;54(28):8208-8212. doi:10.1002/anie.201503153

169. Supasai T, Rujisamphan N, Ullrich K, Chemseddine A, Dittrich T. Formation of a passivating CH 3 NH 3 PbI 3 /PbI 2 interface during moderate heating of CH 3 NH 3 PbI 3 layers. *Appl Phys Lett*. 2013;103(18):183906. doi:10.1063/1.4826116

170. Kim YC, Jeon NJ, Noh JH, et al. Beneficial Effects of PbI 2 Incorporated in Organo-Lead Halide Perovskite Solar Cells. *Adv Energy Mater*. 2016;6(4):1502104. doi:10.1002/aenm.201502104

171. Chen Q, Zhou H, Song T-B, et al. Controllable self-induced passivation of hybrid lead iodide perovskites toward high performance solar cells. *Nano Lett*. 2014;14(7):4158-4163. doi:10.1021/nl501838y

172. Liu C, Zhang L, Li Y, et al. Highly Stable and Efficient Perovskite Solar Cells with 22.0% Efficiency Based on Inorganic-Organic Dopant-Free Double Hole Transporting Layers. *Adv Funct Mater*. May 2020:1908462. doi:10.1002/adfm.201908462

173. Lee D-Y, Na S-I, Kim S-S. Graphene oxide/PEDOT:PSS composite hole transport layer for efficient and stable planar heterojunction perovskite solar cells. *Nanoscale*. 2016;8(3):1513-1522. doi:10.1039/C5NR05271H

174. Etgar L. *Hole Conductor Free Perovskite-Based Solar Cells*. Cham and s.l.: Springer International Publishing; 2016. doi:10.1007/978-3-319-32991-8

175. Liu D, Yang J, Kelly TL. Compact layer free perovskite solar cells with 13.5% efficiency. *J Am Chem Soc*. 2014;136(49):17116-17122. doi:10.1021/ja508758k

176. Huang C, Lin P, Fu N, et al. Facile fabrication of highly efficient ETL-free perovskite solar cells with 20% efficiency by defect passivation and interface engineering. *Chem Commun (Camb)*. 2019;55(19):2777-2780. doi:10.1039/C9CC00312F

177. Liao J-F, Wu W-Q, Jiang Y, Zhong J-X, Wang L, Kuang D-B. Understanding of carrier dynamics, heterojunction merits and device physics: towards designing efficient carrier transport layer-free perovskite solar cells. *Chem Soc Rev*. 2020;49(2):354-381. doi:10.1039/C8CS01012A

178. Wu W-Q, Wang Q, Fang Y, et al. Molecular doping enabled scalable blading of efficient hole-transport-layer-free perovskite solar cells. *Nat Commun*. 2018;9(1):1625. doi:10.1038/s41467-018-04028-8

179. Liu D, Wang Q, Traverse CJ, et al. Impact of Ultrathin C 60 on Perovskite Photovoltaic Devices. *ACS Nano*. 2018;12(1):876-883. doi:10.1021/acsnano.7b08561

180. Bachmann J, Buerhop-Lutz C, Deibel C, et al. Organic solar cells characterized by dark lock-in thermography. *Sol Energy Mater Sol Cells*. 2010;94(4):642-647. doi:10.1016/j.solmat.2009.11.006

181. Bai Z, Yang J, Wang D. Thin film CdTe solar cells with an absorber layer thickness in micro- and sub-micrometer scale. *Appl Phys Lett*. 2011;99(14):143502. doi:10.1063/1.3644160

182. Shvydka D, Rakotoniaina JP, Breitenstein O. Lock-in thermography and nonuniformity modeling of thin-film CdTe solar cells. *Appl Phys Lett*. 2004;84(5):729-731. doi:10.1063/1.1645322

183. Breitenstein O, Warta W, Langenkamp M. *Lock-in Thermography: Basics and Use for Evaluating Electronic Devices and Materials*. Vol 10. 2. ed. Heidelberg: Springer; 2010. http://lib.myilibrary.com?id=298206.

184. Scanlon DO, Dunnill CW, Buckeridge J, et al. Band alignment of rutile and anatase TiO$_2$. *Nat Mater*. 2013;12(9):798-801. doi:10.1038/nmat3697

185. AL-Oqla FM, Sapuan SM, Fares O. Electrical–Based Applications of Natural Fiber Vinyl Polymer Composites. In: *Natural Fibre Reinforced Vinyl Ester and Vinyl Polymer Composites*. Elsevier; 2018:349-367. doi:10.1016/B978-0-08-102160-6.00018-4

186. Stepniak G, Schüppert M, Bunge C-A. Polymer-optical fibres for data transmission. In: *Polymer Optical Fibres*. Elsevier; 2017:217-310. doi:10.1016/B978-0-08-100039-7.00008-7

187. Mathiazhagan G, Wagner L, Bogati S, et al. Double-Mesoscopic Hole-Transport-Material-Free Perovskite Solar Cells: Overcoming Charge-Transport Limitation by Sputtered Ultrathin Al 2 O 3 Isolating Layer. 2020. doi:10.1021/acsanm.9b02563

188. Mali SS, Hong CK, Inamdar AI, Im H, Shim SE. Efficient planar n-i-p type heterojunction flexible perovskite solar cells with sputtered TiO2 electron transporting layers. *Nanoscale*. 2017;9(9):3095-3104. doi:10.1039/C6NR09032J

189. Ge S, Xu H, Wang W, et al. The improvement of open circuit voltage by the sputtered TiO2 layer for efficient perovskite solar cell. *Vacuum*. 2016;128:91-98. doi:10.1016/j.vacuum.2016.03.013

190. Gong J, Darling SB, You F. Perovskite photovoltaics: life-cycle assessment of energy and environmental impacts. *Energy Environ Sci*. 2015;8(7):1953-1968. doi:10.1039/C5EE00615E

191. Stevanovic A, Ma S, Yates JT. Photoexcited Electron Hopping between TiO 2 Particles: Effect of Single-Walled Carbon Nanotubes. *J Phys Chem C*. 2014;118(41):23614-23620. doi:10.1021/jp508061w

192. Krückemeier L, Rau U, Stolterfoht M, Kirchartz T. How to Report Record Open--Circuit Voltages in Lead--Halide Perovskite Solar Cells. *Adv Energy Mater*. 2019:1902573. doi:10.1002/aenm.201902573

Perovskite solar cells (PSCs) are gaining increasing importance and attention in the last decade. Even though high conversion efficiencies have been reached, one of the major bottlenecks for the commercialization of PSCs is their stability. Issues at the interfaces in the multilayered PSC architecture are suspected to be the significant contributor in causing low stability.

This doctoral thesis focusses on the analysis of various interfaces present in PSCs and traces methods to improve them. The investigation of individual interfaces is performed by developing suitable sub-cells, i.e., comprising only the particular interface of interest. Various optical and structural characterization methods are used to determine layer and interface properties. After this step, complete devices are manufactured from the sub-cells, and their final performance is investigated to conclude the role and optimization of the interfaces.

ISBN 978-3-8396-1839-4

Fraunhofer VERLAG